

Estimation of heat transport coefficients in fusion plasmas

Citation for published version (APA):

Berkel, van, M. (2015). *Estimation of heat transport coefficients in fusion plasmas*. [Phd Thesis 1 (Research TU/e / Graduation TU/e), Mechanical Engineering]. Technische Universiteit Eindhoven.

Document status and date:

Published: 01/01/2015

Document Version:

Publisher's PDF, also known as Version of Record (includes final page, issue and volume numbers)

Please check the document version of this publication:

- A submitted manuscript is the version of the article upon submission and before peer-review. There can be important differences between the submitted version and the official published version of record. People interested in the research are advised to contact the author for the final version of the publication, or visit the DOI to the publisher's website.
- The final author version and the galley proof are versions of the publication after peer review.
- The final published version features the final layout of the paper including the volume, issue and page numbers.

[Link to publication](#)

General rights

Copyright and moral rights for the publications made accessible in the public portal are retained by the authors and/or other copyright owners and it is a condition of accessing publications that users recognise and abide by the legal requirements associated with these rights.

- Users may download and print one copy of any publication from the public portal for the purpose of private study or research.
- You may not further distribute the material or use it for any profit-making activity or commercial gain
- You may freely distribute the URL identifying the publication in the public portal.

If the publication is distributed under the terms of Article 25fa of the Dutch Copyright Act, indicated by the "Taverne" license above, please follow below link for the End User Agreement:

www.tue.nl/taverne

Take down policy

If you believe that this document breaches copyright please contact us at:

openaccess@tue.nl

providing details and we will investigate your claim.

ESTIMATION OF HEAT TRANSPORT COEFFICIENTS IN FUSION PLASMAS

MATTHIJS VAN DER KEL

mmxv



This research, supported by the FOM programme 120 and the European Communities under the contract of the Association EUROATOM/FOM, was carried out within the framework of the European Fusion Programme. The views and opinions expressed in this thesis do not necessarily reflect those of the European Commission.

This work was supported by the Japan Society for the Promotion of Science (JSPS) under the Postdoctoral Fellowship for North American and European Researchers (Short-Term) program 2014.



The work was carried out at the Control Systems Technology group at the Mechanical Engineering department of the Eindhoven University of Technology in collaboration with the National Institute for Fusion Science (Japan), and the Vrije Universiteit Brussel (Belgium).

A catalogue record is available from the Eindhoven University of Technology Library.
ISBN: 978-90-386-3868-3

Reproduction: Ipskamp Drukkers, Enschede, The Netherlands.

Cover: Monochrome of the inside of the Large Helical Device. Photo provided by the National Institute for Fusion Science and reproduced with permission.

©2015 by M. van Berkel. All rights reserved.

Estimation of heat transport coefficients in fusion plasmas

PROEFSCHRIFT

ter verkrijging van de graad van doctor aan de
Technische Universiteit Eindhoven, op gezag van de
rector magnificus prof.dr.ir. F.P.T. Baaijens, voor een
commissie aangewezen door het College voor
Promoties, in het openbaar te verdedigen
op dinsdag 2 juni 2015 om 16.00 uur

door

Matthijs van Berkel

geboren te 's-Hertogenbosch

Dit proefschrift is goedgekeurd door de promotoren en de samenstelling van de promotiecommissie is als volgt:

voorzitter:	prof.dr. L.P.H. de Goey
1 ^e promotor:	prof.dr. M.R. de Baar
2 ^e promotor:	prof.dr.ir. G. Vandersteen (Vrije Universiteit Brussel)
copromotor:	prof.dr. H.J. Zwart
leden:	dr. G.M.D. Hogewij (FOM DIFFER)
	prof.dr. K. Ida (National Institute for Fusion Science)
	prof.dr. N.J. Lopes Cardozo
	prof.dr. S. Weiland

in cauda venenum

聖子へ

Contents

1	Introduction	1
1.1	Fusion	1
1.1.1	Magnetic confinement	2
1.1.2	Magnetic equilibrium	3
1.1.3	Classical and neo-classical transport	3
1.1.4	Turbulent transport	4
1.2	Measuring transport	5
1.2.1	Steady-state and perturbative transport analysis	5
1.2.2	Overview of perturbative experiments	6
1.2.3	Perturbative experiments: actuator and sensor	7
1.3	Methods for estimating transport coefficients	9
1.4	Objectives and contributions of this thesis	11
1.4.1	Activities and layout	11
1.4.2	Specific contributions	12
1.5	Outline of this thesis	14
2	Mathematical modeling of heat transport in tokamaks and stellarators	17
2.1	Transport modeling	18
2.1.1	Conservation of energy and particles	18
2.1.2	Perturbative transport analysis	19
2.1.3	Slab geometry representation and its relationship to cylindrical geometry	20
2.2	Analytical solutions in the Laplace domain	21
2.2.1	Slab geometry	21
2.2.2	Cylindrical geometry	22
2.3	Logarithmic derivative and transfer function	23
2.3.1	Semi-infinite domain and logarithmic temperature derivative	23

2.3.2	Transfer function and spatial derivatives	26
2.3.3	Double spatial derivatives of A and ϕ	28
2.4	Directionality of heat waves	29
2.5	Conclusion and summary	31
3	Estimation of the transport coefficients using slab geometry (semi-infinite)	33
3.1	Derivation of explicit approximations based on slab geometry . .	34
3.1.1	Approximations for χ in the presence V and τ_{inv}	34
3.1.2	Approximations for V and τ_{inv}	35
3.1.3	Approximations assuming $\tau_{inv} = 0$	36
3.2	Estimating χ under influence of V and τ_{inv}	37
3.2.1	Diffusivity only	37
3.2.2	Diffusivity and damping	38
3.2.3	Diffusivity, convectivity, and damping	39
3.3	Estimating the convectivity and damping	41
3.3.1	Estimation of V and τ_{inv} in a semi-infinite cylindrical geometry	41
3.3.2	The effect of boundary conditions and radial dependent profiles	43
3.4	Summary	45
4	Estimation of the transport coefficients for heat waves propagating outwards (semi-infinite)	49
4.1	Derivation of explicit approximations	50
4.1.1	Continued fractions	50
4.1.2	Asymptotic expansions	52
4.1.3	Multiple harmonics	55
4.2	Outward solutions	56
4.2.1	Overview of possible explicit approximations	57
4.2.2	Diffusivity only	57
4.2.3	Diffusivity and damping only	61
4.2.4	Diffusivity and convectivity with $\tau_{inv} = 0$ and $\tau_{inv} = 2$. .	62
4.2.5	Summary	62
4.3	Choice and validation of approximations	63
4.4	Conclusions and summary	65
5	Estimation of the transport coefficients for heat waves propagating inwards (symmetry)	67
5.1	Derivation of explicit approximations using continued fractions .	67
5.1.1	Derivation of inward approximations for the diffusivity and the damping only	68
5.1.2	Diffusivity, convectivity, and damping	69
5.2	Inward solutions	71

5.2.1	Overview of possible explicit approximations	71
5.2.2	Selection of interesting approximations	75
5.2.3	Diffusivity and damping only	76
5.2.4	Diffusivity and convectivity with $\tau_{inv} = 0$ and $\tau_{inv} = 2$	76
5.3	Conclusion and summary	77
6	Estimation of the diffusivity taking frequency measurement un-	
	certainties into account	81
6.1	Distributions of phase and amplitude and its spatial derivatives	83
6.1.1	Gaussian noise as the result of the central limit theorem	83
6.1.2	Normal complex circular distributed noise	84
6.1.3	Amplitude and phase distributions and their confidence bounds	85
6.1.4	Distributions of ϕ' and A'/A	87
6.2	Distributions of the diffusivity χ	90
6.2.1	Inverse non-central chi-squared distribution	90
6.2.2	Confidence bounds non-central inverse chi-squared distribution	91
6.2.3	Inverse product distribution function	92
6.3	Estimating means and (co-)variances from measurements	94
6.3.1	Noise distribution of ASDEX Upgrade measurements	94
6.3.2	Estimating the Fourier coefficients and variances	95
6.3.3	Resulting A'/A and ϕ' for AUG 17175 at $\rho_t = 0.473$ and $\rho_t = 0.484$	98
6.4	Estimating χ	100
6.4.1	Combining amplitude and phase estimates	100
6.4.2	Combining different harmonics for ϕ' and A'/A only	103
6.4.3	Combining different harmonics using the product $\phi' A'/A$	106
6.4.4	Calibration errors	110
6.4.5	Summary estimating χ with confidence	111
6.5	Conclusions and discussion	113
7	Frequency domain sample maximum likelihood estimation for	
	spatially dependent parameter estimation in PDEs	115
7.1	Introduction	115
7.2	Modeling	118
7.2.1	Considered partial differential equation	119
7.2.2	Local domain based on two measurements	119
7.2.3	Local domain based on three measurements	120
7.2.4	Change of variables	120
7.3	Sample maximum likelihood estimator	121
7.3.1	Error model: errors-in-variables	122
7.3.2	Maximum likelihood cost	122

7.3.3	Optimization and confidence bounds	123
7.3.4	Cost function model validation	124
7.3.5	Input design and choice of domain	124
7.4	Simulation results	125
7.4.1	Estimator and confidence bound validation	126
7.4.2	Finite difference simulation	126
7.4.3	Model validation of finite difference simulation	127
7.5	Conclusions and discussion	129
8	Conclusions, discussion and recommendations	131
8.1	Conclusions	131
8.2	Discussion and recommendations	135
8.2.1	Improvement of the estimation	135
8.2.2	Study of transport	138
8.2.3	Extension to other fields	139
A	Analytic eigenfunctions of PDEs	141
A.1	The Bessel and confluent hypergeometric ODEs	141
A.2	Power series representation	142
A.2.1	Example: derivation of power series solution of the Bessel function of first kind of order $\nu = 0$	143
A.3	Numerical evaluation	145
A.4	Solutions in terms of Bessel and confluent hypergeometric func- tions	147
A.4.1	Cylindrical geometry with constant coefficients	147
B	Derivation of approximations using continued fractions	151
B.1	Continued J -fraction of the ratio of Bessel functions of the second kind	151
B.2	Continued C -fraction of the ratio of Bessel functions of the second kind	152
B.3	Continued T -fraction of the ratio of Bessel functions of the first kind	152
B.4	Continued C -fraction of confluent hypergeometric functions . . .	153
B.5	Continued J -fraction in case $V = \tau_{inv} = 0$	156
B.6	Approximation for the continued S -fraction for $V = \tau_{inv} = 0$. .	156
B.7	Asymptotic expansion based on the Bessel function of the second kind	157
C	Distribution functions of A and ϕ and numerical calculation of confidence bounds	159
C.1	Distributions of amplitude and phase	159
C.2	Numerical calculation confidence bounds	160

Summary	175
Societal summary	179
Acknowledgements	181
List of publications	185
Curriculum vitae	189

Chapter 1

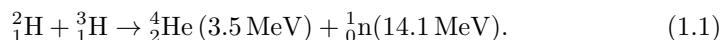
Introduction

In controlled nuclear fusion hydrogen isotopes are fused in a reactor with the view to produce significant amounts of energy. The efficiency of the reactor depends on the thermal transport. Several actuators influence the thermal transport and need to be (actively) controlled. This requires an accurate measurement of thermal transport and, in particular, the coefficients with which this transport is modeled. Therefore, it is important to think about estimation methods which are fast and have high accuracy (minimum variance).

In this thesis, methodologies to estimate the transport coefficients based on perturbative experiments in fusion plasmas are developed. Special attention is paid to the inclusion of measurement uncertainty and to the estimation of the coefficients on local domains. Note that the focus lies on the estimation methods and thus not on the interpretation and comparison of transport coefficients for various fusion reactors.

1.1 Fusion

In controlled nuclear fusion, conditions are set-up in which the hydrogen isotopes (H), deuterium and tritium, react to form helium (He) and a neutron (n) with the view to release significant amounts of energy per fusion reaction, i.e., [McCracken, 2005]



Deuterium occurs naturally in seawater and is virtually inexhaustible on earth. On the other hand, tritium is rare on earth due to its short half-life time [Kaufman, 1954]. Tritium can be produced by neutron-irradiation of lithium (Li). It is conceivable that in the future, the produced neutrons in the fusion process could

be used to neutron-irradiate lithium to produce tritium in significant amounts needed for sustainable controlled nuclear fusion [Roux, 1998].

The figure of merit for fusion reactors is the triple product of density n , confinement time τ_e , and temperature T . This triple product should exceed a certain critical value to produce more energy than necessary to create and sustain the fusion process.

For the reaction in (1.1) this critical value should exceed

$$nT\tau_e \geq 5 \cdot 10^{21} \text{ keV m}^3/\text{s}, \quad (1.2)$$

which holds for fusion optimal temperatures, i.e., $T \sim 10^8 \text{ }^\circ\text{C}$ [Wesson, 2011]. Moreover, in magnetic confinement reactors the density cannot be increased beyond certain limits [Giannone, 2000; Greenwald, 2002]. Therefore, the confinement time τ_e needs to be optimized. This τ_e is a measure for the loss processes in fusion reactors and is closely related to the local transport coefficients, for which estimation methodologies are developed in this thesis.

1.1.1 Magnetic confinement

At the high temperatures required for fusion, the hydrogen gas consisting of deuterium and tritium is fully ionized resulting in a state known as plasma. Plasma can be confined using magnetic fields, i.e., as a result of the Lorentz forces, the charged particles gyrate around the magnetic field lines in a so-called gyro-motion. The plasma particles are free to move along the magnetic field lines [Wesson, 2011]. Hence, the presence of a magnetic field significantly reduces the transport of energy and particles in the direction perpendicular to the magnetic field. This concept is known as magnetic confinement.

Generally, a toroidal magnetic field is used to confine the plasma as it provides a closed volume without end-losses. This results in a torus shaped plasma, which forms the basis for the most common magnetic confinement fusion reactor designs; the tokamak and the stellarator [Freidberg, 2007].

Applying only a toroidal field would introduce charge separation, which would result in an overall outward radial movement of the plasma [Wesson, 2011]. Therefore, a poloidal field is used to prevent this outward radial movement. The superposition of the toroidal and poloidal fields results in a helical field.

In a tokamak, the toroidal field is generated by toroidal field coils, while the poloidal field is generated by driving a toroidal current in the plasma in addition to dedicated coils for the shaping, positioning, and exhaust of the plasma. In stellarators, the helical field is generated with a set of complex external coils. The toroidal and poloidal field coils and the resulting currents and magnetic fields for a tokamak are presented in Figure 1.1.

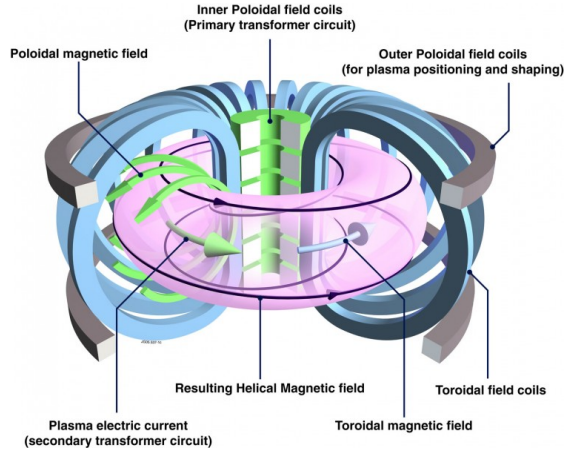


Figure 1.1. Schematic representation of a tokamak showing the field coils and the resulting magnetic fields. This figure is taken from [Eurofusion, 2015].

1.1.2 Magnetic equilibrium

The magnetic field lines span nested surfaces or torii, which are called magnetic flux surfaces. These are surfaces of constant pressure in which the magnetic field lines and the field lines for the current density are embedded. The toroidal and poloidal magnetic flux are constant on these surfaces. The flux surfaces are labeled with the dimensionless radius ρ . The magnetic axis, i.e., the center of the plasma, corresponds to $\rho = 0$ and the last-closed flux surface, i.e., the edge of the plasma, corresponds to $\rho = 1$ [Wesson, 2011]. As particles can move freely along field lines, the transport along the flux surfaces is significantly larger than perpendicular to the flux surfaces. Consequently, the electron temperatures can be considered constant over the flux surfaces. In cases of low centrifugal forces (low plasma rotation) on a flux surface also other thermodynamic quantities, e.g, the electron density can be assumed constant [Freidberg, 2007].

The overall energy confinement time τ_e is the result of the transport perpendicular to the flux surfaces [Wesson, 2011], which can be shown to be significantly smaller than the parallel transport. This forms the basis for magnetic confinement and motivates a one-dimensional description of the transport physics as a function of the flux label ρ only.

1.1.3 Classical and neo-classical transport

Classical transport theory describes the transport in a fusion plasma assuming Coulomb collisions of the particles in a cylindrical plasma. In such a plasma

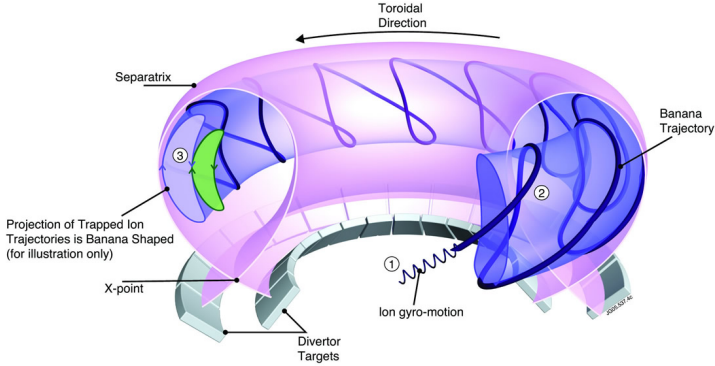


Figure 1.2. Schematic representation of the banana orbits of the particle. This figure is taken from [Eurofusion, 2015].

the transport is small as particles can only move from one magnetic surface to another in a random walk fashion with typical step size the gyro-radius. However, in a tokamak the magnetic field is not cylindrical but toroidal.

Transport due to Coulomb collisions in a toroidal plasma is described by neo-classical transport. In a toroidal confined plasma the magnetic field on the inboard side of the torus is higher (high-field side) than the magnetic field on the outboard side (low-field side). Consequently, a fraction of the particles starts carrying-out a banana orbit: the particles bounce at the high-field side and as such they alternate upwards and downwards movements. A schematic representation of such orbits is shown in Figure 1.2. The poloidal projection of the particle orbit resembles the banana, hence its name (see Figure 1.2). An important consequence of the banana orbit is that the step size is no longer the gyro-radius, but the width of the banana orbit. Consequently, perpendicular transport is larger than predicted by classical transport theory. This can also be expressed in terms of the particle diffusion coefficient (D) and the electron thermal diffusivity (χ), which are of the order [Balescu, 2005]

$$\chi \approx D = \mathcal{O}(10^{-2}) \text{ m}^2/\text{s}.$$

Extensive comparison between the neo-classical transport coefficients and the experimentally observed transport coefficients has been carried out. In most cases, the experimentally observed transport coefficients exceed the neo-classical predictions by a few orders of magnitude [Wagner, 1993].

1.1.4 Turbulent transport

The observation that transport is much larger than predicted by neo-classical transport theory, implies that the transport in tokamaks is not only due to

Coulomb collisions, but also due to collective motion or plasma turbulence. The most likely candidate-instabilities for this collective behavior are the so-called micro-instabilities [Freidberg, 2007]. These micro-instabilities are driven unstable by gradients in the temperature and density distributions [Jenko, 2000]. Various micro-instabilities can correlate and together form coherent structures with significant radial extensions. These structures effectively drive the transport, and affect the distribution of angular momentum in the plasma [Ryter, 2010]. In turn the change in angular momentum influences the coherent structures [Diamond, 2005].

The interactions between the turbulent structures result in a variety of effects, which imply that transport is non-linear [Ryter, 2010]. These non-linearities are, for instance, included using a dependence on T^α and $(-\nabla T)^\beta$ in the heat flux with scalar values α and β [Ida, 2006; Peters, 1996]. Moreover, it is observed that under certain conditions the gradients in the temperature profiles become virtually independent of the applied heat flux, which is known as profile stiffness [Garbet, 2004]. Other models for the heat flux also exist see, e.g., [Inagaki, 2013; Lopes Cardozo, 1995; Peters, 1996]. As in this thesis only linearized models are considered in the analysis, the heat flux will not be further analyzed.

Experimental evidence also suggests that the distributions of angular momentum and the current density inside the plasma can be manipulated using various actuators, with the view of suppressing the turbulence [Angioni, 2009; deGrassie, 2009; Lin, 1998; Terry, 2000]. This could significantly increase the performance of fusion reactors [Citrin, 2010]. The study of the effect of various actuators on the thermal transport requires modeling and accurate estimation of the transport coefficients. The latter is the subject of this thesis.

1.2 Measuring transport

1.2.1 Steady-state and perturbative transport analysis

Transport can be analyzed either in steady-state ($\partial/\partial t = 0$) or by perturbing the transport quantities. In case the temperature is perturbed this is also known as heat pulse propagation. If the perturbation is small enough, the measurements are described by a linear model which is the result of the linearization of the transport equations around an operating point. This linearization can be performed for different transport channels such as the particle transport, ion thermal transport, and electron thermal transport, which all result in the following basic form in the review article [Lopes Cardozo, 1995]

$$\frac{\partial \mathbf{u}}{\partial t} = A \nabla^2 \mathbf{u} + B \nabla \mathbf{u} + C \mathbf{u} + \mathbf{S}. \quad (1.3)$$

Here, \mathbf{u} is the vector of the perturbed observables, e.g., density and temperature. The source terms \mathbf{S} can be time dependent. The matrices A , B , C

contain many different terms including the values at the operating point of the observables and their derivatives [Gentle, 1988]. Note that (1.3) is the resulting Partial Differential Equation after linearization for many different non-linear model dependencies, e.g., the heat flux, and only holds for sufficiently small perturbations. Generally, only one transport channel is studied. However, there are some exceptions such as the study of the combination of heat and particle transport to determine A in (1.3) using both density and heat perturbations induced by the sawtooth instability [Hogeweyj, 1992].

In this thesis, the analysis is restricted to one transport channel in cylindrical geometry, then (1.3) simplifies to

$$\frac{\partial u}{\partial t} = \frac{1}{\rho} \frac{\partial}{\partial \rho} \left(\rho \chi(\rho) \frac{\partial u}{\partial \rho} + \rho V(\rho) u \right) - \frac{1}{\tau(\rho)} u + S, \quad (1.4)$$

which gives the standard form of the Partial Differential Equation used in this thesis. This form also considers the transport coefficients to be estimated, i.e., the diffusivity χ , convectivity V , and damping τ ($\tau > 0$). The source term is denoted by S , and u is the perturbed transport species, e.g., the electron temperature. Here, the convectivity and damping are not actual physical quantities, but are the resulting combination of the different other contributions to the transport [Gentle, 1988]. In addition, as (1.4) can also be interpreted as the linearization around an operating point, the convectivity and damping can also be the result of, for instance, the earlier mentioned non-linear dependencies of the heat flux on T^α and $(\nabla T)^\beta$.

The classic approach to quantify these non-diffusive terms is to compare the calculated diffusivity in steady-state to the perturbative diffusivity. It can be shown, see Chapter 2, that by modulating with a sufficiently high frequency, the effect of V and $1/\tau$ is negligible. As such it is possible to determine the “pure” diffusivity χ in (1.4), which is called the incremental diffusivity χ^{inc} for a general transport channel or in case of the electron temperature, the heat pulse diffusivity χ^{HP} .

Alternatively, χ can be determined in steady-state ($\partial/\partial t = 0$) by assuming $V = 1/\tau = 0$ and taking all the sources and sinks into account. This results in the so-called χ^{PB} (power balance). If V and $1/\tau$ are negligible, then $\chi^{inc} \approx \chi^{PB}$ under the assumption that the perturbation is small enough such that non-linear dependencies can be neglected. On the other hand, if the non-diffusive terms V and $1/\tau$ are not negligible $\chi^{HP} \neq \chi^{PB}$. Therefore, the comparison of χ^{inc} and χ^{PB} gives a measure for the non-diffusive terms, which is extensively analyzed in the literature for different transport channels.

1.2.2 Overview of perturbative experiments

The perturbative transport analysis is used for the study of various transport mechanisms using various actuators [Lopes Cardozo, 1995; Ryter, 2010]. Exam-

ples are the electron heat transport using Electron Cyclotron Resonance Heating (ECRH) [Inagaki, 2011; Ryter, 2003]; the momentum transport using modulated Neutral Beam Injection to modulate the torque [Mantica, 2010; Tala, 2009; Tardini, 2009]; the ion heat transport using Ion Cyclotron Resonance Heating [Mantica, 2009]; and the analysis of impurity transport [Hangyu, 2014; Howard, 2012; Zurro, 2011]. More recently perturbative experiments were used to determine the diffusivity inside magnetic islands [Hözl, 2009; Spakman, 2008]. The standard techniques to determine the transport coefficients have been used in various tokamaks like JET [Gambier, 1990; Hogewej, 1991; Lopes Cardozo, 1990], RTP [Mantica, 1996, 2000], ASDEX Upgrade [Ryter, 2003, 2005], DIII-D [DeBoo, 2005, 2012], and TFTR [Fredrickson, 2000]; and in stellarators like W7-AS [Giannone, 1992] and LHD [Inagaki, 2006].

1.2.3 Perturbative experiments: actuator and sensor

In this thesis, we focus on electron thermal transport. Therefore, briefly the concepts of Electron Cyclotron Resonance Heating (ECRH) and Electron Cyclotron Emission (ECE) are introduced. ECRH is used to locally heat the plasma and ECE is used to measure the electron temperature fluctuations.

This section is by no means exhaustive in its description of ECRH and ECE, but aims to describe the characteristics of ECRH and ECE necessary to understand the work presented in this thesis. Consequently, many important details are not discussed here, e.g., optical thickness, resonance broadening, for which the reader is referred to a number of review articles [Bornatici, 1983; Hartfuss, 1997; Hutchinson, 2002] and the references therein.

Electrons gyrate around magnetic field lines with an Electron Cyclotron (EC) frequency which is proportional to the local magnetic field amplitude B and has a frequency of 28 GHz per Tesla. Hence, the local EC frequency is constant on curves with constant magnetic field strength. The magnetic field is stronger on the high field side of the tokamak than it is on the low field side. As a result the EC frequency depends on the distance from the center of the tokamak.

Microwave radiation with a predefined frequency is generated and aimed at the plasma using a steerable launcher (mirror). The microwave radiation transfers its energy at the location where the generated frequency is resonant with a multiple of the local EC frequency, leading to ECRH [Prater, 2004]. The absorption location depends on the local EC frequency which in turn depends on the distance from the center of the tokamak. The absorption location can also be expressed in terms of the magnetic flux surface labeled by its coordinate ρ . Due to the fast transport on flux surfaces, heating a point on the flux surface is practically equivalent to heating the entire flux surface. By changing the launcher angle the absorption location of ECRH can be changed such that microwave radiation is absorbed at a different flux surface ρ . This is shown in green in Figure 1.3.

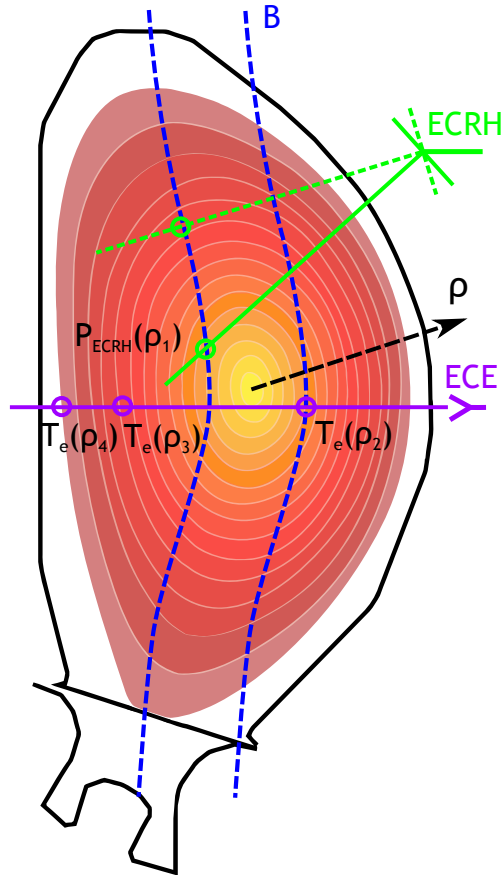


Figure 1.3. Schematic representation of ECRH (green), ECE (purple), and the magnetic equilibrium in a tokamak. The white ellipsoids are determined by the magnetic equilibrium and correspond to a certain ρ . The blue lines represent the locations in the plasma with constant magnetic field B . As the ECRH beam (the green and green dashed lines) is resonant with a certain local magnetic field, a tilt-able launcher can be used to change the deposition location in terms of ρ , as indicated by the green circles. In addition, the plasma emits ECE, the frequency of which depends on the local magnetic field and can be used for local temperature measurements (purple circles). The ECE locations and the surfaces of constant B are presented for didactic purposes only. In practice these depend in detail on the specific conditions, e.g., optical thickness, the chosen harmonics and their overlap.

Electrons also emit microwave radiation known as Electron Cyclotron Emission (ECE) due to their gyration at the EC frequency. This radiation can be measured by a heterodyne radiometer, which collects microwave radiation via an antenna [Hartfuss, 1997]. Along a specific line of sight the emission in a small frequency band stems from a small region in the fusion plasma while the intensity of this radiation is proportional to the local temperature (provided that the optical thickness is sufficient and a Maxwell-Boltzmann distribution holds for the electrons) [Bornatici, 1983]. This emission region could also be expressed in terms of the magnetic flux surface labeled by its coordinate ρ . This is shown in purple in Figure 1.3.

In principle ECE can be calibrated independently, but in practice it is more common to carry out a cross-calibration against Thomson scattering. This diagnostic uses a laser pulse to scatter photons from the electrons. These photons are collected by the diagnostic. The total number of collected photons is a measure for the electron density and the Doppler broadening of the scattered light is a measure for the electron temperature [Hutchinson, 2002].

To relate emission and absorption positions to the magnetic flux surfaces in terms of ρ , the magnetic equilibrium needs to be known. Typically the equilibrium is determined by solving the Grad-Shafranov equation under a set of constraints [Wesson, 2011]. A variety of codes is used for this purpose, the implementation of which is adapted to the particular experiment [Lao, 1990; Moret, 2015]. In this thesis we assume that the magnetic equilibrium is fixed and hence the impact of temperature and density fluctuations on the equilibrium is negligible.

The here introduced diagnostics and actuator are used to perform perturbative experiments in fusion reactors. A typical measurement during such an experiment is shown in Figure 1.4 for the RTP-tokamak. This figure shows the measurement of the ECRH power modulation, which is generally binary, and the resulting temperature fluctuations. By decomposing the temperature fluctuations in its sinusoidal components in terms of amplitude and phase (Fourier transform), and studying the amplitude and phase difference between different locations ρ , the transport coefficients can be determined.

1.3 Methods for estimating transport coefficients

Perturbative analysis of thermal transport in magnetically confined plasmas started in the 1970s, using natural heat waves that originated from the sawtooth instability [Jahns, 1978; Soler, 1979]. The first methodologies to analyze the perturbed transport were also derived in this period, e.g., [Callen, 1977]. These were extended in the 1980s [Fredrickson, 1986; Lopes Cardozo, 1988] and the 1990s [Jacchia, 1991]. All these methodologies use the spatial derivatives of the harmonic components, i.e., the amplitude and phase, of the temperature perturbations at different radial locations to determine the perturbative electron

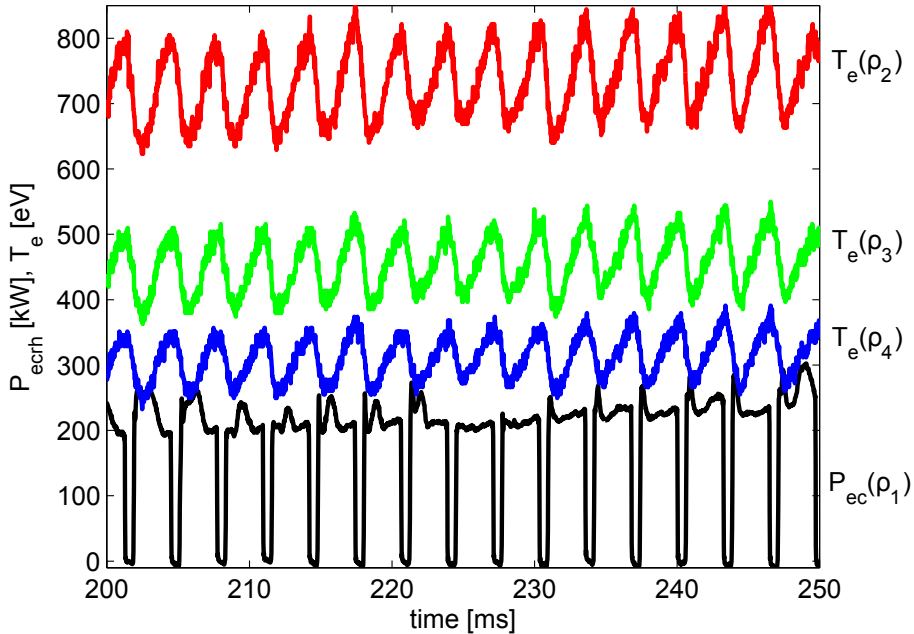


Figure 1.4. Local electron temperature measurements $T_e(\rho)$, measured using ECE, during a heat pulse propagation experiment using modulated ECRH, P_{ech} , in the RTP-tokamak.

diffusivity χ . These methodologies, referred to as approximations in this thesis, are now commonly used to analyze transport [DeBoo, 2012; Inagaki, 2006; Lopes Cardozo, 1995; Mantica, 2006a; Rytter, 2010]. These approximations consider mainly the diffusivity and some are extended to contain also the effect of damping. Therefore, as explained earlier, the standard approach is to use high frequency modulation to suppress the non-diffusive terms, i.e., convectivity (and damping), such that it is possible to estimate the diffusivity. Also the convectivity can be analyzed indirectly by comparing the spatial decay rates of amplitude and phase [Lopes Cardozo, 1995; Luce, 1992].

Recently, two new methods have been introduced to estimate the transport coefficients in [Escande, 2012; Mechhoud, 2015]. In [Mechhoud, 2015] a Kalman filtering approach is introduced based on a model with only diffusivity, hence, taking noise properties and an unknown source term into account. In [Escande, 2012] this model is extended to also contain a convectivity term, but in contrast to the previous method, it does not consider noise and the source term is considered to be known. This method is based on calculating also the profiles of

the derivatives of amplitude and phase from the measured amplitude and phase profiles. Initially, the method in [Escande, 2012] was designed for the particle transport, but very recently it is also applied to the problem of electron heat transport [Sattin, 2014]. The latter two methods distinguish themselves from the other methods discussed here, in that they no longer use the standard assumption of semi-infinite domains and constant spatial parameter dependencies.

1.4 Objectives and contributions of this thesis

The literature overview in Section 1.3 shows a renewed interest in estimation methods for the transport coefficients. This is due to the search for better confinement regimes by using various actuators and due to a better understanding and more accurate modeling of turbulent transport, which needs to be compared to the estimated transport coefficients. Therefore, this thesis has following objective

Develop practical methods to reduce the uncertainty of the estimated transport coefficients allowing for the validation of the chosen transport model. These methods should not restrict the modulation of the source, such that optimal excitations can be applied.

We attempt to achieve this objective by combining methods and models familiar to the fusion community with system identification techniques. Thereby, we aim not only to improve the estimation methodologies, but also to link these to the fields of system identification and distributed parameter systems in which many tools are readily available.

1.4.1 Activities and layout

In Chapter 2 the modeling and a number of approximations to determine the diffusivity are reviewed specifically in terms of the mathematical concepts used in system identification. Then, a large number of new approximations are derived to determine the transport coefficients inline with the fusion literature (Chapters 3-5). These methods are explicit and as such easy to implement. However, one of the important issues is that they rely on the spatial derivatives of amplitude and phase instead of directly the Fourier coefficients to calculate the transport coefficients. Therefore, the derivatives are approximated using fits of the spatial amplitude and phase profiles. This can lead often to many undesired effects such as a bias and errors due to noise, i.e., the variance-bias trade off [Hall, 2010]. Another common problem of the explicit methods is that the number of unknown transport coefficients exactly matches the number of amplitudes and phases necessary. For example, for one harmonic, the amplitude and phase exactly match to the pair of diffusivity and convectivity or diffusivity and damping. Generally, in practice more harmonics are present, hence, these harmonics

need to be combined to give an overall estimate of the diffusivity, the convectivity, and the damping. However, as not every harmonic component has the same Signal to Noise Ratio (SNR), the effect of measurement uncertainty needs to be considered. Taking simply the average of the estimated diffusivities results in a biased estimate of the overall transport coefficient. The estimate of the overall diffusivity can be improved by introducing a different averaging method, which reduces the bias and uncertainty significantly. For the methodologies proposed in [Jahns, 1978; Soler, 1979] this approach is sufficient. However, for the methodologies in [Jacchia, 1991] and the newly presented methodologies, which also include damping and convectivity, such averaging methods are less applicable. This is described and derived in detail in Chapter 6 and as such it forms the link between methodologies used in fusion and system identification.

Chapter 7 introduces a new approach based on sample Maximum Likelihood Estimation in the frequency domain. This method is used to determine also the convectivity and damping using multiple harmonics considering also their uncertainty in terms of variances. The resulting estimates using this method are consistent, which means that if more frequency lines are added they converge to the true values, and have a variance close to the theoretical lower bound. In addition, validation tests are introduced, which allow for the validation of the assumed transport and noise model in relation to the measurement data. Moreover, the whole step of approximating the derivatives is avoided by using directly the Fourier coefficients and their (co-)variances. A disadvantage of this method is that the optimization problem is non-convex and that it still relies on the assumption of constant parameter dependencies between three measurement points

1.4.2 Specific contributions

- *Extensions to improve accuracy of approximations and inclusion of convectivity (Chapters 3 and 4 or [van Berkel, 2014a,b]):* A large number of new approximations are derived. These extend the known methods to calculate the diffusivity, in terms of accuracy, by the inclusion of convectivity, and the inclusion of damping. By including the convectivity and damping lower modulation frequencies can be chosen such that a better SNR can be achieved. These approximations are found using the logarithmic temperature derivatives in terms of Bessel functions and Confluent Hypergeometric Functions, which then can be approximated using continued fractions [Cuyt, 2008; Jones, 1980] and asymptotic expansions [Erdélyi, 1956; Slater, 1960]. Interestingly, using this new methodology also a number of the approximations in the literature are derived.
- *Inward heat wave propagation (Chapter 5 or [van Berkel, 2014c]):* There is a profound difference between heat waves propagating towards the edge and towards the center. This difference is largely ignored in the literature,

hence, only approximations have been derived on the basis of semi-infinite domains. In this thesis next to investigating the usefulness of the approximations based on semi-infinite domains, a number of new approximations are derived. These approximations, based on a symmetric domain, perform better in strong cylindrical geometry when inward heat wave propagating is considered, for example, in case of off-axis heating.

- *Modeling and implications (Chapters 2, 3, and 4 or [van Berkel, 2014a,b,c])* Errors introduced by a semi-infinite boundary condition are discussed in the literature [Goedheer, 1986]. On the other hand, the underlying assumption of constant transport coefficients from the measurement point up till infinity (or the center) is not so well known in the literature. Therefore, this thesis includes a more thorough analysis and gives a more structured overview of the underlying assumptions and derivations. This analysis shows that even if the diffusivity is spatially varying, it can often still be estimated using the approaches used in this thesis. On the other hand, this often does not hold for the convectivity and certainly not for the damping. In addition, this structured approach also allows to clarify the relationship between the amplitude and phase and its spatial (logarithmic) derivatives.
- *Multiple harmonics, measurement uncertainty, and distribution of diffusivity (Chapter 6 or [van Berkel, 2014d])*: In most experiments multiple harmonics can be used for the estimation of the diffusivity, which are compared qualitatively. However, to truly combine and compare multiple harmonics also the uncertainty needs to be taken into account. Therefore, in this thesis the distribution functions of the harmonics are determined based on measurements and assumptions. By taking the distribution functions into account, more accurate estimates of the diffusivity can be acquired. Consequently, a new method is introduced to combine and analyze different harmonics in terms of amplitude and phase. The analysis is based on the assumption that the Fourier coefficients are distributed according to a Circular Complex Normal Distribution (CCND) distribution function. This often results in an inverse non-central chi-squared distribution function for the diffusivity. The diffusivity that is found by sampling this inverse non-central chi-squared distribution will always be biased and averaging of multiple estimated diffusivities will not necessarily improve the estimation. Nevertheless, this distribution allows for the construction of confidence bounds to illustrate the uncertainty in the diffusivity for several of the slab geometry relationships. Moreover, a different method of averaging is introduced based on the knowledge of the distribution functions, that reduces the uncertainty significantly. The methodology is also extended to the case where damping is included.

- *Maximum Likelihood: near minimum variance, validation tests, and extended models (Chapter 7 or [van Berkel, 2013, 2014e]):* In this thesis a new methodology is developed to estimate the transport coefficients using a sample Maximum Likelihood Estimator (SMLE) in the frequency domain. This method is used because only measurements are considered (Errors-In-Variables problem) such that the transport coefficients can be estimated with near minimum variance. In addition, it optimally takes into account multiple harmonics by weighting them with their certainty. Moreover, as this method is implicit, i.e., it is based on the minimization of a cost function, it not only allows to use the standard modeling used in the literature, but also the use of more complicated models. In this case, a new modeling is introduced based on three measurements points. Two measurement points replace the boundary conditions such that true local estimates can be achieved, excluding the influence of neighboring domains. Finally, a test is introduced to validate the assumed model based on statistics.

1.5 Outline of this thesis

This thesis is organized as follows. Chapter 2 gives an overview of the relevant heat transport models, simplifications, and assumptions. It also introduces the relationships to determine the transport coefficients as found in the standard fusion literature. As such it forms the basis for the rest of this thesis. Then, in Chapter 3 new relationships to determine explicitly the transport coefficients in a cylindrical geometry based on slab geometry are derived. More, importantly Chapter 3 also contains a discussion on errors introduced by the simplifying assumptions. Then, in Chapter 4 new explicit approximations are derived, based directly on the semi-infinite cylindrical domain. These are compared to the relationships in the literature for different parameter ranges of the transport coefficients. In contrast to Chapter 4, Chapter 5 introduces new explicit approximations to determine the transport coefficients for heat waves propagating towards the center.

The explicit relationships introduced in Chapters 2-5 do not consider the uncertainty in the measurements. Therefore, in Chapter 6 measurement uncertainty is introduced to determine the transport coefficients with their confidence bounds. This is based on the assumption of a CCND and estimates of the variance of the Fourier coefficients such that the distribution functions of the amplitude and phase, and the diffusivity can be determined. The analysis is performed using ASDEX Upgrade measurement data for the classic relationships introduced in Chapter 2. This already shows that although the estimation of the diffusivity can be improved, the resulting diffusivity estimate is sub-optimal and that the complexity that will be encountered for the relationships in Chapters 2-5 makes it impractical to use such an analysis. As such Chapter 6 also

forms the basis for Chapter 7, which introduces an implicit method, i.e., sample Maximum Likelihood Estimation, to determine the transport coefficients. The method allows to use both the standard modeling on which the approximations in Chapters 2-5 are based and more complex modeling. Thus it avoids errors introduced due the assumptions on the boundary conditions. In addition, Chapter 7 also introduces a method to validate the estimated model with respect to the measurements using the estimates of the variances of the Fourier coefficients. Hereafter, in Chapter 8, the conclusions and a number of recommendations are presented.

Chapter 2

Mathematical modeling of heat transport in tokamaks and stellarators

This chapter introduces transport models, which are often used to determine and analyze the electron heat transport in fusion devices.

The thermal and particle transport are briefly introduced in the first section. Transport in fusion devices is often modeled using cylindrical geometry in terms of Partial Differential Equations (PDE) with spatial dependent transport coefficients. This cylindrical geometry can also be approximated for larger radii using slab geometry, which simplifies the calculations significantly. Both in slab geometry and cylindrical geometry, the PDEs need to be further simplified such that they can be solved analytically in the Laplace domain. Therefore, a number of standard assumptions are discussed. These analytical solutions in the Laplace domain can be further simplified by eliminating or choosing the boundary conditions in a mathematically convenient way. This allows for the derivation of relationships which directly express the unknown diffusivity in terms of the spatial derivatives of amplitude and phase, which is often used in the

This chapter is based on the following articles:

van Berkel, M., et al. [2014]. Explicit approximations to estimate the perturbative diffusivity in the presence of convectivity and damping I Semi-infinite slab approximations, *Phys. Plasmas* **21**: 112507.

van Berkel, M., et al. [2014]. Explicit approximations to estimate the perturbative diffusivity in the presence of convectivity and damping II Semi-infinite cylindrical approximations, *Phys. Plasmas* **21**: 112508.

van Berkel, M., et al. [2014]. Explicit approximations to estimate the perturbative diffusivity in the presence of convectivity and damping III Cylindrical approximations for heat waves traveling inwards, *Phys. Plasmas* **21**: 112509.

fusion literature. A disadvantage of using spatial derivatives is that the relationship between the actual amplitude and phase and their derivatives is unknown. Therefore, transfer functions are introduced to re-establish this relationship and to give a description that directly uses the Fourier coefficients without the need for approximating the derivatives. Moreover, a different approach is discussed given in the literature based on eliminating double derivatives of amplitude and phase. Finally, the influence of directionality of the propagation of the heat waves on the modeling is discussed.

2.1 Transport modeling

This section considers the coupled equations of conservation of energy and particles for the electrons, which is briefly introduced here. These coupled equations are used to derive the one-dimensional PDEs in cylindrical and slab geometry containing the transport coefficients we wish to determine.

2.1.1 Conservation of energy and particles

This thesis focuses on the analysis of the electron heat transport. As only a periodically modulated electron heating source (P_{mod}) will be used, which dominates over other possible fluctuations in time, it is reasonable to consider only the coupled equations of conservation of energy and particles defined in [Bishop, 1990; De Haas, 1991; Gentle, 1988; Lopes Cardozo, 1995]

$$\frac{\partial n}{\partial t} = -\nabla\Gamma + S_p, \quad (2.1)$$

$$\frac{\partial}{\partial t} \left(\frac{3}{2}nT \right) = -\nabla q + \nabla \left(\frac{5}{2}T\Gamma \right) + \frac{1}{n}\Gamma\nabla(nT) + S_h, \quad (2.2)$$

where q denotes the heat flux, Γ the particle flux, T the electron temperature, n the density, and S_p the particle sources. Based on [Freidberg, 2007] the source term S_h can include the external heating power density S_f contributing to the energy balance, S_r the radiation losses due to Bremsstrahlung, S_{ohm} ohmic heating power, and P_{mod} . This leads to

$$S_h = S_f + S_{ohm} - S_r + P_{mod}. \quad (2.3)$$

In this thesis, it is assumed that all source terms except P_{mod} in S_h are static (do not depend on time). Therefore, their variation in time should be negligible compared to the perturbation induced by P_{mod} . Usually P_{mod} will be modulated Electron Cyclotron Resonance Heating. However, in principle any localized electron heating could be used, for instance, Ion Cyclotron Heating in a suitable minority heating scheme. Density fluctuations are assumed to be negligible, hence, are not considered, i.e., $\partial n/\partial t = 0$. The exact descriptions for the heat

flux q and particle flux Γ are unknown. However, classically they are modeled by the laws of Fick [De Haas, 1991]

$$\Gamma = -D\nabla n \quad (2.4)$$

and Fourier

$$q = -n\chi\nabla T, \quad (2.5)$$

with D the particle diffusion coefficient and χ the electron diffusivity. Variations of these laws exist, for instance by considering a convective velocity term U in q [Lopes Cardozo, 1995]

$$q = -n\chi\nabla T - nUT. \quad (2.6)$$

Based on these equations it is possible to derive a one-dimensional PDE, which can be used to identify the electron diffusivity χ .

2.1.2 Perturbative transport analysis

Thermal transport inside a fusion reactor is modeled as radial one-dimensional transport in a cylinder due to the magnetic confined plasma topology [Lopes Cardozo, 1995]. This allows to rewrite (2.2), using (2.6), in terms of partial derivatives with respect to the dimensionless radius ρ

$$\begin{aligned} \frac{\partial}{\partial t} \left(\frac{3}{2}nT \right) &= \frac{1}{\rho} \frac{\partial}{\partial \rho} \left(\rho n\chi \frac{\partial T}{\partial \rho} + \rho nUT \right) + \\ &\frac{1}{\rho} \frac{\partial}{\partial \rho} \left(\rho \frac{5}{2}T\Gamma \right) + \frac{1}{n} \Gamma \frac{1}{\rho} \frac{\partial}{\partial \rho} (\rho nT) + S_h, \end{aligned} \quad (2.7)$$

where the dependencies on ρ have been omitted. Although non-linear dependencies exist, e.g., on T and ∇T , it is assumed that the temperature perturbation in S_h used to analyze the transport is small enough to assume linearity around the equilibrium temperature. Then, the simplified PDEs given in (2.7) must be seen as the result of a linearization of transport equations [Gentle, 1988; Lopes Cardozo, 1995]. In such a linearization, other effects can also be captured in the diffusivity, convectivity, and a damping term, e.g., the electron-ion heat equipartition can be adequately captured in a damping term. In addition, non-linear dependencies of for instance χ on T and ∇T is then partly accounted for in the convective term and/or damping. Therefore, the one-dimensional parabolic PDE in cylindrical geometry is generally expressed in a simplified form

$$\frac{\partial}{\partial t} \left(\frac{3}{2}nT \right) = \frac{1}{\rho} \frac{\partial}{\partial \rho} \left(\rho n\chi(\rho) \frac{\partial T}{\partial \rho} + \rho nV(\rho)T \right) - \frac{3}{2}n\tau_{inv}(\rho)T + S_h, \quad (2.8)$$

where V and τ_{inv} denote the convectivity and damping in cylindrical geometry. Based on (2.7) $V = U + \frac{7}{2}\frac{\Gamma}{n}$ and $\tau_{inv} = \frac{2}{3}\frac{1}{n} \left(\Gamma' - \frac{n'}{n}\Gamma \right)$. The prime, in e.g., n' ,

denotes the spatial derivative with respect to ρ . In contrast to the literature here is chosen to denote the damping by its inverse, i.e., $\tau_{inv} \equiv \tau^{-1}$, because τ_{inv} is bounded contrary to τ . The diffusivity $\chi(\rho)$, the (effective) convectivity $V(\rho)$, and the (inverse) damping $\tau_{inv}(\rho)$ in front of T , T' , and T'' can be identified by only considering electron temperature perturbations.

Unfortunately, (2.9) is difficult to use in practice for the estimation of χ from measurements. Therefore, a number of standard simplifications are applied [Jacchia, 1991]. Only measurements are considered for which the transients due to the initial conditions can be neglected. It is assumed that the parameters are constant with respect to time and space. Thus the parameters are assumed to be homogenous or uniform [Jacchia, 1991; Lopes Cardozo, 1995]. In addition, only spatial regions are considered where $P_{mod} = 0$, i.e., outside the region where the heating is deposited to perturb the plasma. An important argument for this choice is that the exact deposition power and profile are often not known. These assumptions result in a simplification of (2.9), i.e.,

$$\frac{\partial}{\partial t} \left(\frac{3}{2} nT \right) = \frac{1}{\rho} \frac{\partial}{\partial \rho} \left(\rho n \chi \frac{\partial T}{\partial \rho} + \rho n V T \right) - \frac{3}{2} n \tau_{inv} T. \quad (2.9)$$

This equation is often used in the literature [Jacchia, 1991; Lopes Cardozo, 1995] to analyze heat wave propagation in a cylindrical geometry. Alternatively, the slab geometry representation of (2.9) is used to analyze transport in a cylindrical geometry as it gives a good approximation of the transport coefficients for large ρ [Jacchia, 1991; Lopes Cardozo, 1988, 1995].

2.1.3 Slab geometry representation and its relationship to cylindrical geometry

In slab geometry the following representation is used to determine χ explicitly [Lopes Cardozo, 1995]

$$\frac{3}{2} \frac{\partial T}{\partial t} = \chi \frac{\partial^2 T}{\partial \rho^2} + V_s \frac{\partial T}{\partial \rho} - \frac{3}{2} \tau_{invs} T, \quad (2.10)$$

where the diffusivity χ , the convectivity in slab geometry V_s , and the inverse damping in slab geometry τ_{invs} are independent of ρ . It is important to realize that the effective convectivity $V \neq V_s$ and the inverse damping $\tau_{inv} \neq \tau_{invs}$ represent something different in (2.10) and (2.9). This can be investigated by transforming (2.9) assuming $n' = 0$:

$$\frac{\partial}{\partial t} \left(\frac{3}{2} T \right) = \chi \frac{\partial^2 T}{\partial \rho^2} + \left(V + \frac{\chi}{\rho} \right) \frac{\partial T}{\partial \rho} - \frac{3}{2} \left(\tau_{inv} - \frac{2V}{\rho} \right) T. \quad (2.11)$$

This means that only when $\rho \rightarrow \infty$, $V = V_s$ and $\tau_{inv} = \tau_{invs}$. Hence, (2.10) will be a proper approximation of (2.9) when n' is negligible and the variations

χ/ρ and V/ρ are small with respect to V and τ_{inv} , respectively. The diffusivity term χ in front of T'' is unaffected by this change of geometry. On the other hand, the diffusivity term in cylindrical geometry now also appears as a pseudo convectivity χ/ρ in slab geometry.

The next section will derive direct expressions for χ , based on (2.10) to analyze the transport coefficients in a cylindrical geometry.

2.2 Analytical solutions in the Laplace domain

A standard method for solving PDEs is to transform them into the Laplace or frequency domain such that the PDE can be reduced to a complex valued ODE, which can be solved analytically [Haberman, 1983]. Both (2.10) and (2.11) are solved analytically to enable the derivation of an explicit expression of the diffusivity χ in terms of amplitude and phase based on the Fourier transformed measurements of the temperature.

2.2.1 Slab geometry

The Laplace transform of (2.10) results in

$$\frac{3}{2}s\Theta = \chi \frac{d^2\Theta}{d\rho^2} + V_s \frac{d\Theta}{d\rho} - \frac{3}{2}\tau_{invs} \Theta, \quad (2.12)$$

where s is the Laplace variable and $\Theta(\rho, s)$ is the Laplace transform of $T(\rho, t)$ [Curtain, 1995]. The Laplace variable can in practice only be measured on the imaginary axis, thus $s = i\omega$, where $i = \sqrt{-1}$ and ω is the frequency. The general solution of (2.12) is given by [Polyanin, 2003]

$$\Theta(\rho, s) = C_1(s) \exp(\lambda_1^s \rho) + C_2(s) \exp(\lambda_2^s \rho)$$

$$\text{with} \quad \lambda_{1,2}^s = -\frac{V_s}{2\chi} \mp \sqrt{\left(\frac{V_s}{2\chi}\right)^2 + \frac{3s + \tau_{invs}}{\chi}}. \quad (2.13)$$

The quantities $\lambda_{1,2}^s$ play an important role in both slab and cylindrical geometry. However, in slab geometry $\lambda_{1,2}^s$ depends on V_s and τ_{invs} whereas in cylindrical geometry $\lambda_{1,2}$ depends on V and τ_{inv} , hence, the superscript s in slab geometry. The boundary constants $C_1(s)$ and $C_2(s)$, which are independent of ρ , are determined by the choice of the boundary conditions, which is discussed in Section 2.3.

2.2.2 Cylindrical geometry

In cylindrical geometry the PDE (2.11) can also be transformed into the Laplace domain yielding

$$\frac{3}{2}(s + \tau_{inv}) \Theta(\rho, s) = \frac{1}{\rho} \frac{d}{d\rho} \left(\rho \chi \frac{\partial \Theta(\rho, s)}{\partial \rho} + \rho V \Theta(\rho, s) \right), \quad (2.14)$$

where again $\Theta(\rho, s)$ is the Laplace transform of $T(\rho, t)$. This complex valued Ordinary Differential Equation (ODE) can be solved analytically (see Section A.4.1 or [Polyanin, 2003; von Kamke, 1959])

$$\begin{aligned} \Theta(\rho, s) &= e^{\lambda_1 \rho} D_1(s) \Psi \left(\frac{\lambda_2}{\lambda_2 - \lambda_1}, 1, (\lambda_2 - \lambda_1) \rho \right) \\ &\quad + e^{\lambda_1 \rho} D_2(s) \Phi \left(\frac{\lambda_2}{\lambda_2 - \lambda_1}, 1, (\lambda_2 - \lambda_1) \rho \right) \\ \text{with} \quad \lambda_{1,2} &= -\frac{V}{2\chi} \mp \sqrt{\left(\frac{V}{2\chi} \right)^2 + \frac{3s + \tau_{inv}}{\chi}}. \end{aligned} \quad (2.15)$$

The functions $\Phi(\rho, s)$ and $\Psi(\rho, s)$ denote the Confluent Hypergeometric Functions of the first and the second kind, respectively. These functions are also often denoted as ${}_1F_1$ and U , and are extensively described in [Bateman, 1953; Luke, 1969; Slater, 1960]. The boundary constants are denoted by $D_1(s)$ and $D_2(s)$. This solution in terms of Confluent Hypergeometric Functions may not be so familiar, but if simplified by assuming $V = 0$, the well-known solutions in terms of the modified Bessel functions of the first kind I_ν and the second kind K_ν of order ν are found. In particular, if $V = 0$, then $\lambda_1 = -\lambda_2$, $\lambda_2/(\lambda_2 - \lambda_1) = 1/2$, such that $\Phi(\rho, s)$ and $\Psi(\rho, s)$ result in [Bateman, 1953]

$$\Phi \left(\frac{1}{2}, 1, (\lambda_2 - \lambda_1) \rho \right) = \exp \left(\frac{1}{2} (\lambda_2 - \lambda_1) \rho \right) I_0 \left(\frac{1}{2} (\lambda_2 - \lambda_1) \rho \right) \quad (2.16)$$

and

$$\Psi \left(\frac{1}{2}, 1, (\lambda_2 - \lambda_1) \rho \right) = \exp \left(\frac{1}{2} (\lambda_2 - \lambda_1) \rho \right) \frac{K_0 \left(\frac{1}{2} (\lambda_2 - \lambda_1) \rho \right)}{\sqrt{\pi}}, \quad (2.17)$$

respectively. Consequently, (2.15) simplifies to

$$\Theta(\rho, s) = \frac{D_1(s)}{\sqrt{\pi}} K_0 \left(\frac{1}{2} (\lambda_2 - \lambda_1) \rho \right) + D_2(s) I_0 \left(\frac{1}{2} (\lambda_2 - \lambda_1) \rho \right). \quad (2.18)$$

This solution is well known and is studied and referenced in for instance [Carslaw, 1959; Polyanin, 2003]. As the Bessel functions and Confluent Hypergeometric

Functions may not be so familiar a brief overview on the derivation and calculation of these functions in relation to the PDEs presented here is given in Appendix A.

The analytical solutions presented in this section are used to derive hands-on models, which can be used to derive explicit approximations of χ .

2.3 Logarithmic derivative and transfer function

The PDEs (2.9) and (2.10) are typically used to describe electron transport. These PDEs are reduced to complex valued ODEs by means of the Laplace transform. However, to be able to find practical models that can be used to determine χ , the boundary constants need to be either determined or eliminated. The following three approaches are commonly used: (1) the logarithmic temperature derivative, i.e., $(\partial\Theta/\partial\rho)/\Theta = \partial(\ln(\Theta))/\partial\rho$, in which only one boundary constant is determined and where the solution is expressed in terms of the spatial derivatives of the amplitude and phase (Section 2.3.1); (2) transfer functions, in which both $C_1(s)$ and $C_2(s)$ are determined (Section 2.3.2); (3) An approach in which fixing $C_1(s)$ and $C_2(s)$ explicitly are avoided by introducing double spatial derivatives to amplitude and phase (Section 2.3.3). However, as a solution of a second order PDE is only defined by two boundary conditions, there must be a clear relationship between these three approaches. In this section we show how amplitude and phase are related to their spatial derivatives typically used to calculate the diffusivity.

2.3.1 Semi-infinite domain and logarithmic temperature derivative

The choice for a semi-infinite domain and the use of a logarithmic temperature derivative is commonly used in the literature [Jacchia, 1991; Lopes Cardozo, 1995] as it simplifies the solution significantly. This allows for the elimination of one eigenfunction and one boundary condition such that approximations for χ can be derived.

The first step is to eliminate one eigenfunction as it is difficult to derive explicit relationship for χ on the basis of two eigenfunctions, i.e., $\exp(\lambda_1^s \rho)$ and $\exp(\lambda_2^s \rho)$ in (2.13) or $e^{\lambda_1 \rho} \Phi(\rho, s)$ and $e^{\lambda_2 \rho} \Psi(\rho, s)$ in (2.15). One eigenfunction can be eliminated by assuming a semi-infinite domain, which is defined as follows, if $\rho \rightarrow \infty$, then $\Theta \rightarrow 0$. This means that at $\rho = \infty$ all perturbations need to have vanished. Since, we follow the standard convention that for $z \in \mathbb{C}$, $\arg(z) \in (-\pi, \pi]$ and $\arg(\sqrt{z}) = \frac{1}{2} \arg(z)$, the two eigenfunctions in slab geometry, i.e., (2.13), satisfy $\exp(\lambda_1 \rho) \rightarrow 0$ and $|\exp(\lambda_2 \rho)| \rightarrow \infty$ for $\rho \rightarrow \infty$. Hence, $C_2(s) = 0$, otherwise the solution (2.13) would not converge to zero at large ρ . In cylindrical geometry for (2.15), this is more difficult to prove analytically. However, in case $V = 0$ for the semi-infinite domain it is known that $D_2(s) = 0$ in (2.15) [Carslaw,

1959]. This indicates that also $D_2(s) = 0$ in (2.15) when $V \neq 0$. Therefore, it is numerically verified that $D_2(s) = 0$ in (2.15) by comparing it to finite difference simulations with boundary condition $T(\rho \gg 1) = 0$. This shows that the error between the analytic and numerical simulations are small and that the error is decreasing with increasing density of the discretization grid. In addition, the functions Φ and Ψ are numerically evaluated to study the behavior close to $\rho = \infty$, indicating again that this is the correct choice. This means that in slab geometry, (2.13) simplifies to

$$\Theta(\rho, s) = C_1(s) \exp(\lambda_1^s \rho) \quad (2.19)$$

and in a cylindrical geometry, (2.15) simplifies to

$$\Theta(\rho, s) = D_1(s) e^{\lambda_1 \rho} \Psi\left(\frac{\lambda_2}{\lambda_2 - \lambda_1}, 1, (\lambda_2 - \lambda_1) \rho\right). \quad (2.20)$$

In principle, $C_1(s)$ and $D_1(s)$ need to be determined by assuming a second boundary condition. However, in the literature it is common practice to express the solution in terms of the spatial derivatives, thereby eliminating $C_1(s)$ and $D_1(s)$. These boundaries can be eliminated systematically by introducing the logarithmic temperature derivative. Taking the logarithmic derivative of the right hand side of (2.19) and (2.20) results in

$$\frac{\Theta'}{\Theta} = \lambda_1^s \quad (2.21)$$

and

$$\frac{\Theta'}{\Theta} = \lambda_1 - \lambda_2 \frac{\Psi\left(1 + \frac{\lambda_2}{\lambda_2 - \lambda_1}, 2, (\lambda_2 - \lambda_1) \rho\right)}{\Psi\left(\frac{\lambda_2}{\lambda_2 - \lambda_1}, 1, (\lambda_2 - \lambda_1) \rho\right)}, \quad (2.22)$$

respectively (see [Slater, 1960] for the derivative of Ψ). If $V = 0$, then (2.22) can be further simplified to

$$\frac{\Theta'}{\Theta} = -z \frac{K_1(z\rho)}{K_0(z\rho)}, \quad (2.23)$$

where

$$z = \sqrt{\frac{3i\omega + \tau_{inv}}{2\chi}}. \quad (2.24)$$

If the temperature Θ is written in terms of its harmonic components, i.e., $\Theta = A \exp(i\phi)$. Then the spatial derivative of the temperature is given by $\Theta' = A' \exp(i\phi) + i\phi' A \exp(i\phi)$ such that the left-hand side of (2.21), (2.22), and (2.23) results in

$$\frac{\Theta'}{\Theta} = \frac{A'}{A} + i\phi'. \quad (2.25)$$

The idea of this representation is that the continuous profiles A' and ϕ' can be calculated from the experimental data using an approximation of the derivatives of amplitude and phase [Escande, 2012]. This means that if χ can be re-expressed in terms of ρ , $\frac{A'}{A}$, and ϕ' using (2.26), the diffusivity can be explicitly calculated using the approximations of the derivatives. For example, if $V_s = 0$, (2.21) simplifies to

$$\frac{A'}{A} + i\phi' = -\sqrt{\frac{3}{2} \frac{i\omega + \tau_{invs}}{\chi}}, \quad (2.26)$$

such that the square of (2.21) becomes

$$\left(\frac{A'}{A}\right)^2 + 2\frac{A'}{A}\phi'i - (\phi')^2 = \frac{3}{2} \frac{\omega i + \tau_{invs}}{\chi}. \quad (2.27)$$

If also $\tau_{invs} = 0$, then this results in the following two standard relationships to calculate the diffusivity χ from experimental data [Fredrickson, 1986]

$$\chi_{s1} = \frac{3}{4} \frac{\omega}{(\phi')^2}, \quad (2.28)$$

and [Callen, 1977; Soler, 1979]

$$\chi_{s2} = \frac{3}{4} \frac{\omega}{(A'/A)^2}. \quad (2.29)$$

These can also be combined to find

$$\chi_{s3} = \frac{3\omega}{(A'/A + \phi')^2}. \quad (2.30)$$

Note that in this thesis a large number of explicit relationships (approximations) to calculate the transport coefficients, e.g., χ , are derived. Hence, to distinguish them, they all have been indexed, in this case with $s1$, with s for slab.

If also the damping τ_{invs} is considered, then χ can be calculated by considering only the imaginary part of (2.21), [Jacchia, 1991; Lopes Cardozo, 1988]

$$\chi_{s4} = \frac{3}{4} \frac{\omega}{\frac{A'}{A}\phi'}. \quad (2.31)$$

Sometimes, if $\tau_{invs} = 0$, (2.31) is rewritten in terms of χ_{s1} and χ_{s2} to calculate the combined diffusivity of amplitude and phase [Ryter, 2010]

$$\chi_n = \sqrt{\chi_{s1}\chi_{s2}}. \quad (2.32)$$

The damping τ_{invs} can also be calculated by considering also the real part of (2.27)

$$\tau_{s4} = \frac{\omega}{2} \left(\frac{A'/A}{\phi'} - \frac{\phi'}{A'/A} \right). \quad (2.33)$$

This concludes the known slab relationships for χ in the literature.

In case $V_s \neq 0$, there are three unknowns χ , V_s , and τ_{invs} and two known variables ϕ' and A'/A . This means that in principle two harmonics are necessary to calculate the diffusivity χ under the influence of the convectivity and the damping, which is the subject of Chapter 3.

In case of the cylindrical geometry the right-hand sides of (2.22) and (2.23) cannot be inverted analytically. Therefore, an alternative method is developed to calculate χ explicitly, which is explained in Chapter 4.

A common problem using the representations presented here is how to calculate the spatial derivatives A'/A and ϕ' from the measured A and ϕ . This can be avoided by making reasonable assumptions for the second boundary condition, which results in a transfer function representation.

2.3.2 Transfer function and spatial derivatives

The transfer function approach may be less familiar in the fusion literature [Dudok de Wit, 1991; Moret, 1993; Witvoet, 2011], but it is extensively used in the field of system identification, system theory, and control [Ljung, 1999; Pintelon, 2012]. From the available fusion literature on transfer functions it may seem that only rational functions based on measurement data are applicable. However, as will be shown here, transfer functions can also be used to describe simplified models for PDEs [Curtain, 2009], which are of non-rational form.

The most important advantage of this technique over the other two techniques is that it only depends on the measurements and not the derivatives of the measurements. Hence, it is no longer required to approximate the spatial derivative of phase and the spatial logarithmic amplitude derivative. This can be derived based on (2.19)

$$\Theta(\rho, s) = C_1(s) \exp(\lambda_1^s \rho).$$

A logical choice for the other boundary condition is to choose the temperature at a second spatial location ρ_1 , i.e., $\Theta(\rho, s) = \Theta(\rho_1, s)$, which in contrast to the assumption of a semi-infinite domain, is only a weak assumption. In addition, as (2.19) is the solution to the homogeneous PDE, the domain considered for the analysis cannot contain a source term (see Section 2.1.2). Hence, $\Theta(\rho_1, s)$ is used, which is a measured quantity and bounds the domain such that the source term is outside the considered domain. The boundary constant is then given by

$$C_1(s) = \exp(-\lambda_1^s \rho_1) \Theta(\rho_1, s). \quad (2.34)$$

This determines the solution of (2.13), $\Theta(\rho, s)$, such that

$$\Theta(\rho, s) = \exp(\lambda_1^s (\rho - \rho_1)) \Theta(\rho_1, s). \quad (2.35)$$

The solution at a second measurement point $\rho_2 > \rho_1$ is denoted by $\Theta(\rho_2)$. Then (2.35) can be re-expressed as

$$\frac{\Theta(\rho_2, s)}{\Theta(\rho_1, s)} = \exp(\lambda_1^s (\rho_2 - \rho_1)). \quad (2.36)$$

The left hand-side is built from the measured complex valued Fourier coefficients at measurement locations ρ_1 and ρ_2 and the right-hand side contains the unknown transport coefficients. As such this representation can also be used to check if the estimated transport coefficients match the measurements on the left-hand side over the different ω in $s = i\omega$.

Similarly, the transfer functions for a cylindrical domain can be derived

$$\frac{\Theta(\rho_2, s)}{\Theta(\rho_1, s)} = e^{\lambda_1(\rho_2 - \rho_1)} \frac{\Psi\left(\frac{\lambda_2}{\lambda_2 - \lambda_1}, 1, (\lambda_2 - \lambda_1)\rho_2\right)}{\Psi\left(\frac{\lambda_2}{\lambda_2 - \lambda_1}, 1, (\lambda_2 - \lambda_1)\rho_1\right)} \quad (2.37)$$

and if $V = 0$

$$\frac{\Theta(\rho_2, s)}{\Theta(\rho_1, s)} = \frac{K_0(z\rho_2)}{K_0(z\rho_1)}. \quad (2.38)$$

In principle, we want to invert these transfer functions to find explicit relationships for χ , but now in terms of two measurements $\Theta(\rho_1, s)$ and $\Theta(\rho_2, s)$. Therefore, consider again a simplified case of (2.36) in which $V_s = 0$ and only one harmonic is used, i.e., $s = i\omega$. Thus, the temperatures at fixed ω at two spatial locations can be expressed as $\Theta(\rho_1) = A_1 e^{i\phi_1}$ and $\Theta(\rho_2) = A_2 e^{i\phi_2}$ such that the transfer function (2.36) can be rewritten as

$$\frac{A_2 e^{i\phi_2}}{A_1 e^{i\phi_1}} = \exp\left(-\sqrt{\frac{3i\omega + \tau_{invs}}{2}} \frac{\Delta\rho}{\chi}\right), \quad (2.39)$$

where $\Delta\rho = \rho_2 - \rho_1$. Applying the natural logarithm and taking the square of (2.39) results in

$$\ln\left(\frac{A_2}{A_1}\right)^2 - (\phi_2 - \phi_1)^2 + 2\ln\left(\frac{A_2}{A_1}\right) i(\phi_2 - \phi_1) = \frac{3i\omega + \tau_{invs}}{2} \frac{\Delta\rho^2}{\chi}. \quad (2.40)$$

The relationship for χ can be calculated by considering the imaginary part of (2.40)

$$\chi_{s4} = \frac{3}{4} \frac{\omega}{\frac{\ln(A_2) - \ln(A_1)}{\Delta\rho} \left(\frac{\phi_2 - \phi_1}{\Delta\rho}\right)}. \quad (2.41)$$

The diffusivity χ can only be calculated properly if the phases ϕ_1 and ϕ_2 are unwrapped, which means that possible additional 2π rotations between ρ_2 and ρ_1 need to be accounted for.

If (2.41) is compared to the relationship in (2.31), it is immediately clear that the derivatives A'/A and ϕ' in slab geometry are constant and defined as

$$\frac{A'}{A} = \frac{d}{d\rho}(\ln(A)) \equiv \frac{\ln(A_2/A_1)}{\Delta\rho}, \quad \phi' \equiv \frac{\phi_2 - \phi_1}{\Delta\rho}. \quad (2.42)$$

This could also have been derived directly from (2.21) and (2.25) by taking its spatial derivative, which results in

$$\frac{d}{d\rho} \left(\frac{A'}{A} \right) + i\phi'' = 0. \quad (2.43)$$

This also means that from a mathematical point of view if an assumption is made on the boundary conditions and the parameter dependence (here that the transport coefficients are independent of ρ , see Section 2.1.2), then the definition of the spatial derivatives A' and ϕ' as function of A and ϕ follows automatically. On the other hand, if one makes a choice for the approximation of the derivatives, then the spatial dependence on the parameters and boundary condition follows. As such, fitting ϕ' and A' differently from (2.42) is a direct violation of the assumption that the parameters are independent of ρ . On the other hand, if more complicated relationships are used, e.g., cylindrical geometry, the derivatives A'/A and ϕ' are not so easily expressed in terms of A_2 , A_1 , ϕ_1 , and ϕ_2 . This can also be shown by considering (2.23) where $V = 0$

$$\frac{\Theta'}{\Theta} = -z \frac{K_1(z\rho)}{K_0(z\rho)}, \quad (2.44)$$

which results in the following spatial logarithmic amplitude derivative and spatial phase derivative

$$\frac{A'}{A} = \Re \left(-z \frac{K_1(z\rho)}{K_0(z\rho)} \right), \quad \phi' = \Im \left(-z \frac{K_1(z\rho)}{K_0(z\rho)} \right), \quad (2.45)$$

where \Re and \Im denote the real and imaginary part. These relationships show the complexity of the spatial logarithmic amplitude derivative and the spatial phase derivative in cylindrical geometry. The transfer function description avoids this ambiguity of how to determine A'/A and ϕ' . However, from the transfer function description in cylindrical geometry it was not possible to derive explicit relationships for χ . This requires an implicit method, which is discussed in Chapter 7. A third option suggested in the literature is to directly substitute $\Theta = A \exp(i\phi)$ into (2.7), which is explained next.

2.3.3 Double spatial derivatives of A and ϕ

It is also possible to use only spatial derivatives of A and ϕ to calculate χ . The expression for χ will then also include the double spatial derivatives A''

and ϕ'' because a second order PDE is considered. This expression for χ is found by substituting $\Theta = A \exp(i\phi)$, $\Theta' = A' \exp(i\phi) + i\phi' A \exp(i\phi)$, and $\Theta'' = A'' \exp(i\phi) + i\phi' A' \exp(i\phi) + iA' \phi'' \exp(i\phi) - (\phi')^2 A \exp(i\phi) + iA\phi'' \exp(i\phi)$ in (2.12) and by dividing by $A \exp(i\phi)$.

In slab geometry, ϕ'' and $d(A'/A)/d\rho$ are equal to zero, hence, this substitution is not useful to derive new approximations if the transport coefficients are independent of ρ . On the other hand, expressing (2.12) in terms of double spatial derivatives again shows that the three approaches are equivalent and that the boundary conditions and spatial dependencies are again contained within the spatial derivatives.

Θ' and Θ'' can be substituted in the PDE in cylindrical geometry, i.e., (2.7) without a source. This results for the imaginary part in [Jacchia, 1991]

$$\chi(\rho) = \frac{1.5\omega - \left(2.5\frac{\Gamma}{n} + \Gamma\right) \phi'}{\phi'' + \left(2\frac{A'}{A} + \frac{1}{\rho} + \frac{n'}{n} + \frac{\chi'}{\chi} + \frac{U(\rho)}{\chi}\right) \phi'}. \quad (2.46)$$

Note that in this representation Γ and n and its gradient n' have been included, which would allow to take density gradients into account. However, in this thesis we assume $n' = 0$ unless stated otherwise. To be able to use (2.46) to calculate χ , again χ needs to be assumed constant such that $\chi'/\chi = 0$ and the convective velocity needs to be assumed zero, i.e., $U(\rho) = 0$. More importantly, the double derivatives are difficult to approximate in practice due to noise and the spacing between measurement channels. Therefore, ϕ'' is assumed to be zero, which is acceptable in slab like geometry (large radii), to arrive at a feasible expression for χ [Jacchia, 1991] and χ can be calculated using the simplified form of (2.46), i.e.,

$$\chi_c = \frac{3}{4} \frac{\omega}{\left(\frac{A'}{A} + \frac{1}{2\rho}\right) \phi'}. \quad (2.47)$$

The assumption of $\phi'' = 0$ means that ϕ' is assumed constant as was the case in slab geometry. On the other hand, in cylindrical geometry $\phi'' \neq 0$, see (2.45), as such (2.47) is not a true cylindrical expression, but an approximation. This approximation (2.47), together with those based on slab geometry (2.28), (2.29), (2.30), and (2.31) are the standard relationships used in the literature to calculate χ .

2.4 Directionality of heat waves

Section 2.3 discussed semi-infinite domains, implying that perturbations generated at a certain location should vanish at infinity. This also implies that heat waves are propagating outwards. Hence, the semi-infinite domain is less suitable for heat waves propagating inwards. This will be discussed in detail in Chapter 5. A natural choice in a cylindrical geometry is a symmetric domain, i.e.,

using a Neumann boundary condition at $\rho = 0$

$$\frac{\partial \Theta}{\partial \rho}(\rho = 0) = 0. \quad (2.48)$$

An advantage of using (2.48) is that $D_1(s) = 0$ in (2.15). This is again not easily proven analytically. However, if $V = 0$, then $D_1(s) = 0$ [Carslaw, 1959]. This suggests that also $D_1(s) = 0$ in (2.15) when $V \neq 0$. This again has been numerically verified in (2.15) by comparing it to finite difference simulations using the boundary condition given in (2.48). This shows that the error between the analytic and numerical simulations are small and that the error is decreasing with increasing density of the discretization grid. Hence, it is concluded that $D_1(s) = 0$ for a Neumann boundary condition in (2.15) such that (2.15) reduces to

$$\Theta(\rho, s) = D_2(s) e^{\lambda_1 \rho} \Phi\left(\frac{\lambda_2}{\lambda_2 - \lambda_1}, 1, (\lambda_2 - \lambda_1) \rho\right). \quad (2.49)$$

Again, there are two possibilities to handle the unknown $D_2(s)$ when $s = i\omega$. One possibility is to use the logarithmic temperature derivative to eliminate $D_2(s)$ resulting in (see [Slater, 1960] for the definition of the derivative of Φ)

$$\frac{\Theta'}{\Theta} = \lambda_1 + \lambda_2 \frac{\Phi(a + 1, 2, (\lambda_2 - \lambda_1) \rho)}{\Phi(a, 1, (\lambda_2 - \lambda_1) \rho)}. \quad (2.50)$$

In this relationship V is assumed constant. However, at $\rho = 0$, $V = 0$ this means that this relationship can only be used as an approximation of the underlying PDE at some distance from $\rho = 0$. Another important aspect is that the derivatives are defined in terms of ρ and not in terms of distance to the source. Hence, the derivatives are defined positively for heat waves propagating towards the center. If $V = 0$, (2.50) simplifies to

$$\frac{\Theta'}{\Theta} = z \frac{I_1(z\rho)}{I_0(z\rho)}, \quad (2.51)$$

where z is defined according to (2.24). This last relationship is well known in the literature [Carslaw, 1959; Jacchia, 1991]. Alternatively, the transfer function representation can be used. In that case $D_2(s)$ needs to be determined by a second boundary condition. The most logical choice for a second boundary condition is $\Theta(\rho, s) = \Theta(\rho_1, s)$. The transfer function using (2.49) then becomes

$$\frac{\Theta(\rho_2, s)}{\Theta(\rho_1, s)} = e^{\lambda_1 \Delta \rho} \frac{\Phi\left(\frac{\lambda_2}{\lambda_2 - \lambda_1} a, 1, (\lambda_2 - \lambda_1) \rho_2\right)}{\Phi\left(\frac{\lambda_2}{\lambda_2 - \lambda_1}, 1, (\lambda_2 - \lambda_1) \rho_1\right)}, \quad (2.52)$$

or when $V = 0$

$$\frac{\Theta(\rho_2, s)}{\Theta(\rho_1, s)} = \frac{I_0(z\rho_2)}{I_0(z\rho_1)}, \quad (2.53)$$

where the solutions at a second measurement point $\rho_1 > \rho_2$ is used as resulting temperature $\Theta(\rho_2)$. However, using the transfer function it was not possible to derive explicit relationships for χ , V , and τ_{inv} using this relationship. This also holds for a number of other choices of boundary conditions as these choices would result in a combination of two eigenfunctions, which are difficult to invert to express χ explicitly in terms of amplitude and phase. For instance, a logic choice for the boundary condition at the edge of the plasma would be a Robin boundary condition of the form $\partial\Theta(\rho_{edge})/\partial\rho = q_{loss} \cdot \Theta(\rho_{edge})$, where the heat flux q_{loss} describes a steady heat loss. Another option is to bound (2.14) by two measurement points, instead of only one as was described here. These options are also possible, but in these cases an implicit scheme, such as the one used in Chapter 7, is necessary.

2.5 Conclusion and summary

In this chapter, PDEs have been introduced to describe heat transport in tokamaks and stellarators. A number of assumptions have been introduced, which allow to calculate the analytic solutions of the PDEs in terms of transfer functions and logarithmic temperature derivatives. This clarified the relationship between the amplitude and phase and its spatial derivatives, in case a homogeneous domain is assumed.

Based on the logarithmic temperature derivative and transfer function in slab geometry, the diffusivity can be directly expressed in terms of the spatial derivatives of amplitude and phase when the convectivity is assumed zero. However, ideally the convectivity should also be considered, which is shown in Section 2.1.2. This also holds for the approximation in cylindrical geometry described in Section 2.3.3. Moreover, it has been shown that slab geometry and (2.47) only give an approximation of the diffusivity in cylindrical geometry. Therefore, in the next three chapters the quality of the approximations presented here and new approximations to calculate the diffusivity, convectivity, and damping in a cylindrical geometry are derived. The proposed method takes the convectivity and cylindrical geometry better into account. These derivations are based on the logarithmic temperature derivative in line with the fusion literature. More specifically, Chapter 3 takes the convectivity into account in slab geometry giving a relationship, which also gives a better approximation of the transport coefficients in cylindrical geometry. Additionally, the influence of a number of simplifying assumptions made in this chapter are also discussed in Chapter 3. Then, in Chapter 4 new approximations are calculated based on the semi-infinite domain assumption for heat waves propagating towards the edge.

In Chapter 5 the symmetry boundary condition is used to derive approximations for heat waves propagating towards the center. The subsequent chapters will use the introduced modeling techniques in combination with statistics to take measurement uncertainties into account.

Chapter 3

Estimation of the transport coefficients using slab geometry (semi-infinite)

This chapter deals with semi-infinite slab geometry approximations to calculate the transport coefficients using the amplitude and phase of temperature fluctuations induced by a periodic perturbation. The relationships given in the literature, which are described in Section 2.3.1 and Section 2.3.3 do not consider a convective term. However, the modeling in Section 2.1.1 suggests that a convective term should be included. This especially holds for approximations of χ that are derived in slab geometry since this introduces a pseudo convective term χ/ρ in (2.11). This chapter derives new relations based on slab geometry, which also includes both convectivity and damping. However, if both a convective and a damping term need to be considered, it is necessary to consider at least two harmonics instead of one, as is often considered in fusion research. The new relationships are derived using the logarithmic derivative and modeling introduced in Chapter 2 and these are compared to the standard relationships in the literature using the analytical solutions for cylindrical geometry. The diffusivity in cylindrical geometry is not affected directly by the cylindrical geometry, but the calculation of the convectivity and damping are. Therefore, a compensation is suggested to calculate the convectivity and damping in cylindrical geometry using the slab geometry relationships. Finally, the consequences of the assumptions used to simplify the PDEs on the calculation of the transport coefficients are studied through an example.

This chapter is based on the following article: van Berkel, M., et al. [2014]. Explicit approximations to estimate the perturbative diffusivity in the presence of convectivity and damping I Semi-infinite slab approximations, *Phys. Plasmas* **21**: 112507.

3.1 Derivation of explicit approximations based on slab geometry

New approximations for determining the χ , V , and τ_{inv} in cylindrical geometry are introduced based on slab geometry, which use one or two harmonics. First, a new approximation for χ is derived using only the phase of two harmonics. Then, approximations for V_s and τ_{invs} are derived and finally approximations are derived assuming $\tau_{invs} = 0$.

3.1.1 Approximations for χ in the presence V and τ_{inv}

In principle, every harmonic fixes two degrees of freedom, which means in practice that either χ and τ_{inv} or χ and V can be estimated if only one harmonic is used. The estimation of χ , V and τ_{inv} together, requires at least two harmonics. Therefore, consider the semi-infinite slab geometry solution in (2.21)

$$\frac{A'}{A} + i\phi' = \lambda_1^s. \quad (3.1)$$

where the spatial derivatives are defined according to (2.42). The principal square root in λ_1^s can be split in its real and imaginary parts using, see (2.13)

$$\lambda_1^s = -\frac{V_s}{2\chi} - (\alpha + \beta i), \quad (3.2)$$

where

$$(\alpha + \beta i)^2 = \left(\frac{V_s}{2\chi}\right)^2 + \frac{3}{2} \frac{(\tau_{invs} + i\omega)}{\chi}, \quad (3.3)$$

with

$$\alpha^2 - \beta^2 = \left(\frac{V_s}{2\chi}\right)^2 + \frac{3}{2} \frac{\tau_{invs}}{\chi} \quad (3.4)$$

and

$$2\alpha\beta = \frac{3}{2} \frac{\omega}{\chi}. \quad (3.5)$$

The coefficients α and β can also be used to express A'/A and ϕ' defined according to (2.42), by taking the real and imaginary part of λ_1^s using (2.21), (3.2), and (2.25), i.e.,

$$\frac{A'}{A} = -\left(\frac{V_s}{2\chi} + \alpha\right) \quad \text{and} \quad \phi' = -\beta. \quad (3.6)$$

The constants α and β are determined by rewriting (3.4) and (3.5) to

$$4\chi^2\alpha^4 - C_V\alpha^2 = \frac{9}{4}\omega^2, \quad (3.7)$$

$$4\chi^2\beta^4 + C_V\beta^2 = \frac{9}{4}\omega^2. \quad (3.8)$$

where $C_V = V_s^2 + 6\chi\tau_{invs}$. Both (3.7) and (3.8) are fourth order equations yielding four solutions for α and four for β . Fortunately, not all of these solutions are feasible because under natural assumptions, $\omega > 0$, $\chi > 0$, and in a semi-infinite domain ϕ' is negative. This means that according to (3.6), $\beta > 0$. In addition, following the definition in (3.5), the product of α and β is always positive, hence $\alpha > 0$.

There are three degrees of freedom (unknowns) in (3.3), which means that at least two harmonics ω_1 and ω_2 must be used. Consequently, one derivative is unnecessary, e.g., $\phi'(\omega_1)$ or $A'(\omega_2)/A(\omega_2)$. However, χ can be determined by only using $\phi'(\omega_1)$ and $\phi'(\omega_2)$ because (3.8) only contains two unknowns, χ and C_V , such that

$$\chi_\phi = \frac{3}{4} \sqrt{\frac{(\omega_1\phi'_{\omega_2})^2 - (\omega_2\phi'_{\omega_1})^2}{\phi_{\omega_1}^{\prime 2}\phi_{\omega_2}^{\prime 2}(\phi_{\omega_1}^{\prime 2} - \phi_{\omega_2}^{\prime 2})}}, \quad (3.9)$$

using the notations $\phi'_{\omega_1} = \phi'(\omega_1)$ and $\phi'_{\omega_2} = \phi'(\omega_2)$ and to differentiate between approximations the notation χ_ϕ is used instead of χ . The definition of the spatial phase derivatives in (3.9) is given by (2.42). The advantage of using only phase is that the estimate of χ is less insensitive to calibration errors. On the other hand, useful amplitude information is ignored, which can reduce the accuracy of the estimate significantly.

3.1.2 Approximations for V and τ_{inv}

The convectivity V_s denoted for this specific approximation by V_ϕ is found by solving for α in (3.7) and substituting it into (3.6) such that

$$V_\phi = -2\chi_\phi \frac{A'}{A} - \sqrt{\frac{C_V + \sqrt{C_V^2 + 36\chi_\phi^2\omega^2}}{2}}, \quad (3.10)$$

where C_V can be calculated in terms of χ_ϕ based on (3.8)

$$C_V = \frac{9}{4}\omega^2(\phi')^{-2} - 4\chi_\phi^2(\phi')^2. \quad (3.11)$$

The damping τ_{invs} , denoted as τ_ϕ , is calculated from the definition of C_V

$$\tau_\phi = \frac{C_V - V_\phi^2}{6\chi_\phi}. \quad (3.12)$$

It is not possible to calculate the convectivity or damping from the phase only, unless either the damping or convectivity is considered negligible. In the noiseless

slab geometry case, it does not matter if ω_1 or ω_2 is used for ω in A'/A and ϕ' . Here, only one variation has been given to calculate χ , V_s , and τ_{invs} using mainly the phase. There exists a number of other variations using also $A'(\omega_1)/A(\omega_1)$ and $A'(\omega_2)/A(\omega_2)$.

3.1.3 Approximations assuming $\tau_{inv} = 0$

In the special case that τ_{invs} is assumed zero, a single harmonic suffices to estimate both χ and V_s . This can be derived from (3.4) and (3.5), which results in

$$\chi_V = \frac{3}{2} \frac{\omega \frac{A'}{A}}{\left(\left(\frac{A'}{A}\right)^2 + (\phi')^2\right) \phi'} \quad (3.13)$$

and

$$V_V = \frac{3}{2} \frac{\omega \left((\phi')^2 - \left(\frac{A'}{A}\right)^2 \right)}{\left(\left(\frac{A'}{A}\right)^2 + (\phi')^2\right) \phi'}. \quad (3.14)$$

These approximations together with the well known relationships in the literature will be used to approximate χ , V , and τ_{inv} in cylindrical geometry.

3.2 Estimating χ under influence of V and τ_{inv}

In this section, the explicit approximations for χ , i.e., (2.28), (2.29), (2.30), (2.41), (3.9), and (2.47) are compared for different values of ρ , ω , χ , V , and τ_{inv} . For the comparison, the true values of A'/A and ϕ' in a semi-infinite cylindrical geometry are used based on the analytical solution in (2.22) to generate A'/A and ϕ' for ρ and specific transport coefficients. This section consists of three parts: a presentation and discussion on the selection of the best approximations when only χ is considered; a similar discussion when χ and τ_{inv} are considered ($V = 0$); and when χ , V , and τ_{inv} are considered.

It is cumbersome to make a comparison of the different approximations for five parameters (ρ , ω , χ , V , and τ_{inv}). Therefore, the transport coefficients are normalized with ω by dividing (2.14) by ω resulting in

$$\frac{3}{2}i\Theta(\rho, s) = \frac{1}{\rho} \frac{d}{d\rho} \left(\rho \frac{\chi}{\omega} \frac{\partial \Theta(\rho, s)}{\partial \rho} + \rho \frac{V}{\omega} \Theta(\rho, s) \right) - \frac{3}{2} \frac{\tau_{inv}}{\omega} \Theta(\rho, s). \quad (3.15)$$

Consequently, the normalized transport coefficients in a cylindrical geometry are given by $\bar{\chi} = \chi/\omega$, $\bar{V} = V/\omega$, and $\bar{\tau}_{inv} = \tau_{inv}/\omega$ such that the heat-equation and its solutions no longer depend on ω explicitly. In case two harmonics are necessary, $\phi'(\omega_1)$ and $\phi'(\omega_2)$ are calculated using $\omega_1 = \omega$ and $\omega_2 = 2\omega$ corresponding to the first and second harmonic.

3.2.1 Diffusivity only

The comparison for χ only ($V = 0$ and $\tau_{inv} = 0$) is made based on a large number of possibilities of χ , ω , and ρ in terms of the normalized $\bar{\chi}$. The approximations are shown in Figure 3.1 in terms of the relative error with respect to the true diffusivity χ .

All the approximations perform well in a slab-like geometry, i.e., they approximate χ well if the ratio $\rho/\bar{\chi} \gg 0$. In χ_c large relative errors are observed for small $\rho/\bar{\chi}$, which can be understood by considering χ_c in (2.47). The large error is caused by ρ^{-1} term in χ_c , which overcompensates resulting in a higher estimated diffusivity [Jacchia, 1991]. The A'/A and ϕ' are negative quantities for heat waves propagating outwards. Hence, the sum of ρ^{-1} and A'/A results in zero at the center of the dark red area. On the other hand, it is also clear that compared to the other slab geometry approximations χ_c and χ_ϕ perform better. The approximation χ_ϕ is more accurate in a slightly larger region than the approximation χ_c . However, it is also important to note again that χ_ϕ is based on the phase of two harmonics instead of amplitude and phase of one harmonic as is the case for χ_c making it less comparable to the other relationships.

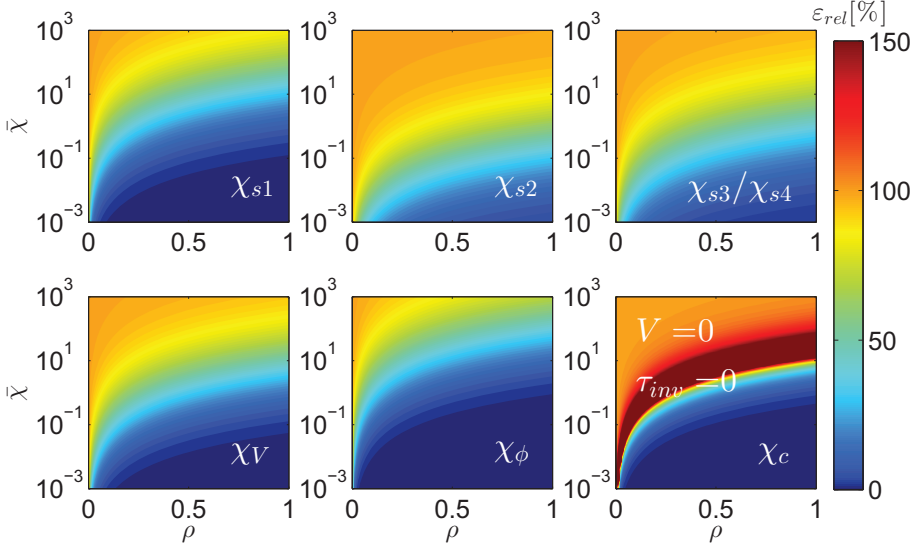


Figure 3.1. Comparison between the different relative errors of the χ estimates for a large range of $\bar{\chi} = \chi/\omega$ and ρ . The relative error is defined as $\varepsilon_{rel} = 100 \times \frac{|\chi - \chi_{est}|}{\chi}$ [%], where χ_{est} is one of the possible approximations. Note, that $\bar{V} = \tau_{inv} = 0$ is the same as $\bar{V} = \bar{\tau}_{inv} = 0$. In this case χ_{s3} and χ_{s4} were almost exactly the same in terms of their error. This comparison is based on a cylindrical geometry using an infinite domain boundary condition assuming χ independent of ρ and $V = \tau_{inv} = 0$, where the heat waves travel outwards. The darkest blue represents $\varepsilon_{rel} < 1\%$ and the darkest red represents all $\varepsilon_{rel} > 150\%$.

3.2.2 Diffusivity and damping

Only three approximations are available to estimate χ under the influence of the damping τ_{inv} , i.e., χ_{s4} in (2.41), χ_ϕ in (3.9), and χ_c in (2.47). The approximations are presented at a limited number of spatial locations ρ . In order to have significant impact on the heat pulse propagation, τ should be of the order of the energy confinement time (τ_e), i.e., 1 s for JET or ITER. Therefore, the range of τ is chosen such that $0.5 < \tau < \infty$ ($\tau = \infty$ meaning no damping), i.e., $0 \leq \tau_{inv} \leq 2$. This range is the same for the normalized $\bar{\tau}_{inv}$ as the applicable range of ω is $\omega > 1$ [rad/s].

In general the effect of damping τ_{inv} is not directly influenced by the cylindrical geometry ($V = 0$), which can be understood by comparing (2.10) and (2.11). In addition, τ_{inv} acts as a shift parameter in (2.10), which basically shifts the solution in ρ . This means that for large τ_{inv} , the regions in which χ are approximated well is extended for increasing τ_{inv} . However, these effects

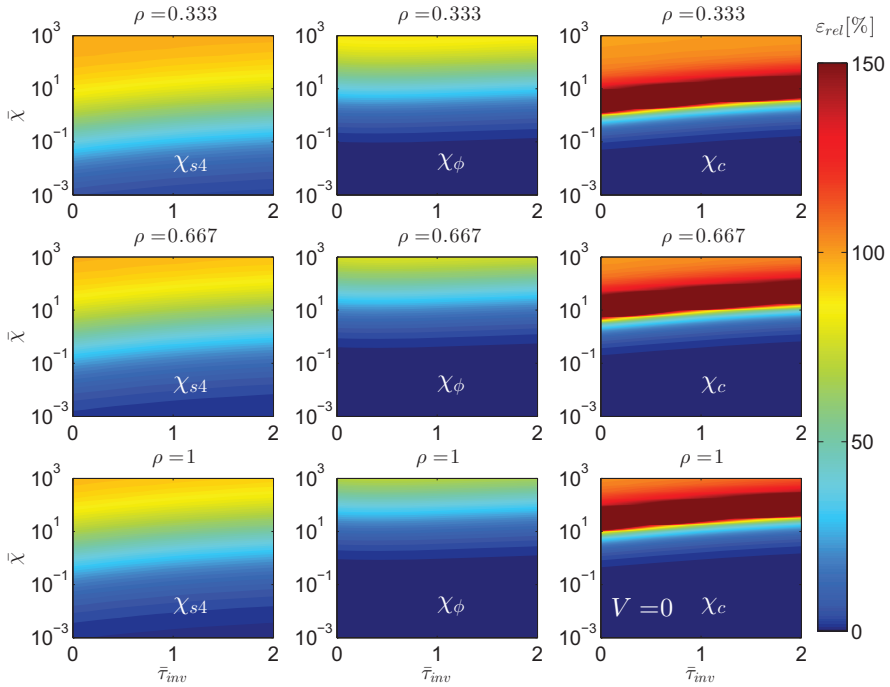


Figure 3.2. Comparison between the relative errors of the χ estimates using χ_{s4} , χ_ϕ , and χ_c for a large range of $\bar{\chi} = \chi/\omega$, $\bar{\tau}_{inv}$ and ρ . This comparison is based on a cylindrical geometry using an infinite domain boundary condition assuming constant spatial dependencies of χ and τ_{inv} . The darkest blue represents $\varepsilon_{rel} < 1\%$ and the darkest red represents all $\varepsilon_{rel} > 150\%$.

are also influenced by the approximation error in χ and V . Therefore, it is not a one-to-one relationship. This can also be seen in Figure 3.2 where with increasing τ_{inv} also the approximation region increases for all approximations. All approximations under the influence of damping behave similar to the case of χ only.

3.2.3 Diffusivity, convectivity, and damping

At least two harmonics are necessary if three parameters, i.e., χ , V , and τ_{inv} , need to be estimated. This also means that it is no longer possible to estimate χ with χ_c as is illustrated in Figure 3.3, which is also well known in the literature [Jacchia, 1991]. On the other hand, χ can be estimated using χ_ϕ for a large

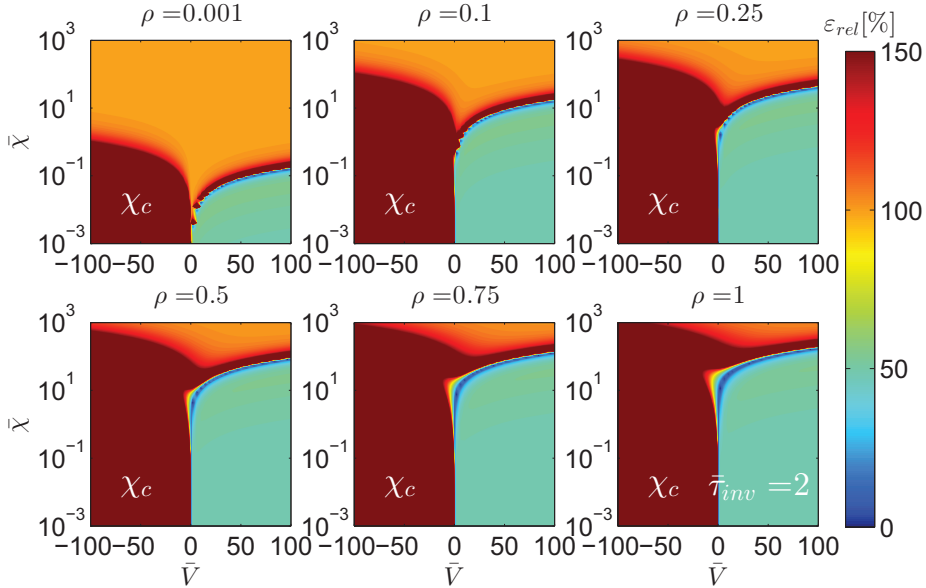


Figure 3.3. The relative errors of the χ_c estimates as function of $\bar{\chi} = \chi/\omega$, \bar{V} and ρ . These errors are based on a cylindrical geometry using an infinite domain boundary condition where χ , V , and $\tau_{inv} = 2$ are independent of ρ . The heat waves travel outwards. The darkest blue represents $\varepsilon_{rel} < 1\%$ and the darkest red represents all $\varepsilon_{rel} > 150\%$.

range of parameters as is shown in Figure 3.4 on page 41. It is unclear what a good range is for the parameter $\bar{V} = V/\omega$. Therefore, an arbitrary choice for this range is made $-100 \leq \bar{V} \leq 100$. In general χ can be approximated well for large ρ as it then behaves more slab-like. On the other hand, for large $\bar{\chi}$ and small ρ the cylindrical effects are stronger, thus the errors are large. The effect of the damping coefficients is not shown here as it is rather small. The approximation χ_V can also be used when $\tau_{inv} = 0$ and performs well, but only for positive V . In the next section, it is discussed how to estimate the convectivity and damping and their common errors.

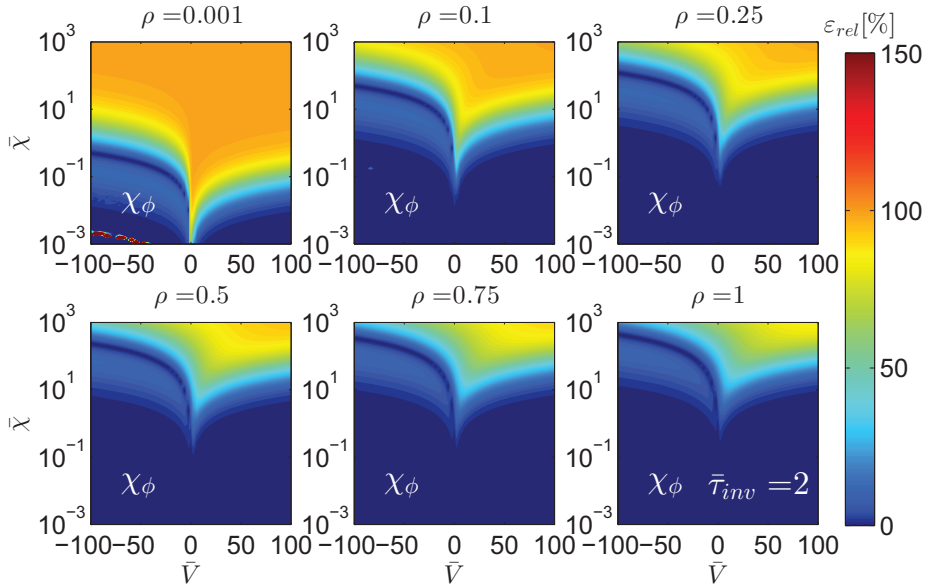


Figure 3.4. The relative errors of the χ_ϕ estimates as function of $\bar{\chi} = \chi/\omega$, \bar{V} and ρ . The errors are based on a cylindrical geometry using an infinite domain boundary condition where χ , V , and $\bar{\tau}_{inv} = 2$ are independent of ρ . The heat waves travel outwards. The darkest blue represents $\varepsilon_{rel} < 1\%$ and the darkest red represents all $\varepsilon_{rel} > 150\%$.

3.3 Estimating the convectivity and damping

In this section, the possibility of estimating the convectivity V and damping τ_{inv} in a semi-infinite cylindrical domain is investigated based on the slab geometry estimates V_ϕ and τ_ϕ . Then, the effect of model errors arising from idealized assumptions are studied. A slab geometry example is used avoid errors arising from the idealized assumptions are being mixed up by errors arising from cylindrical geometry.

3.3.1 Estimation of V and τ_{inv} in a semi-infinite cylindrical geometry

The only possibility to estimate χ in a cylindrical geometry under the influence of V and τ_{inv} presented here is by using χ_ϕ in (3.9). The accompanying V_ϕ in (3.10) and τ_ϕ in (3.12) give the slab estimates V_s and τ_{invs} and not the cylindrical V and τ_{inv} . This is explained in Section 2.1.3. The quality of these estimates using V_s and τ_{invs} is investigated on the basis of a semi-infinite cylindrical geometry

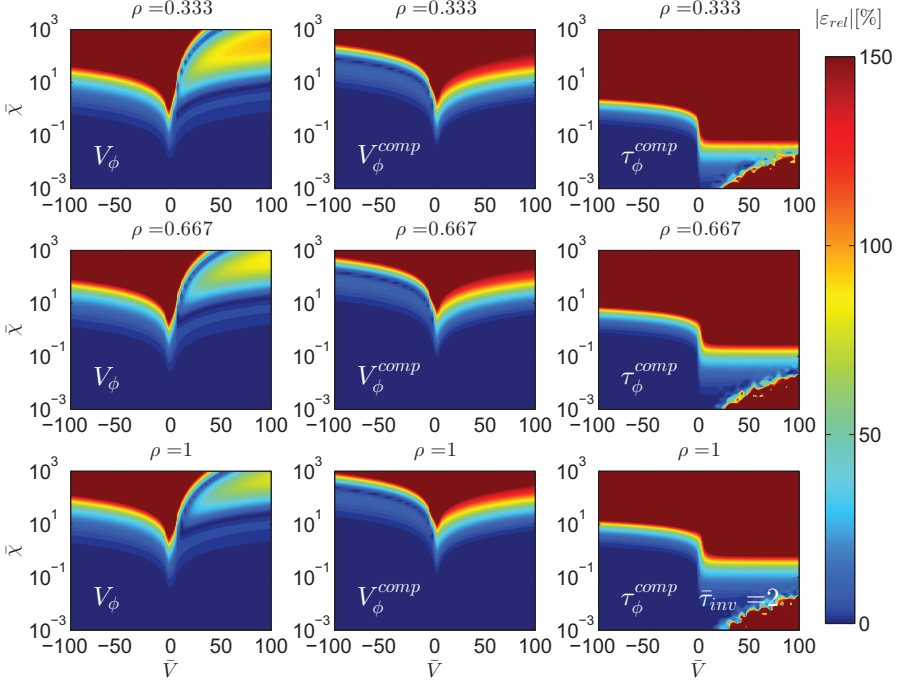


Figure 3.5. The relative error of the estimates of V and τ_{inv} using the approximations V_ϕ , V_ϕ^{comp} , and τ_ϕ^{comp} for a large range of $\bar{\chi}$, \bar{V} , and ρ . This comparison is based on a cylindrical geometry using a semi-infinite domain, where the heat waves travel outwards. The darkest blue represents $\varepsilon_{rel} < 1\%$ and the darkest red represents all $\varepsilon_{rel} > 150\%$.

and is presented in Figure 3.5.

The slab approximation V_ϕ still gives a good estimate of the cylindrical geometry because the damping takes part of the model errors into account (see (2.11)). However, this also means that the estimates of τ_{inv} in a cylindrical geometry are poorly approximated by τ_ϕ (not shown here). As an alternative, it is also possible to compensate for the model errors based on (2.11), i.e.,

$$V_\phi^{comp} = V_\phi - \frac{\chi_\phi}{\rho}, \text{ and } \tau_\phi^{comp} = \tau_\phi + \frac{2}{3} \frac{V_\phi}{\rho}. \quad (3.16)$$

The compensated V_ϕ^{comp} improves the estimate of V in some regions, but decreases it in other regions. This can be understood by comparing V_ϕ^{comp} to χ in Figure 3.4. The region where V_ϕ^{comp} approximates V well is almost an exact copy of the region where χ_ϕ approximates χ well in Figure 3.4. In (3.16), it also

becomes clear that there is a clear relationship between the chosen base geometry (slab, cylindrical) and the spatial variation of the transport coefficients. If one allows the transport coefficients V_s and τ_{invs} to be spatial dependent, then it is possible to transform a cylindrical geometry into a slab geometry.

The damping can only be estimated by the use of τ_ϕ^{comp} in a limited region. One might expect that by replacing V_ϕ by V_ϕ^{comp} to calculate τ_ϕ^{comp} might increase the approximation region, but the differences are rather small.

It is clear that the slab approximations with or without compensation can approximate the convectivity and damping in a semi-infinite cylindrical geometry with constant parameters in certain parameter ranges of $\bar{\chi}$, \bar{V} , $\bar{\tau}_{inv}$, and ρ . However, in reality the profiles can vary spatially and a different boundary condition is present than the infinite domain. The effect of these varying profiles and different boundary conditions on the estimates of χ , V , and τ_{inv} is investigated next.

3.3.2 The effect of boundary conditions and radial dependent profiles

Errors originating from (varying) spatial dependent profiles and boundary conditions different from the ones assumed used here are important in practice. It has been shown that using slab geometry approximations to estimate the transport coefficients in a cylindrical geometry also introduces errors. Therefore, a slab geometry simulation is used here to distinguish between errors originating from varying profiles/boundary conditions and cylindrical geometry. Although only the errors for (3.9), (3.10), and (3.12) are shown, these errors occur for all approximations based on semi-infinite domains, including the ones from the literature, as they are based on the same assumptions. This also holds for the ones based on symmetry boundary conditions discussed in Section 2.4.

The choice of an infinite domain description allows the derivation of explicit equations, which is an important advantage over other choices of the boundary conditions. However, the disadvantages are generally not so clear, but should also be considered:

1. It is assumed that the parameters are independent of ρ from $[\rho_i, \infty)$, so even spatial variations far from the used A'/A and ϕ' will introduce an error on the estimated diffusivity, even if the domain on which A'/A and ϕ' are calculated are constant in space.
2. There is a difference between the modeled and the real boundary, i.e., estimates close to the real boundary will show a significant bias (errors). This was already shown in [Goedheer, 1986] using analytic expansions.

The introduced bias due to mismodeling is partly suppressed in practice because (2.10) acts as a low-pass filter, suppressing high-frequency errors more strongly

than low-frequency information. The amount of suppression also depends on the distance to the boundary, on the variation of the parameters, and on the distance of this variation to the location ρ . However, as τ_{inv} and V are influenced by low-frequency information, they are affected more strongly by these errors, making it often impossible to find the correct τ_{inv} and V . These effects can be demonstrated through an example.

Consider as an example a heat-transport model in slab geometry (2.10) is discretized using finite difference and simulated with boundary conditions $\partial T/\partial\rho(\rho=0)=0$ and $T(\rho=2.2)=0$ with a (point) source term at $\rho=0.0025$. Heat waves are studied propagating towards edge at $\rho=2.2$. The choice for slab geometry and heat waves towards the edge is made since χ_ϕ , V_ϕ , and τ_ϕ , using (3.9), (3.10), and (3.12), determine χ , V_s , and τ_{inv} exactly under these assumptions. Hence, only the effect of varying profiles and boundary conditions influence the result. The finite difference simulation uses 2000 measurement (spatial grid) points, which are equidistant with $\Delta\rho=0.0011$. The phase and amplitude as function of ρ are calculated from this finite difference simulation. The corresponding A'/A and ϕ' are calculated using (2.42), because this is the correct way to calculate A'/A and ϕ' in the case of slab geometry. In addition, as the distance between two points, $\Delta\rho$, is small, the errors in A'/A and ϕ' are negligible. The dimensionless radius ρ has been extended here to $\rho=2$ to show the errors originating from varying profiles and boundary conditions more clearly. The result is shown in Figure 3.6 on page 46, where a varying profile of χ and V_s in terms of steps are shown.

It is clear that the estimates of χ_ϕ feel the step in $\chi(\rho)$ before it occurs, which is, as explained, a direct consequence of choosing infinite domains. However, interestingly at the step in $\chi(\rho)$ ($\rho=0.5$) the estimates χ_ϕ and V_ϕ are close to the true values. The small difference at the step in $\chi(\rho)$ at $\rho=0.5$ is caused by the step in $V_s(\rho)$ at $\rho=1.25$, which influences the estimates at $\rho=0.5$. The same phenomenon can be observed at the step in $V_s(\rho)$ where both the estimates χ_ϕ and V_ϕ are exact. Due to (2.35) the estimates are insensitive to what happens before $\phi_1=\phi(\rho_1)$. However, in principle, they are sensitive to what happens at $\rho>\rho_1$, hence τ_{inv} is not exact at the steps. The estimates that come close to the boundary condition will also show errors, as was already discussed in [Goedheer, 1986].

A different aspect is the magnitude of variation in the estimates due to variations in the profiles and boundary conditions. Therefore, it is important to consider the y-scales in Figure 3.6 on page 46. The variations in the profiles influence χ to a lesser extent, but are disastrous for the estimates of V_s and τ_{inv} . Moreover, a step in $\chi(\rho)$ has a large influence on the estimates V_ϕ and τ_ϕ , but a step in $V_s(\rho)$ and $\tau_{inv}(\rho)$ (not shown here) influences χ_ϕ to a lesser extent. Note that the step in $V_s(\rho)$ is 10 times larger than the step in $\chi(\rho)$.

The errors introduced by the boundary errors show a similar behavior, which are significantly larger for V_ϕ and τ_ϕ . The main reason why the errors are

significantly larger for τ_ϕ and to a lesser extent V_ϕ is that errors propagate further at low frequencies. Both, $V_s(\rho)$ and $\tau_{invs}(\rho)$ are only important at low frequencies, see (2.13). This also explains why the estimate of χ using 25 Hz show larger errors than the estimate based on 100 Hz.

We refrain here from making statements about direction and absolute values of errors as this depends on too many factors such as the boundary conditions, the absolute values and the variation of profiles, frequency, how A'/A and ϕ' are approximated, etc. Therefore, only the qualitative behavior is shown, which also led us to the conclusion that V_s and τ_{invs} will be very difficult to study in practice using semi-infinite domains. This also holds for the estimates of the cylindrical V and τ_{inv} . On the other hand, a step in a profile is also the most extreme case. This means that it is not always impossible to estimate V_s and τ_{invs} or V and τ_{inv} in practice, but great care should be taken and different approximation methods for V and τ_{inv} may be necessary.

The argument could be made that these errors are suppressed by increasing the frequency of the perturbation source, but that will lead to noisy measurements due to the low-pass characteristic of the heat-transport, e.g., (2.36). A better solution is to use implicit methods discussed in Chapter 7, which allow the use of more complex models without many of the problems encountered by semi-infinite domains. In that case the approximations presented in this chapter form a tool for finding starting values for such implicit methods and to have a rough idea of the values of $\chi(\rho)$.

3.4 Summary

In this chapter, the problem of determining the diffusivity in cylindrical geometry using slab geometry relationships based on temperature fluctuations has been revisited. A number of new approximations have been introduced to estimate χ , V , and τ_{inv} directly from A'/A and ϕ' for different combinations of χ , V , and τ_{inv} . The approximations are based on semi-infinite slab geometry using standard assumptions in the literature.

The main result is the approximation of χ , under the influence of V and τ , based on the phases of two harmonics, which cannot be found in the fusion literature. The new approximation extends the region in which χ can be approximated compared to the well known relationship in [Jacchia, 1991] for cylindrical geometry even if $V = 0$. However, it should be noted that unlike the relationship in [Jacchia, 1991], the new approximation does not take density gradients into account and is based on the phase of two harmonics instead of amplitude and phase of one harmonic. This approximation performs well in a large region when convectivity is present for which this is the first direct expression in the literature. Here, the use of two harmonics cannot be seen as a deficit as at least two harmonics will be necessary.

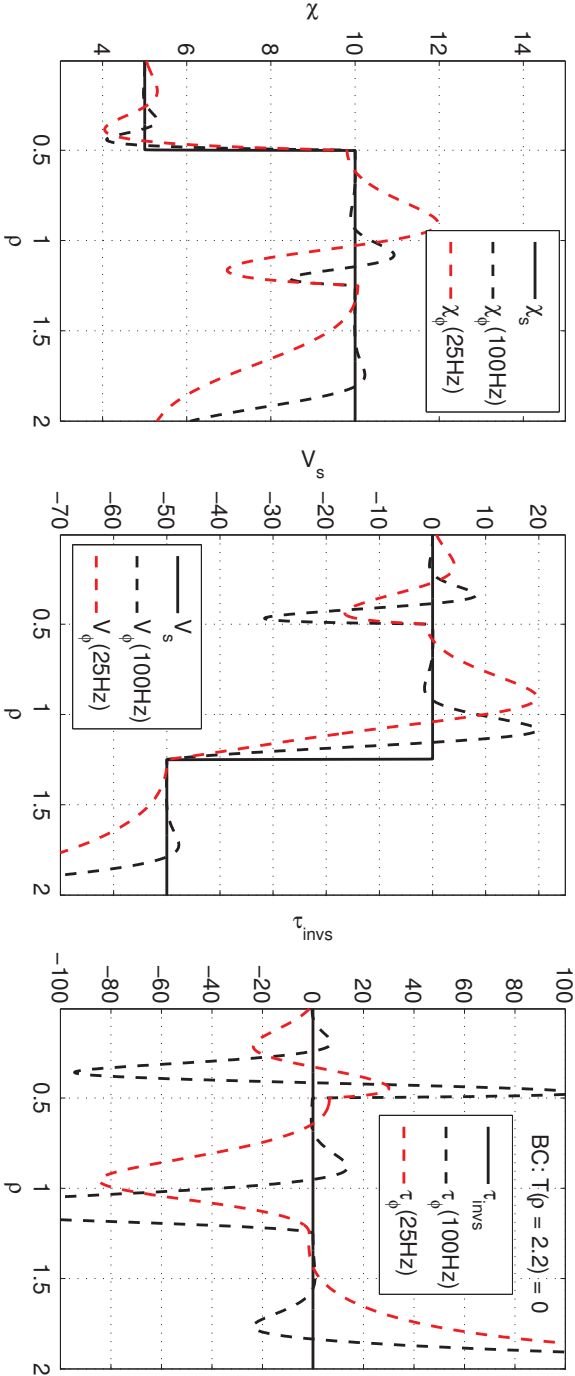


Figure 3.6. Comparison between two estimated profiles with a step in the $\chi(\rho)$ profile at $\rho = 0.5$ and in the $V_s(\rho)$ at $\rho = 1.25$. In addition, following boundary condition $T(\rho = 2.2) = 0$ is applied. Two estimates of χ , V_s , and τ_{invs} expressed as, χ_ϕ , V_ϕ , and τ_ϕ , are presented when using the first two harmonics ($\omega_2 = 2\omega_1$) for a base frequency 25 Hz and 100 Hz, i.e., the first two harmonics are used.

The use of semi-infinite domains necessary to arrive at explicit approximations introduces errors, which are related to varying profiles and boundary conditions at finite length. Moreover, these errors influence the convectivity and damping significantly, making the estimated V and τ_{inv} often erroneous. On the other hand, it is important to still estimate V and τ_{inv} as they can be used to select the proper approximation and to verify if the estimates of χ in the presence of V and τ_{inv} are correct. This will be explained in the next chapter, where a number of new approximations are derived, which are based on a semi-infinite cylindrical domain.

Chapter 4

Estimation of the transport coefficients for heat waves propagating outwards (semi-infinite)

In this chapter approximations are derived based directly on semi-infinite cylindrical geometry, that can be used to calculate the diffusivity, convectivity, and damping from the spatial derivatives of amplitude and phase of temperature fluctuations. In combination with the approximations based on slab geometry derived in Chapter 3, these can be used to calculate the transport coefficients for heat waves propagating outwards.

Three methodologies are used to find approximations for χ , V , and τ , namely continued fractions, asymptotic expansions, and multiple harmonics. A large number of approximations are found for various combinations of transport coefficient dependencies. These are compared for different values of the transport coefficients, dimensionless radius, and frequency. In practice, the transport coefficients are unknown. Therefore, also a method is introduced to select and test the accuracy of the approximation without knowing the actual transport coefficients.

This chapter is based on the following article: van Berkel, M., et al. [2014]. Explicit approximations to estimate the perturbative diffusivity in the presence of convectivity and damping II Semi-infinite cylindrical approximations, *Phys. Plasmas* **21**: 112508.

4.1 Derivation of explicit approximations

Three new methods are introduced to find approximations for determining the diffusivity in cylindrical geometry using (2.22) and (2.23). They are based on continued fractions, asymptotic expansions, and multiple harmonics. A great number of new approximations are derived in this chapter. Therefore, in this section only the basic ideas are explained to increase the readability. The full derivations are summarized in the next section and their derivations can be found in Appendix B.

4.1.1 Continued fractions

The solution to the Bessel Differential Equation (A.1) and Confluent Hypergeometric Differential Equation (A.2) can be found by substitution of a power series (see Appendix A). This yields the recurrence relationship and is used to calculate the infinite series representation of Bessel functions and Confluent Hypergeometric Functions. Moreover, if a fraction of these functions is studied, the recurrence relationships and series representation can also be rewritten in terms of a continued fractions representation [Cuyt, 2008; Jones, 1980]. By truncating this continued fraction, the ratio of Bessel functions and Confluent Hypergeometric Functions can be approximated. This approximation is then inverted such that the transport coefficients can be directly calculated.

The use of a continued fraction to derive an explicit approximation for χ is best explained by means of an example. Therefore, consider again (2.23) with $V = 0$ and z defined in (2.24)

$$\frac{\Theta'}{\Theta} = -z \frac{K_1(z\rho)}{K_0(z\rho)}, \text{ with } z = \sqrt{\frac{3}{2} \frac{i\omega + \tau_{inv}}{\chi}}.$$

The Laplace variable s has been replaced by $i\omega$ as s can only be measured on the imaginary axis. The continued J -fraction from [Cuyt, 2008; Jones, 1980] can be used to calculate the ratio

$$\frac{K_1(z\rho)}{K_0(z\rho)} = 1 + \frac{1}{2z\rho} - \frac{(4z\rho)^{-1}}{2z\rho + 2 - \frac{9/4}{2z\rho + 4 - \frac{25/4}{2z\rho + 6 - \frac{64/4}{\dots}}}}. \quad (4.1)$$

This continued fraction can be truncated to find explicit approximations for χ . The most simple truncation is

$$\frac{\Theta'}{\Theta} = -z \left(1 + \frac{1}{2z\rho} \right). \quad (4.2)$$

This can be rewritten by substituting (2.25) and rewriting in terms of z

$$z = -\left(\frac{A'}{A} + i\phi' + \frac{1}{2\rho}\right). \quad (4.3)$$

By substituting (2.24) and squaring (4.3), it is possible to find χ and τ_{inv} using the imaginary part and real part

$$\chi_c = \frac{3}{4} \frac{\omega}{\left(\frac{A'}{A} + \frac{1}{2\rho}\right) \phi'}$$

and

$$\tau_c = \frac{\omega}{2} \left(\frac{\left(\frac{A'}{A} + \frac{1}{2\rho}\right)}{\phi'} - \frac{\phi'}{\left(\frac{A'}{A} + \frac{1}{2\rho}\right)} \right). \quad (4.4)$$

The index, here c , is used to distinguish between the different approximations. The same approximation for χ is found in [Jacchia, 1991], i.e., (2.47), using a different approach. In contrast to the approach in [Jacchia, 1991], using this method also the corresponding τ_{inv} is found, which is denoted by τ_c .

More accurate approximations can be found by using more terms in the continued fraction. In principle, it is possible to find an approximation of arbitrary accuracy. However, in practice solving for χ beyond third order polynomials in z is too complicated. The reason is that finding zeros for a fourth or higher order polynomial in z is not straightforward. In addition, different solutions apply for different regions of interest because the coefficients in the polynomials in z depend on A'/A and ϕ' . Hence, mathematical bifurcations can occur.

The continued fraction in (4.1) can also be truncated at a later stage, for the first three terms of (4.1) resulting in

$$\frac{\Theta'}{\Theta} = -z + \frac{1}{2\rho} + \frac{1}{\rho} \left(-\frac{1/4}{2z\rho + 2 - \frac{9/4}{2z\rho + 4}} \right). \quad (4.5)$$

It can be rewritten in terms of z resulting in the third order polynomial

$$0 = a_3 z^3 + a_2 z^2 + a_1 z + a_0, \quad (4.6)$$

with coefficients

$$a_3 = 16\rho^3, a_2 = 16\frac{\Theta'}{\Theta}\rho^3 + 56\rho^2, \\ a_1 = 48\frac{\Theta'}{\Theta}\rho^2 + 45\rho, \text{ and } a_0 = 23\frac{\Theta'}{\Theta}\rho + 7.5, \quad (4.7)$$

where Θ'/Θ is given by (2.25). The third order polynomial yields three solutions. On the other hand, the argument of z must lie in the domain $[0, \pi/4]$ since χ , τ_{inv} , and ω are larger than zero. Consequently, generally there is only one solution which satisfies this constraint on z . However, this is difficult to derive analytically. Hence, the correct solution (zero) has been verified numerically. This gives that the solution for the semi-infinite domain approximations of the third order polynomial, i.e., (4.6), is always given by

$$z = -\frac{a_2}{3a_3} - \frac{\sqrt[3]{2}p_0}{3a_3p_1} + \frac{p_1}{3\sqrt[3]{2}a_3}, \quad (4.8)$$

where $p_0 = 3a_1a_3 - a_2^2$, $p_1 = \sqrt[3]{p_2 + \sqrt{4p_0^3 + p_2^2}}$, and $p_2 = -27a_0a_3^2 + 9a_1a_2a_3 - 2a_2^3$. Similarly, the correct solution can be found for a second order polynomial in z . Then, the solution for χ is found by squaring and using the imaginary part and the real part of z^2

$$\chi = \frac{3}{2} \frac{\omega}{\Im(z^2)}. \quad (4.9)$$

The diffusivity χ can always be found for such polynomials in z using (4.9), which is based on (2.24). Therefore, in case the approximations are based on z , only the polynomials in terms of z are given and not the explicit approximation in χ . The approximation for τ_{inv} can also be found based on (2.24)

$$\tau_{inv} = \omega \frac{\Re(z^2)}{\Im(z^2)}. \quad (4.10)$$

However, the damping τ_{inv} is much more sensitive to errors due to mismodeling (see Section 3.3.2). Therefore, they generally do not give reasonable values for the true damping. This also holds for approximations of the convectivity V , which are derived in the next sections. Nevertheless, they play an important role in the validation of the χ estimates. In Appendix B other continued fractions are used to find explicit approximations for χ .

4.1.2 Asymptotic expansions

An alternative to continued fractions are asymptotic expansions. An asymptotic expansion of a function can be based on either a truncation of its series expansion or on an approximation of the defining Ordinary Differential Equation for the function [Bateman, 1953; Erdélyi, 1956; Slater, 1960]. The asymptotic expansions can be calculated for the Bessel functions and for the Confluent Hypergeometric Function of the second kind Ψ . Here, an approximation is derived based on (2.22) in terms of Ψ . The derivation of the approximation for χ based on Bessel functions of the second kind can be found in Appendix B.

The asymptotic expansion for $x \approx 0$ of $\Psi(a, b, x)$ are given in [Abramowitz, 1976; Slater, 1960]. Using this we find for $(\lambda_1 - \lambda_2)\rho$ small

$$\Psi(a, 1, (\lambda_2 - \lambda_1)\rho) \approx -\frac{1}{\Gamma(a)} (\ln((\lambda_2 - \lambda_1)\rho) + F(a) + 2\gamma), \quad (4.11)$$

and

$$\Psi(a + 1, 2, (\lambda_2 - \lambda_1)\rho) \approx \frac{((\lambda_2 - \lambda_1)\rho)^{-1}}{\Gamma(a + 1)}, \quad (4.12)$$

where $a = \lambda_2/(\lambda_2 - \lambda_1)$, γ is the Euler-Mascheroni constant and Γ is the gamma function. It should not be confused with the particle flux Γ . The logarithmic derivative of Γ is the digamma function denoted by F , which is often also denoted as ψ . The logarithmic temperature derivative can be calculated by substituting (4.11) and (4.12) into (2.22)

$$\frac{\Theta'}{\Theta} = \lambda_1 + \lambda_2 \frac{\frac{1}{\Gamma(a+1)} ((\lambda_2 - \lambda_1)\rho)^{-1}}{\frac{1}{\Gamma(a)} (\ln((\lambda_2 - \lambda_1)\rho) + F(a) + 2\gamma)}. \quad (4.13)$$

This can be simplified using $a = \lambda_2/(\lambda_2 - \lambda_1)$ and using the property $\Gamma(a + 1) = a\Gamma(a)$ [Nielsen, 1906]

$$\frac{\Theta'}{\Theta} = \lambda_1 + \frac{1}{\rho (\ln((\lambda_2 - \lambda_1)\rho) + F(a) + 2\gamma)}. \quad (4.14)$$

The digamma function $F(a)$ as function of a and the appearance of λ_1 in and outside the logarithm pose important obstacles to find approximations for χ . Therefore, two simplification steps are necessary. The asymptotic expansion is based on $x \approx 0$, which implies that $\rho \approx 0$. Thus, the term with $1/\rho$ will dominate over λ_1 , hence (4.14) can be simplified to

$$\frac{\Theta'}{\Theta} = \frac{1}{\rho (\ln((\lambda_2 - \lambda_1)\rho) + F(a) + 2\gamma)}. \quad (4.15)$$

However, if $V \neq 0$ the problem of $F(a)$ remains.

In case $V = 0$, $a = 1/2$ such that F simplifies to $F(1/2) = -2\ln(2) - \gamma$, which simplifies (4.15) towards

$$\frac{\Theta'}{\Theta} = \frac{1}{\rho (\ln((\lambda_2 - \lambda_1)\rho) - 2\ln(2) + \gamma)}. \quad (4.16)$$

This can be rearranged as

$$\lambda_2 - \lambda_1 = \frac{1}{\rho} \exp\left(\frac{1}{\frac{\Theta'}{\Theta}\rho} + 2\ln(2) - \gamma\right), \quad (4.17)$$

such that

$$\frac{1}{2}(\lambda_2 - \lambda_1) = \frac{\gamma_1}{\rho} \exp\left(\left(\frac{\Theta'}{\Theta}\rho\right)^{-1}\right), \quad (4.18)$$

where $\gamma_1 = 2 \exp(-\gamma)$. The approximation in terms of z is given by

$$z = \frac{\gamma_1}{\rho} \exp\left(\left(\frac{\Theta'}{\Theta}\rho\right)^{-1}\right), \quad (4.19)$$

for which the solution in terms of χ and τ_{inv} are given in (4.9) and (4.10). Note that in this special case, χ and τ_{inv} can also be expressed in terms of geometrical functions

$$\chi_{AE\Psi} = \frac{3}{2}\omega \frac{\rho^2}{\gamma_1^2} \exp\left(\frac{2}{\rho} \frac{A'/A}{|\Theta'/\Theta|^2}\right)^{-1} \sin\left(-\frac{2}{\rho} \frac{\phi'}{|\Theta'/\Theta|^2}\right)^{-1}, \quad (4.20)$$

and

$$\tau_{AE\Psi} = \omega \left(\tan\left(-\frac{2}{\rho} \frac{\phi'}{|\Theta'/\Theta|^2}\right)\right)^{-1}. \quad (4.21)$$

A similar relationship is derived based on the asymptotic expansions of Bessel functions in Appendix B. This approximation only differs from (4.20) by the factor γ_1 . The comparison of the approximations with and without γ_1 shows that using the factor γ_1 improves the result, thus only (4.19) is presented here.

When $V \neq 0$ it is not possible to rewrite (4.15) such that the diffusivity χ can be estimated explicitly. Therefore, another approximation step is introduced when $V \neq 0$ by replacing $F(a)$ by $F(1/2)$. Then, it is still possible to estimate χ well in cases where $a \approx 1/2$, e.g., $V \approx 0$ or $\ln((\lambda_2 - \lambda_1)\rho) \gg F(a)$. The reason is that V is also contained in $\lambda_2 - \lambda_1$. In that case (4.15) is expressed as

$$\left(\frac{V}{2\chi}\right)^2 + \frac{3}{2} \frac{\tau_{inv}}{\chi} + \frac{3}{2} \frac{i\omega}{\chi} = \frac{\gamma_1^2}{\rho^2} \exp\left(\left(\frac{\Theta'}{\Theta}\rho\right)^{-1}\right)^2. \quad (4.22)$$

Interestingly, the estimate (4.20) for the diffusivity χ does not change as the imaginary part only contains χ . If $\tau_{inv} = 0$ in (4.22), then

$$|V_{AE\Psi}| = \frac{3}{2} 2\omega \frac{\sqrt{\Re(z^2)}}{\Im(z^2)}. \quad (4.23)$$

However, the possibility to estimate V in practice using (4.23) is questionable. The combination of V and τ_{inv} cannot be calculated using this approximation.

4.1.3 Multiple harmonics

Every harmonic fixes two degrees of freedom, which means in practice that either χ and τ_{inv} or χ and V can be estimated if only one harmonic is used. Therefore, to estimate χ , V , and τ_{inv} together, it is necessary to use at least two harmonics. In Section 2.3.3 an approximation is given in (2.46) based on [Jacchia, 1991]

$$\chi(\rho) = \frac{1.5\omega - (2.5\frac{\Gamma}{n} + \Gamma)\phi'}{\phi'' + \left(2\frac{A'}{A} + \frac{1}{\rho} + \frac{n'}{n} + \frac{\chi'}{\chi} + \frac{U(\rho)}{\chi}\right)\phi'}.$$

Section 2.3.3 shows that, to make this approximation applicable, the diffusivity χ is assumed constant such that $\chi'/2\chi = 0$, $V = 0$, $\Gamma = 0$, and $\phi'' = 0$. However, in case two harmonics are used, only the assumptions $\Gamma = 0$ and $\phi'' = 0$ need to be retained because the term $\chi'/2\chi + V/2\chi$ can be eliminated. As such, it is possible to calculate χ , V , and τ_{inv} , if accepting errors caused by the $\phi'' = 0$ assumption. Therefore, rewrite (2.46) in terms of the unknown quantities

$$\chi\left(\frac{A'}{A} + \frac{1}{2\rho} + \frac{n'}{2n}\right) - \frac{3}{4}\frac{\omega}{\phi'} = -\chi\left(\frac{\chi'}{2\chi} + \frac{V}{2\chi}\right). \quad (4.24)$$

This gives for two harmonics ω_1 and ω_2 at the same ρ

$$\chi\left(\frac{A'_{\omega_1}}{A_{\omega_1}} + \frac{1}{2\rho} + \frac{1}{2}\frac{n'}{n}\right) - \frac{3}{4}\frac{\omega_1}{\phi'_{\omega_1}} = \chi\left(\frac{A'_{\omega_2}}{A_{\omega_2}} + \frac{1}{2\rho} + \frac{1}{2}\frac{n'}{n}\right) - \frac{3}{4}\frac{\omega_2}{\phi'_{\omega_2}}, \quad (4.25)$$

where the short-hand notation $\phi'_{\omega_2} = \phi'(\omega_2)$ and $A'_{\omega_2}/A_{\omega_2} = A'(\omega_2)/A(\omega_2)$ is used. Solving (4.25) yields

$$\chi_{c2H} = \frac{3}{4}\frac{\frac{\omega_1}{\phi'(\omega_1)} - \frac{\omega_2}{\phi'(\omega_2)}}{\left(\frac{A'}{A}(\omega_1) - \frac{A'}{A}(\omega_2)\right)}. \quad (4.26)$$

Note that (4.26) is insensitive to density gradients. The convectivity V is found by rewriting (4.24) and assuming $\phi'' = 0$ and $\chi' = 0$

$$V_{c2H} = -2\left(\frac{A'}{A} + \frac{1}{2\rho} + \frac{1}{2}\frac{n'}{n}\right)\chi_{c2H} + \frac{3}{2}\frac{\omega}{\phi'}, \quad (4.27)$$

where ω can be freely chosen. However, calculating the damping is more difficult. Therefore, after the substitution of Θ' and Θ'' into (2.9) the real part should be considered

$$\chi\left(\frac{A''}{A} - (\phi')^2\right) = \frac{3}{2}\tau_{inv} - \left(\frac{1}{\rho}V + V' + \frac{n'}{n}V\right) - \left\{\frac{1}{\rho}\chi + \frac{n'}{n}\chi + V\right\}\frac{A'}{A}. \quad (4.28)$$

This can be rewritten in terms of τ_{inv}

$$\tau_{c2H} = \frac{2}{3}\chi\left(\left(\frac{A''}{A} - (\phi')^2\right) + \left(\frac{1}{\rho}\frac{V}{\chi} + \frac{V'}{\chi} + \frac{n'}{n}\frac{V}{\chi}\right) + \left\{\frac{1}{\rho} + \frac{n'}{n} + \frac{V}{\chi}\right\}\frac{A'}{A}\right). \quad (4.29)$$

After the substitution of (4.24) it yields

$$\begin{aligned} \tau_{c2H} = & \frac{2}{3}\chi \left(\left(\frac{A''}{A} - (\phi')^2 \right) + \frac{V}{\chi} \left(\frac{1}{\rho} + \frac{V'}{V} + \frac{n'}{n} \right) + \right. \\ & \left. \left\{ \frac{1}{\rho} + \frac{n'}{n} + \left(\frac{3}{4} \frac{\omega}{\phi'\chi} - \left(2 \frac{A'}{A} + \frac{1}{\rho} + \frac{n'}{n} \right) \right) \right\} \frac{A'}{A} \right). \end{aligned} \quad (4.30)$$

Two unknowns are still present in (4.30), thus, in the spirit of neglecting ϕ'' , $\frac{\partial}{\partial \rho} \left(\frac{A'}{A} \right)$ is also neglected. Additionally, the standard assumption that V is constant in space is used such that $V' = 0$. This results in

$$\begin{aligned} \tau_{c2H} = & \frac{2}{3}\chi \left(\left(\frac{A'}{A} \right)^2 - (\phi')^2 + \frac{V}{\chi} \left(\frac{1}{\rho} + \frac{n'}{n} \right) + \right. \\ & \left. \left\{ \frac{1}{\rho} + \frac{n'}{n} + \left(\frac{3}{4} \frac{\omega}{\phi'\chi} - 2 \left(\frac{A'}{A} + \frac{1}{\rho} + \frac{n'}{n} \right) \right) \right\} \frac{A'}{A} \right). \end{aligned} \quad (4.31)$$

The calculation of τ_{inv} is based on a complex relationship. In addition, assuming $\phi'' = 0$ and $\frac{\partial}{\partial \rho} \left(\frac{A'}{A} \right) = 0$ introduces additional errors when estimating χ , V , and τ_{inv} . This influences the approximations τ_{c2H} and V_{c2H} more significantly and hence these are not so useful in practice.

It may seem that assuming χ to be constant is no longer necessary by eliminating χ' in (4.26). However, if χ' is non-zero, it also modifies ϕ'' . As such, it is questionable if better estimates of χ can be achieved. The density gradient is still included here to show that it is possible to take it into account. However, in this thesis the density is assumed to be constant such that $n'/n = 0$.

The methods of continued fractions, asymptotic expansions, and multiple harmonics are used to derive many different explicit approximations of χ . They are all approximations and all have a different region in which their approximation is good and regions in which it is bad. The other explicit approximations are presented in Appendix B, which together with the approximations presented here are summarized and compared in the next section.

4.2 Outward solutions

In this section, the explicit approximations for χ in a semi-infinite cylindrical geometry with constant spatial parameter dependencies are summarized and compared. The compared approximations, based on (2.22) and (2.23), are presented in tabularized form. In addition, the slab geometry formulas from Chapter 3 are also considered here. This section consists of four parts: the overview table with all the derived approximations; a presentation and discussion on the

selection of the best approximations when only χ is considered; a similar discussion when χ and τ_{inv} are considered ($V = 0$); and when χ , V , and τ_{inv} are considered. The comparison is based on combinations of ρ , ω , χ , V , and τ_{inv} and is presented in terms of normalized transport coefficients, i.e., $\bar{\chi} = \chi/\omega$, $\bar{V} = V/\omega$, and $\bar{\tau}_{inv} = \tau_{inv}/\omega$. A more detailed discussion on the normalization can be found in the beginning of Section 3.2. Whenever two harmonics are necessary, $A'/A(\omega_1)$, $A'/A(\omega_2)$, $\phi'(\omega_1)$, and $\phi'(\omega_2)$ are calculated using $\omega_1 = \omega$ and $\omega_2 = 2\omega$ corresponding to the first and second harmonic.

4.2.1 Overview of possible explicit approximations

Table 4.1 on page 58 summarizes the derived approximations to calculate χ from Section 4.1 and Appendix B, including some relationships from the literature derived in Chapter 2. The following notation is used to express approximations based on continued fractions χ_{Kj3} : K denotes the Bessel function of the second kind, lower case j denotes the J -fraction, and 3 denotes the approximation order (truncation). The approximations derived from asymptotic expansions are denoted as follows: $\chi_{AE\Psi}$, where AE means Asymptotic Expansion and Ψ the Confluent Hypergeometric Function of the second kind on which it is based.

Many approximations can also be expressed using polynomials in terms of z , Θ'/Θ , and ρ to directly calculate χ and τ_{inv} . Therefore, Table 4.2 on page 59 gives the coefficients of these polynomials with their solutions to calculate z . Note that the approximations for τ_{inv} and V in Table 4.1 on page 58 can show large deviations from the true values. Therefore, they should be used carefully.

The different approximations for χ in this table are compared in the following subsection.

4.2.2 Diffusivity only

The comparison for χ only ($V = 0$ and $\tau_{inv} = 0$) is made based on a large number of possibilities of χ , ω , and ρ .

There are different methods to find ϕ' and A'/A , which can influence the results significantly. Therefore, to avoid any ambiguity on how the derivatives ϕ' and A'/A should be approximated and how they affect the comparison, the true derivatives generated by (2.23) are used. The most interesting and best approximations are shown in Figure 4.1 on page 60 in terms of the relative error with respect to the true diffusivity χ .

The approximations χ_ϕ , χ_c , χ_{Kj3} , χ_{Kc2} , and χ_{Kc5} are basically extensions of the slab geometry case as they estimate χ well if the ratio $\rho/\bar{\chi}$ is large. Perturbations with large ω or small χ penetrate less deep. This also holds for errors and the influence of cylindrical geometry, which allows χ to be estimated well by χ_ϕ , χ_c , χ_{Kj3} , χ_{Kc2} , and χ_{Kc5} .

It is important to remember that χ_ϕ is based on the phases of two harmonics

χ	Equation for χ	Equation for V	Equation for τ_{inv}	Equations
χ_{s1}	$\frac{3}{4} \frac{\omega}{(\phi')^2}$	0	0	(2.28)
χ_{s2}	$\frac{3}{4} \frac{\omega}{(A'/A)^2}$	0	0	(2.29)
1	$\frac{3\omega}{(A'/A+\phi')^2}$	0	0	(2.30)
a	$\chi_{s4} \quad \frac{3}{4} \frac{\omega}{(A'/A)\phi'}$	0	$\frac{\omega}{2} \left(\frac{A'/A}{\phi'} - \frac{\phi'}{A'/A} \right)$	(2.31)
b	$\chi_V \quad \frac{3}{2} \frac{\omega \frac{A'}{A}}{\left(\left(\frac{A'}{A} \right)^2 + (\phi')^2 \right) \phi'}$	$\frac{3}{2} \frac{\omega \left((\phi')^2 - \left(\frac{A'}{A} \right)^2 \right)}{\left(\left(\frac{A'}{A} \right)^2 + (\phi')^2 \right) \phi'}$	0	(3.13)
	$\chi_\phi \quad \frac{3}{4} \sqrt{\frac{(\omega_1 \phi' \omega_2)^2 - (\omega_2 \phi' \omega_1)^2}{\phi'^2 \omega_1^2 \omega_2^2 (\phi'^2 - \phi''^2)}}$	$-2\chi \frac{A'}{A} - \sqrt{\frac{C_V + \sqrt{C_V^2 + 36X^2 \omega^2}}{2}}$	$\frac{C_V - V^2}{6\chi}$	(3.9)
		with $C_V = \frac{9}{4} \omega^2 (\phi')^{-2} - 4\chi^2 (\phi')^2$		
c	$\chi_c \quad \frac{3}{4} \frac{\omega}{\phi' \left(\frac{A'}{A} + \frac{1}{2\rho} \right)}$	0	$\frac{\omega}{2} \left(\frac{\left(\frac{A'}{A} + \frac{1}{2\rho} \right)}{\phi'} - \frac{\phi'}{\left(\frac{A'}{A} + \frac{1}{2\rho} \right)} \right)$	(2.47)
y	$\chi_{KJ1A} \quad \frac{3}{4} \frac{\omega}{\left(\frac{A'}{A} + \frac{1}{2\rho} \right)^2}$	0	0	(B.29)
1	$\chi_{c2H} \quad \frac{3}{4} \frac{\omega_1 / \phi' \omega_1 - \omega_2 / \phi' \omega_2}{(A'_{\omega_1} / A_{\omega_1} - A'_{\omega_2} / A_{\omega_2})}$	$-2\chi \left(\frac{A'}{A} + \frac{1}{2\rho} \right) + \frac{3}{2} \frac{\omega}{\phi'}$	$\frac{3}{2} \chi \left(\left(\frac{A'}{A} \right)^2 - (\phi')^2 + \frac{1}{\rho} \frac{A'}{A} + \frac{V}{X} \frac{A'}{A} \right)$	(4.26)
	$\chi_z \quad \frac{3}{2} \frac{\omega}{\Im(z^2)}$	0	$\frac{\Re(z^2)}{\Im(z^2)}$	(4.9)

Table 4.1. Overview of approximations for χ based on a semi-infinite domain where heat waves are propagating towards the edge in a cylindrical geometry and slab geometry. From left to right, the columns denote: the geometry on which it is based; the approximation of χ either explicit or in terms of z in which case Table 4.2 on page 59 gives the relationship for z ; and the equations for V and τ_{inv} . In the last column, the reference to the corresponding equation is given. The short-hand notations $\phi'(\omega_1) = \phi'_{\omega_1}$ and $A'(\omega_1)/A(\omega_1) = A'_{\omega_1}/A_{\omega_1}$ are used.

χ_z	Equation for z	Equations
χ_{AEK}	$z = \rho^{-1} \exp \left(\left(\rho \frac{\Theta'}{\Theta} \right)^{-1} \right)$	(4.20)
$\chi_{AE\Psi}$	$z = \frac{\tau_1}{\rho} \exp \left(\left(\frac{\Theta'}{\Theta} \rho \right)^{-1} \right)$	(4.19)
Quadratic polynomials in z		
	$z = \left(-b_1 + \sqrt{b_1^2 - 4b_0b_2} \right) / (2b_2)$	
χ_{Kc2}	$b_2 = 4\rho, \quad b_1 = 3 + 4\frac{\Theta'}{\Theta}\rho, \quad b_0 = \frac{\Theta'}{\Theta}$	(B.4)
χ_{Kj2}	$b_2 = 8\rho^2, \quad b_1 = 8\rho^2\frac{\Theta'}{\Theta} + 4\rho, b_0 = 8\frac{\Theta'}{\Theta}\rho - 3$	(B.2)
Cubic polynomials in z		
	$z = \frac{1}{a_3} \left(-\frac{a_2}{3} - \frac{\sqrt[3]{2p_0} + \frac{p_1}{3\sqrt[3]{2}}}{3p_1} \right), p_2 = -27a_0a_3^2 + 9a_1a_2a_3 - 2a_2^3,$ $p_1 = \sqrt[3]{p_2 + \sqrt{4p_0^3 + p_2^2}}, p_0 = 3a_1a_3 - a_2^2$	
χ_{Kj3}	$a_3 = 16\rho^3, a_2 = 16\frac{\Theta'}{\Theta}\rho^3 + 56\rho^2, a_1 = 48\frac{\Theta'}{\Theta}\rho^2 + 45\rho, a_0 = 23\frac{\Theta'}{\Theta}\rho + 7.5$	(4.7)
χ_{Kc5}	$a_3 = 16\rho^2, a_2 = 36\rho + 16\rho^2\frac{\Theta'}{\Theta}, a_1 = 15 + 28\rho\frac{\Theta'}{\Theta}, a_0 = 3\frac{\Theta'}{\Theta}$	(B.5)

Table 4.2. Overview of approximations for χ in terms of z for heat waves propagating towards the edge in a cylindrical geometry where a semi-infinite domain is assumed. This table is used to calculate z using $\Theta'/\Theta = A'/A + i\phi'$ and ρ , where z is used to calculate $\chi = \frac{3}{2}\omega/\mathfrak{S}(z^2)$ and $\tau_{inv} = \omega\Re(z^2)/\mathfrak{S}(z^2)$ based on the definition of z in (2.24). The constant $\gamma_1 = 1.12291896713377$. The equation numbers refer either to Section 4.1 or Appendix B.

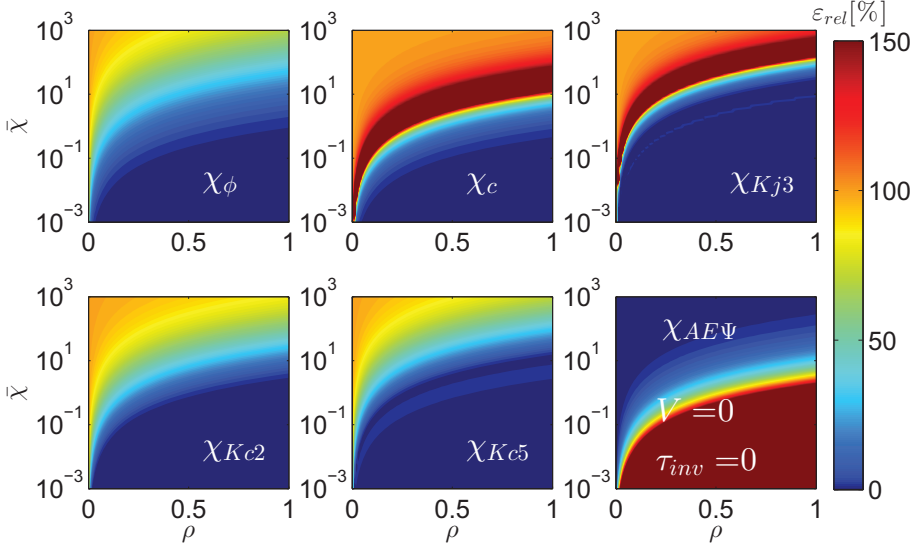


Figure 4.1. Comparison between the different relative errors of the χ estimates for a large range of $\bar{\chi} = \chi/\omega$ and ρ . The relative error is defined as $\varepsilon_{rel} = 100 \times \frac{|\chi - \chi_{est}|}{\chi}$ [%], where χ_{est} is either χ_ϕ (2 harmonics are used, which are $\omega_1 = \omega$ and $\omega_2 = 2\omega$), χ_c , χ_{Kj3} , χ_{Kc2} , χ_{Kc5} , and $\chi_{AE\Psi}$ from Table 4.1 on page 58. This comparison is based on a cylindrical geometry using a semi-infinite domain with χ and $V = \tau_{inv} = 0$, where the heat waves travel outwards. The darkest blue represents $\varepsilon_{rel} < 1\%$ and the darkest red represents all $\varepsilon_{rel} > 150\%$.

making it more difficult to compare them with the other approximations. In χ_c and χ_{Kj3} large relative errors are observed for small ρ and large $\bar{\chi}$. Why these large errors occur for χ_c is discussed in Section 3.2.1. Intuitively, one expects a similar behavior for χ_{Kj3} as it is based on the same continued fraction. However, this is difficult to show analytically. The approximation χ_{Kj3} is more accurate and extends the region in which χ can be estimated well, which is a logical consequence of taking more terms in the continued fraction before truncation. Clearly, χ_{Kc2} and χ_{Kc5} do not suffer from the zero crossing causing the large errors in χ_c and χ_{Kj3} . The region in which χ is estimated well by χ_{Kc5} is slightly larger than χ_c and smaller than χ_{Kj3} .

Generally, χ_{Kj3} gives the best approximation of χ , except when $\rho/\bar{\chi}$ is small. In that region the asymptotic expansions play an important role. They estimate χ well for $z\rho \approx 0$, which can be clearly seen in Figure 4.1 for $\chi_{AE\Psi}$, which gave the best result of the two asymptotic expansions. This also means that almost the entire region of χ is estimated well if χ_{Kj3} and $\chi_{AE\Psi}$ are combined.

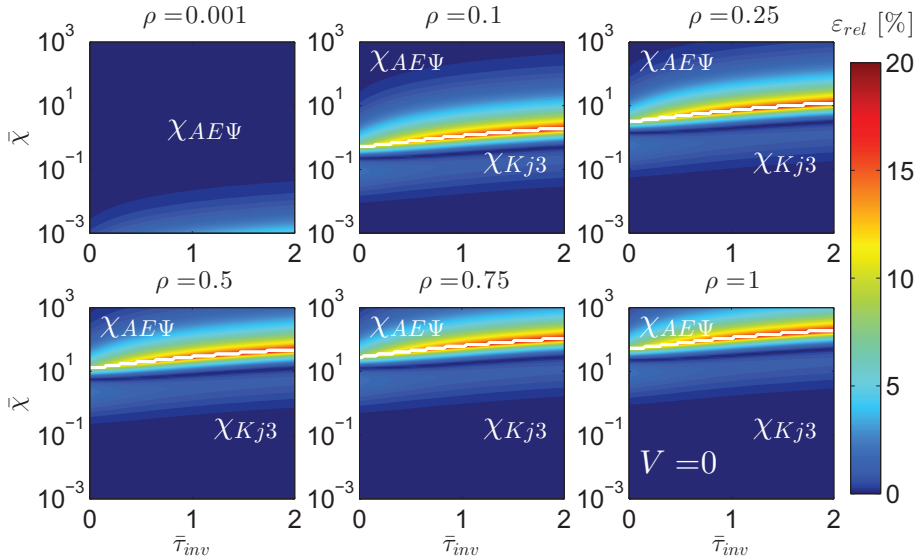


Figure 4.2. Relative error of the χ estimates for the combination of χ_{Kj3} and $\chi_{AE\Psi}$ presented for different $\bar{\chi} = \chi/\omega$ and $\bar{\tau}_{inv} = \tau_{inv}/\omega$ represented at a number of spatial locations ρ . The relative error is defined as $\varepsilon_{rel} = 100 \times \frac{|\chi - \chi_{est}|}{\chi}$ [%]. This figure combines the approximations χ_{Kj3} and $\chi_{AE\Psi}$ which take both χ and τ_{inv} into account and are separated by the boundary represented by the white line (middle of the largest error). The resulting error is based on a cylindrical geometry using a semi-infinite domain with χ and $V = 0$, where the heat waves travel outwards.

4.2.3 Diffusivity and damping only

There are a number of suitable approximations to determine χ in the presence of τ_{inv} . However, it suffices, with a minimal loss of accuracy, to use the approximations χ_{Kj3} and $\chi_{AE\Psi}$ to estimate χ in the region of interest, which is shown in Figure 4.2.

The white line shows approximately the boundary of the applicability of χ_{Kj3} and $\chi_{AE\Psi}$. This does not mean that χ_{Kj3} and $\chi_{AE\Psi}$ estimate χ with the highest accuracy compared to the other approximations in the presented region, but they have the largest region of approximation and are the most accurate in a large region. In addition, χ_{Kj3} and $\chi_{AE\Psi}$ are the best approximations around the white line where the errors are largest. This can also be understood by considering Figure 4.1 on page 60.

In general, the effect of damping τ_{inv} acts as a shift parameter and is not directly influenced by the cylindrical geometry (see Chapter 3). However, these effects are also influenced by the approximation used. This means that for large

τ_{inv} the regions in which χ are estimated well is extended for χ_{Kj3} , and similarly for χ_ϕ , χ_c , χ_{Kc2} , and χ_{Kc5} . On the other hand, it is reduced for $\chi_{AE\Psi}$, which is also shifted in the same direction.

The maximum relative error for the combination of $\chi_{AE\Psi}$ and χ_{Kj3} over the entire presented region is $\varepsilon_{rel} < 20\%$. It is also important to note that in some regions χ_{Kc2} , χ_{Kc5} , and χ_{Kj2} give a slightly better approximation. In some isolated regions other approximations have a smaller error than the previously mentioned approximations are better approximations than , but generally with a comparable accuracy. Note that the absolute error for large $\bar{\chi}$ will be larger than 20%.

4.2.4 Diffusivity and convectivity with $\tau_{inv} = 0$ and $\tau_{inv} = 2$

Most of the previously discussed approximations poorly estimate the diffusivity in the presence of convectivity. In principle, only four relationships are available to analyze χ for heat waves propagating outwards, i.e., χ_V , χ_ϕ , $\chi_{AE\Psi}$, and χ_{c2H} (see Table 4.1 on page 58). It is unclear what a good range is for $\bar{V} = V/\omega$. Therefore, an arbitrary choice for this range is used, i.e., $-100 \leq \bar{V} \leq 100$.

It turns out that χ_ϕ outperforms all other approximations except when $\rho/\bar{\chi}$ is small. There $\chi_{AE\Psi}$ performs better. On the other hand, χ_{c2H} performs similar to χ_ϕ , both in error and the size of the region in which it estimates χ well, making them almost interchangeable. Although they are both based on (the first) two harmonics, χ_ϕ only uses the phase. Therefore, only χ_ϕ and $\chi_{AE\Psi}$ are presented in Figure 4.3 for $\tau_{inv} = 0$ and Figure 4.4 for $\tau_{inv} = 2$.

Figure 4.3 on page 64 and Figure 4.4 on page 63 show similar regions. In general χ can be estimated well for large ρ , but there is an area with larger errors. Although this area is influenced by the damping, its effect is rather small. In addition, there is a small region which has large errors ($\varepsilon_{rel} > 150\%$) for large negative V and for small ρ and $\bar{\chi}$.

4.2.5 Summary

In this section many different approximations are introduced. For problems with convective velocity, χ_ϕ and $\chi_{AE\Psi}$ should be used. Otherwise, $\chi_{AE\Psi}$, χ_ϕ , and χ_{Kj3} are the best approximations. The other approximations can also be used. Although these other approximations are sometimes more accurate, their accuracy is in general comparable to the approximations given in Figure 4.2 on page 61 and Figure 4.3 on page 63. Section 4.3 will elaborate on how to select the proper approximation based on the underlying models.

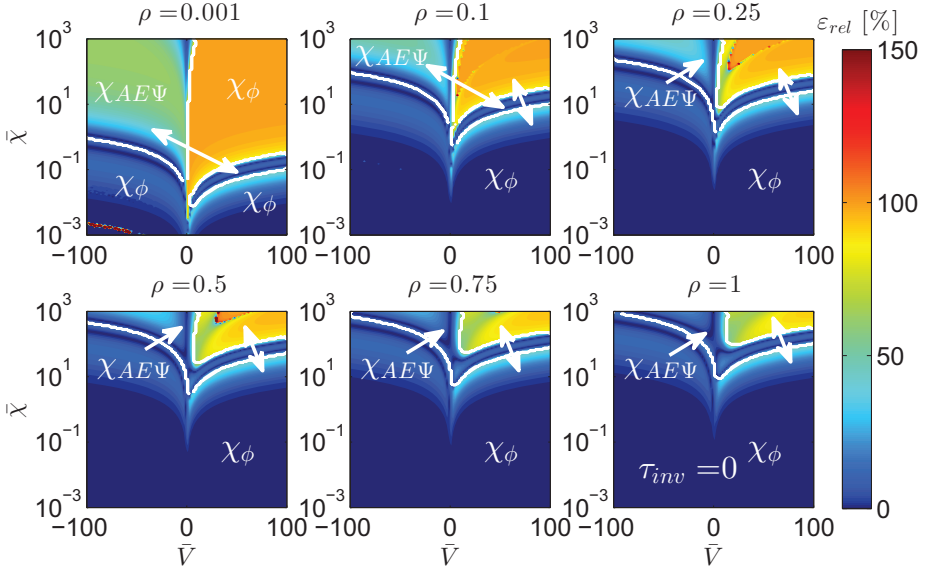


Figure 4.3. Relative error of the χ estimates for the combination of χ_ϕ and $\chi_{AE\Psi}$ presented for different $\bar{\chi} = \chi/\omega$ and $\bar{V} = V/\omega$ represented at a number of spatial locations ρ . The relative error is defined as $\varepsilon_{rel} = 100 \times \frac{|\chi - \chi_{est}|}{\chi}$ [%]. The approximation regions of χ_ϕ and $\chi_{AE\Psi}$ are separated by white lines. This comparison is based on a cylindrical geometry using a semi-infinite domain with $\tau_{inv} = 0$, where the heat waves travel outwards. The darkest blue represents $\varepsilon_{rel} < 1\%$ and the darkest red represents all $\varepsilon_{rel} > 150\%$.

4.3 Choice and validation of approximations

The previous section presented many different approximations. The validity ranges of these approximations do not only depend on ρ and ω , but also on the unknown transport coefficients χ , V , and τ_{inv} . This may seem to be a problem, but this can be solved partly using the original models in terms of Bessel functions or Confluent Hypergeometric Functions in (2.22) and (2.23). These original models can be used to explicitly calculate estimates of the original A'/A and ϕ' , denoted by $\widehat{A'/A}$ and $\widehat{\phi'}$. They can be calculated by substituting the estimated transport coefficients with corresponding ρ and ω in (2.22) and (2.23). This should result in approximately the same $\widehat{A'/A}$ and $\widehat{\phi'}$ as the original A'/A and ϕ' .

The procedure to select the approximation for the cases with only χ and τ_{inv} is shown through an example.

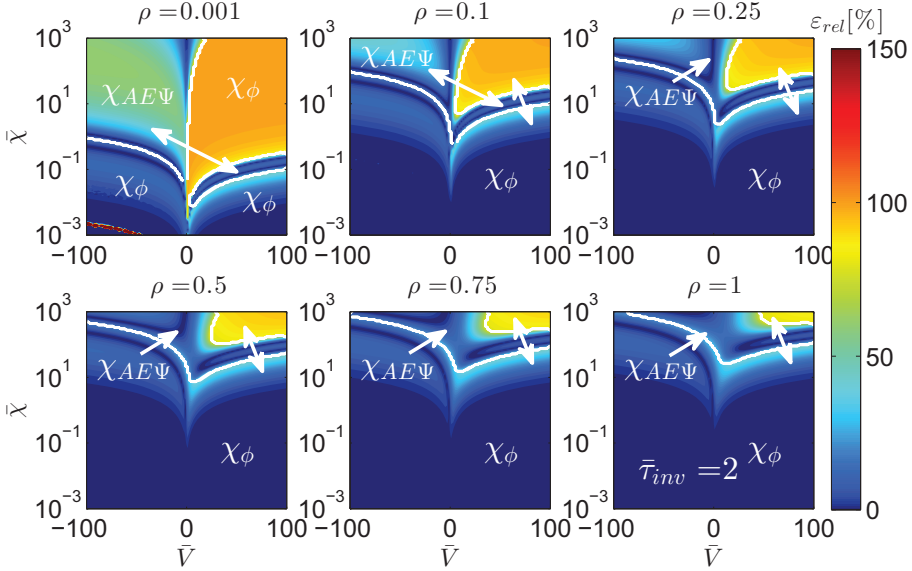


Figure 4.4. Relative error of the χ estimates for the combination of χ_ϕ and $\chi_{AE\Psi}$ presented for different $\bar{\chi} = \chi/\omega$ and $\bar{V} = V/\omega$ represented at a number of spatial locations ρ . The relative error is defined as $\varepsilon_{rel} = 100 \times \frac{|\chi - \chi_{est}|}{\chi}$ [%]. The approximation regions of χ_ϕ and $\chi_{AE\Psi}$ are separated by white lines. This comparison is based on a cylindrical geometry using a semi-infinite domain with $\bar{\tau}_{inv} = 2$, where the heat waves travel outwards. The darkest blue represents $\varepsilon_{rel} < 1\%$ and the darkest red represents all $\varepsilon_{rel} > 150\%$.

Example: Consider a measurement at $\rho = 0.1$ where $A'/A = -7.0593$ and $\phi' = -3.5588$ with $\omega = 50\pi$ and assuming that $V = 0$. Basically, two approximations are best tried first, i.e., χ_{Kj3} and $\chi_{AE\Psi}$. This results in $\chi_{Kj3} = 7.8629$, $\tau_{Kj3} = -5.0253$ and $\chi_{AE\Psi} = 13.1327$, $\tau_{AE\Psi} = 72.4163$ using Table 4.1 on page 58 and Table 4.2 on page 59. Clearly, the τ_{inv} 's are erroneous. To test which is the proper approximation, substitute the values of χ and τ_{inv} back into the original model, which in this case is (2.23). This results in $\widehat{A'/A} + \widehat{\phi'}i = -7.0377 - 3.6514i$ for χ_{Kj3} , and $\widehat{A'/A} + \widehat{\phi'}i = -6.8527 - 2.2746i$ for $\chi_{AE\Psi}$. Consequently, χ_{Kj3} is the best approximation as $\widehat{A'/A} \approx A'/A$ and $\widehat{\phi'} \approx \phi'$.

It is also possible to use χ_c and χ_{Kj2} resulting in $\chi_c = 10.7168$, $\tau_c = -90.2764$ and $\chi_{Kj2} = 7.9655$, $\tau_{Kj2} = -18.1707$, with $\widehat{A'/A} + \widehat{\phi'}i = -5.9559 - 4.1495i$ and $\widehat{A'/A} + \widehat{\phi'}i = -6.8924 - 3.7907i$, respectively. Again, χ_{Kj3} is closest to the true A'/A and ϕ' and hence should be selected.

In this example, the true values are $\chi = 8$ and $\tau_{inv} = 0.5$ such that actually χ_{Kj2} is closest to the true χ . However, due to the much larger error in τ_{Kj2} the $\widehat{A'/A}$ and $\widehat{\phi'}$ deviate significantly from the true A'/A and ϕ' .

Hence, it is the combination of χ and τ_{inv} , which is tested. Nevertheless, this test gives a clear statement of which χ estimate is trustworthy with respect to (2.22) and (2.23). In most cases $A'/A \approx \widehat{A'/A}$ and $\phi' \approx \widehat{\phi'}$ are found with some small rounding error, unlike the example presented here.

Similarly, other approximations can be tested, which are based on one harmonic only. However, two harmonics are necessary for the mixed case of χ, V , and τ_{inv} . This procedure is more difficult. It is still possible to compare $\widehat{A'/A}$ and $\widehat{\phi'}$ to A'/A and ϕ' , but this comparison also depends on A'/A and ϕ' of the second harmonic, which can also introduce a difference even if the estimated parameters are correct. Nevertheless, this comparison still gives valuable information on the quality of the approximation used. In case χ_ϕ or χ_V are used, the transformation in Section 3.3 can be helpful to calculate V and τ_{inv} .

If $V \neq 0$, then also an implementation of the Confluent Hypergeometric Function is required, which is not always available especially for complex valued arguments. In this thesis, Mathematica[©] is used to calculate Ψ . Alternatively, it is also possible to use the continued fraction on p. 326 in [Cuyt, 2008], which can in principle be used to calculate (2.22) with a desired accuracy using truncation. However, selecting a priori the number of terms necessary to arrive at a desired accuracy is not easy.

The procedure presented here checks the quality of the approximation with respect to its underlying model. It does not give any validation of the true χ as it depends on many other factors such as variation of the profiles, boundary conditions, approximation A'/A and ϕ' , disturbances such as noise, and non-linearities. Noise and non-linearities require an extensive study based on statistics and higher harmonics.

4.4 Conclusions and summary

A large number of new approximations have been introduced in this chapter to estimate χ directly from A'/A and ϕ' for different combinations of χ, V , and τ_{inv} . These approximations and the approximations from Chapter 2, and Chapter 3 have been compared for heat waves propagating outwards (semi-infinite domain).

The quality of the approximations is presented in several figures. In case only χ and τ_{inv} are considered ($V = 0$), the relative error of the χ estimate for the region of interest is in general 1%. In a small region, the errors are larger with a maximum relative error of 20%. These errors are achievable by combining χ_{Kj3} and $\chi_{AE\Psi}$ assuming that (2.22) is exact. If V is also considered, the new approximations show a significant region in which χ can be estimated well, but also regions in which no suitable approximation exists. In this case, combining

$\chi_{AE\Psi}$ and χ_ϕ covers a large region where χ can be well estimated.

Several figures present the ranges where χ can be estimated well as function of ρ , ω , and the transport coefficients. However, in practice these figures are less useful as the true transport coefficients are unknown. Therefore, in Section 4.3 a simple test is presented to check if the chosen approximation reproduces the original A'/A and ϕ' . This means that, without using knowledge of the actual transport coefficients, a proper approximation can be selected. Therefore, it is also necessary to determine the convectivity and damping. However, this test does not give information about the quality of the approximation with respect to the original PDE (2.8). More extensive validation tests are discussed in Chapter 7.

This chapter discussed the estimation of χ in a cylindrical geometry using several approximations based on perturbative measurements for heat waves propagating outwards. In Chapter 5, approximations to estimate χ are derived and discussed for heat waves propagating towards the center (inwards) based on a symmetry boundary condition. Some of the approximations based on semi-infinite domains might also be applicable for heat waves propagating towards the center in cases where the influence of cylindrical geometry is not so strong.

Chapter 5

Estimation of the transport coefficients for heat waves propagating inwards (symmetry)

In this chapter approximations are obtained of the heat-equation in a cylindrical domain assuming a symmetric domain (Neumann boundary condition) and unknown diffusivity χ , convectivity V , and damping τ . These approximations should be used in case of an off-axis perturbative heating source, i.e., when heat waves travel towards the center of the plasma. This chapter has a similar structure as Chapter 4, using the ratio of modified Bessel functions of the first kind or Confluent Hypergeometric Functions of the first kind are used. Both can be approximated by truncation of continued fractions.

5.1 Derivation of explicit approximations using continued fractions

In this section, a number of continued fractions are used to find approximations for the transport coefficients in cylindrical geometry using (2.50) and (2.51). The three most important approximations are derived in this section. The other approximations are derived and given in Appendix B. A summary of the approximations is given in three tables in the next section.

This chapter is based on the following article: van Berkel, M., et al. [2014]. Explicit approximations to estimate the perturbative diffusivity in the presence of convectivity and damping III Cylindrical approximations for heat waves traveling inwards, *Phys. Plasmas* **21**: 112509.

5.1.1 Derivation of inward approximations for the diffusivity and the damping only

The continued fraction for a ratio of Bessel functions of the first kind is used to find approximations for χ under influence of damping by assuming that $V = 0$. Therefore, the logarithmic temperature derivative introduced in (2.51) is used. The following continued S -fraction of the ratio of Bessel functions can be found in [Cuyt, 2008](page 362)

$$\frac{I_1(z\rho)}{I_0(z\rho)} = \frac{a_1}{1 + \frac{a_2}{1 + \frac{a_3}{1 + \dots}}}, \quad (5.1)$$

where $a_{k+1} = (z\rho)^2 / (4k(k+1))$ for $k \geq 1$ and $a_1 = z\rho/2$. If this continued fraction is truncated taking only the first term a_1 into account, then the logarithmic temperature derivative in (2.51) is approximated by

$$\frac{\Theta'}{\Theta} = z \frac{z\rho}{2}. \quad (5.2)$$

This can be solved in terms of χ and τ_{inv} using (2.24), resulting in

$$\chi_{Is\phi} = \frac{3}{4} \frac{\omega}{\phi'} \rho \quad \text{and} \quad \tau_{Is\phi} = \frac{\omega}{\phi'} \frac{A'}{A}. \quad (5.3)$$

This relationship can also be found based on the asymptotic expansions given in [Abramowitz, 1976].

Continued fractions can also be used to find more accurate approximations by using more terms in the continued fraction before truncation. In this case the best approximation is found by truncating at a_4 in (5.1), which can be written in terms of a second order polynomial in z^2

$$0 = c_2 z^4 + c_1 z^2 + c_0, \quad (5.4)$$

with coefficients

$$c_2 = 12\rho^3 - \frac{\Theta'}{\Theta} \rho^4, \quad c_1 = 192\rho - 72 \frac{\Theta'}{\Theta} \rho^2, \quad \text{and} \quad c_0 = -384 \frac{\Theta'}{\Theta}, \quad (5.5)$$

where Θ'/Θ is given by (2.25). The second order polynomial yields two solutions in terms of z^2 where z^2 must lie in the first quadrant of the complex plane since $\chi > 0$, $\tau_{inv} > 0$, and $s = i\omega$ with $\omega > 0$. Therefore, generally only one zero of the second order polynomial in z^2 satisfies this constraint. This zero is used to calculate χ . However, using a truncation of (5.1) at location a_5 results in more solutions within this domain. Hence, it is no longer straightforward to select the

correct solution. Therefore, truncations higher than a_4 will not be considered here. For the truncation using a_4 as the last term, it has been numerically determined that the zero in z^2 is given by

$$z^2 = \frac{-c_1 + \sqrt{c_1^2 - 4 c_0 c_2}}{2c_2}, \tag{5.6}$$

covers the largest region of interest. The solutions for the diffusivity χ and the damping τ_{inv} are found using (4.9) and (4.10), respectively. The continued fraction in (5.1) can also be used to find two other approximations belonging to a_2 and a_3 , which are named χ_{Is2} and χ_{Is3} , respectively. These can be found in Table 5.2 and are derived in Appendix B. This also holds for another approximation based on the continued fraction for the ratio of Bessel functions of the first kind.

In this subsection, the convectivity is assumed zero such that the continued fractions for Bessel functions can be considered. The next subsection considers non-zero V . Therefore, the continued fraction for the ratio of Confluent Hypergeometric Functions of the first kind is used to find approximations for χ .

5.1.2 Diffusivity, convectivity, and damping

The logarithmic amplitude derivative A'/A and phase derivative ϕ' are given in (2.50) as a function of χ , V , and τ_{inv} . However, only two quantities are known, i.e., A'/A and ϕ' , whereas the right-hand side contains three unknowns. Therefore, a third quantity needs to be introduced to calculate the transport coefficients, which can be done by introducing measurements on a second harmonic, i.e., $A'(\omega_2)/A(\omega_2)$ or $\phi'(\omega_2)$. In addition, the expression in (2.50) needs to be approximated using a continued fraction. In this case the continued C -fraction of the ratio of Confluent Hypergeometric Functions of the first kind [Cuyt, 2008](page 324) is used

$$\frac{\Phi(a+1, b+1, z)}{\Phi(a, b, z)} = \frac{1}{1 - \frac{b-a}{(b+0)(b+1)}z \left| \begin{array}{l} \\ \\ \\ \\ \end{array} \right. \frac{a+1}{(b+1)(b+2)}z \Big|_I \frac{b-a+1}{(b+2)(b+3)}z \left| \begin{array}{l} \\ \\ \\ \\ \end{array} \right. \frac{a+2}{(b+3)(b+4)}z \Big|_{II} \dots} \tag{5.7}$$

This continued fraction needs to be truncated and substituted into (2.50) to find a proper approximation for χ . Here, (5.7) is truncated at locations I and II because in these special cases there are no square roots in the resulting approximation of the logarithmic temperature derivative in (2.50). Hence, it is easier to derive explicit approximations for χ , V , and τ_{inv} . In Appendix B, the truncations at locations I and II are derived for various combinations of amplitude and phase. In this section, only the truncation at location II is given using two amplitudes and one phase, i.e., $A'(\omega_1)/A(\omega_1)$, $\phi'(\omega_1)$, and $A'_2(\omega)/A(\omega_2)$ because it gave the best numerical result. This does not necessarily mean that in practice it also gives the best result. For instance, calibration errors will influence this approximation more than the one based on two phases because the sensitivity of the amplitude to calibration errors is larger.

Although it is now possible to calculate explicit solutions for χ , V , and τ_{inv} , the calculations are too complicated to do by hand. Therefore, Mathematica[®] was used to derive approximations for χ , V , and τ_{inv} based on the truncation in (5.7). Truncating at location II results in a third order polynomial such that there are three solutions. However, only one is different from the zero solutions $\chi = 0$, and is given by

$$\chi_{\Phi 4a} = \frac{3}{2} \frac{6859\rho^3\omega_1^2\phi'_1 o_2 dA}{8(o_3 + 27436\omega_1^3 dA^3 + 45o_1^3)}, \quad (5.8)$$

where

$$dA = \frac{A'_1}{A_1} - \frac{A'_2}{A_2},$$

$$o_1 = \omega_1 \left(dA \left(\frac{A'_1}{A_1} \rho - 4 \right) + \rho (\phi'_1)^2 \right) - \rho \omega_2 \phi'_1 \phi'_2,$$

$$o_2 = \omega_1^2 \left(dA^2 + (\phi'_1)^2 \right) - 2\omega_1 \omega_2 \phi'_1 \phi'_2 + \omega_2^2 (\phi'_2)^2,$$

and

$$o_3 = 1311o_1^2\omega_1 dA + 10108o_1\omega_1^2 dA^2.$$

The corresponding V and τ_{inv} are given by

$$V_{\Phi 4a} = -\chi_{\Phi 4a} \frac{30o_1}{38\rho\omega_1 dA}, \quad (5.9)$$

and

$$\tau_{\Phi 4a} = \frac{3}{2} \chi \frac{-15\rho^2 \frac{\omega}{\chi} \frac{A'_1}{A_1} - 6 \left(\frac{V}{\chi} \right)^2 \rho^2 \phi' - 19\rho^2 \omega \frac{V}{\chi^2}}{15\rho^2 \phi'}$$

$$+ \frac{3}{2} \chi \frac{48 \left(\frac{V}{\chi} \right) \rho \phi' + 60\rho \frac{\omega}{\chi} - 120\phi'}{15\rho^2 \phi'}, \quad (5.10)$$

where the subscripts $\Phi 4a$ on the right-hand side have been omitted. These solutions are complicated, but are the only explicit approximations found for the combined problem of estimating χ under convectivity and damping. The other approximations are given in Appendix B. All the approximations are summarized and compared in the next section.

5.2 Inward solutions

In this section, the different approximations to determine χ , V , and, τ_{inv} are summarized and compared for heat waves propagating towards the center. The approximations are based on the underlying models (2.50) and (2.51), which are used to calculate A'/A and ϕ' for a large number of combinations of the transport coefficients. In addition, the semi-infinite approximations derived in Chapter 4 can also be used. The comparison is again based on five parameters ρ , ω , χ , V , and τ_{inv} , which are presented in terms of normalized transport coefficients, i.e., $\bar{\chi} = \chi/\omega$, $\bar{V} = V/\omega$, and $\bar{\tau}_{inv} = \tau_{inv}/\omega$. In case two harmonics are necessary, $A'/A(\omega_1)$, $A'/A(\omega_2)$, $\phi'(\omega_1)$, and $\phi'(\omega_2)$ are calculated using $\omega_1 = \omega$ and $\omega_2 = 2\omega$.

5.2.1 Overview of possible explicit approximations

Table 5.1 summarizes all derived approximations from Section 5.1 and Appendix B to estimate χ . Some semi-infinite domain solutions from Chapter 4 are also included. The reason is that if cylindrical effects are small, i.e., the ratio of $\omega\rho/\chi$ is large, the semi-infinite domain approximations give a good approximation again. However, different solutions need to be selected if polynomials in z are used based on semi-infinite domains. The reason is that A'/A and ϕ' are negative for heat waves propagating outwards and that they are positive for heat waves propagating towards the center.

Table 5.1 only states χ explicitly to keep the table compact. The corresponding equation numbers of V and τ_{inv} are given instead. In Table 5.2 on page 73 the polynomials expressed in terms of z using $\Theta'/\Theta = A'/A + i\phi'$ and ρ to directly calculate χ and τ_{inv} are given. Table 5.3 on page 74 presents the approximations in terms of polynomials in z for approximations based on semi-infinite domains.

The useful solutions of the polynomials in z are different from those used for the analysis of heat waves propagating towards the wall because the sign of A'/A and ϕ' is opposite. Therefore, to distinguish between the solutions for outward heat waves and inward heat waves the superscript *inv* (inward) is added. The useful solutions have been selected by comparing the three possibilities numerically. The other solutions based on semi-infinite domains and summarized in Tables 4.1 and 4.2 on pages 58 and 59 can also be used when the influence of the cylindrical geometry is weak. However, χ_{AEK} and $\chi_{AE\Phi}$ are not suitable

χ	Equation for χ	V	τ_{inv}
Approximations based on symmetry boundary condition			
$\chi_{Is\phi}$	$\frac{3}{4} \frac{\omega}{\phi'} \rho$	0	(5.3)
$\chi_{Is2\phi}$	$\frac{3}{2} \omega \rho \frac{2 + \sqrt{4 - \rho^2 (\phi')^2}}{8\phi'}$	0	0
χ_{Is2A}	$\omega \frac{3\rho^3 \sqrt{4 - A'/A\rho}}{16\rho^2 \sqrt{A'/A}}$	0	0
$\chi_{\Phi 2V}$	$\frac{9\rho\omega}{4\phi'(\frac{A'}{A}\rho + 3)}$	(B.14)	0
$\chi_{\Phi 4V}$	$\frac{3}{2} \frac{6859\rho^3 \omega \phi'}{l_2 + (6\frac{A'}{A}\rho(15\frac{A'}{A}\rho + 32) + 680) \cdot (2\frac{A'}{A}\rho - l_1 + 30)}$	(B.21)	0
	with $l_1 = \sqrt{4(\frac{A'}{A}\rho + 15)^2 - 285\rho^2(\phi')^2}$, $l_2 = 114\rho^2(\phi')^2 \left(32\frac{A'}{A}\rho + l_1 + 62\right)$		
$\chi_{\Phi 4a}$	$\frac{3}{2} \frac{6859\rho^3 \omega_1^2 \phi_1' dA o_2}{8(o_3 + 27436\omega_1^3 dA^3 + 45o_1^3)}$	(5.9)	(5.10)
	with $o_1 = \omega_1 \left(dA \left(\frac{A'}{A_1}\rho - 4\right) + \rho(\phi_1')^2\right) - \rho\omega_2\phi_1'\phi_2'$, $o_2 = \omega_1^2 \left(dA^2 + (\phi_1')^2\right) + \omega_2^2 (\phi_2')^2 - 2\omega_1\omega_2\phi_1'\phi_2'$, $o_3 = 1311o_1^2\omega_1 dA + 10108o_1\omega_1^2 dA^2$		
$\chi_{\Phi 4b}$	$\frac{3}{2} \frac{6859d\omega\rho^3\omega_1\phi_1' \left(\omega_2^2 \left(dA^2 + (\phi_1')^2\right) + \omega_1\phi_2'(d\omega - \omega_2\phi_1')\right)}{8(19d\omega + o)(1444d\omega^2 + 456d\omega o + 45o^2)}$	(B.25)	(B.26)
	with $d\omega = \omega_1\phi_2' - \omega_2\phi_1' dA = \frac{A'}{A_1} - \frac{A'}{A_2}$, $o = \frac{A'}{A_1}\rho\omega_1\phi_2' - \frac{A'}{A_2}\rho\omega_2\phi_1' - 4d\omega$		
Approximations based on semi-infinite domain			
χ_c	$\frac{3}{4} \frac{\omega}{\phi' \left(\frac{A'}{A} + \frac{1}{2\rho}\right)}$	0	(2.47)
χ_ϕ	$\frac{3}{4} \sqrt{\frac{(\omega_1\phi_1'\omega_2)^2 - (\omega_2\phi_1'\omega_1)^2}{\phi_1'^2\phi_2'^2(\phi_1'^2 - \phi_2'^2)}}$	(3.10)	(3.9)

Table 5.1. Overview of the approximations for χ for heat waves propagating towards the center in a cylindrical geometry where a symmetry boundary condition is assumed. From left to right the columns denote: the approximation of χ either explicit or in terms of z in which case the tables on pages 73 and 74 give the relationship for z ; the equation numbers for χ , V and τ_{inv} refer either to Section 5.1 or to Appendix B.

χ	Equation for z	Equations
Quadratic polynomial in z	$z = \left(-b_1 + \sqrt{b_1^2 - 4 b_0 b_2} \right) / (2 b_2)$	
$\chi_{I t 1}$	$b_2 = \rho, b_1 = -\frac{\Theta'}{\Theta} \rho, b_0 = -2 \frac{\Theta'}{\Theta}$	(B.7)
Quadratic polynomials in z^2	$z^2 = \left(-c_1 + \sqrt{c_1^2 - 4 c_0 c_2} \right) / (2 c_2)$	
$\chi_{I s 2}$	$c_2 = \frac{\Theta'}{\Theta} \rho^2 - 4\rho, c_1 = 0, c_0 = 8 \frac{\Theta'}{\Theta}$ (at a_2)	(5.1)
$\chi_{I s 3}$	$c_2 = \rho^3, c_1 = 24\rho - 8\rho^2 \frac{\Theta'}{\Theta}, c_0 = -48 \frac{\Theta'}{\Theta}$ (at a_3)	(5.1)
$\chi_{I s 4}$	$c_2 = 12\rho^3 - \frac{\Theta'}{\Theta} \rho^4, c_1 = 192\rho - 72 \frac{\Theta'}{\Theta} \rho^2, c_0 = -384 \frac{\Theta'}{\Theta}$	(5.5)
Cubic polynomial in z	$z = \frac{1}{a_3} \left(-\frac{a_2}{3} - \frac{\sqrt[3]{2} p_0}{3 p_1} + \frac{p_1}{3 \sqrt[3]{2}} \right), p_2 = -27 a_0 a_2^2 + 9 a_1 a_2 a_3 - 2 a_2^3$ $p_0 = 3 a_1 a_3 - a_2^2, p_1 = \sqrt[3]{p_2 + \sqrt{4 p_0^3 + p_2^2}}$	
$\chi_{I t 3}$	$a_3 = 2\rho^2, a_2 = \left(3\rho - 2\rho^2 \frac{\Theta'}{\Theta} \right), a_1 = -4\rho \frac{\Theta'}{\Theta}, a_0 = -6 \frac{\Theta'}{\Theta}$	(B.8)

Table 5.2. Overview of approximations for χ in terms of z for heat waves propagating towards the center in a cylindrical geometry where a symmetry boundary condition is assumed. This table is used to calculate z using $\Theta'/\Theta = A'/A + i\phi'$ and ρ , where z is used to calculate $\chi = \frac{3}{2} \omega / \Im(z^2)$ and $\tau_{inv} = \omega \Re(z^2) / \Im(z^2)$; the equation numbers refer either to Section 5.1 or to Appendix B.

χ_z^{inw}	Equation for z	Equations
Quadratic polynomials in z	$z = \left(-b_1 - \sqrt{b_1^2 - 4b_0b_2} \right) / (2b_2)$	
χ_{Kc2}^{inw}	$b_2 = 4\rho, b_1 = 3 + 4\frac{\Theta'}{\Theta}\rho, b_0 = \frac{\Theta'}{\Theta}$	(B.4)
χ_{Kj2}^{inw}	$b_2 = 8\rho^2, b_1 = 8\rho^2\frac{\Theta'}{\Theta} + 4\rho, b_0 = 8\frac{\Theta'}{\Theta}\rho - 3$	(B.2)
Cubic polynomials in z	$z = \frac{1}{a_3} \left(-\frac{a_2}{3} + \frac{1-i\sqrt{3}}{3\sqrt[3]{4}} \frac{p_0}{p_1} - \frac{1+i\sqrt{3}}{6\sqrt[3]{2}} p_1 \right), p_2 = -27a_0a_3^2 + 9a_1a_2a_3 - 2a_2^3,$ $p_1 = \sqrt[3]{p_2 + \sqrt{4p_0^3 + p_2^2}}, p_0 = 3a_1a_3 - a_2^2$	
χ_{Kj3}^{inw}	$a_3 = 16\rho^3, a_2 = 16\frac{\Theta'}{\Theta}\rho^3 + 56\rho^2, a_1 = 48\frac{\Theta'}{\Theta}\rho^2 + 45\rho, a_0 = 23\frac{\Theta'}{\Theta}\rho + 7.5$	(4.7)
χ_{Kc5}^{inw}	$a_3 = 16\rho^2, a_2 = 36\rho + 16\rho^2\frac{\Theta'}{\Theta}, a_1 = 15 + 28\rho\frac{\Theta'}{\Theta}, a_0 = 3\frac{\Theta'}{\Theta}$	(B.5)

Table 5.3. Overview of approximations for χ in terms of z for heat waves propagating towards the edge in a cylindrical geometry where a semi-infinite domain is assumed. This table is used to calculate z using $\Theta/\Theta = A/A + i\phi'$ and ρ , where z is used to calculate $\chi = \frac{2}{\omega} \Im(z^2) / \Im(z^2)$; the equation numbers refer to Section 5.1 or to Appendix B.

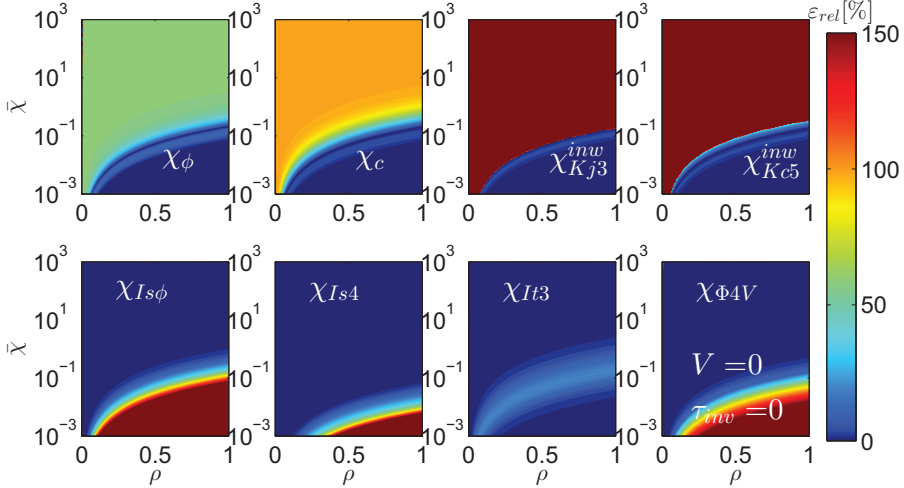


Figure 5.1. Comparison between the different relative errors of the χ estimates for a large range of $\bar{\chi} = \chi/\omega$ and ρ . The relative error is defined as $\varepsilon_{rel} = 100 \times \frac{|\chi - \chi_{est}|}{\chi}$ [%], where χ_{est} is χ_ϕ , χ_c , χ_{Kj3}^{inw} , and χ_{Kc5}^{inw} , which can be found in the tables on pages 72, 73, and 74. These approximations are based on semi-infinite domains (first row). The true cylindrical models (second row) are estimated by $\chi_{Is\phi}$ from (5.3), χ_{Is4} from (5.5), χ_{It3} from (B.8), and $\chi_{\Phi4V}$ from (B.17). This figure is based on a cylindrical geometry using a symmetry boundary condition with χ and $V = \tau_{inv} = 0$, where the heat waves travel inwards. The darkest blue represents $\varepsilon_{rel} < 1\%$ and the darkest red represents all $\varepsilon_{rel} > 150\%$.

because they approximate χ in a strong cylindrical geometry for the semi-infinite domain.

The approximations in Tables 5.1, 5.2, and 5.3 are compared in the rest of this section.

5.2.2 Selection of interesting approximations

The comparison of the approximations when only the diffusivity χ is present, i.e., $V = 0$ and $\tau_{inv} = 0$, is made based on a large number of possibilities of ρ and the combined parameter $\bar{\chi} = \chi/\omega$. Therefore, (2.50) and (2.51) are used to generate A'/A and ϕ' . The most interesting and best approximations are shown in Figure 5.1 in terms of the relative error with respect to the true diffusivity χ .

The use of semi-infinite domain approximations for heat waves propagating towards the center give a good approximation if the ratio $\rho\omega/\chi$ is large. In that case χ_c has the largest region with a good accuracy. The highest accu-

racy is generally given by χ_{Kj3} in the region where both approximate $\bar{\chi}$ well. In that case the approximations based on cylindrical geometry for heat waves propagating towards the center give good approximations for χ . Hence, χ_{It3} almost approximates the entire presented region well, albeit with less accuracy than χ_{Is4} . Also, $\chi_{\Phi 4V}$ performs well, although it was mainly derived to perform well under convectivity. $\chi_{Is\phi}$ is also shown as it is the most simple cylindrical approximation found. Unfortunately, its region of applicability is much smaller than the other approximations.

In summary, χ_{It3} has the largest region of applicability. Its relative error is maximally $\varepsilon_{rel} \approx 30\%$ in a small region. In this region, different approximations are necessary, for instance χ_{Kj3} or χ_c and χ_{Is4} .

5.2.3 Diffusivity and damping only

It is not possible to use one approximation to approximate χ well for all combinations of χ , ω , ρ , and τ_{inv} . However, it turns out that by combining two approximations to estimate χ almost the entire presented region of interest for heat waves propagating inwards can be covered. This is shown in Figure 5.2 on page 77, where the maximum relative error over the entire presented region is below 2%. Hence, it is always possible to get an accurate result for the presented combination of χ , ω , τ_{inv} , and ρ . Both χ_{Kj3}^{inv} and χ_{Is4} have been chosen because they give the most accurate approximations in their regions of applicability and they are complementary. The white line shows the approximate boundary of the regions of applicability of χ_{Kj3}^{inv} and χ_{Is4} . The error is largest at this boundary.

5.2.4 Diffusivity and convectivity with $\tau_{inv} = 0$ and $\tau_{inv} = 2$

For the inward case, multiple approximations are available to estimate V . It is not easy to choose a suitable approximation before the measurements have been analyzed because the approximations all depend on different harmonic information. For instance, χ_ϕ uses only the phases of two harmonics, but $\chi_{\Phi 4a}$ uses two phases and one amplitude. On the other hand, when $\tau_{inv} = 0$, then $\chi_{\Phi 4V}$ can be used, which uses only one harmonic. Therefore, it is not possible to point out the best approximation. However, the regions of applicability of the approximation are again clearly defined. χ_ϕ which originates from slab geometry is best at approximating χ for large $\omega\rho/\chi$. On the other hand, the approximations based on the symmetry boundary conditions estimate χ well for small $\omega\rho/\chi$.

From a numerical point of view, $\chi_{\Phi 4Va}$ performed best, but it is comparable to the other cylindrical approximations. Therefore, it is chosen to combine $\chi_{\Phi 4Va}$ and χ_ϕ separated by the white line, which is shown in Figure 5.3 on page 78 and Figure 5.4 on page 79 for $\tau_{inv} = 0$ and $\tau_{inv} = 2$, respectively. Both figures show similar regions where χ can be estimated well and where not. The large error

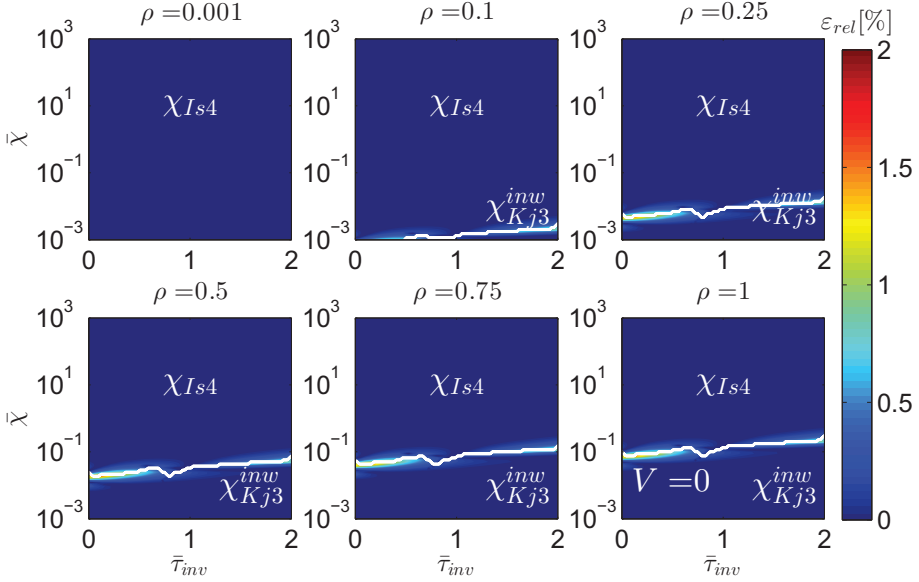


Figure 5.2. The relative error of the χ estimates for the combination of χ_{Is4} and χ_{Kj3}^{inn} presented for different $\bar{\chi} = \chi/\omega$ and $\bar{\tau}_{inn} = \tau_{inn}/\omega$ at a number of spatial locations ρ . The relative error is defined as $\varepsilon_{rel} = 100 \times \frac{|\chi - \chi_{est}|}{\chi}$ [%]. This figure combines the approximations χ_{Is4} and χ_{Kj3}^{inn} , which are separated by the boundary represented by the white line. This figure is based on a cylindrical geometry using a symmetry boundary condition with $V = 0$, where the heat waves travel inwards.

close to the boundary is caused by the limited region of approximation. There is no suitable approximation, which handles the regions with large errors.

5.3 Conclusion and summary

A large number of new approximations have been introduced to estimate χ directly from A'/A and ϕ' for different combinations of χ , V , and τ_{inn} for heat waves propagating towards the center. This corresponds to the case of off-axis heating. The approximations are based on a symmetry boundary condition and are derived on the basis of cylindrical geometry using standard assumptions.

The quality of the approximations is presented in several figures. In case only χ and τ_{inn} are considered ($V = 0$), the relative error of the χ estimate for the region of interest is smaller than 2% with respect to (2.50). These errors are achievable by combining χ_{Kj3}^{inn} and χ_{Is4} . In case also V is considered, the new approximations show a significant region in which χ can be estimated well, but

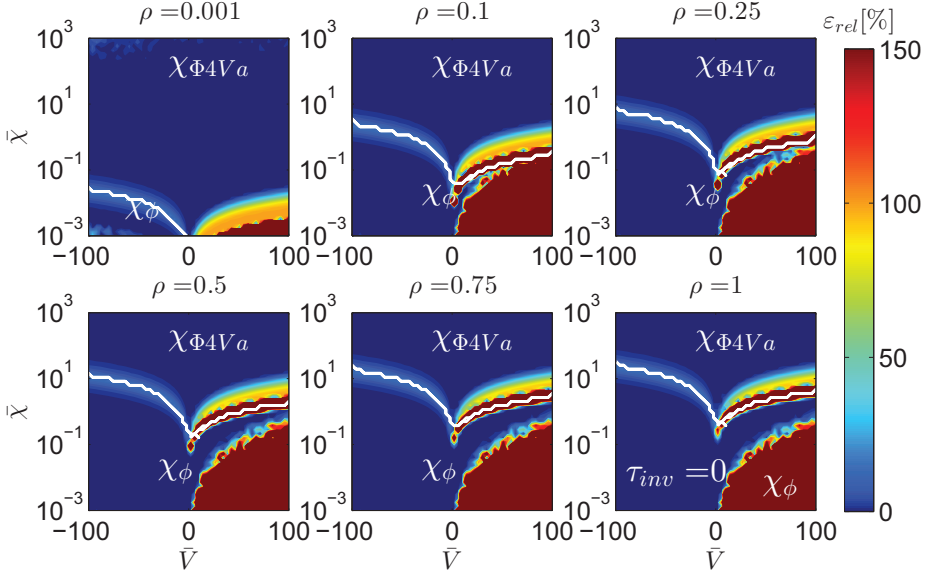


Figure 5.3. The relative error of the χ estimates for the combination of $\chi_{\Phi 4Va}$ and χ_{ϕ} presented for different $\bar{\chi} = \chi/\omega$ and $\bar{V} = V/\omega$ at a number of spatial locations ρ . The relative error is defined as $\varepsilon_{rel} = 100 \times \frac{|\chi - \chi_{est}|}{\chi}$ [%]. This figure combines the approximations $\chi_{\Phi 4Va}$ and χ_{ϕ} , which are separated by the boundary represented by the white line. This figure is based on a cylindrical geometry using a symmetry boundary condition with $\tau_{inv} = 0$, where the heat waves travel inwards. The darkest blue represents $\varepsilon_{rel} < 1\%$ and the darkest red represents all $\varepsilon_{rel} > 150\%$.

also regions in which no suitable approximation exists. Combining $\chi_{\Phi 4Va}$ and χ_{ϕ} cover a large region where χ can be well estimated.

This concludes the parts in which analytic solutions have been derived. All approximations have been derived either based on one or two harmonics. However, in practice more harmonics are available. As such the diffusivity is calculated for the individual harmonics and compared qualitatively. In the next chapter, it is investigated if it is also possible to find an estimate of the best diffusivity for multiple harmonics taking measurement noise into account.

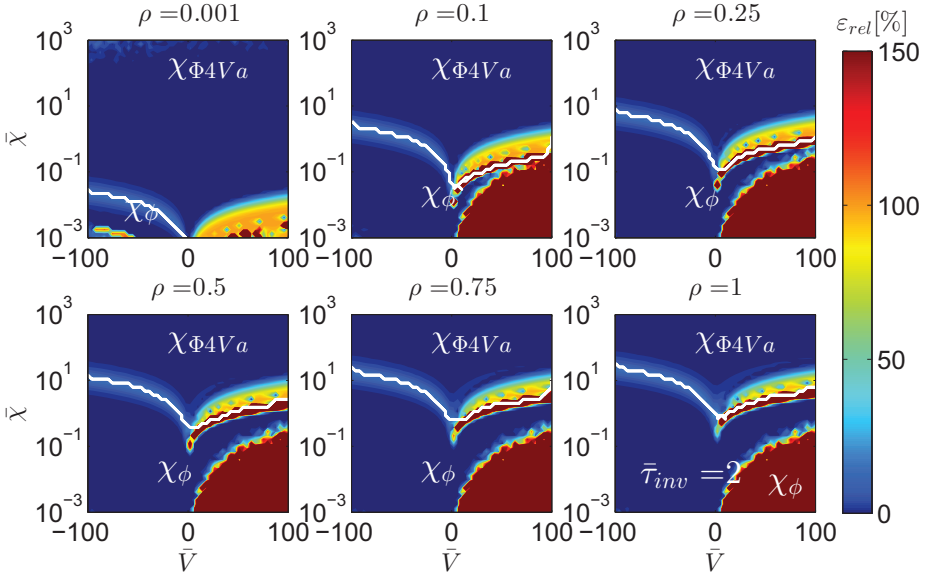


Figure 5.4. The relative error of the χ estimates for the combination of $\chi_{\Phi 4Va}$ and χ_{ϕ} presented for different $\bar{\chi} = \chi/\omega$ and $\bar{V} = V/\omega$ at a number of spatial locations ρ . The relative error is defined as $\varepsilon_{rel} = 100 \times \frac{|\chi - \chi_{est}|}{\chi}$ [%]. This figure combines the approximations $\chi_{\Phi 4Va}$ and χ_{ϕ} , which are separated by the boundary represented by the white line. This figure is based on a cylindrical geometry using a symmetry boundary condition with $\bar{\tau}_{inv} = 2$, where the heat waves travel inwards. The darkest blue represents $\varepsilon_{rel} < 1\%$ and the darkest red represents all $\varepsilon_{rel} > 150\%$.

Chapter 6

Estimation of the diffusivity taking frequency measurement uncertainties into account

In the previous three chapters various relationships are derived to determine the perturbative electron diffusivity χ based on slab or cylindrical geometry using different assumptions on the non-diffusive contributions, i.e., convectivity and damping. These relationships are based on a single harmonic or two harmonics, ω , ω_1 and ω_2 , respectively. However, in practice more harmonics are available and the measurements are uncertain, which is not considered in these relationships. This often leads to accuracy loss of the diffusivity estimate and the other transport coefficients. The reason for this accuracy loss is due to the calculation method and how different harmonic components are combined, which is directly associated with the underlying Probability Density Function (PDF) of χ .

The combinations of ρ , A'/A , and ϕ' in Chapters 3, 4, and 5 are rather complicated. Therefore, in this chapter we focus first on the approximations found in the literature because those consist of simple combinations of A'/A and ϕ' , i.e., (2.28), (2.29), (2.30), (2.31), (2.32), and (2.47). For these approximations, it is shown in this chapter that the resulting PDFs of χ are non-Gaussian and have long tails. This has two important implications:

1. The estimated diffusivities have a high upper uncertainty.
2. Taking the average of estimated diffusivities, e.g., for different harmonics, will result in a biased diffusivity estimate.

This chapter is based on the following article: van Berkel, M., et al. [2014]. Estimation of the thermal diffusion coefficient in fusion plasmas taking frequency measurement uncertainties into account, *Plasma Phys. Control. Fusion* **56**: 105004.

Both implications are demonstrated in this chapter.

The standard assumption of Circular Complex Normal Distributed (CCND) noise on the Fourier coefficients is used in the analysis part of this chapter. This distribution is the result of the Fourier transform of several different additive noise distributions including a Gaussian noise distribution. Based on the CCND and some minor conditions on the initial Signal to Noise Ratio (SNR), it is shown that the resulting PDF of the diffusivity is an inverse non-central chi-squared-distribution. This PDF is derived via an analysis of the propagation of noise from the time domain to the estimated diffusivity. This analysis also gives insight on how to arrive at the optimal diffusivity estimate by averaging the different harmonics, amplitude, and phase. A weighted averaging method using Maximum Likelihood Estimation is proposed [Martin, 2012]. This weighting is a sub-optimal solution in the sense that the resulting bias and variance on the diffusivity estimate is larger than the theoretically achievable bias and variance given the measurements. Nevertheless, it will still increase the accuracy significantly and gives a direct method for calculating the diffusivity without using complicated algorithms. If the damping is included, i.e., (2.31), the distribution of the product of ϕ' and A'/A needs to be used. As no closed-form expression for the PDF exists for this product of random Gaussian variables, a Gaussian approximation is used. This approximation is based on recent work related to this topic [Oliveira, 2013]. This introduces some error, which are studied using a Monte Carlo analysis.

The Cumulative Density Function (CDF) of χ is derived analytically. Hence, the accuracy of the estimated diffusivities can be determined through the construction of confidence bounds.

This chapter is structured as follows. Section 6.1 shortly introduces the commonly used relationships to calculate χ and their main assumptions. Moreover, it explains that Gaussian noise is the dominant noise on ECE-measurements used to measure the temperature. This allows for the derivation of the PDFs of amplitude and phase, which can be approximated under certain conditions by Gaussian distributions. The PDFs of the phase derivative and the logarithmic amplitude derivatives are calculated using an alternative method, which also includes cross-correlation terms between real and imaginary parts. Section 6.2 uses these Gaussian approximations of the phase derivative and logarithmic amplitude derivative to determine the resulting PDFs of the diffusivities. The corresponding CDFs are used to construct confidence bounds on the diffusivity. In addition, the PDF for χ is introduced based on the Gaussian approximation of the product $\phi'A'/A$. Section 6.3 focuses on the practical aspects of estimating mean values and variances of the Fourier coefficients. Direct methods for measuring the mean values and (co-)variances of the Fourier coefficients are presented, which are necessary to determine the PDFs of the diffusivity.

Section 6.4 introduces weighting methods to combine amplitude, phase, and different harmonics to achieve a combined overall diffusivity estimate. These

techniques are applied to simulations using realistic values for the Fourier coefficients and the measurement noise extracted from ASDEX Upgrade¹ data. Moreover, the influence of static errors, such as calibration errors is discussed. Finally, the main conclusions of this chapter are summarized in Section 6.5.

6.1 Distributions of phase and amplitude and its spatial derivatives

The uncertainty on measurements can be quantified by studying the PDFs of the measurement data. First, it is motivated why the Gaussian distribution is the most probable noise distribution on our time domain measurements. Then, this information is used to derive the PDFs of the Fourier coefficients, amplitude, and phase and their spatial derivatives. Moreover, the conditions are determined when the PDFs of amplitude and phase may be approximated by Gaussian distributions.

6.1.1 Gaussian noise as the result of the central limit theorem

In many applications the noise on measurements can be modeled using a Gaussian distribution function. This distribution is often the result of the central limit theorem, which states that, if many noise sources of different distributions are combined (hence their PDFs are convoluted), the resulting distribution tends towards a Gaussian distribution. More formal formulations of this theorem can be found in many statistics textbooks, e.g., [Billingsley, 2012]. This is the general argument for assuming a Gaussian distribution. However, for ECE-measurements there is a stronger argument.

In this chapter, ECE-measurements are used to determine the diffusivity from the electron temperature perturbations. The dominant measurement noise on ECE-measurements is the thermal noise, which is generally Gaussian distributed [Hartfuss, 1997]. More specifically, the thermal noise distribution on the output temperature measurements of the radiometer depends on the ratio between the intermediate frequency bandwidth B_{IF} and the video bandwidth B_V . If $B_{IF} \gg B_V$, which holds for most radiometers used in fusion, the resulting distribution is Gaussian. This is theoretically derived in [Emerson, 1953] and experimentally verified in [Sattler, 1993].

¹The author wishes to acknowledge the ASDEX Upgrade team and specifically Dr. François Rytter for the support and allowing the use of ASDEX Upgrade measurement data in this chapter.

6.1.2 Normal complex circular distributed noise

By assuming a Gaussian noise distribution in the time domain, the distribution functions of the Fourier coefficients can be also determined. These distribution functions are determined for every Fourier coefficient corresponding to a specific frequency ω .

The PDF of a Fourier coefficient at frequency ω can be determined by taking the Fourier transform of a sinusoidal signal $T(t)$ with amplitude M and phase θ and a Gaussian distributed zero-mean additive noise term $e(t)$ with variance σ_t^2

$$T(t) = M \cos(\omega t + \theta) + e(t). \quad (6.1)$$

The Fourier transform of (6.1) is not easily calculated. It requires the noise to be split in its harmonic components and the use of Hilbert transform properties. This transformation is described in [Goodman, 1963; Whalen, 1971] and is easily verified using a Monte Carlo analysis [Kroese, 2011]. The Fourier coefficient Θ at frequency ω has a bivariate distribution (PDF) in terms of its real part Θ_{\Re} and imaginary part Θ_{\Im}

$$f_{\Theta}(\Theta_{\Re}, \Theta_{\Im}) = \frac{1}{2\pi\sigma_F^2} \exp\left(-\frac{1}{2}\left(\frac{\Theta_{\Re} - \mu_{\Re}}{\sigma_F}\right)^2 - \frac{1}{2}\left(\frac{\Theta_{\Im} - \mu_{\Im}}{\sigma_F}\right)^2\right). \quad (6.2)$$

The mean values of this distribution μ_{\Re} and μ_{\Im} can also be related to the mean value of the Fourier coefficient, i.e., $\bar{\Theta} = \mu_{\Re} + i\mu_{\Im}$. The variance σ_F^2 directly depends on σ_t^2 , but also on the cross-correlation of the time domain noise. Therefore, instead of calculating σ_F^2 from σ_t^2 , a different method is used, which directly estimates $\sigma_F^2(\omega_k)$ from the measurements. This method is presented in Section 6.3.2.

The distribution $f_{\Theta}(\Theta_{\Re}, \Theta_{\Im})$ is shown in Figure 6.1 and is called a Circular Complex Normal Distribution (CCND). The real part Θ_{\Re} and imaginary part Θ_{\Im} are independently identically distributed (i.i.d.) and have a Gaussian distribution, see (6.2) or [Goodman, 1963; Pintelon, 2012]. It belongs to one Fourier coefficient at a specific frequency ω . This implies that for every Fourier coefficient $\Theta(\omega_k)$, where k denotes the excited harmonic, such a distribution can be defined, but with a different μ_{\Re} , μ_{\Im} , and σ_F^2 . Moreover, the distribution of $\Theta(\omega_k)$ is independent from the distribution of $\Theta(\omega_{k+1})$ [Goodman, 1963; Pintelon, 2012], which is important when different harmonics need to be combined.

The distribution $f_{\Theta}(\Theta_{\Re}, \Theta_{\Im})$ can also be expressed in polar coordinates using the amplitude $A = \sqrt{\Theta_{\Re}^2 + \Theta_{\Im}^2}$ and the phase ϕ defined as $\tan(\phi) = \Theta_{\Im}/\Theta_{\Re}$

$$f_{A\phi}(A, \phi) = \frac{A}{2\pi\sigma_F^2} \exp\left(-\frac{(A \cos(\phi) - M \cos \theta)^2}{2\sigma_F^2} - \frac{(A \sin(\phi) - M \sin \theta)^2}{2\sigma_F^2}\right), \quad (6.3)$$

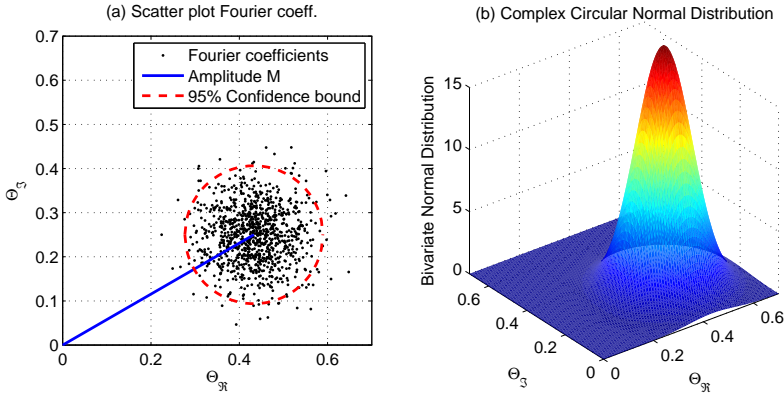


Figure 6.1. (a) A scatter plot of the Fourier coefficients calculated per period at frequency ω of $x(t) = 0.5 \sin(\omega t + \frac{\pi}{6}) + e(t)$, where $e(t)$ is Gaussian distributed noise. The Fourier coefficients are presented in the complex plane where Θ_{\Re} and Θ_{\Im} are its real and imaginary parts, respectively. In addition, the 95% circular confidence bound is presented (red dashed). (b) The corresponding histogram/PDF of the Circular Complex Normal Distribution in the complex plane.

where $\mu_{\Re} = M \cos \theta$ and $\mu_{\Im} = M \sin(\theta)$ [Whalen, 1971]. This form is more useful to calculate the PDFs of amplitude and phase, which will be necessary to determine the diffusivity. Finally, it is worth noting that the CCND is a good approximation of the Fourier transform for many other distributions in the time domain. However, whether the distribution is CCND depends on the number of time samples in one period of the Fourier transform and a number of noise properties, which are not so easily derived [Brillinger, 2001; Pintelon, 2012]. This can also be easily verified using Monte Carlo simulations. Therefore, in this chapter, rather than assuming a Gaussian distribution in the time domain, a CCND in the frequency domain is assumed. This extends the subsequent analysis to a much broader class of noise distributions in time domain.

6.1.3 Amplitude and phase distributions and their confidence bounds

The relationships introduced to determine the diffusivity are based on the amplitude and phase of the measurements [Lopes Cardozo, 1995; Ryter, 2010]. Therefore, the PDFs of the amplitude and phase are investigated. If the SNR, defined here as M/σ_F , is large enough it can be shown that the PDFs of the phase and amplitude can be well approximated by a Gaussian distribution function.

The PDF of the amplitude can be found by integrating (6.3) over all the

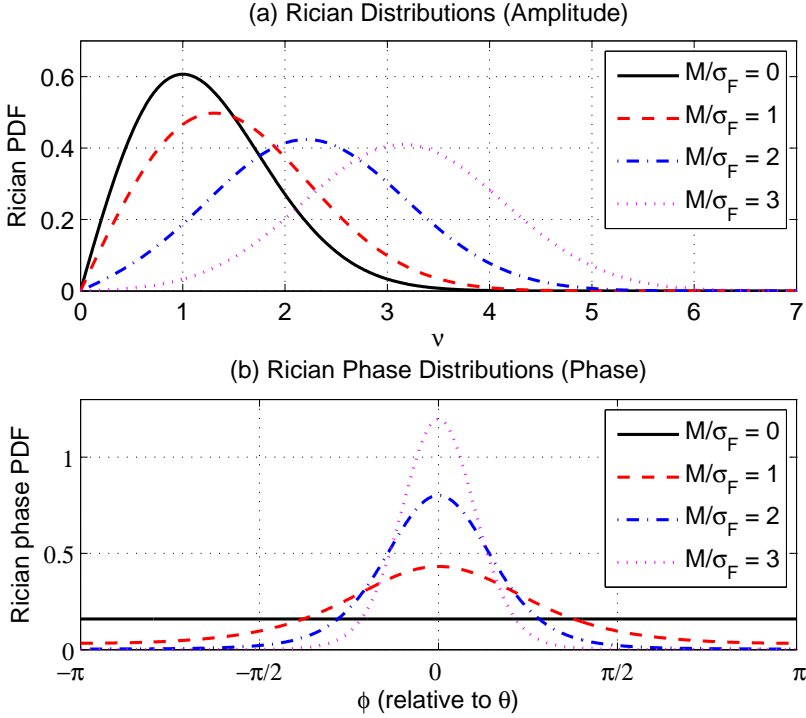


Figure 6.2. (a) Rician PDF of the amplitude for different values of the SNR using $\nu = A/\sigma_F$ as a scaling parameter. In the special case of $M/\sigma_F = 0$, the Rician distribution becomes a Rayleigh distribution. (b) The Rician phase PDF for different values of the SNR. In the special case of $M/\sigma_F = 0$, the Rician phase distribution reduces to a uniform distribution.

phases on a circle. The PDF of the phase can be found by integrating over all amplitudes on a line starting at the origin. The resulting PDF of the amplitude is the Rician distribution, which has two limit cases: the Rayleigh distribution when $M = 0$ and the Gaussian distribution when $M/\sigma_F \rightarrow \infty$, [Whalen, 1971]. The resulting PDF of the phase is sometimes referred to as the Rician phase distribution [Simon, 2005] and is defined on the range $-\pi \leq \theta < \pi$. It has again two limit cases: the uniform distribution for $M = 0$ and the Gaussian distribution for SNR $M/\sigma_F \gg 0$. The analytic expressions for the Rician and Rician phase distributions can be found in Appendix C.

The evolution of the Rician distribution and Rician phase distribution for different values of the M/σ_F is presented in Figure 6.2. It shows that if the SNR

M/σ_F is large enough it can be well approximated by a Gaussian distribution function. Consequently, the mean value μ and the variance σ^2 of this Gaussian approximation need to be determined. The mean values of amplitude and phase are simply $\mu_A = M$ or $\mu_\phi = \theta$. However, the corresponding variances σ_A^2 and σ_ϕ^2 need to be calculated, for which we use propagation of uncertainty. This is also known as propagation of errors [Martin, 2012; Pintelon, 2012]. It can be considered as a first order Taylor approximation for random variables around the mean value. In case of the phase this results in $\theta = \arctan(\mu_{\Im}/\mu_{\Re})$

$$\sigma_\phi^2 = J_\phi \text{cov}(\Theta_{\Re}, \Theta_{\Im}) J_\phi^T,$$

$$\text{with } J_\phi = \left[\frac{\partial \arctan(\mu_{\Im}/\mu_{\Re})}{\partial \mu_{\Re}}, \frac{\partial \arctan(\mu_{\Im}/\mu_{\Re})}{\partial \mu_{\Im}} \right], \quad (6.4)$$

where $\text{cov}(\Theta_{\Re}, \Theta_{\Im})$ is a diagonal matrix with on the diagonal the variance of Θ_{\Re} and Θ_{\Im} , i.e., σ_F^2 because $f_\Theta(\Theta_{\Re}, \Theta_{\Im})$ is i.i.d. This results in the phase variance $\sigma_\phi^2 = \sigma_F^2/M^2$. Similarly, also the variance of the amplitude can be calculated, which is $\sigma_A^2 = \sigma_F^2$. The corresponding confidence bounds for this Gaussian approximation are calculated as follows [Martin, 2012]

$$C_\phi = \theta \pm \frac{\sigma_F}{M} \sqrt{2} \text{erf}^{-1}(\mathbf{p}) \text{ or } C_A = M \pm \sigma_F \sqrt{2} \text{erf}^{-1}(\mathbf{p}) \quad (6.5)$$

in terms of a confidence \mathbf{p} , e.g., $\mathbf{p} = 0.95$. However, these confidence bounds only hold if the individual harmonics have a large SNR as is shown in Figure 6.3, where also the true confidence bounds are shown. It shows that for a $\text{SNR} > 5$, the Gaussian bound approximates the real confidence bounds well.

The Rician distribution is non-symmetric. Consequently, we have chosen for a 95% central confidence interval such that the two confidence bounds are given by 2.5% ($\mathbf{p} = 0.025$) and 97.5% ($\mathbf{p} = 0.975$). In Appendix C the derivation and calculation of the confidence bounds of amplitude and phase using Rician (phase) distributions are given.

The determination of χ requires the distributions of the scaled amplitude derivative A'/A and phase ϕ' derivative, which are derived next.

6.1.4 Distributions of ϕ' and A'/A

In the previous section the phase and amplitude distributions are calculated on the basis of a CCND. In this section, the distributions of the spatial derivatives ϕ' and A'/A are approximated. Although there are different methods used in the literature to calculate these spatial derivatives, here the definition in (2.42) is used. The reason is that for the slab geometry approximations this is the only mathematical consistent choice with respect to the assumption of a homogenous domain (see Chapter 2).

Based on the Gaussian distribution of ϕ and A and the definitions for the derivatives it can be shown that both ϕ' and A'/A can be well approximated by a

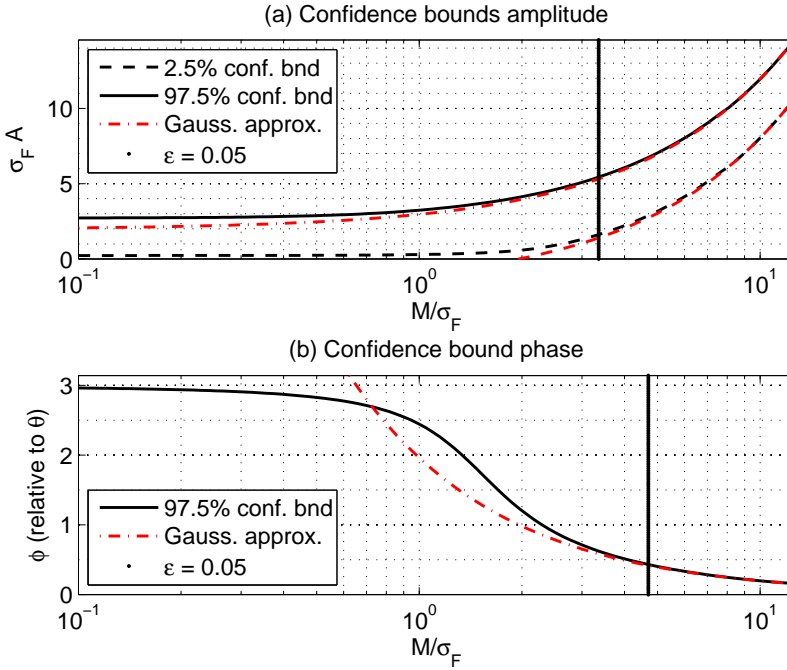


Figure 6.3. Comparison between the real Rician 95% confidence interval compared to the approximated confidence bound based on a Gaussian distribution. In addition, the vertical line (dotted line) represents the SNR where the relative error $\varepsilon = |\sigma_{Rice}^2 - \sigma_{Gauss}^2| / \sigma_{Gauss}^2$ in terms of the variances equals 5%. (a) The 2.5% (dashed line) and 97.5% (solid line) confidence bounds (95% confidence interval) based on the Rician distribution function and the Gaussian approximations (red dashed-dotted line) of the confidence bounds for the 95% confidence interval. The y-axis is the amplitude A scaled with σ_F . (b) the 97.5% confidence bound of the phase (solid line) based on the Rician phase distribution and the Gaussian approximation of the confidence bound (red dashed-dotted line). Note that the Rician phase distribution is symmetric around ϕ (relative to θ) such that one confidence bound suffices. The CDF to calculate the true confidence bounds can be found in Appendix C.

Gaussian distribution function for reasonable SNRs. However, this is not easily derived as the resulting distribution functions depend on five variables, the mean values, the variances, and the covariance. In addition, two approximation steps are necessary namely, one from the Fourier coefficients to phase and amplitude, and one to their derivatives. Here, we wish to avoid these steps and directly calculate the distributions for ϕ' and A'/A from the Fourier coefficients.

The mean value and the variance of both these quantities can be calculated using the first term in a Taylor expansion (propagation of uncertainty). The mean values are calculated using (2.42) such that

$$\mu_{A'/A} = \frac{1}{\Delta\rho} \ln \left(\frac{M(\rho_{i+1})}{M(\rho_i)} \right) \text{ and } \mu_{\phi'} = \frac{\theta(\rho_{i+1}) - \theta(\rho_i)}{\Delta\rho}. \quad (6.6)$$

The following symmetric covariance matrix is used to represent the (co-)variances of the real and imaginary parts of the Fourier coefficients at two locations (ω_k has been omitted)

$$\text{cov}(\omega_k, \Theta_{\Re}(\rho_i), \Theta_{\Re}(\rho_{i+1}), \Theta_{\Im}(\rho_i), \Theta_{\Im}(\rho_{i+1})) = \begin{bmatrix} \sigma_{\Re}^2(\rho_i) & \sigma_{\Re\Re}^2(\rho_i, \rho_{i+1}) & \sigma_{\Re\Im}^2(\rho_i) & \sigma_{\Re\Im}^2(\rho_i, \rho_{i+1}) \\ & \sigma_{\Re}^2(\rho_{i+1}) & \sigma_{\Re\Im}^2(\rho_{i+1}, \rho_i) & \sigma_{\Re\Im}^2(\rho_{i+1}) \\ & & \sigma_{\Im}^2(\rho_i) & \sigma_{\Im\Im}^2(\rho_i, \rho_{i+1}) \\ & & & \sigma_{\Im}^2(\rho_{i+1}) \end{bmatrix}, \quad (6.7)$$

where the exact definitions of the (co-)variances are given in Section 6.3.2. When assuming CCND noise, this matrix can be further simplified using $\sigma_{\Im}^2(\rho_i) = \sigma_{\Re}^2(\rho_i)$ and $\sigma_{\Re\Im}^2(\rho_i) = \sigma_{\Re\Im}^2(\rho_{i+1}) = 0$, which is explained in detail in Section 6.3.2. Here, we have chosen to use the full covariance matrix for its generality. Because, this full covariance matrix can also be used under the weak assumption that the real and imaginary parts at spatial locations ρ_i and ρ_{i+1} are jointly Gaussian distributed and the resulting distributions of A'/A and ϕ' can be approximated by a Gaussian distribution.

The (co-)variances of A'/A and ϕ' can be found in terms of the covariance matrix $\text{cov}(\omega_k, A'/A, \phi')$ using (6.7) and the Jacobian based on the derivative with respect to the real and imaginary parts of (2.42)

$$\text{cov}(\omega_k, A'/A, \phi') =$$

$$J(\omega_k) \text{cov}(\omega_k, \Theta_{\Re}(\rho_i), \Theta_{\Re}(\rho_{i+1}), \Theta_{\Im}(\rho_i), \Theta_{\Im}(\rho_{i+1})) J^T(\omega_k), \quad (6.8)$$

where the Jacobian is given by

$$J(\omega_k) = \frac{1}{\Delta\rho} \begin{bmatrix} -\frac{\mu_{\Re}(\rho_i)}{M^2(\rho_i)} & \frac{\mu_{\Re}(\rho_{i+1})}{M^2(\rho_{i+1})} & -\frac{\mu_{\Im}(\rho_i)}{M^2(\rho_i)} & \frac{\mu_{\Im}(\rho_{i+1})}{M^2(\rho_{i+1})} \\ \frac{\mu_{\Im}(\rho_i)}{M^2(\rho_i)} & -\frac{\mu_{\Im}(\rho_{i+1})}{M^2(\rho_{i+1})} & -\frac{\mu_{\Re}(\rho_i)}{M^2(\rho_i)} & \frac{\mu_{\Re}(\rho_{i+1})}{M^2(\rho_{i+1})} \end{bmatrix}. \quad (6.9)$$

The resulting covariance matrix takes the following form

$$\text{cov}(\omega_k, A'/A, \phi') = \begin{bmatrix} \sigma_{A'/A}^2 & \sigma_{A'/A\phi'}^2 \\ \sigma_{\phi'A'/A}^2 & \sigma_{\phi'}^2 \end{bmatrix}, \quad (6.10)$$

where $\sigma_{A'/A}^2$ and $\sigma_{\phi'}^2$ are the variances of A'/A , respectively, and where ϕ' and $\sigma_{\phi'A'/A}^2$ is the covariance between A'/A and ϕ' . In case the confidence on (2.28) and (2.29) needs to be calculated, the corresponding variances $\sigma_{\phi'}^2$ and $\sigma_{A'/A}^2$ can be extracted. The confidence of (2.31) and (2.47) are determined using the full covariance matrix.

Here, Gaussian approximations of A'/A and ϕ' have been calculated using propagation of uncertainty based on the estimated (co-)variances. In the next section, the distribution of χ and its confidence bounds are calculated based on the assumption of Gaussian distributed A'/A and ϕ' .

6.2 Distributions of the diffusivity χ

This section derives the distribution functions of χ . These are used to determine the confidence bounds on χ . First, the PDF for χ is determined based on the case where the damping is zero. The corresponding CDF is calculated allowing for the calculation of the confidence bounds for χ . Secondly, the PDF of χ based on a Gaussian approximation of $\phi'A'/A$ is analyzed, which corresponds to the case where also damping is included.

6.2.1 Inverse non-central chi-squared distribution

Here, the resulting distributions for (2.28) and (2.29) are discussed. The diffusivity is calculated using the squared reciprocal of the spatial derivatives of the phase or the amplitude, which results in a non-Gaussian distribution. The derivation of these PDFs of χ can be simplified by introducing a variable γ , where γ denotes either A'/A or ϕ' when (2.28) or (2.29) are considered. The PDF of γ is then denoted by $g(\gamma)$. This, $g(\gamma)$ is transformed to $h(\chi)$, the PDF of χ , using conservation of area. Then, it follows from (2.28) or (2.29) that $\gamma = \sqrt{3/4 \cdot \omega/\chi}$ and that the derivative equals $|d\chi/d\gamma|^{-1} = \sqrt{3/16 \cdot \omega/\chi^3}$. Hence, the resulting distribution function of χ is given by

$$h(\chi \{ \gamma \}) = \begin{cases} \sqrt{\frac{3}{16} \frac{\omega}{\chi^3}} \{g(\gamma) + g(-\gamma)\} & \chi > 0 \\ 0 & \chi \leq 0. \end{cases} \quad (6.11)$$

If a Gaussian approximation of $g\left(\frac{A'}{A}\right)$ or $g(\phi')$ is used, then

$$g(\gamma) = \frac{1}{\sqrt{2\pi\sigma_\gamma^2}} \exp\left(-\frac{(\gamma - \mu_\gamma)^2}{2\sigma_\gamma^2}\right). \quad (6.12)$$

In this case, $h(\chi)$ is a special case of the general inverse non-central chi-squared distribution. This distribution is positive non-symmetric with a large (positive) tail and only resembles a Gaussian for small variances. Figure 6.4 shows the inverse non-central chi-squared distribution, $h(\chi)$. It shows that $h(\chi)$ has a long tail especially when the variance σ_γ^2 is large. The long tail also results in a bias, which is defined as the difference between the expected value $\mathbb{E}\{\chi\}$ and the true value of χ . The bias, i.e., the expected value $\mathbb{E}\{\chi\}$, is defined by the improper integral

$$\mathbb{E}\{\chi\} = \int_0^\infty \chi h(\chi) d\chi = \infty \quad (6.13)$$

is divergent. This has important implications, because it means that if the diffusivity is determined a number of times from an experiment with the same μ_γ and σ_γ^2 , the average of these experiments will not result in the true diffusivity χ , i.e., it will be biased. Even worse, the diffusivity estimate will diverge to ∞ for an increasing number of estimates and its divergence rate depends on the variance σ_γ^2 .

6.2.2 Confidence bounds non-central inverse chi-squared distribution

The confidence bounds on the diffusivity can now also be calculated based on (6.11) by calculating its Cumulative Density Function (CDF). The CDF $H(X)$ of the PDF $h(\chi)$ is given by $H(X) = \int_0^X h(\chi) d\chi$, which can be solved analytically

$$H(X) = \begin{cases} 1 - \frac{1}{2} \operatorname{erf}\left(\frac{\sqrt{\frac{3}{4}\frac{\omega}{X}} + \mu_\gamma}{\sigma_\gamma \sqrt{2}}\right) - \frac{1}{2} \operatorname{erf}\left(\frac{\sqrt{\frac{3}{4}\frac{\omega}{X}} - \mu_\gamma}{\sigma_\gamma \sqrt{2}}\right) & X > 0 \\ 0 & X \leq 0. \end{cases} \quad (6.14)$$

The CDF $H(X)$ is non-symmetric, which means that two confidence bounds need to be calculated. We are interested in the central confidence interval such that the lower bound X_{min} is determined by $H(X_{min}) = (1 - \mathbf{p})/2$ and the upper bound by $H(X_{max}) = (1 + \mathbf{p})/2$. The CDF and the corresponding $\mathbf{p} = 0.95$ central confidence interval is shown in Figure 6.4.

In practice, $H(X)$ is difficult to invert analytically. On the other hand, the bounds can be easily calculated by finding the zero crossing of $H(X) - (1 - \mathbf{p})/2$ and $H(X) - (1 + \mathbf{p})/2$, for which many algorithms exist.

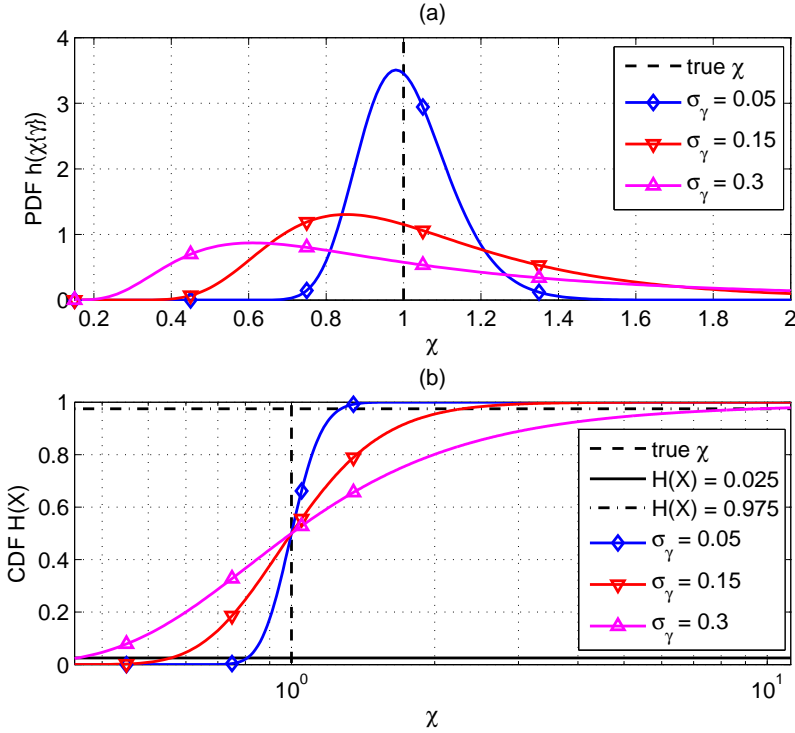


Figure 6.4. (a) The inverse non-central chi-squared distribution for different values of the variance σ_γ^2 , where $\mu_\gamma = 0.866$ and $\omega = 1$. This corresponds to $\chi = 1$ represented by the dashed line. (b) The Cumulative Density Function $H(X)$ of the inverse non-central chi-squared distribution corresponding to the presented PDFs. The dashed line represents the value of χ when $\sigma_\gamma^2 \rightarrow 0$. The solid line show the values at which $H(X) = 0.025$ and the dashed-dotted line where $H(X) = 0.975$ corresponding to a central 95% confidence interval.

6.2.3 Inverse product distribution function

The product of the Gaussian distributed variables ϕ' and A'/A plays an important role in (2.31) and (2.47) in which the effect of damping is suppressed. The distribution for χ (6.11) is a special case of the distribution discussed here as it assumes that $\mu_{\phi'} = \mu_{A'/A}$ and $\sigma_{A'/A}^2 = \sigma_{\phi'}^2$. As such it is a simplification of the general product of ϕ' and A'/A . The distribution function of the general product of ϕ' and A'/A is treated here separately, because it does not have a closed-form expression [Seijas-Macias, 2012]. This also holds for the PDF of

χ based on (2.31). This complicates the calculation of the confidence bounds significantly, because the CDF needs to be solved using a double integral.

As the closed-form expression does not exist, other approaches are necessary. Therefore, the distribution function is generally approximated using various distribution functions for the different limit cases [Aroian, 1978] in the literature. In case the ratio's $\mu_{A'/A}/\sigma_{A'/A}$ and $\mu_{\phi'}/\sigma_{\phi'}$ are large, then the product can be approximated well by a Gaussian distribution [Craig, 1936]. However, it is difficult to translate this into numbers as it also depends on the mean values itself. Nevertheless, we have chosen to always approximate the product using a Gaussian approximation. As the alternative of using other distribution functions would result in a more complicated analysis [Aroian, 1978].

The recommended approach in the literature is used to approximate the moments of the Gaussian distribution using the moment generating function [Craig, 1936; Oliveira, 2013; Ware, 2003]. It is used to generate the first moment, i.e., the mean

$$\mu_p = \mu_{A'/A}\mu_{\phi'} + \sigma_{A'/A\phi'}^2, \quad (6.15)$$

which includes also a bias term equal to the covariance $\sigma_{A'/A\phi'}^2$. The second moment, the variance, is given by

$$\begin{aligned} \sigma_p^2 &= \mu_{A'/A}^2\sigma_{\phi'}^2 + \mu_{\phi'}^2\sigma_{A'/A}^2 + \sigma_{A'/A}^2\sigma_{\phi'}^2 \\ &+ 2\sigma_{A'/A\phi'}^2\mu_{A'/A}\mu_{\phi'} + \sigma_{A'/A\phi'}^2\sigma_{A'/A}\sigma_{\phi'}. \end{aligned} \quad (6.16)$$

Both (6.15) and (6.16) can be used to replace the mean value and variance in the Gaussian approximation. The Gaussian approximation of the distribution function of $\phi'A'/A$ is then given by

$$g_p(\phi'A'/A) = \frac{1}{\sqrt{2\pi\sigma_p^2}} \exp\left(-\frac{(\phi'A'/A - \mu_p)^2}{2\sigma_p^2}\right). \quad (6.17)$$

The distribution function of χ can be approximated using again preservation of area

$$h(\chi(\mu_p)) = \frac{3}{4} \frac{\omega}{\chi^2} \frac{1}{\sqrt{2\pi\sigma_p^2}} \exp\left(-\frac{\left(\frac{3\omega}{4\chi} - \mu_p\right)^2}{2\sigma_p^2}\right). \quad (6.18)$$

This distribution is not further studied here because it is only an approximation of the real distribution. Section 6.3 studies (6.18) more extensively and compares it also to the actual distribution of (2.31) calculated using a Monte Carlo simulation. The CDF of (6.18) is not presented here as it does not have a closed-form expression. However, the CDF can be found by numerically approximating a single integral such that the confidence bounds can still be calculated. This is described in more detail in Appendix C.

In (2.47) also an approximation is given which is based on cylindrical geometry. This can be included by replacing the mean value of A'/A with $\mu_{A'/A} = A'/A + 1/(2\rho)$.

In the next section, the mean values and variances are estimated based on real measurements.

6.3 Estimating means and (co-)variances from measurements

In the next section, we discuss how to estimate the diffusivity from real measurements. In this section realistic values for the Fourier coefficients and its corresponding variances are calculated first. These are acquired from ASDEX Upgrade discharge 17175, where the modulated ECRH is deposited off-axis at toroidal normalized radius $\rho_t = 0.6$. A detailed description of this discharge can be found in [Mantica, 2006a,b]. Here, the distribution function is investigated based on the measurement data and it is explained how to calculate the mean values and variances of the Fourier coefficients. In addition, the mean values and (co-)variances are calculated at two specific spatial locations.

6.3.1 Noise distribution of ASDEX Upgrade measurements

In Section 6.1.1 it is explained why ECE-measurements are Gaussian distributed. This is further investigated using the measurement data from ASDEX Upgrade. Although the time interval where the periodic perturbations are present can be used to extract the variances (see next section), it is unsuitable to determine the PDF due to the low number of periods available. Therefore, the time domain noise is extracted from a time interval where the plasma is not perturbed by a heat source, which gives the natural noise distribution. The normalized histograms of the ECE-signals considered are presented in Figure 6.5 (left).

A Gaussian distribution can be recognized, albeit disturbed due to quantization (discretization). However, we are interested in frequency domain properties at the perturbed harmonics ω_k . Therefore, extra random samples are generated, which have the same normalized distribution function as the quantized noise distribution shown in Figure 6.5. Then, the Fourier transform is calculated per period, which results in many Fourier coefficients for the ground frequency ω_1 . This process is performed for two ECE-measurements at different radial locations. The resulting distributions of these Fourier coefficients are presented in Figure 6.5. Both, the real and imaginary parts are Gaussian distributed with similar variances and uncorrelated such that the distribution function is close to that of a CCND. However, this does not guarantee that in case of perturbative measurements we also have a CCND because other disturbances are present.

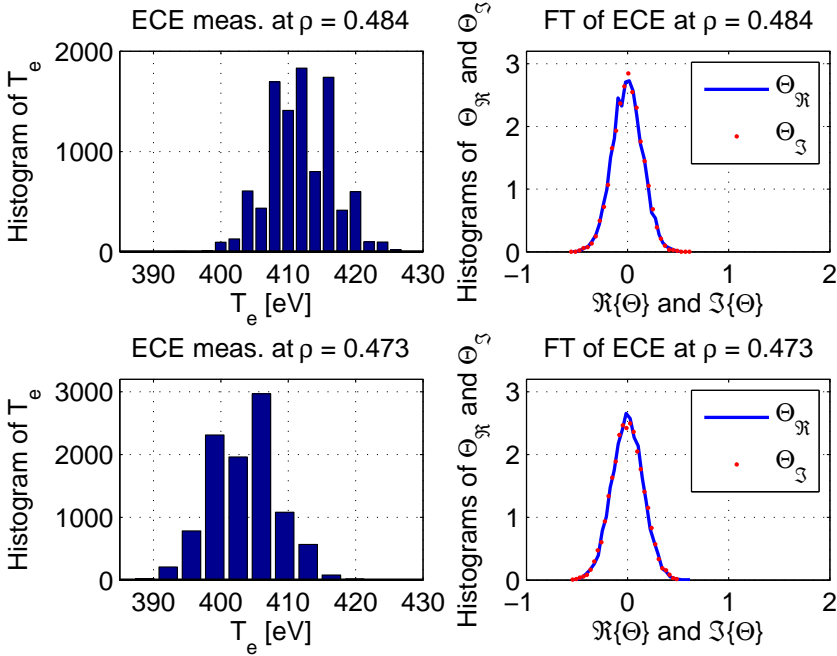


Figure 6.5. Histograms of AUG 17175 ECE measurements at locations $\rho = 0.484$ and $\rho = 0.473$ measured between 1.67 – 2 s in the plasma and distributions (left). On the right the histograms of Θ_{\Re} and Θ_{\Im} , respectively the real and imaginary part of the Fourier coefficients at 14.71 Hz (first harmonic) at radial locations $\rho = 0.484$ and $\rho = 0.473$. The distributions in time (left) are used to generate many samples (10000 periods at 14.71 Hz). These periods are Fourier transformed and the real and imaginary parts of the Fourier coefficients at 14.71 Hz are extracted. These are used to construct the histograms of Θ_{\Re} and Θ_{\Im} , which clearly show that the resulting distribution is CCND.

6.3.2 Estimating the Fourier coefficients and variances

This subsection explains how to estimate the Fourier coefficients and variances based on periodic perturbations. The estimated Fourier coefficients are denoted by $\hat{\Theta}(\omega_k)$ (hat denotes estimates), which can also be seen as the mean value of the Fourier coefficient. There are two possibilities to calculate the mean values of the Fourier coefficients: (1) the Fourier transform can be applied over the entire time interval or (2) the Fourier coefficients can be calculated per period, which are then averaged to find the mean values of the Fourier coefficients

$\hat{\Theta}(\omega_k) = \hat{\mu}_{\Re}(\omega_k) + i \cdot \hat{\mu}_{\Im}(\omega_k)$, i.e.,

$$\hat{\Theta}(\omega_k) = \frac{1}{M} \sum_{m=1}^M \Theta^{[m]}(\omega_k), \quad (6.19)$$

where $\Theta^{[m]}(\omega_k)$ is the Fourier coefficient of the individual period m for frequency ω_k and M is the total number of periods, also called realizations. Calculating the Fourier transform (FFT) of one period, and averaging over all periods is equivalent to calculating the Fourier transform of the entire time trace, for the common frequencies (if the number of periods M is integer and without using a window). For the example presented in this chapter, a time-trace of 680 ms is used, which contains exactly ten periods $M = 10$.

The advantage of determining the Fourier coefficients per period $\Theta^{[m]}(\omega_k)$ is that they can also be used to directly estimate the variances. The variance for the Fourier coefficient $\hat{\sigma}_c^2$ can be estimated using

$$\hat{\sigma}_c^2(\omega_k) = \frac{1}{M(M-1)} \sum_{m=1}^M \left| \Theta^{[m]}(\omega_k) - \hat{\Theta}(\omega_k) \right|^2. \quad (6.20)$$

Alternatively, the variances for the real and imaginary parts can be estimated. For the real part it is given by

$$\hat{\sigma}_{\Re}^2(\omega_k) = \frac{1}{M(M-1)} \sum_{m=1}^M \left| \Theta_{\Re}^{[m]}(\omega_k) - \hat{\Theta}_{\Re}(\omega_k) \right|^2, \quad (6.21)$$

where $\Theta_{\Re}^{[m]}$ is the real part of $\Theta^{[m]}$. Similarly, the variance $\hat{\sigma}_{\Im}^2(\omega_k)$ of the imaginary part can be determined.

The covariances between the Fourier coefficients at different spatial locations can be estimated using the definition

$$\begin{aligned} & \hat{\sigma}_{j,i}^2(\omega_k, \rho_j, \rho_i) = \\ & \frac{1}{M(M-1)} \sum_{m=1}^M \left(\Theta^{[m]}(\omega_k, \rho_j) - \hat{\Theta}(\omega_k, \rho_j) \right) \overline{\left(\Theta^{[m]}(\omega_k, \rho_i) - \hat{\Theta}(\omega_k, \rho_i) \right)}, \end{aligned} \quad (6.22)$$

Again it is also possible to estimate the covariances directly for the real and imaginary parts for $j = i + 1$, $\sigma_{\Re\Im}^2(\omega_k, \rho_i, \rho_{i+1})$, $\sigma_{\Im\Im}^2(\omega_k, \rho_i, \rho_{i+1})$, $\sigma_{\Re\Re}^2(\omega_k, \rho_i)$ using similar definitions, e.g., for $\hat{\sigma}_{\Im\Re}^2(\omega_k, \rho_{i+1}, \rho_i)$

$$\begin{aligned} & \hat{\sigma}_{\Im\Re}^2(\omega_k, \rho_{i+1}, \rho_i) = \frac{1}{M(M-1)} \\ & \sum_{m=1}^M \left(\Theta_{\Im}^{[m]}(\omega_k, \rho_{i+1}) - \hat{\Theta}_{\Im}(\omega_k, \rho_{i+1}) \right) \left(\Theta_{\Re}^{[m]}(\omega_k, \rho_i) - \hat{\Theta}_{\Re}(\omega_k, \rho_i) \right). \end{aligned} \quad (6.23)$$

These variances refer to the variation of the Fourier coefficients with respect to their mean values and the co-variances to the common variations of the Fourier coefficients. The advantage of using the (co-)variances is that it takes into account the uncertainty based on the measurements directly. The variances can be the result of for instance thermal noise inside the radiometer. On the other hand, cross-correlations can also be the result of thermal noise due to common components or it can be directly related to common temperature fluctuations in the plasma due to the perturbation source or other sources such as edge localized modes and sawteeth.

In case of a CCND, the full covariance matrix (6.7) can be simplified significantly because the real and imaginary parts at the same spatial location are i.i.d., i.e., $\sigma_{\Re}^2(\omega_k) = \sigma_{\Im}^2(\omega_k) = \hat{\sigma}_F^2(\omega_k)$. This also gives $\hat{\sigma}_F^2 = \hat{\sigma}_c^2(\omega_k)/2$, which can also be directly calculated from (6.20) by separating the real and imaginary parts

$$\hat{\sigma}_c^2(\omega_k) = \hat{\sigma}_{\Re}^2(\omega_k) + \hat{\sigma}_{\Im}^2(\omega_k). \quad (6.24)$$

The easiest method to calculate (6.7) in case of a CCND is to use the covariance matrix of the Fourier coefficients at ω_k

$$\text{cov}(\omega_k, \Theta(\rho_i), \Theta(\rho_{i+1})) = \begin{bmatrix} \sigma_c^2(\rho_i) & \sigma_c^2(\rho_i, \rho_{i+1}) \\ \sigma_c^2(\rho_i, \rho_{i+1}) & \sigma_c^2(\rho_{i+1}) \end{bmatrix}, \quad (6.25)$$

which can be constructed using (6.20) and (6.22). The covariance matrix (6.7) can then be constructed using (6.25)

$$\begin{aligned} & \text{cov}(\omega_k, \Theta_{\Re}(\rho_i), \Theta_{\Re}(\rho_{i+1}), \Theta_{\Im}(\rho_i), \Theta_{\Im}(\rho_{i+1})) = \\ & \frac{1}{2} \begin{bmatrix} \Re(\text{cov}(\omega_k, \Theta(\rho_i), \Theta(\rho_{i+1}))) & -\Im(\text{cov}(\omega_k, \Theta(\rho_i), \Theta(\rho_{i+1}))) \\ \Im(\text{cov}(\omega_k, \Theta(\rho_i), \Theta(\rho_{i+1}))) & \Re(\text{cov}(\omega_k, \Theta(\rho_i), \Theta(\rho_{i+1}))) \end{bmatrix}. \end{aligned} \quad (6.26)$$

Its form can also be understood as follows: on the diagonal are the variances, which are the same for the real and imaginary parts at the same spatial location as such they are half that of σ_c^2 , see (6.24). The covariance between the real and imaginary part at the same spatial location is zero. This results in zeros at a number of locations and the same covariances between the real and imaginary parts at two different locations. The sign difference is sometimes introduced due to the complex nature of the random variables (complex conjugate).

The covariance matrix (6.10) of A'/A and ϕ' in the CCND case can also be simplified due to the reduced degrees of freedom in (6.26)

$$\text{cov}_c(\omega_k, A'/A, \phi') = \begin{bmatrix} \sigma_{\gamma'}^2 & 0 \\ 0 & \sigma_{\gamma'}^2 \end{bmatrix}, \quad (6.27)$$

where $\sigma_{\gamma'}^2 = \sigma_{A'/A}^2 = \sigma_{\phi'}^2$. This means that the cross-correlation between A'/A and ϕ' does not need to be considered if a CCND is assumed and the definition of the derivatives (2.42) is used.

It is important that the variances of real and imaginary part are used instead of directly using the amplitude and phase per period and its corresponding variances to derive the overall amplitude and phase. The reason is that the distributions of amplitude and phase are not necessarily Gaussian. In addition, the phase can also be mapped differently in the complex plane as large error angles are added shifting the phase beyond $-\pi$ or π because of the high noise level. This would result in a totally different and thus a wrong phase average.

6.3.3 Resulting A'/A and ϕ' for AUG 17175 at $\rho_t = 0.473$ and $\rho_t = 0.484$

Here, the mean values and variances are calculated based on real measurements from ASDEX Upgrade. These are necessary to estimate χ with its corresponding confidence. In this thesis, only the procedure to estimate χ and its confidence bounds is investigated. Therefore, only the confidence at two spatial locations $\rho_t = 0.4726$ and $\rho_t = 0.4844$ for AUG 17175 are investigated. This discharge is chosen as it has many low-frequent harmonics, which thus have more harmonics with acceptable SNRs. On the other hand, the effect of non-diffusive contributions such as convectivity and damping cannot be excluded. The observation that the amplitude and phase do not describe a purely diffusion model for AUG 17175 is also made in [Mantica, 2006b]. Therefore, often in the analysis in this chapter not only the true mean values of the Fourier coefficients are used, but are sometimes replaced with known values. This not only excludes the effect of these non-diffusive terms, but also helps the interpretation of the results as the resulting diffusion coefficient is known a priori.

The mean values $\mu_{\phi'}$ and $\mu_{A'/A}$ and their covariance matrix are estimated as follows for the first harmonic ω_1 . Based on (6.19) the Fourier coefficients of the first harmonic can be calculated resulting in $\Theta(\rho_i, \omega_1) = 1.69 + 28.75i$ and $\Theta(\rho_{i+1}, \omega_1) = 2.78 + 26.77i$. The mean values $\mu_{A'/A}(\omega_1) = 5.75$ and $\mu_{\phi'}(\omega_1) = 3.77$ are calculated using (6.6). The next step is to estimate the covariance matrix using (6.21) and (6.23). This results in

$$\text{cov}(\omega_1, \Theta_{\Re}(\rho_i), \Theta_{\Re}(\rho_{i+1}), \Theta_{\Im}(\rho_i), \Theta_{\Im}(\rho_{i+1})) = \begin{bmatrix} 0.49 & 0.45 & -0.09 & -0.09 \\ 0.45 & 0.43 & -0.10 & -0.09 \\ -0.09 & -0.10 & 0.28 & 0.30 \\ -0.09 & -0.09 & 0.30 & 0.31 \end{bmatrix}. \quad (6.28)$$

This covariance matrix together with the mean values are used extensively in the next section. The corresponding covariance matrix of A'/A and ϕ' is calculated using (6.8). This gives

$$\text{cov}(\omega_1, A'/A, \phi') = \begin{bmatrix} 0.09 & 0.04 \\ 0.04 & 0.15 \end{bmatrix}, \quad (6.29)$$

k	ω_k	A'/A		ϕ'		$\phi' A'/A$	$\chi = 5$
		$\mu_{A'/A}$	$\sigma_{A'/A}^2$	$\mu_{\phi'}$	$\sigma_{\phi'}^2$	$\sigma_{\phi' A'/A}^2$	θ'
1	92.4	5.75	0.09	3.77	0.15	0.04	3.72
2	184.8	6.40	0.34	4.94	0.70	-0.11	5.27
3	277.2	8.03	1.05	5.52	1.58	-0.11	6.45
4	369.6	12.29	3.28	7.72	3.07	-0.58	7.45
5	462.0	12.55	7.68	5.95	13.90	-0.72	8.32

Table 6.1. The mean values and variances of A'/A and ϕ' at different ω_k , for time trace $t = 3.26 - 3.94$ and radial locations $\rho_t = 0.484$ and $\rho_t = 0.473$.

where the diagonal terms are the variance of phase $\sigma_{\phi'}^2$ and amplitude $\sigma_{A'/A}^2$, respectively. The off-diagonal term is the covariance denoted by $\sigma_{A'/A\phi'}^2$, which is sometimes also expressed in terms of the Pearson factor $\rho_{pearson} = 0.3356$ defined as $\rho_{pearson} = \sigma_{A'/A\phi'} / (\sigma_{\phi'} \sigma_{A'/A})$ [Martin, 2012]. This also means that it is likely that the measurements are not distributed according to a CCND as this would demand that A'/A and ϕ' are uncorrelated. Although one needs to consider that only 10 periods are used to calculate the variances, resulting in a relatively large uncertainty on the (co-)variance estimates. Nevertheless, we have chosen for this specific example to no longer assume a CCND, but to work with (6.28) and to use propagation of uncertainty and assume Gaussian approximations. In addition, the cross-correlation between different harmonics was numerically evaluated, which showed that it is reasonable to assume that independence over different harmonics.

The steps to calculate $\mu_{A'/A}(\omega_k)$, $\mu_{\phi'}(\omega_k)$, and $\text{cov}(\omega_1, A'/A, \phi')$ are repeated for the first five harmonics ω_k , which fulfill the necessary SNRs. These are presented in Table 6.1 and are extensively used in this section. If the mean values $\mu_{A'/A}(\omega_1)$ and $\mu_{\phi'}(\omega_1)$ and its corresponding variances $\sigma_{\phi'}^2$ and $\sigma_{A'/A}^2$ are compared, then it can be observed that the confidence bounds do not overlap. This indicates that the measurements cannot be described by a model with diffusivity only. Hence, this uncertainty analysis also offers a zero-order test to see if the measurements fit such a model. Such type of analysis will be further extended in Chapter 7. As here the performance of the different methods is investigated, a known value of χ is used. The first harmonic has generally the best

SNR, hence, it is a good choice for χ . As the phase is considered less sensitive to calibration errors, the phase has been chosen resulting in $\chi = 4.88$. This has been rounded to the closest integer, i.e., $\chi = 5$, to simplify the interpretation of the different figures and errors. Then, (2.28) is rewritten to express $\mu_{\phi'}$ ($\chi = 5$). This results in new means for $\mu_{\phi'}$ denoted as θ' . The difference between $\mu_{\phi'}(\omega_k)$ and the new $\theta'(\omega_k)$ are not so large. Therefore, the original variances σ_k^2 of A'/A and ϕ' are retained. These new values are also included in Table 6.1 and are used to study the estimation of χ in the next section.

6.4 Estimating χ

In this section a number of aspects of estimating χ are discussed namely: (a) how to combine A'/A and ϕ' optimally; (b) how to combine different harmonics such that the resulting estimate of χ has a small bias and high accuracy. Finally, the necessary steps to estimate χ are summarized at the end of this section.

6.4.1 Combining amplitude and phase estimates

Here, different possibilities are proposed to combine phase and amplitude. In the analysis the mean values are replaced by known values to exclude the effect of non-diffusive terms, as the interest goes out to the statistical properties. The main question of this subsection is how to estimate χ using both amplitude and phase, which can be seen as independent measurements of χ containing correlated noise.

In Section 6.3.3 it has been shown that the cross-correlation between A'/A and ϕ' is significant. This cross-correlation can be exploited to increase the accuracy of the χ estimate. Therefore, the generalized weighted mean can be used to give a resulting combination of A'/A and ϕ' with minimum variance. The Gauss–Markov theorem states that it results in minimum variance for unbiased estimators of the mean value [Cox, 2006]. This generalized weighted mean is calculated as follows

$$\mu_M = \sigma_M^2 W^T \text{cov}(A'/A, \phi')^{-1} [\mu_{A'/A}(\omega_1), \mu_{\phi'}(\omega_1)]^T, \quad (6.30)$$

and its corresponding variance is determined using

$$\sigma_M^2 = \left(W^T \text{cov}(A'/A, \phi')^{-1} W \right)^{-1} \text{ with } W = [1 \ 1]^T. \quad (6.31)$$

There are three different possibilities presented here to combine A'/A and ϕ' namely χ_{s3} in (2.29), χ_{s4} in (2.31), and the generalized weighted mean in (6.30). The product (2.32) is not included since (2.31) and (2.32) are theoretically the same for one harmonic.

The three different possibilities are compared using a Monte Carlo simulation which uses (6.28) and the mean Fourier coefficients. In a Monte Carlo simulation samples are generated from a distribution, which can be seen as possible measurements. Then, these samples are used to calculate χ using the different proposed relationships. This process is repeated many times such that the PDF of the diffusivity estimates can be generated. The analytic distributions of χ for the generalized mean and (6.18) are also presented.

Three simulations are performed for different cases:

- (a) Using the original measurement data.
- (b) A simulation where the original variances in (6.7) are retained, but the mean values in Section 6.3.3 are replaced by $\Theta(\rho_i, \omega_1) = 1.67 + 28.75i$ and $\Theta(\rho_{i+1}, \omega_1) = 2.80 + 27.42i$ such that both mean values $\mu_{A'/A}(\omega_1)$ and $\mu_{\phi'}(\omega_1)$ give $\chi = 5$ when the variance is zero.
- (c) A simulation where next to the replaced mean values also the third diagonal element of (6.7) is replaced by the first diagonal element, i.e., $\sigma_{\mathfrak{S}}^2(\rho_i) = 0.4904$ in (6.28).

Figure 6.6 shows the resulting PDFs of the diffusivity denoted by $h(\chi)$. The confidence bounds corresponding to the distributions presented in Figure 6.6 are given in Table 6.2. Figure 6.6(a) clearly shows that the distribution function $h(\chi_M)$, calculated using the weighted average (6.30), has the smallest variance. This is followed by the distribution calculated using (2.30), because unlike the product, the sum of two Gaussian distribution functions is still Gaussian before calculating the reciprocal. Therefore, the tail is shorter compared to the product distribution.

Figure 6.6(b) shows that the PDFs are almost the same since their mean values have been fixed to be the same and the covariance matrix results in an almost equal variance for both amplitude and phase (after taking cross-correlation into account). This means that there is hardly any difference between the different relationships to calculate χ . The best result is achieved using (6.30) as it has the smallest variance. This is especially clear in Figure 6.6(c). Moreover, this distribution can also be analytically calculated using the variance (6.31). This is also supported by the confidence bounds in Table 6.2. Again, looking at the confidence bounds in Table 6.2 it shows that the sum performs better than the product. However, the product of $\phi'A'/A$ excludes the effect of damping. Therefore, also the analytical approximation of $h(\chi(\mu_p))$ is shown in Figure 6.6, which matches quite well, but also shows some errors. On the other hand, the analytic approximation of $h(\chi(\mu_M))$ matches perfectly.

Summarizing, the generalized weighted mean gives the best result, which is consistent with theoretical predictions.

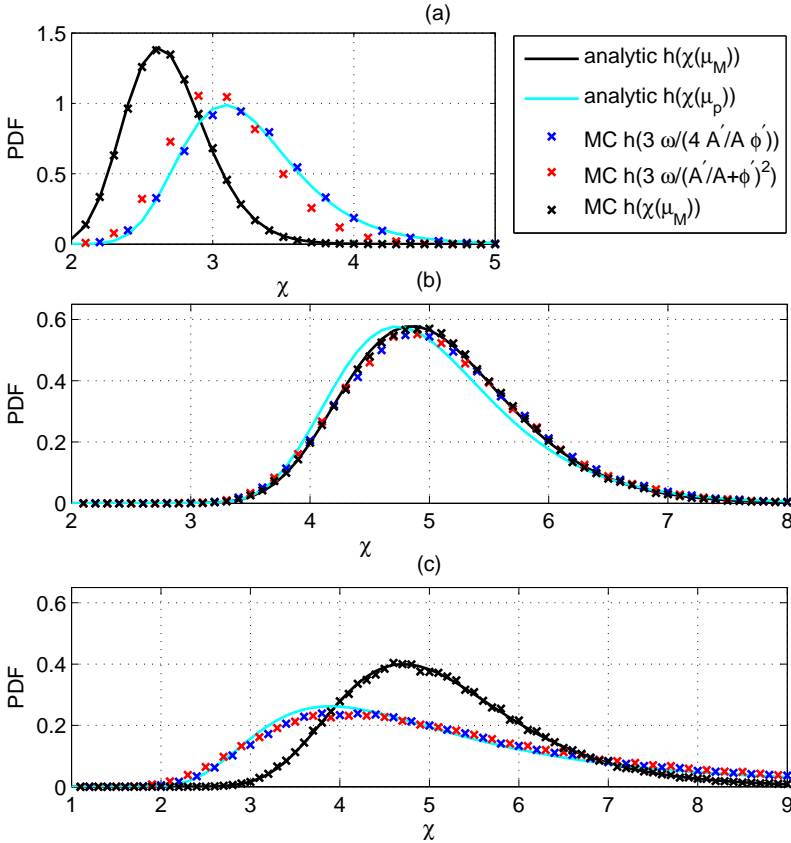


Figure 6.6. Normalized histograms (PDFs) for the proposed calculation methods to combine phase and amplitude, i.e., (2.31) represented by (blue) \times , (2.30) represented by (red) \times , and (6.32) using (black) \times . The distributions are generated using a Monte Carlo simulation (MC). The analytic approximations of the distribution functions $h(\chi(\mu_M))$ and $h(\chi(\mu_p))$ are presented using a black and cyan line, respectively. These distributions are solely based on analytical calculations using (6.32) to find μ_M with corresponding σ_M^2 and (6.11) to calculate the PDF of χ , i.e., $h(\chi(\mu_M))$. In the product case, (6.15) and (6.16) are used to calculate μ_p and σ_p^2 , which are used in (6.18) to calculate $h(\chi(\mu_p))$. Three simulations are presented: (a) using the original mean value and variance; (b) using the corrected mean values, but the original covariance matrix; (c) using the corrected mean value and a different covariance matrix.

Confidence bounds	Fig. 6.6(a)			Fig. 6.6(c)		
	2.5%	χ	97.5%	2.5%	χ	97.5%
$\chi_{MC} = \frac{3\omega}{4\phi'A'/A}$	2.50	3.20	4.19	2.66	5.00	17.82
$\chi_{anal}(\mu_p, \sigma_p^2)$	2.54	3.19	4.29	2.67	4.89	19.20
$\chi_{MC} = \frac{3\omega}{(\phi'+A'/A)^2}$	2.43	3.06	3.89	2.57	5.00	14.12
$\chi_{MC} = \frac{3\omega}{4\mu_M^2}$	2.16	2.68	3.30	3.43	5.00	7.84
$\chi_{anal}(\mu_M, \sigma_M^2)$	2.17	2.68	3.33	3.44	5.00	7.88

Table 6.2. The numerically determined central interval confidence bounds for the diffusivity χ_{MC} based on a Monte Carlo simulations (MC) for the different methods to combine phase and amplitude. In addition, the analytically calculated confidence bounds for the generalized weighted mean method $\chi_{anal}(\mu_M, \sigma_M^2)$ and the product approximation $\chi_{anal}(\mu_p, \sigma_p^2)$ are presented as well. The results are presented for the measurements (left) and using the adjusted Fourier coefficients in combination with the adjusted covariance matrix (right). Note that the χ value is calculated using the corresponding equations and are not based on the Monte Carlo analysis.

6.4.2 Combining different harmonics for ϕ' and A'/A only

In this section, methods are discussed to combine different harmonics. They are presented on the basis of the phase derivative distribution only because the replaced means $\theta'(\omega_k)$ are used to exclude the effect of non-diffusive terms. The calculations are based on the values presented in Table 6.1.

Different combining methods are compared here using a Monte Carlo simulation, which is based on samples from five Gaussian distributions with mean values $\mu_{\phi'}(\omega_k)$ and variances $\sigma_{\phi'}^2(\omega_k)$. The simplest method of combining different harmonics is by averaging the diffusivity estimates calculated for every harmonic, i.e., $E\{\chi\}$. The resulting PDF of χ is then denoted by $h(E\{\chi\})$ and it is presented in Figure 6.7 with (blue) crosses. The resulting PDF of χ is non-symmetric and has a long tail. The reason is that $h(E\{\chi\})$ is the result of averaging five PDFs of $\chi(\omega_k)$, which are distributed according to (6.11). These individual PDFs of $\chi(\omega_k)$ already have a long tail and contain a bias. This bias depends on the individual variances $\sigma_{\phi'}^2(\omega_k)$. This tail and bias are the result of taking the squared reciprocal of the phase derivative and are retained when

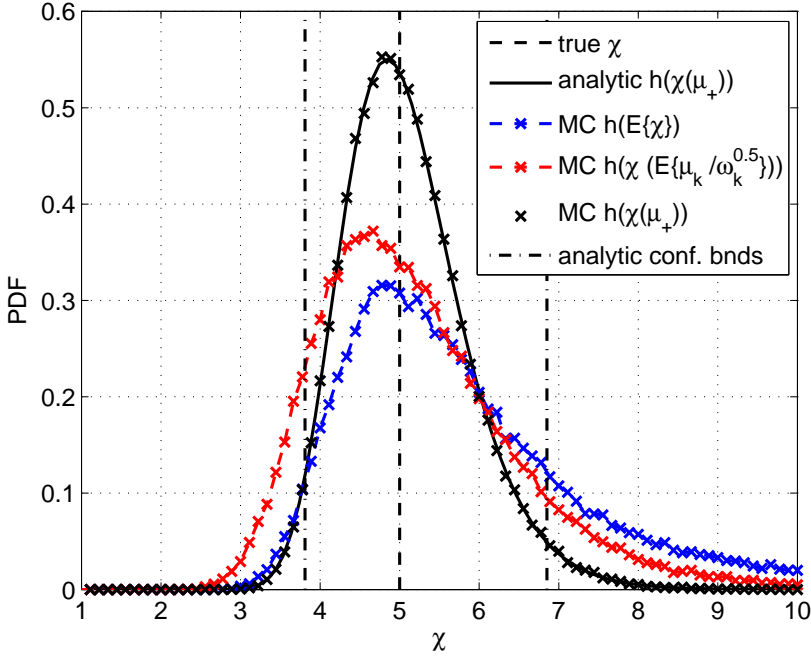


Figure 6.7. Normalized histograms (PDFs) for the three proposed calculation methods to calculate χ from either phase (or amplitude) using multiple harmonics generated using a Monte Carlo simulation (MC). The PDF $h(E\{\chi\})$ represented by (blue) \times is calculated using the mean value of the different χ 's of the different harmonics. The PDF $h(\chi(E\{\mu_k/\sqrt{\omega_k}\}))$ represented by (red) \times gives the PDF of χ using the weighted average of the phase derivatives using only the weighting $\sqrt{\omega_k}$. The PDF $h(\chi(\mu_+))$ is represented by \times , where a weighted average in (6.32) is used to calculate χ . In addition, the theoretically determined PDF $h(\chi(E\{\mu_+\}, E\{\sigma_+^2\}))$ based on the mean value of μ_+ and the mean value of σ_+^2 is presented. The true value of χ is presented (dashed) and the 95% confidence interval for $h(\chi(\mu_+))$ is presented by the dashed-dotted vertical lines (left 2.5% and right 97.5%), which are calculated analytically.

averaging these estimates.

A better option is to directly average the phase derivatives because their distributions are approximately Gaussian, see Figure 6.2. However, the diffusivity does not only depend on ϕ' , but also on the frequency ω in (2.28). Therefore, the Gaussian distributions can only be averaged if they are first weighted with the frequencies, i.e., $\mu_{\phi'}(\omega_k)/\sqrt{\omega_k}$ and $\sigma_{\phi'}^2(\omega_k)/\omega_k$. Then, a new Gaussian distribution is found, which is used to calculate the resulting PDF of χ . This PDF is denoted by $h(\chi(E\{\mu_{\phi'}(\omega_k)/\sqrt{\omega_k}\}))$. In this case, the resulting distribution can be determined analytically by calculating the new mean value and variance of the combined Gaussian distribution and then using (6.11) again. This, PDF based on weighting with $\sqrt{\omega_k}$ can also be determined using Monte Carlo simulations, which is shown in Figure 6.7 using (red) \times .

It is clear that the side tail is still present, but has become smaller. The diffusivity has become more certain due to the smaller side tail, but the uncertainty region has shifted to the left. However, this method does not take the uncertainty on ϕ' into account. This means that there is no difference between estimates of the phase derivative with small variance compared to phase derivatives with high variance. In other words, the uncertain higher harmonics contaminate the harmonics with high SNR close to the ground harmonic in the diffusivity estimates. Consequently, the diffusivity estimate can be improved by taking the variance of the different harmonics into account, which have been estimated from the periodic measurements. This results in the weighted mean, which also includes a weighting with $\sqrt{\omega_k}$, i.e.,

$$\mu_+ = \frac{\sum_{k=1}^K w_k \mu_k \omega_k^{-0.5}}{\sum_{k=1}^K w_k} \quad \text{with } w_k = \frac{\omega_k}{\sigma_k^2}, \quad (6.32)$$

where $\mu_k = \mu(\omega_k)$. This equation (6.32) is also applicable to the amplitude. This type of weighting gives the Maximum Likelihood Estimate of the mean value for Gaussian distributed variables [Martin, 2012], which has the smallest variance when combining a number of independent Gaussian distributions. The resulting PDF of χ using the weighted average, $h(\chi(\mu_+))$ is presented in Figure 6.7 using black \times . The tail of this distribution has been reduced significantly such that the diffusivity estimate has become more certain. The use of the weighted mean gives the best result for the compared methods in this section and should be used to combine the different harmonics in case of a purely diffusive model.

The distribution $h(\chi(\mu_+))$ can also be determined analytically by calculating the variance σ_+^2

$$\sigma_+^2 = \frac{1}{K-1} \frac{\sum_{k=1}^K w_k (\mu_k \omega_k^{-0.5} - \mu_+)^2}{\sum_{k=1}^K w_k}, \quad (6.33)$$

taking into account that σ_+^2 is an estimate [Martin, 2012]. The confidence bounds are calculated by setting the mean value $\mu_\gamma = \mu_+$, the variance $\sigma_\gamma^2 = \sigma_+^2$, and

Confidence bounds	2.5%	χ	97.5%
$\chi_{MC} (E \{\chi\})$	3.73	6.37	45.09
$\chi_{MC} (E \{\mu_k / \sqrt{\omega_k}\})$	3.32	6.02	8.32
$\chi_{MC} (\mu_+)$	3.81	5.11	6.84
$\chi_{anal} (E \{\mu_+\}, E \{\sigma_+^2\})$	3.81	5.11	6.84

Table 6.3. The central interval confidence bounds for χ_{MC} using the different combination methods based on a Monte Carlo simulations (MC). In addition, the analytically calculated confidence bounds for the weighted mean method χ_{anal} .

$\omega = 1$ in (6.14). They can also be used to calculate the analytic PDF, which is plotted in Figure 6.7. The analytic PDF (solid black line) is the same as the PDF constructed using the Monte Carlo simulations.

A comparison of the different combination methods can also be made using the confidence bounds, which are numerically determined from the Monte Carlo simulations. These confidence bounds are summarized in Table 6.3. It again shows that the weighted mean gives the best result and that in this case the accuracy of the combined diffusivity estimate is increased 13 times compared to averaging the individual diffusivities estimate. Note that the diffusivity estimate still has a tailed distribution, which is caused by the method of calculation, i.e., taking the squared inverse.

For the experimental data using both amplitude and phase (no damping), the resulting mean value and variance are $\mu_+ = 0.48$ and $\sigma_+^2 = 5.93 \cdot 10^{-4}$ based on the first five frequencies. This is smaller than any of the individual (frequency weighted) variances. The corresponding diffusivity is $\chi = 3.29$ with the 95% confidence bounds $\chi_{min} = 2.72$ and $\chi_{max} = 4.06$. The confidence bounds are larger than that of the first harmonic in absolute sense. This is a consequence of the non-linear dependence of the confidence bounds on the mean value.

6.4.3 Combining different harmonics using the product $\phi' A' / A$

In section 6.4.2, we have established, that for a purely diffusive model, the combination of A' / A and ϕ' using the generalized weighted mean gives the best result. For the combination of different harmonics, the weighted mean results in the χ estimate with the smallest variance for the methods compared in this

chapter.

If no longer a purely diffusive model is assumed, but also the damping needs to be included, then we could use for instance (2.31) in slab geometry. Therefore, we investigate how to reduce the uncertainty using (2.31) and the re-expressed form (2.32) to estimate χ .

The product $\phi' A' / A$ is used to exclude the effect of damping, as the amplitude and phase can no longer be used to reduce the uncertainty using the generalized mean. In principle, one harmonic would suffice to estimate the damping. The estimated damping could then potentially be used in the weighting process. However, such a weighting is difficult to apply in the direct calculations of χ . Instead, the product is applied for every harmonic. This means that for five harmonics, four degrees of freedom are ignored, which potentially could be used to reduce the uncertainty. An optimal method to estimate also the damping is introduced in Chapter 7. Here, it is chosen to disregard this loss in optimality and try to combine the different harmonics based on (2.31) and (2.32). Therefore, the original measurement values from Table 6.1 are used again. Again, three possibilities are compared using a Monte Carlo simulation based $\mu_{A'/A}(\omega_k)$, $\mu_{\phi'}(\omega_k)$, and $\text{cov}(\omega_k, A'/A, \phi')$:

1. The simple average of the χ estimates per harmonic using (2.31).
2. The weighted average of $\phi' A' / A$ taking only ω_k into account.
3. The weighted average using the Gaussian approximations with mean value (6.15) and variance (6.16) taking both ω_k and $\text{cov}(\omega_k, A'/A, \phi')$ into account.

The product of $\phi' A' / A$ is used, thus a weighting with ω_k is necessary instead of $\sqrt{\omega_k}$ in (6.32) as now (2.31) is used instead of (2.28). Consequently, (6.32) and (6.33) become for the weighted mean of the product

$$\mu_{mp} = \frac{\sum_{k=1}^K w_k \mu_p(\omega_k) / \omega_k}{\sum_{k=1}^K w_k} \text{ with } w_k = \frac{\omega_k^2}{\sigma_k^2}, \quad (6.34)$$

and

$$\sigma_{mp}^2 = \frac{1}{K-1} \frac{\sum_{k=1}^K w_k (\mu_p(\omega_k) / \omega_k - \mu_{mp})^2}{\sum_{k=1}^K w_k}, \quad (6.35)$$

where the mean of the product μ_p and its corresponding variance σ_p^2 are defined in (6.15) and (6.16). The samples used in the Monte Carlo analysis are generated from the mean values and covariance matrices in Table 6.1. The three proposed techniques are applied to these samples to analyze the difference again. In addition, the analytic Gaussian approximation is calculated by substituting μ_{mp} and σ_{mp} into (6.18) ($\omega = 1$). The results are presented in Figure 6.8. The corresponding confidence bounds are presented in Table 6.4. The results are

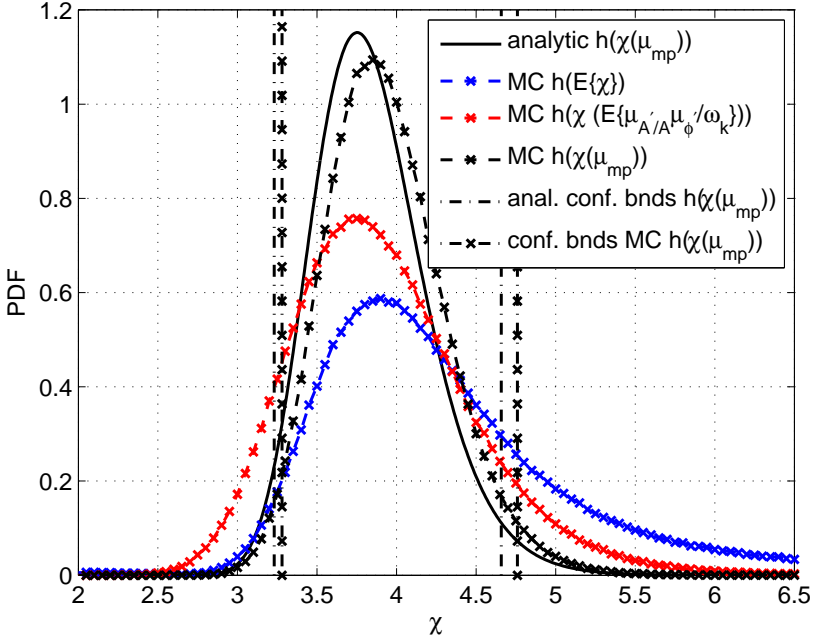


Figure 6.8. Normalized histograms (PDFs) for the three proposed calculation methods to calculate χ from either phase (or amplitude) using multiple harmonics generated using a Monte Carlo simulation (MC). The PDF $h(E\{\chi\})$ represented by (blue) \times is calculated using the mean value of the different χ 's of the different harmonics. The PDF $h(\chi(E\{\mu_{\phi'}(\omega_k)\mu_{A'/A}(\omega_k)/\omega_k\}))$ represented by (red) \times gives the PDF of χ using only ω_k in the weighted average. The PDF (MC) $h(\chi(\mu_{mp}))$ is represented by \times , where a weighted average in (6.34) is used to calculate χ . In addition, the theoretically determined PDF $h(\chi(\mu_{mp}))$ based on the mean value of μ_{mp} and the mean value of σ_{mp}^2 is presented. The 95% confidence intervals (left 2.5% and right 97.5%) are presented using dashed-dotted lines for the analytical approximation based on $h(\chi(\mu_{mp}, \sigma_{mp}^2))$ and are presented using dashed-dotted lines with \times for (MC) $h(\chi(\mu_{mp}))$. The latter is based on numerical calculations.

Confidence bounds	2.5%	χ	97.5%
$\chi_{MC}(E\{\chi\})$	-2.07	3.97	11.26
$\chi_{MC}(E\{\mu_{\phi'}\mu_{A'/A}/\omega_k\})$	3.97	3.81	5.23
$\chi_{MC}(\mu_{mp})$	3.28	3.82	4.76
$\chi_{anal}(\mu_{mp}, \sigma_{mp})$	3.23	3.82	4.66

Table 6.4. The central interval confidence bounds belonging to the lines in Figure 6.8. The bounds based on Monte Carlo simulations χ_{MC} are calculated numerically. In addition, the analytically calculated confidence bounds for the weighted mean method $\chi_{anal}(\mu_{mp}, \sigma_{mp})$ are presented.

similar to that in Section 6.4.2. Taking simply the average results in a long tail distribution function. This also implies that the use of (2.32) should be avoided if more harmonics are combined. Another interesting aspect is that the lower bound is negative. This is physically not possible, but results from the fact that the product $\phi'A'/A$ can become negative.

The averaging of long tail distributions can be avoided by averaging first the product $\mu_{\phi'}(\omega_k)\mu_{A'/A}(\omega_k)$ over the harmonics using the weight ω_k , this average is then used to calculate the overall diffusivity. This increases the confidence on the estimate, which does not require any knowledge of the noise variances. The confidence is further increased using the weighting that also includes the variances.

The analytic calculation is clearly different from the one generated by the Monte Carlo analysis due to the Gaussian approximations used. If the error in terms of confidence bounds is considered, then it is clear that the lower bound is over estimated and the upper bound is under estimated. The reason is that the product of $\phi'A'/A$ is skewed with a tail to the right, which is not captured by the Gaussian approximation. However, the difference between the confidence bounds of the analytic calculation and the Monte Carlo analysis is small. This means that this method can be used to estimate χ and its confidence bounds. However, if the skewness of $\phi'A'/A$ is large the calculated confidence bounds deviate significantly from the true confidence bounds.

We have chosen to use the moment generating function (Section 6.2.3) instead of a Taylor expansion (Section 6.1.4) to approximate the mean value and the variance for the product $\phi'A'/A$. The advantage of this approach over the Taylor expansion approach is that the confidence bounds found are smaller than that of the Taylor expansion both numerically for the Monte Carlo analysis as analyti-

cally. In addition, the distribution function, thus also the confidence bounds, is better approximated using (6.18) when different harmonics are combined using the moment generating function. On the other hand, (6.15) introduces an error on the mean (bias term: $\sigma_{A'/A\phi'}^2$). Hence, for a better estimate of the mean value it is sometimes desirable to use the Taylor expansion instead.

6.4.4 Calibration errors

Measurements can also be prone to calibration errors. These errors cannot be quantified by studying the perturbative measurements. They are constant for the entire time trace, otherwise the error would increase the variance. However, they can influence the uncertainty of the parameter estimation.

The amplitude errors can be modeled by introducing scaling factors α and β , that describe the calibration error in the measured amplitude \hat{A} , such that $\hat{A}_1 = \alpha A_1$ and $\hat{A}_2 = \beta A_2$. Note that the calibration error influences only the gain and is assumed to be constant for all frequencies. By applying a weighted average similar to (6.32) for the amplitude measurements, an overall \hat{A}_1 or \hat{A}_2 can be determined. The new amplitude with calibration error can then be substituted in (2.29) giving

$$\chi = \frac{3}{4}\omega \left(\ln \left(\alpha \hat{A}_2 / \beta \hat{A}_1 \right) / \Delta\rho \right)^{-2}, \quad (6.36)$$

and rewriting yields

$$\chi = \frac{3\omega}{4\Delta\rho^2} \left(\ln(\alpha/\beta) + \ln \left(\hat{A}_2 / \hat{A}_1 \right) \right)^{-2}. \quad (6.37)$$

The resulting uncertainty on χ depends on the ratio of α and β . If α and β are stochastic, in the sense that they can be presented by a distribution independent of time, and $\ln(\alpha/\beta)$ can be approximated by a Gaussian an extension is possible. However, if $\ln(\alpha/\beta)$ cannot be approximated well by a Gaussian, the calculation becomes more complicated and probably numerical tools are necessary, e.g., Monte Carlo analysis. Note that in practice it can be even more cumbersome due to possible correlations between α and β . On the other hand, if the calibration errors α and β are the same for both radial locations, then the calibration error vanishes.

Commonly, it is presumed that the phase ϕ is insensitive to calibration errors. Although this is true for the mean value, it is not true if ϕ is treated as being stochastic. The reason is that the variance of the phase depends on the amplitude in (6.5), which is a direct consequence of the fact that amplitude and phase are correlated quantities. This can be understood if one considers Figure 6.1 again, but with varying amplitude M as a result of calibration errors.

Figure 6.9 clearly shows that in case of a calibration error also the uncertainty on the phase is different. The difference depends on the mean value of the

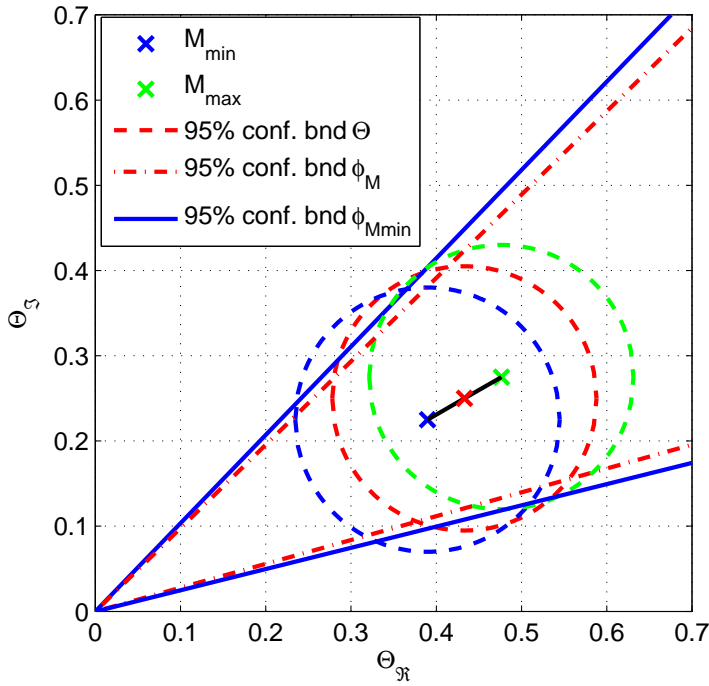


Figure 6.9. Circular confidence bounds for $M = 0.5$ and $\theta = \pi/6$, and the new circular confidence bounds for amplitude errors of 10%, i.e., $M_{min} = 0.45$ (blue) and $M_{max} = 0.55$ (green). In addition, the phase confidence bounds are presented for M and M_{min} only, which clearly shows that if M is smaller due to a calibration error, i.e., M_{min} , the uncertainty on the phase increases, which is expressed through the broader confidence bounds.

amplitude and the variance. However, considering uncertainty on the variance is rather cumbersome. Therefore, in practice, it is easier to replace the mean value M by the minimal possible M_{min} due to calibration errors, which gives a conservative confidence bound on ϕ .

Although the effect of calibration errors can be significant, due to its analytical complexity, it will not be further considered in this thesis.

6.4.5 Summary estimating χ with confidence

Here, a summary is given of the necessary steps to calculate the overall diffusivities:

1. First, calculate the mean value and covariance matrices of the different excited frequencies ω_k .
2. Calculate the phase and amplitudes and determine if they can be approximated by Gaussian distributions ($\text{SNR} > 5$).
3. Determine the mean values $\mu_{A'/A'}(\omega_k)$ and $\mu_{\phi'}(\omega_k)$ and the covariance matrix $\text{cov}(A'/A, \phi')$ for every harmonic using the Jacobian, which is described in Section 6.1.4.
4. Make a distinction between (a) $(\phi')^2$ and $(A'/A)^2$ and (b) the product of $\phi'A'/A$ (including cylindrical approximation).

(a) Case: $(\phi')^2$ and $(A'/A)^2$

- i. Calculate the generalized weighted mean for every harmonic using (6.30) and its variance using (6.31). If phase and amplitude are analyzed separately, then skip this step.
- ii. Combine the different mean values $\mu_M(\omega_k)$ and the variances $\sigma_M^2(\omega_k)$ to determine μ_+ and its variance σ_+^2 using (6.32) and (6.33).
- iii. Calculate the overall diffusivity

$$\chi = \frac{3}{4} \mu_+^{-2}. \quad (6.38)$$

- iv. The corresponding confidence bounds are calculated by replacing $\mu_\gamma = \mu_+$, $\sigma_\gamma^2 = \sigma_+^2$, and $\omega = 1$ in (6.14) and determine the confidence bounds using the CDF.

(b) Case: the product of $\phi'A'/A$ or $\phi'A'/A + 1/(2\rho)$

- i. Approximate mean values and variances using the moment generating function for every harmonic.
- ii. Combine the different mean values $\mu_p(\omega_k)$ and variances $\sigma_p^2(\omega_k)$ using (6.34), but with weighting ω_k instead of $\sqrt{\omega_k}$ to determine μ_{mp} and its variance σ_{mp}^2 using (6.35).
- iii. Calculate the overall diffusivity

$$\chi = \frac{3}{4} \frac{1}{\mu_{mp}}. \quad (6.39)$$

- iv. The corresponding confidence bounds are calculated by substituting μ_{mp} , σ_{mp}^2 , and $\omega = 1$ in (6.18) and determining the CDF, which is acquired by numerically integrating (6.18).

In practice, the diffusivity is often rescaled in terms of SI units. The confidence bounds should also be rescaled accordingly.

6.5 Conclusions and discussion

In this chapter, the effect of uncertainty on the estimates of the diffusivity is studied. The properties of ECE-measurements and of the Fourier transform are used to determine the noise distribution of the Fourier coefficients. It is assumed that the spatial derivatives of amplitude and phase are well approximated by Gaussian distributions for large SNRs. In this case the diffusivity is distributed according to the inverse non-central chi-squared distribution when the relationships in (2.28) and (2.29) are used. Its analytically derived CDF is used to determine the confidence bounds on the diffusivity, i.e., its accuracy.

Different methods to combine harmonics, amplitude, and phase are compared based on the distributions of χ and its confidence bounds. The (generalized) weighted mean gives the resulting Gaussian distribution with the smallest variance for the results presented here. In case the diffusivity is calculated using a relationship containing the product of phase and amplitude derivatives, the corresponding distribution function is approximated, which introduces some errors.

The weighted average outperforms other methods commonly used to combine different harmonics, amplitudes, and phases. Moreover, it gives an estimate of the variance, which is necessary to determine the confidence bounds on χ . In addition, the direct diffusivity estimate based on the ASDEX Upgrade data of the first harmonic already shows a near Gaussian distribution, which is an indication that it is close to the optimal solution in this specific case. However, many issues arise from using amplitude and phase to determine the diffusivity directly. Taking the squared reciprocal of Gaussian distributed variables always gives a distribution with a long tail and hence a high upper uncertainty. This effect becomes much larger when the variances increase. Therefore, relationships based on inverting Gaussian distributed variables, as, e.g., the phase and amplitude, should be avoided for an optimal estimate of χ and the other transport coefficients. This also holds for the relationships derived in Chapters 3, 4, and 5 because they have more complicated combinations of the spatial derivatives of amplitude and phase. A better alternative is to determine the diffusivity and the other transport coefficients using an implicit estimation scheme. In the next chapter such an implicit method is developed based on Maximum Likelihood Estimation in the frequency domain, which allows estimates of the transport coefficients with near minimum variance given the assumptions.

Frequency domain sample maximum likelihood estimation for spatially dependent parameter estimation in PDEs

7.1 Introduction

In the previous chapters methods have been introduced to directly calculate the transport coefficients based on the amplitude and phase. However, it is also shown that approximations need to be made, the derivatives need to be estimated, and non-optimal combination methods for the different harmonics are necessary. Therefore, in this chapter a new method based on sample Maximum Likelihood Estimation is introduced. This method allows the use of more complicated models, to estimate the transport coefficients close to minimum variance, and is directly based on the measurements instead of the derivatives. A disadvantage of the method presented here is that the calculation is based on the minimization of a cost-function and thus an iterative optimization algorithm is necessary.

The proposed method is also closely related to a number of system identification methods and it is well situated in (more general) identification of infinite

This chapter is based on the following articles:

van Berkel, M., et al. [2014]. Frequency domain sample maximum likelihood estimation for spatially dependent parameter estimation in PDEs, *Automatica* **50**(8): 2113 – 2119.

van Berkel, M., et al. [2013]. Maximum likelihood estimation of diffusion and convection in tokamaks using infinite domains, *IEEE Multi-conference on Systems and Control*, pp. 1230–1234.

dimensional systems or Distributed Parameter Systems (DPS) literature. Therefore, this chapter gives many references to the literature in these fields and uses also the terminology standard in these fields.

A good overview of the parameter estimation problems discussed in the DPS literature is given in the monograph by Banks and Kunisch [Banks, 1989], and references therein. In addition, different methodologies exist to identify spatially varying parameters in PDEs [Kravaris, 1985], of which a number focus specifically on parabolic PDEs [Banks, 1985; Kunisch, 1991; Mochi, 1999]. Their emphasis is on the regularization of the least-squares cost-function used to estimate the parameters, on the well-posedness in Hadamard's sense, i.e., guaranteeing of the existence of its solution, and on the uniqueness of the solution and its stability with respect to the measurement data [Vogel, 2002]. In addition, regularization is often used to make the optimization problems convex and to constrain the solution in some sense [Ito, 2008]. Moreover, different methods for reducing the infinite dimensional PDEs to finite dimension exist and are discussed in the above mentioned references. Generally, they are using some discretization of the spatial coordinate [Heath, 1997; Smith, 1985] or basis functions [Banks, 1983; Canuto, 1988].

A different approach to estimate the parameters is to solve the problem in the frequency domain via the Laplace Transform [Curtain, 1995]. This reduces the PDE to a parameterized Ordinary Differential Equation (ODE). These ODEs can be approximated or sometimes even be solved analytically, thereby avoiding approximation errors. The solutions are generally non-rational or fractional functions [Curtain, 2009], of which the parameters can be identified using frequency domain identification techniques [Gabano, 2011; Jalloul, 2011; Pintelon, 2005; Valério, 2007]. The disadvantage of this approach is that the non-rational form of the function can complicate the identification significantly. On the other hand, the use of periodic excitations enables the removal of the unexcited noisy frequency lines from the measured data, hence high Signal to Noise Ratios (SNR) can be obtained at the excited frequency lines by averaging the signals over consecutive periods. In addition, it is no longer required to use rational approximations in the frequency domain, making the identification easier.

We again consider the following second order parabolic PDE with spatially varying parameters on a one-dimensional spatial domain

$$\frac{\partial T}{\partial t} = f_x(\rho, \theta) \frac{\partial^2 T}{\partial \rho^2} + f_V(\rho, \theta) \frac{\partial T}{\partial \rho} + f_\tau(\rho, \theta) T + P(\rho, t), \quad (7.1)$$

which is a generalized form of (2.8). We assume that the functions $f_x(\rho, \theta)$, $f_V(\rho, \theta)$, and $f_\tau(\rho, \theta)$ depend on the unknown transport coefficients (parameters) θ , which we want to identify.

As in the previous chapters, it is assumed that the initial conditions are unknown. Hence, only measurements are considered for "t \gg the dominant time constant" such that the transients are negligible compared to the forced

response. The heat source term periodically excites the plasma and is defined as

$$P(\rho, t) = \begin{cases} p(\rho) \sum_{k=1}^K A_k \cos(\omega_k t + \phi_k) & \rho_1 \leq \rho \leq \rho_2 \\ 0 & \textit{elsewhere}, \end{cases} \quad (7.2)$$

where A_k , ϕ_k , and ω_k are the amplitude, phase, and frequency, respectively. The spatial dependence of the source $p(\rho)$ is unknown, but $p(\rho) \neq 0$. In addition, we assume that the temperature measurements are distributed according to a CCND in the frequency domain (see Chapter 6).

The estimation of parameters from noisy measurements only is known as an Errors-in-Variables problem (EIV). In the EIV literature it is well known that the least-squares estimator is not consistent [Söderström, 2007], i.e., the parameter estimates will be biased. Moreover, this bias depends on the SNR, which decreases with the distance to the source $P(\rho, t)$. This is caused by the low-pass characteristic of (7.1), which also causes the higher frequencies to contain more noise than the lower frequencies. This problem can be partly overcome using a low-pass filter to suppress the noisy “high-frequency” components in the measurements when using time-domain estimators [Söderström, 1999]. However, the optimal cut-off frequency of this filter depends on the unknown system parameters.

This chapter presents a frequency domain sample Maximum Likelihood Estimator (SMLE) for this EIV problem. The SMLE is based on the Probability Density Function of the noise, allowing for a consistent estimate under weak assumptions [Pintelon, 2012]. Moreover, it naturally weights the different frequency components avoiding the necessity of a low-pass filter. In the SMLE framework, the confidence bounds on the estimated parameters can be calculated and model validation tests exist. However, the SMLE requires knowledge about noise properties of the measurements. Compared to other methods in the EIV, a disadvantage of the SMLE is that its optimization is a non-linear least-squares problem, which is no longer convex in contrast to linear least-squares estimators.

The SMLE will be used to estimate a set of small sub-domains, instead of modeling the entire domain or working with the spatial derivatives A'/A and ϕ' . On each sub-domain again a complex valued non-rational analytic model description is used such that discretization errors can be avoided in comparison to numerical schemes [Bhikaji, 2001]. The advantage of this approach is that the decoupling in sub-domains assures that errors do not propagate from one sub-domain to the others. In addition, the SMLE optimization problem remains solvable, because only a few parameters need to be estimated.

In this chapter, two approaches are discussed for the choice of models on this sub-domains. The SMLE can be used in combination with the transfer functions derived in (2.36), (2.37), and (2.52). The advantage of this choice is that only

two spatial points need to be used for every domain giving the most local domain on which the parameters are estimated. In addition, the resulting models that need to be estimated are Single-Input Single-Output, which makes the analysis and estimation simpler. On the other hand, a semi-infinite domain or symmetry boundary condition is assumed, which is a simplification of the real boundary condition and the transport coefficients are assumed constant up to $\rho = \infty$ or up to the center at $\rho = 0$ (see Section 2.3 and Section 2.4). Therefore, this chapter also introduces a second approach based on measurement points only, without making assumptions on the boundary conditions. This does not mean that (7.1) does not have boundary conditions at the ends of the entire domain. This would imply that it does not have a unique solution. It means that the boundary conditions are unknown and as such we make no assumptions about them. Consequently, the smallest sub-domain that can be defined needs to contain at least three measurement points. The reason is that two measurements act as the boundary conditions (inputs) as such defining the solution of the second order PDE. At least one measurement point between the boundaries (output) is necessary to compare it with the solution of the PDE at that location. This solution is determined by the parameters, the model structure, and the real boundary conditions. In principle the number of measurements can be extended, but then a Multiple-Input Multiple-Output system needs to be identified. Therefore, in this chapter we limit the discussion to three adjacent measurements to define a sub-domain. Note that we again only consider sub-domains that are outside the interval $[\rho_1, \rho_2]$, i.e., domains that do not contain an excitation source $p(\rho)$ (see (7.1) and (7.2)). The reason is that the exact dependency of $p(\rho)$ on ρ is unknown (see Section 2.1).

A general framework for different spatial dependencies and geometries is discussed, but results are only shown for sub-domains on which parameters can be modeled as constants. Consequently, only piecewise smooth profiles are identifiable.

An implicit identification scheme consists of the following three components: a model of the system, derived in Section 7.2; a cost function minimization scheme based on a realistic noise model, explained in Section 7.3; and simulation data which is generated by means of a finite difference model such that the result can be validated. The latter is discussed in Section 7.4. Finally, a number of conclusions are summarized and discussed.

7.2 Modeling

This section derives the transfer functions based on a smart choice of the boundary conditions. The most important concept is the replacement of boundary conditions by measurements. In addition, derivations are done without specifying any spatial dependency.

7.2.1 Considered partial differential equation

This subsection is a small repetition of Chapter 2, but considering a more generalized form of the PDEs under consideration. It considers the homogeneous form of (7.1) outside the source domain, where the localized source $P(\rho, t)$ perturbs (excites) the plasma. It is possible to solve the inhomogeneous PDE, allowing the use of a domain with a source. However, the inhomogeneous PDE results in a more complex relationships and will not be discussed in this thesis.

The Laplace transform of (7.1) simplifies the PDE towards a complex valued Ordinary Differential Equation (ODE) of the form

$$0 = f_{\chi}(\rho, \theta) \frac{d^2 \Theta}{d\rho^2} + f_V(\rho, \theta) \frac{d\Theta}{d\rho} + (f_{\tau}(\rho, \theta) - s) \Theta, \quad (7.3)$$

with $\Theta = \mathcal{L}\{T\}$ and the Laplace variable $s = i\omega$. The functions $f_{\chi}(\rho, \theta)$, $f_V(\rho, \theta)$, and $f_{\tau}(\rho, \theta)$ depend on the spatial coordinate ρ and the time-invariant, unknown parameters, θ . In many cases this ODE can be solved analytically, with the general solution given by

$$\Theta(\rho, s) = E_1(s) \xi(\rho, \theta, s) + E_2(s) \zeta(\rho, \theta, s), \quad (7.4)$$

where $E_1(s)$ and $E_2(s)$ denote the free variables set by the boundary conditions for which two specific cases are described in Section 2.2. The choice of the spatially dependent functions $f_{\chi}(\rho, \theta)$, $f_V(\rho, \theta)$, and $f_{\tau}(\rho, \theta)$ in (7.3) determine the solutions $\xi(\rho, \theta, s)$ and $\zeta(\rho, \theta, s)$, which are the complex eigenfunctions of (7.3). Solutions for many different choices of $f_{\chi}(\rho, \theta)$, $f_V(\rho, \theta)$ and $f_{\tau}(\rho, \theta)$ exist, such as constant, and linear functions. An extended list of these analytic solutions can be found in Appendix A and [Polyanin, 2003]. The next step is to derive the local transfer functions.

7.2.2 Local domain based on two measurements

In Chapter 2 the semi-infinite domain and the symmetric domain has been introduced. This results in transfer function descriptions based on two measurement points. For semi-infinite domains the transfer functions have been derived in (2.36), (2.37), and (2.38)

$$\Theta(\rho_{i+1}) = \frac{\xi(\rho_{i+1})}{\xi(\rho_i)} \Theta(\rho_i) \quad (7.5)$$

and for symmetric domains in (2.52) and (2.53)

$$\Theta(\rho_{i+1}) = \frac{\zeta(\rho_{i+1})}{\zeta(\rho_i)} \Theta(\rho_i). \quad (7.6)$$

These relationships can also be expressed in terms of a Single-Input Single-Output system of the form

$$Y(s) = G_1(\theta, s) U_1(s), \quad (7.7)$$

where $Y(s) = \Theta(\rho_{i+1})$, $U_1(s) = \Theta(\rho_i)$, and G_1 is either $\xi(\rho_{i+1})/\xi(\rho_i)$ or $\zeta(\rho_{i+1})/\zeta(\rho_i)$.

In the rest of this chapter the description of the algorithm is based on two transfer functions. The here used description can still be used by choosing $G_2(\theta, s) = 0$.

7.2.3 Local domain based on three measurements

Alternatively, a set of small sub-domains can be defined based on three measurements, where no longer assumptions are necessary on the boundary conditions in contrast to the previous subsection. Every domain uses three adjacent frequency spectra of the measurements to estimate the local parameters. The outer two measurements act as the boundary conditions, i.e., $\Theta(\rho_{i-1}, s)$ and $\Theta(\rho_{i+1}, s)$. These two boundary conditions allow for the calculation of $E_1(s)$ and $E_2(s)$. Rearranging and defining $\Theta(\rho_i, s)$ as the output measurement results in the following Multiple-Input Single-Output system where ξ and ζ are known (dependencies on θ and s are omitted):

$$\begin{aligned} \Theta(\rho_i) &= \left(\frac{\xi(\rho_{i+1})\zeta(\rho_i) - \zeta(\rho_{i+1})\xi(\rho_i)}{\zeta(\rho_{i-1})\xi(\rho_{i+1}) - \zeta(\rho_{i+1})\xi(\rho_{i-1})} \right) \Theta(\rho_{i-1}) \\ &\quad - \left(\frac{\xi(\rho_{i-1})\zeta(\rho_i) - \zeta(\rho_{i-1})\xi(\rho_i)}{\zeta(\rho_{i-1})\xi(\rho_{i+1}) - \zeta(\rho_{i+1})\xi(\rho_{i-1})} \right) \Theta(\rho_{i+1}), \end{aligned} \quad (7.8)$$

with $i = 2, \dots, m-1$, where m denotes the number of sensors. The inputs and outputs are defined as $U_1(s) = \Theta(\rho_{i-1}, s)$, $U_2(s) = \Theta(\rho_{i+1}, s)$, and $Y(s) = \Theta(\rho_i, s)$ on the interval $[\rho_{i-1}, \rho_{i+1}]$:

$$Y(s) = G_1(\theta, s) U_1(s) - G_2(\theta, s) U_2(s). \quad (7.9)$$

In (7.8), the choices of $\xi(\rho, \theta, s)$ and $\zeta(\rho, \theta, s)$ are deliberately undefined, as different dependencies of f_X , f_V , and f_τ can be used. Here, we only consider constant parameters as such only the solutions in (2.13) and (2.15) need to be considered.

7.2.4 Change of variables

The parameters will be estimated by minimizing a cost function. The computation time and possibly avoidance of local minima can be improved by simplifying

the equations to be evaluated. In Section 2.2, we have seen that the important quantity $\lambda_{1,2}$ takes the form

$$\lambda_{1,2} = -\frac{V}{2\chi} \mp \sqrt{\left(\frac{V}{2\chi}\right)^2 + \frac{3}{2} \frac{s + \tau_{inv}}{\chi}}, \quad (7.10)$$

for both slab and cylindrical geometry. Therefore, a substitution is introduced to avoid parameter divisions, i.e.,

$$\lambda_{1,2} = -a \mp \sqrt{a^2 + \frac{3}{2}b + \frac{3}{2}cs}, \quad (7.11)$$

$$\text{with } a = \frac{V}{2\chi}, \quad b = \frac{\tau_{inv}}{\chi}, \quad \text{and } c = \frac{1}{\chi}.$$

This parameter set will be denoted as $\theta = [a \ b \ c]^T$ and the estimated set by $\hat{\theta}$. Although not discussed here, similar simplifications are possible for other choices of the spatial dependent functions.

In the next section, not only the parameters are estimated, but also their covariance. Consequently, the covariance matrix of the estimated parameters can be recalculated using (see (6.4) for details)

$$\text{Cov}(\hat{\chi}, \hat{V}, \tau_{inv}) = J_{\chi} \text{Cov}(\hat{\theta}) J_{\chi}^T$$

$$\text{with } J_{\chi} = \frac{1}{\hat{c}^2} \begin{bmatrix} 0 & 0 & -1 \\ 2\hat{c} & 0 & -2\hat{a} \\ 0 & -\hat{c} & \hat{b} \end{bmatrix}. \quad (7.12)$$

7.3 Sample maximum likelihood estimator

In this section, the Errors-in-Variables (EIV) problem is discussed, for which the sample Maximum Likelihood Estimator (SMLE) offers a solution. It is also discussed how to minimize the sample Maximum Likelihood cost function, how to construct confidence bounds on the estimated parameters, and how to validate the estimated models.

Maximum Likelihood Estimation is a method for estimating parameters which maximizes a known likelihood function. The likelihood function can be interpreted as a Probability Density Function (PDF), but with respect to the measured data. For example, if the difference between the measured output and a predicted output based on the model and measured input is studied, the remainder in the absence of model errors is fully characterized by the likelihood function of the noise. The sample likelihood function differs from the likelihood function in the sense that the real noise (co-)variances are unknown and are replaced by sample variances determined using a pre-processing step.

7.3.1 Error model: errors-in-variables

The transfer functions introduced in (7.9) are based on local spatial measurements. This means that an EIV approach is necessary to handle the noise on the measurements. In this chapter, the EIV problem is solved via the sample Maximum Likelihood Estimator (SMLE) in the frequency domain. It is based on additive circular complex normally distributed noise in the frequency domain (CCND) (see Chapter 6 or [Pintelon, 2012]), which is the result of Gaussian noise in the time domain [Goodman, 1963].

In the SMLE, the true unknown noise (co-)variances are replaced by sample estimates obtained from the periodic signal. This is achieved by calculating the averages and (co-)variances over the different periods per frequency line, which is described in detail in Section 6.3.2. A minimum number of 4 periods is necessary to make a parameter estimate, however, if at least 7 periods are used other desirable properties of the SMLE are also retained (see [Schoukens, 1997] for the details). In principle, also measurements containing transients can be used to obtain the (co-)variances using the local polynomial method, but at the cost of a more complex pre-processing step (see [Pintelon, 2010]).

Other approaches to handle EIV problems often rely on multiple experiments and specific assumptions on the noise. An overview of the different methods can be found in [Söderström, 2007]. In contrast, to the frequency domain (sample) MLE, also MLEs in time domain exist [Åström, 1980; Diversi, 2007], which handle the spectral factorization and possible transients differently [Söderström, 2007]. Moreover, MLEs can also be constructed for non-Gaussian noise distributions [Goodwin, 1977]. However, the MLE for Gaussian noise are more extensively studied, e.g., [Pintelon, 2012; Söderström, 2010].

7.3.2 Maximum likelihood cost

The sample MLE cost function is derived on the basis of the system model and the error model. The sample log-likelihood cost function V_{SMLE} is used [Pintelon, 2012]. It is defined as

$$V_{SMLE} = \frac{1}{F} \sum_{k=1}^F \frac{|e(\omega_k, \theta)|^2}{\sigma_e^2(\omega_k, \theta)}, \quad (7.13)$$

with ω_k the excited frequencies and F the number of frequencies used. The error $e(\omega_k, \theta)$ is defined as

$$e(\omega_k, \theta) = Y(\omega_k) - (G_1(\theta)U_1(\omega_k) - G_2(\theta)U_2(\omega_k)), \quad (7.14)$$

where the transfer functions G_1 and G_2 are evaluated at ω_k . The variability, which takes the different noise contributions into account, is given by (depen-

dency on ω_k and θ are omitted)

$$\begin{aligned} \sigma_e^2(\omega_k, \theta) &= \sigma_Y^2 + \sigma_{U_1}^2 |G_1|^2 + \sigma_{U_2}^2 |G_2|^2 \\ &\quad - 2 \operatorname{Re} (G_1 \sigma_{U_1 U_2}^2 \overline{G_2} + \sigma_{Y U_1}^2 \overline{G_1} - \sigma_{Y U_2}^2 \overline{G_2}), \end{aligned} \quad (7.15)$$

where the variances and covariances are estimated for every ω_k using M realizations (periods) calculated using (6.20) and (6.22). The complex conjugate of G is denoted as \overline{G} . The parameters are estimated by minimizing V_{SML}

$$\hat{\theta} = \arg \min_{\theta} V_{SML}(\omega_k, \theta). \quad (7.16)$$

Minimizing this cost function gives the estimated parameters. For filtered white noise disturbances the minimizer of (7.13), based on the non-rational transfer models, has exactly the same asymptotic ($F \rightarrow \infty$) properties as the SMLE for rational transfer function models. For example, it is consistent and asymptotically normally distributed (see [Pintelon, 2012] for the details). The cost function (7.13) can be naturally interpreted as a weighting of the error with the uncertainty of the measurements. Measurements with small noise variances have a higher weighting and vice versa. If σ_e is constant for all ω_k , then (7.13) reduces to a non-linear least-squares (NLS) estimator.

7.3.3 Optimization and confidence bounds

The minimization of (7.13) is in principle a non-convex problem. On the other hand, only a few parameters need to be estimated. Therefore, the entire relevant parameter space can easily be searched for the cost function's minimum. In addition, if the noise levels are reasonable and the parameters are optimized in terms of θ , it has been observed that the gradient based algorithms converge to the global minimum for many initialization values. These gradient methods are computationally cheap, especially if an analytic Jacobian is used.

The analytical Jacobian can also be used to estimate the confidence bounds on the parameters found by minimizing (7.13) using the Jacobian from a first-order Taylor series expansion

$$J_{\theta} = \frac{\partial}{\partial \theta} \left(\frac{e(\omega_k, \theta)}{\sigma_e(\omega_k, \theta)} \right), \quad (7.17)$$

which is similar to the approach in Section 6.1.4. The resulting covariance matrix in terms of θ is given by

$$\operatorname{Cov}(\hat{\theta}) \approx \left(\frac{M-1}{M-3} \right) [\operatorname{Re}(2J_{\theta}^H J_{\theta})]^{-1}, \quad (7.18)$$

with M the number of realizations (periods) [Pintelon, 2003]. The correction term in M is necessary, because the estimated sample covariance matrix is used instead of the real one. The uncertainty on the real valued parameters can be calculated by (7.12).

7.3.4 Cost function model validation

A cost function analysis is used to detect model errors. If the noise is indeed normally distributed, no model errors are present, and under some weak assumptions [Pintelon, 2012], the expected value of the sample Maximum Likelihood cost function equals the number of frequency lines F minus the number of free real-valued parameters n_θ divided by two, i.e.,

$$V_{noise} = \left(F - \frac{n_\theta}{2}\right). \quad (7.19)$$

In addition, the theoretical variance of the SMLE cost equals V_{noise} . However, as co-variances are estimated using M repeated experiments, a correction is necessary to take this extra uncertainty into account, i.e.,

$$\mathbb{E}\{V_{SML}\} = \frac{M-1}{M-2}V_{noise} \quad (7.20)$$

and

$$\text{var}\{V_{SML}\} = \frac{(M-1)^3}{(M-3)(M-2)^2}V_{noise}. \quad (7.21)$$

The estimated variance is used to construct confidence bounds. The cost function is a real valued function such that the confidence bounds can be constructed based on a real valued normal distribution

$$C_{bnd}(\mathbf{p}) = \mathbb{E}\{V_{SML}\} \pm \sqrt{2 \text{var}\{V_{SML}\}} \text{erf}^{-1}(\mathbf{p}). \quad (7.22)$$

with confidence \mathbf{p} . If $V_{SML}(\hat{\theta})$ resides between the bounds C_{bnd} , then the model is validated with respect to this test. Model errors generally lead to a higher value of the cost function at the global minimum. Values lower than the confidence bounds are mostly introduced by an incorrect modeling of the uncertainty. The whiteness residual test and the measured frequency response functions with their confidence bounds can also be compared to analyze the quality of the model. These are clearly defined for a Single-Input Single-Output system as given in Section 7.2.2 (see [Pintelon, 2003; van Berkel, 2013]). A similar whiteness residual test exist for a Multiple-Input Multiple-Output system [Pintelon, 2003]. However, its applicability for the specific case of a Multiple-Input Single-Output system where the transfer functions have coupled coefficients should be further investigated.

7.3.5 Input design and choice of domain

The SMLE developed here always considers a local domain of two or three measurement points. In case of three measurement points the measurement locations can be non-uniformly distributed. In principle, the larger the domain, the better the estimate of the parameters. The reason is that the suppression of the

amplitude increases with the distance due to the source. Hence, the amplitude difference between the input(s) and output is also larger. However, the larger the domain, the more stringent the assumption of constant parameters becomes. This means there is a trade-off between the sensor distance and the assumption of constant parameters. These considerations are more important than the overall number of sensors used, because every domain is treated separately in the approach used in this chapter. The validation test and confidence bounds can be helpful in making a choice for the sensor locations. If the model (of constant parameters) is rejected by the validation test, the model assumption is incorrect. In that case the sensor locations should be closer to each other. On the other hand, if the confidence bounds are large then increasing the distance between the sensors could improve the accuracy.

The other important aspect is the source defined in (7.2). The theoretical minimum number of sinusoidal components in the source should be $F > n_\theta/2$. However, every extra sinusoidal component increases the accuracy of the estimated parameters. The domain to be identified is preferably close to the source, but should not contain the source. In case the domain has some distance to the source, the diffusive process acts as a low-pass filter, which generally reduces the optimal frequencies ω_k with respect to the parameter accuracy when compared with a similar domain closer to the source. In addition, the (unknown) parameters on the domain, and between the source and the domain, directly influence the choice of the optimal excitation frequency. On the other hand, τ_{inv} can be estimated using sine components at a very low-frequency, which follows from $s \rightarrow 0$, and V is best identified somewhere in the intermediate region.

It is clear, that selecting the optimized identification accuracy is complex and depends on many factors. Moreover, it depends on which parameters and domains need to be identified accurately. The accuracy can be evaluated using the Fisher information matrix. As such this matrix plays an important role in designing optimal excitation signals and sensor placement. However, the exact design of the optimal excitation signal and sensor placement is complicated, and will not be considered in this chapter. The reader is referred to [Rafajlowicz, 1983; Ucinski, 2004] for a treatment of sensor placement and excitation design in DPS. On the other hand, the design of optimal excitation signals for transfer functions is treated in, e.g., [Rojas, 2007; Schoukens, 1991]. Note that non-linear effects need to be considered also in the design of the excitation signal [Pintelon, 2012].

7.4 Simulation results

This section shows a number of analysis steps for the validation of the estimation procedure presented in the previous sections using a Monte Carlo simulation. In addition, a finite difference simulation is presented, which shows the estimation results for varying profiles in slab geometry of χ and V_s . The models estimated

using a finite difference simulation are validated by means of a cost function analysis.

7.4.1 Estimator and confidence bound validation

The possibility to construct confidence bounds on the estimated parameters is an important advantage of the SMLE. However, the implementation of any estimation algorithm can be error-prone. Therefore, it is important to validate the implementation. This especially holds for schemes which use an analytic Jacobian. A number of trivial tests, such as Finite Difference Model comparison, convergence to the true minimum, and comparison of the Fourier transforms are done.

Next to validate the model, the estimated confidence bounds on the estimator need to be verified. The SMLE has a number of advantages when compared to the least-squares estimators. The estimates remain consistent if the additive complex circular normal noise is filtered or if the different noise sources are correlated (covariance), because the noise models are also estimated based on the realizations of the periodic signals. Under the conditions of filtered or colored noise, the estimator should find a consistent estimate and should approximate the confidence bounds accordingly. This can be tested by means of Monte Carlo simulations. The noise sources have been filtered and are correlated between different spatial locations. The original model is used and different noise realizations (10000) with the same variance and mean are simulated. The confidence bounds were validated under these conditions. It turned out that the parameter $b = \tau_{inv}/\chi$ is extremely sensitive to noise. This is caused by the necessity of excitation signals with very low ω_k and the presence of V and χ . Therefore, in the simulation in the next section the damping τ_{inv} is not considered.

7.4.2 Finite difference simulation

In this section, a simulation example is presented in Figure 7.1 where the diffusivity χ and convectivity V_s are estimated assuming a slab geometry. Both the diffusivity profile and convective profile contain a step (simulated by an erf function), but at different locations. These profiles were chosen to show that the domains can be identified independently from the profile outside the domain.

The excitation source $P(\rho, t)$ is placed at $\rho = 0.1$ and hence influences the estimates in the gray area of Figure 7.1. The sensors are positioned at $\rho = 0.1, 0.15, \dots, 0.95$, with the exception of $\rho = 0.75$. The source is a multi-sine with equal amplitude exciting the harmonics from 20 to 400 Hz (20 harmonics). In total 40 periods are observed (2 s). Normally distributed noise is added which is for 20% uncorrelated and 80% correlated (over different ρ_i), to simulate a realistic situation. The simulation data is generated with a finite difference model of 4000 grid points, a time step of 0.1 ms, and the boundary conditions

are $\partial T(\rho = 0) / \partial \rho = 0$ and $T(\rho = 1) = 0$.

In this example, the SMLE will be compared to the non-linear least-squares (NLS) estimator (7.13) with $\sigma_e = 1$, which is comparable to an output error approach in the time-domain [Ljung, 1993] (Parseval's theorem). For the optimization a simple grid search algorithm (brute-search) is used to find the global minima for both the SMLE and the NLS. Exactly the same global minima are found using a gradient based method (Levenberg-Marquardt) for the SMLE even in the case of high noise levels. The resulting local estimates are presented in Figure 7.1.

At low noise levels the SMLE and the NLS performance is similar. If the measurements become more noisy, due to a larger distance to the source, the estimates diverge from the true values. However, the confidence bounds for the SMLE are still correct. At higher noise levels the NLS estimates diverge significantly from the true values and perform worse than the SMLE. Moreover, the estimated χ seems relatively insensitive for a step in $f_{V_s}(\rho)$. In addition, the estimates of the non-symmetric domains using the measurements at $\rho = [0.65, 0.7, 0.8]$ and $\rho = [0.7, 0.8, 0.85]$, which are plotted at $\rho = 0.7$ and $\rho = 0.8$, respectively, perform as expected. Although the performance at the steps seems good, it is still necessary to validate the modeling.

7.4.3 Model validation of finite difference simulation

In Section 7.3.4 a model validation test is introduced, which is used here to validate the estimates of the finite difference simulation. The value of the cost function at the global minimum should equal the degrees of freedom (7.19) within some confidence region. This is verified in Figure 7.2, where not only the values of the cost function are plotted but also the cost function as function of the parameters at one spatial location.

Figure 7.2(a) shows the cost function, due to the parameter transformation introduced in Section 7.2.4. Many initialization values will allow for a gradient based method to converge to the global minimum or its neighborhood. Figure 7.2(b) shows that most models describe the data well. However, if lower noise levels than the noise level chosen here are used, the estimated models at the step in $f_\chi(\rho)$, and to a lesser extent at the step in $f_{V_s}(\rho)$, will be rejected by the cost function validation. Figure 3.6 is comparable in terms of the geometry and steps in the profiles. In that example the transport coefficients calculated based on the semi-infinite domains showed serious deviations after the step. This behavior has disappeared by considering domains with three measurement points, which is the main advantage for choosing three measurement point domains over two measurement point domains.

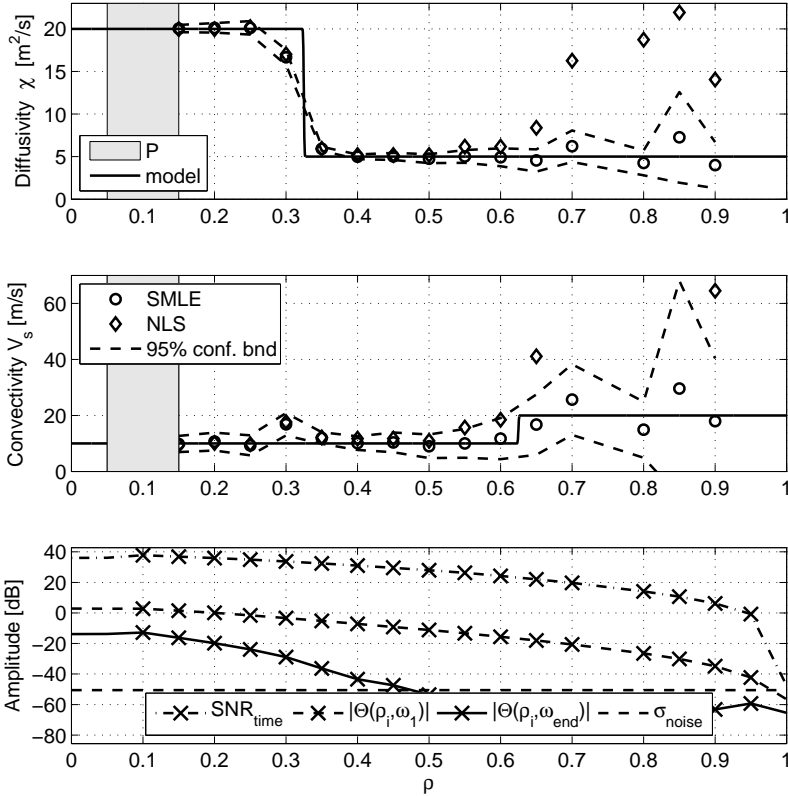


Figure 7.1. Comparison between the SMLE and the NLS. The true profiles (solid lines) end estimates of χ and V_s are presented including the 95% confidence bounds (SMLE only). Some NLS estimates of V_s become very large, are not included. The estimate is plotted at the central measurement ρ_i of the domain. The amplitude of the ground frequency $|\Theta(\rho_i, \omega_1)|$ and the amplitude of the highest excited frequency $|\Theta(\rho_i, \omega_{20})|$ are shown. The other amplitudes of the excited frequencies are situated in between. In addition, the standard deviation of the noise in the frequency domain $|\sigma_{noise}(\rho_i, \omega_k)| = \sigma_y$ is presented, which is constant for all frequencies. In comparison also the SNR in the time domain is presented, which is defined as $SNR_{time}(\rho_i) = 20 \log_{10} \left(\frac{T_{rms}(\rho_i)}{noise_{rms}(\rho_i)} \right)$. The crosses represent the measurement locations.

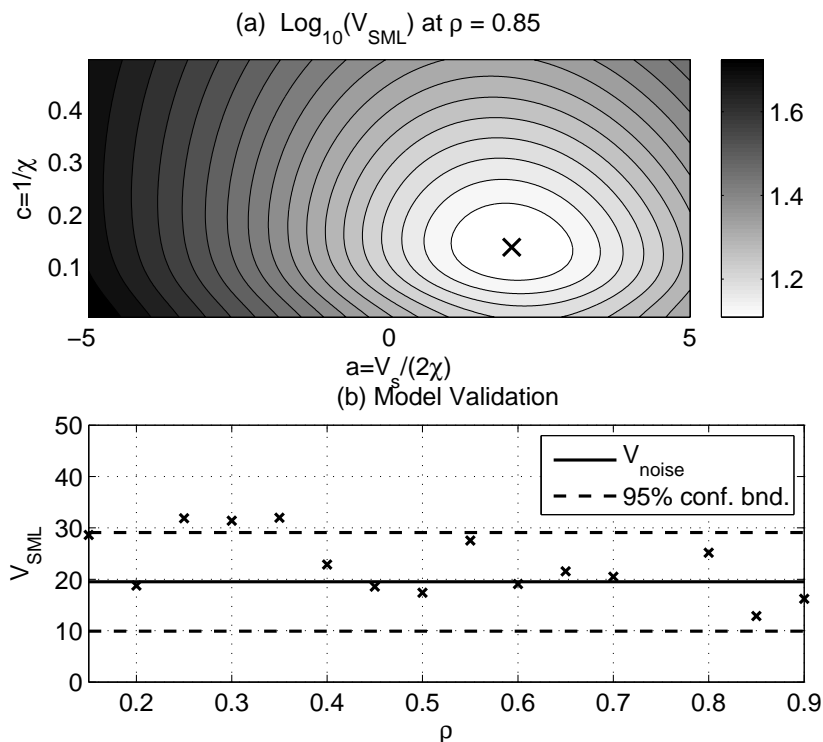


Figure 7.2. (a) Contour plot of the cost function values as function of the transformed parameters a and c at a specific spatial location. Note that the original parameters are defined in terms of θ so χ is plotted from 1 to 200 and a is a more complicated combination of χ and V_s . (b) The values of the cost function at the global minimum (\times), V_{SML} for the different spatial estimates (\times). The dashed lines are the 95% confidence bounds based on the expected variance of V_{SML} .

7.5 Conclusions and discussion

This chapter presents a new methodology to identify the spatial dependent parameters. The estimation is performed in the frequency domain, allowing analytic models to be used for simple dependencies. A transfer function is derived, based on two or three measurement points such that unknown boundary conditions can be handled. Moreover, a sample Maximum Likelihood Estimator is used to estimate the parameters. It takes the noise into account, which is present at the inputs and the output. This allows for consistent estimates of the parameter values and their uncertainties.

The SMLE performs better than the non-linear least squares estimator at high noise levels. A model validation technique shows that most estimates are accepted. The local estimation with three parameters ensures a simple and robust minimization of the cost function as only a few parameters need to be estimated. The local estimates also overlap, resulting in some redundancy, which can further improve the estimation procedure by using the overlap information.

Extending the methodology to higher dimensions is not straightforward. The main problem is foreseen in terms of the boundary conditions of a domain. The out and inflow of energy between two measurement locations needs to be described, which probably would require some interpolation. In addition, the required number of measurements increases to at least four (triangular element) in 2D. This means that the SMLE needs to be extended accordingly.

Conclusions, discussion and recommendations

A number of new methodologies for the determination of the thermal transport coefficients from electron temperature measurements during power modulation experiments are introduced. Some of these methodologies also take the influence of measurement uncertainty into account. These methodologies range from, quick-and-dirty (the estimate is simple to implement and gives a rough estimate of the transport coefficients), to hard-yet-gracefully (the estimate is difficult to implement, but given the uncertainties of the measurements, provides an optimal estimator for the transport coefficients on a local domain, consisting of two or three measurement points).

8.1 Conclusions

In Section 1.4 the general objective of this thesis is given, i.e.,

Develop practical methods to reduce the uncertainty of the estimated transport coefficients allowing for the validation of the chosen transport model. These methods should not restrict the modulation of the source, such that optimal excitations can be applied.

To achieve this objective, the following steps were taken:

- ***Linking fusion literature with system identification concepts:*** The first step in linking these two fields is analyzing the differences in modeling, i.e., the logarithmic temperature derivative (fusion) and transfer functions (system identification). Comparing the logarithmic temperature derivative

and transfer functions shows that (in slab geometry) the (logarithmic) spatial derivatives of amplitude and phase are constant if the transport coefficients are independent of the radius. In addition, it is shown that the spatial derivatives both in slab and cylindrical geometry are directly linked to the spatial dependence of the transport coefficients and as such cannot be chosen separately. As such transfer functions offer a method in which no longer the derivatives of amplitude and phase need to be calculated directly.

- ***The introduction of a large number of new approximations in cylindrical geometry:*** Based on the logarithmic temperature derivative, approximations for the diffusivity have been derived, as well as approximations for the convectivity and damping. Therefore, it was necessary to extend the modeling, i.e., the logarithmic temperature derivative and transfer functions to include convectivity. This resulted in models in terms of the Confluent Hypergeometric Functions.

Both slab and cylindrical geometries are considered, assuming either a semi-infinite domain or a symmetric domain. In slab geometry, the approximations can be directly calculated in terms of the logarithmic derivative using one or two harmonic components of the temperature perturbation, i.e., harmonics. The approximations in cylindrical geometry are derived using continued fractions and asymptotic expansions. Moreover, if both convectivity and damping are considered next to the diffusivity, two harmonics are necessary.

The approximations based on a semi-infinite domain, with the exception of the asymptotic expansion, estimate the diffusivity well for large radii, high frequencies, and small diffusivities. This holds both for the cases where heat waves travels outwards or inwards. The approximations derived using asymptotic expansions are only applicable for heat waves traveling outwards, enabling the estimation of the transport coefficients for small radii, low frequencies, and large diffusivities. Approximations based on a symmetry boundary condition for heat waves traveling inwards perform well for small radii, low frequencies, and large diffusivities. The approximations based on the continued T -fraction show only some errors in the overlap region of the other approximations.

In this thesis approximations are also compared on the basis of the following three cases:

1. Diffusivity only for which the solution is given in terms of Bessel functions with the exception of the slab approximations.
2. Diffusivity and damping for which the solution is given in terms of Bessel functions with the exception of the slab approximations.
3. Diffusivity, convectivity, and damping for which the solutions are

given in terms of the Confluent Hypergeometric Functions with the exception of the slab approximations.

In case convectivity is negligible, i.e., cases 1 and 2, two approximations suffice to determine the diffusivity well. The relative error of the diffusivity estimate for the region of interest is in general well below 1%. However, in a small region, the errors are larger with a maximum relative error for heat waves traveling towards the edge of 20% and for heat waves traveling towards the center of 2%. For both cases a simple test is introduced to select the proper approximation.

The third case also considers convectivity. In this case the new approximations show a significant region in which the diffusivity can be estimated well, but also regions in which no suitable approximation has been derived. This implies that implicit methods will be necessary to estimate the convectivity also in these regions.

Although the transport coefficients are assumed to be independent of the radius, i.e., if the spatial variation of the profiles is small, it is still possible to determine these spatial varying transport coefficients. However, significant errors can occur due to the assumption of the transport coefficients being independent of the radius in combination with semi-infinite domains or symmetric domains. These errors can even occur when the transport coefficients on the local domain under consideration are constant. The influence of errors due to the variation of the profiles decreases with increasing frequency due to the low-pass character of the heat transport (models). As both convectivity and damping are determined by frequencies below that of the diffusivity, these errors also impact the estimation of the convectivity and the damping more significantly. In addition, the approximations derived for the convectivity and damping are less accurate compared to those for the diffusivity.

- ***Extending the analysis to multiple harmonics such that the frequency content of the modulation can be chosen freely:*** Another important aspect of estimating the transport coefficients is the combination of different harmonics. This can only be done in an optimal way by taking the measurement uncertainties into account. For the methods introduced in Chapter 2 used to determine the diffusivity, it has been shown that the distribution of the diffusivity is described by a non-central inverse chi-squared distribution, under the assumption of a Complex Circular Normal Distribution in the frequency domain. This has serious consequences for combining estimates of the diffusivity determined at different frequencies (harmonics). The resulting distribution function has a long tail resulting in a high upper uncertainty. In addition, the average diffusivity will be biased. Therefore, an alternative approach is introduced, which is closely related to Maximum Likelihood Estimation. This approach first averages

the weighted spatial derivatives, where the spatial derivatives can be seen as Gaussian random variables. On the other hand, this approach is less suitable if products of these spatial derivatives or more complicated combinations appear in the approximations. In such cases clearly an alternative approach is necessary, which is introduced in Chapter 7.

- ***The use of the sample Maximum Likelihood Estimator to reach a near minimum variance on the estimated transport coefficients, which also allows a statistical analysis of the validity of the assumed model:*** The sample Maximum Likelihood Estimator uses the measured Fourier coefficients, mean values and (co-)variances, without the need for approximating the spatial derivatives of amplitude and phase. In addition, the transport coefficients can be estimated using the original transfer functions and hence no additional approximations are needed. Moreover, more complicated models can be used. Therefore, a new local domain is introduced, which considers three measurement points instead of two measurement points in combination with a boundary condition. As such it avoids errors commonly related to the semi-infinite domains or domains based on symmetry boundary conditions. Another important advantage of the sample Maximum Likelihood Estimator is that it is a consistent estimator. It gives the transport estimates with small variance, which is close to the theoretical minimum. Moreover, using some statistical test(s) it is possible to validate the estimated model with respect to the measurement data. Two disadvantages of the sample Maximum Likelihood Estimator with respect to the other methods presented in this thesis are: 1) the implementation is more complicated and 2) the optimization problem is non-convex, hence, convergence to the global minimum is not guaranteed.

In summary, the extension of the modeling with convectivity not only allows estimation, but also allows for the modulation frequencies to be lowered. The reason is that the effect of convectivity no longer needs to be suppressed. In addition, the combination of different harmonics allows the spreading of harmonics over a large frequency range. This is important for estimating the transport coefficients as they are sensitive to different frequency ranges. In addition, taking the measurement noise into account allows for a near optimal estimate of the transport coefficients. Hence, as a near minimum variance parameter estimate is reached, this also allows the validation of the chosen model. In Chapter 7 all these steps come together in the Maximum Likelihood Estimator, albeit, at the cost of a non-convex estimation algorithm. As this algorithm is implicit, it also allowed the use of three point domains, which no longer are subject to errors due to assumptions on boundary conditions necessary in a two point domain. As the implicit methods require starting values, the explicit approximations derived in Chapters 3-5 can be used for this purpose.

The Maximum Likelihood Estimation algorithm does not depend on the chosen perturbation, with the exception of some weak conditions and takes the measurements into account in a near optimal way given the noise assumptions. Hence, one may reach the conclusion that our objective has been reached. However, it is important to realize that the objective has only be reached for local domains and not for entire profiles. In this thesis, we have limited our analysis to constant parameter dependencies. This does not mean that spatial variations cannot be taken into account, but the estimates are non-optimal. The reason for this choice of parameter dependencies is that this thesis focuses on the use of analytical solutions of the underlying Partial Differential Equation, which is a natural continuation of the existing fusion literature. However, during this research it also became clear that the limit of analytical solutions in cylindrical geometry has been reached. Although, theoretically generalized hypergeometric functions could be used to describe non constant profiles, they are not practical in estimation algorithms.

8.2 Discussion and recommendations

This final section describes possible future research directions and discusses a number of issues, which in the opinion of the author should be further investigated. It is subdivided in three parts each focusing on a different aspect of (electron) heat transport studies, i.e., estimation of the transport coefficients, experimental design, and the applicability of the presented methods to other problems.

8.2.1 Improvement of the estimation

This section contains a number of recommendations concerning the methods used to determine the transport coefficients based on perturbative experiments. As such, this section is closest to the work described in this thesis.

- In the Distributed Parameter System (DPS) literature, e.g., [Banks, 1989], many methods have been developed to estimate parameters in Partial Differential Equations (PDEs). To date, this body of knowledge has not been incorporated in the fusion literature, partly due to the mathematical complexity of both the mathematical definitions and the implementations. However, a number of these methods are directly applicable for problems in fusion. In addition, as the MLE introduced in this thesis solves a non-convex problem, a convex alternative from the DPS literature, could be used to generate good start values.
- The MLE developed in this thesis is based on the assumption of local constant parameter dependencies in slab and cylindrical geometry. This is a limiting assumption if domains larger than three measurement channels

are considered because for varying profiles higher order spatial dependencies give a better description. Therefore, the MLE in frequency domain should be extended to also include higher order spatial dependencies. Consequently, discretizing the spatial coordinate will be necessary because generally analytical solutions do not exist with the exception of some special cases. However, the use of higher order spatial dependencies also implies more parameters need to be estimated. Moreover, the MLE optimization problem is non-convex, which means that either good starting values need to be found, for instance by solving the simplified linear least-squares problem possibly with regularization to make the optimization problem convex. A parameter transformation might be necessary to avoid singularities to find the global minimum. Moreover, the uniqueness of the solution should be guaranteed. This is a serious issue when extending the slab geometry MLE that uses three measurement points from constant parameter dependencies to linear parameter dependencies. For some special cases it could already be shown that there is no longer a global minimum, but a global minima line, hence, no longer yielding a unique solution.

- The advantage of the frequency domain estimators over time domain estimators, is that the coefficients are estimated based on a complex valued Ordinary Differential Equation (ODE). Consequently, the solutions of these ODEs (transfer functions, state-space) in terms of inputs and outputs can be calculated using a matrix inversion. As such frequency domain estimators are a serious competitor with other classic methods in the identification of DPS based on the time domain. The commonly used method to discretize the spatial dependency is finite difference. However, calculation time is an important factor as the solution is used in an optimization algorithm. In such cases spectral methods can offer a good alternative. There are many basis functions available and the merits of these basis functions should be investigated. In case of cylindrical geometry it is well known that the eigenfunctions for the simplified case are the Bessel functions (Chapter 2). Moreover, Confluent Hypergeometric Functions can be approximated using a converging series in terms of Bessel functions [Slater, 1960]. As such the Bessel functions are a good candidate to use as basis functions for the spatial discretization. This is also shown in [Heijmans, 2013] where discretization schemes based on Bessel functions as basis functions and finite difference are compared.
- Although in the plasma core of tokamaks and stellarators the density gradients can often be neglected, they can play a more important role towards the wall. In this thesis, the spatial density gradients have been largely neglected. However, when numerical grids are implemented, density gradients can be taken into account assuming measurements of the density are available. If the methods used in this thesis also include a source term,

they can also be used for the estimation of the particle transport. The reason is that particle transport is also modeled according to the second-order parabolic PDE considered in this thesis, with the only difference that the perturbation source is not localized [Mantica, 2010].

- Estimating the transport coefficients based on the spatial derivatives of amplitude and phase is fast and easy. However, the proper combination of multiple harmonics requires a proper weighting (Chapter 6). The weighting can be calculated for simple cases, but this fails for more complicated relationships. Also, such relationships only match each harmonic with two unknown transport coefficient and do not combine the deterministic and statistical properties of all harmonics in one estimate. However, the most important problem is the estimation of the derivative. Virtually every method to approximate the derivative from the amplitude and phase yields a biased estimate with an incorrect variance. This is known as the bias-variance trade-off [Hall, 2010]. As such, an estimate close to the unbiased estimate with a variance close to the minimum variance seems unachievable following the derivative approach.
- The estimation of the Fourier coefficients and their variance as presented in this thesis is based on the assumption of purely periodic measurements. Consequently, trends or slow temperature drifts and temperature change due to the initial conditions are not considered, i.e., transients. As such the part of the measurement interval with non-negligible transients is ignored. However, in this transient part also information is contained on the transport coefficients. This information becomes more important if measurement time is limited as is the case for many discharges. A possible method to determine the Fourier coefficients and their variances under the influence of transients is using the Local Polynomial Method [Pintelon, 2010]. However, under the assumption of the linearity of the transport and no other temperature drifts than those due to the initial conditions, the transient itself could be additionally used to determine the transport coefficients by estimating also the initial condition. This has already been investigated in [Monteyne, 2013] for rational polynomials and the Warburg domain.

8.2.2 Study of transport

This section gives some recommendations related to experimental design and analysis.

- An important recommendation in [Peters, 1996] is to extend gyrotron's function generators to allow for more versatile binary signals. This, to generate modulation signals in which the higher harmonics are larger than the lower harmonics. This to compensate for the stronger damping, i.e., the larger suppression, of the higher harmonics in comparison to the lower harmonics in the heat waves.

Function generators have been extended to accommodate more versatile binary signals. However, the use of more versatile binary signals, e.g., periodic pseudo random binary modulation, are still not widely used. In addition, optimal modulation signals are hard to conceive with binary modulation signals. Therefore, we recommend that the power supply to be extended to allow for even more versatile modulation signals in which not only the timing of the pulses can be modified, but also the power. In the absence of such new power supplies optimal modulations could be approximated by combining two or more gyrotrons and modify their timing and deposition accordingly.

The problem of choosing optimal modulation signals goes further than just increasing the amplitude of higher harmonics to compensate for the suppression. Also the choice of modulation signals is important. For instance, the diffusivity can be estimated using high modulation frequencies based on relationships not considering convectivity and damping. An important disadvantage is that, the resulting measurements will be more noisy because transport acts as a low-pass filter. In this thesis, the effect of convectivity (and damping) has been taken into account in a number of newly introduced approximations and estimators. Therefore, the modulation frequency should be reduced to have less noisy measurements leading to better estimates of the diffusivity and to be able to estimate convectivity with acceptable uncertainty (see [van Berkel, 2013]). This all depends on the number of harmonics used, their amplitudes, and their frequency spread. A possible method to optimize the modulation signals systematically is using the Cramér–Rao lower bound or the closely related Fisher information matrix [Rojas, 2007; Schoukens, 1991; Ucinski, 2004]. These methods do not consider non-linearities, which can be created by large amplitudes in the modulation signal. These non-linear effects should also be considered in the optimization of the modulation signals.

- Transport is non-linear and depends on the specific physics regime or operating point [Inagaki, 2011]. Hence, it is important to confirm, specifically for the regime which is being studied, that the perturbation is indeed small enough to assume linearity. If not, the amount of non-linearity needs to be

quantified. This can be done using a simple test, e.g., increasing the modulation power and compare the output temperature, or using advanced methods such as the Best-Linear-Approximation [Pintelon, 2012], which also allows for the estimation of the dynamic behavior and the even and odd non-linearities.

- Section 6.3.2 introduces a simple method to calculate the variance and co-variance for different spatial locations. As turbulence determines the propagation of the heat waves, it would be interesting to see how the covariance matrix for different measurements is influenced by turbulence and to investigate the possibility of recovering the correlation length from these data.

8.2.3 Extension to other fields

The estimation of transport coefficients in parabolic PDEs is a common problem in physics. As such some of the methods proposed in this thesis are applicable to other applications.

One example is the quantification of groundwater-surface water exchange flux in riverbeds used to study the transport of contaminants and nutrients [Anderson, 2005]. The temperature is measured at different vertical positions using a pole embedded in the riverbed. Based on these temperature measurements and assuming a one dimensional slab geometry, the flow needs to be determined to increase the understanding of the transport of contaminants and nutrients [Rosenberry, 2008]. This flow is related to the convectivity used in this thesis.

Another example is the calibration of infrared imaging video bolometer, which is used to study radiation structures in high temperature plasmas [Peterson, 2000]. The radiation is deposited on a thin foil, whose temperature is measured using an infrared camera. The amount of radiation deposited can be reconstructed taking into account the heat transport on the foil. As the foil is thin ($\approx 2.5 \mu\text{m}$), the transport coefficients (diffusivity) on the foil are not homogenous. Therefore, they need to be estimated to compensate for this transport component in real experiments. Currently, the diffusivity is estimated by giving one laser pulse to heat the foil locally. This induces a circular Gaussian temperature profile in two dimensions allowing the heat propagation to be modeled as a one-dimensional PDE in cylindrical coordinates. The diffusivity is estimated between two time instances on the basis of the decay and widening of the Gaussian temperature profile in the cool down phase after the source has been turned off [Cernuschi, 2001; Pandya, 2014]. The techniques of this thesis can be applied in case a periodic laser pulse is applied in order to increase the Signal to Noise Ratio and possibly to determine also a convective and damping part.

Appendix A

Analytic eigenfunctions of PDEs

The Bessel functions and Confluent Hypergeometric Functions are extensively used in the estimation of the transport coefficients. Therefore, in this appendix a more detailed description of these functions is given. In Section A.1, the underlying Ordinary Differential Equations (ODEs) of these eigenfunctions are discussed. Furthermore, we show they can be solved using power series. Then, in Section A.2, a generalized second order partial differential equation (PDE) with linear parameter dependencies in space is introduced, which includes the different geometries used in this thesis such as the PDE in slab and cylindrical geometry with constant transport coefficients. At the end of this appendix, Section A.4, the transformations from these PDEs to the underlying Bessel ODE and Confluent Hypergeometric ODE are described.

A.1 The Bessel and confluent hypergeometric ODEs

The Bessel functions and Confluent Hypergeometric functions are the resulting eigenfunctions of the Bessel Differential Equation [Abramowitz, 1976]

$$\varrho^2 y'' + \varrho y' + (\varrho^2 - \nu^2) y = 0 \quad (\text{A.1})$$

and the Confluent Hypergeometric Differential Equation [Slater, 1960]

$$\varrho y'' + (b - \varrho) y' - ay = 0, \quad (\text{A.2})$$

respectively. The solution to the Bessel Differential Equation [Abramowitz, 1976] is given by

$$y = D_1 J(\nu, \varrho) + D_2 Y(\nu, \varrho), \quad (\text{A.3})$$

where $J(\nu, \varrho)$ is the Bessel function of the first kind and $Y(\nu, \varrho)$ is the Bessel function of the second kind, both of order ν . The solution to the Confluent Hypergeometric Differential Equation [Slater, 1960] is given by

$$y = D_1 \Phi(a, b; \varrho) + D_2 \Psi(a, b; \varrho), \quad (\text{A.4})$$

where Φ (Kummer function) and Ψ (Tricomi function) denote the Confluent Hypergeometric Functions of the first and second kind, respectively. The Bessel functions and Confluent Hypergeometric Functions can also be defined in terms of other functions, e.g., Airy functions, Whittaker functions, Laguerre polynomials [Bateman, 1953]. The latter functions are derived from different ODEs, which can be transformed into (A.1) and (A.2). Therefore, only the Bessel and Confluent Hypergeometric functions are discussed.

The Bessel functions and Confluent Hypergeometric Functions are transcendental functions meaning that they cannot be expressed in terms of algebraic functions (polynomials, exponentials, etc.). This means that these functions need to be approximated, which is discussed next.

A.2 Power series representation

The Bessel and Confluent Hypergeometric Functions cannot be expressed in terms of algebraic functions, but can be described by converging power series, asymptotic relationships, indefinite integrals, etc. In this section, only converging power series, the most common method to calculate these functions, are discussed. Although this method can be used to calculate the Bessel and Confluent Hypergeometric Functions in a certain parameter ranges of order and argument, the number of terms necessary to calculate accurate solutions is large. In these regions other methods should be used [Bowman, 1958; Slater, 1960].

The general Bessel functions of respectively the first and second kind are defined in terms of power series as [Abramowitz, 1976]

$$J(\nu, \varrho) = \sum_{n=0}^{\infty} \frac{(-1)^n}{n! \Gamma(\nu + n + 1)} \left(\frac{\varrho}{2}\right)^{\nu+2n} \quad (\text{A.5})$$

and

$$Y(\nu, \varrho) = \frac{J(\nu, \varrho) \cos(\pi\nu) - J(-\nu, \varrho)}{\sin(\pi\nu)}, \quad (\text{A.6})$$

where the Gamma function $\Gamma(x)$ is an extension of the factorial $(x+1)!$ to complex and real values [Nielsen, 1906]. The Bessel function of the second kind $Y(\nu, \varrho)$ is only valid for $\nu \neq 0, \pm 1, \pm 2, \dots$ because otherwise a zero division occurs. In this case, other power series exist to calculate the Bessel function. To explain how to arrive at these power series from the ODE, a simple example is presented for $J(0, \varrho)$.

A.2.1 Example: derivation of power series solution of the Bessel function of first kind of order $\nu = 0$

This example shows how to derive the series expression of the Bessel function of the first kind of order $\nu = 0$. For $\nu = 0$, the Bessel Differential Equation defined in (A.1) reduces to following ODE by dividing it with ϱ^2 , i.e.,

$$y'' + \frac{1}{\varrho}y' + y = 0, \varrho \neq 0. \quad (\text{A.7})$$

The power series solution can be derived by substituting $y(\varrho) = \sum_{k=0}^{\infty} a_k \varrho^k$, which is comparable to taking a Taylor expansion in zero. Taking the derivatives gives $y' = \sum_{k=1}^{\infty} k a_k \varrho^{k-1}$ and $y'' = \sum_{k=2}^{\infty} k(k-1) a_k \varrho^{k-2}$. Substituting these in (A.7) gives

$$\sum_{k=2}^{\infty} k(k-1) a_k \varrho^{k-2} + \frac{1}{\varrho} \sum_{k=1}^{\infty} k a_k \varrho^{k-1} + \sum_{k=0}^{\infty} a_k \varrho^k = 0. \quad (\text{A.8})$$

This can be re-indexed such that all summations start from $k = 0$

$$\sum_{k=0}^{\infty} (k+2)(k+1) a_{k+2} \varrho^k + \sum_{k=-1}^{\infty} (k+2) a_{k+2} \varrho^k + \sum_{k=0}^{\infty} a_k \varrho^k = 0. \quad (\text{A.9})$$

Considering $k = -1$ in (A.9) gives $a_1 = 0$. For $k \geq 0$ the terms can be combined

$$\sum_{k=0}^{\infty} \left((k+2)^2 a_{k+2} + a_k \right) \varrho^k = 0.$$

The recursion equation $a_{k+2} = -(k+2)^{-2} a_k$ allows the calculation of the coefficients of $y = \sum_{k=0}^{\infty} a_k \varrho^k$. It is clear that because $a_1 = 0$ all the uneven coefficients are also zero. Therefore, the recursion can be further simplified by choosing $k = 2n$. In Table A.1 the different coefficients are calculated such that a structure can be recognized. The resulting summation series can be rewritten using the identity $\Gamma(n+1) = n!$

$$y = a_0 \sum_{n=0}^{\infty} \frac{(-1)^n}{n! \Gamma(n+1)} \left(\frac{\varrho}{2} \right)^{2n}. \quad (\text{A.10})$$

This can be compared to the power series of the Bessel function of the first kind (A.5) when $\nu = 0$

$$J(0, \varrho) = \sum_{n=0}^{\infty} \frac{(-1)^n}{n! \Gamma(n+1+0)} \left(\frac{\varrho}{2} \right)^{2n+0}, \quad (\text{A.11})$$

n	a_n	Coefficients	$2^{-2n} (-1)^n (n!)^{-2} a_0$
-	a_0	a_0	a_0
0	a_1	$(-1)^1 2^{-2} a_0$	$(-1)^1 2^{-2} a_0$
1	a_2	$(-1)^2 2^{-2} 4^{-2} a_0$	$2^{-2 \cdot 2} (-1)^2 1^{-2} 2^{-2} a_0$
2	a_3	$(-1)^3 2^{-2} 4^{-2} 6^{-2} a_0$	$2^{-2 \cdot 3} (-1)^3 1^{-2} 2^{-2} 3^{-2} a_0$

Table A.1. Coefficients of the series calculated using the recursion equation.

Clearly, the resulting power series are indeed the same when $\nu = 0$ with the exception of a_0 , which is the integration constant. The Bessel Differential Equation is a second order differential equation. Therefore, also a second solution $Y(0, \varrho)$ exists, but it is more difficult to calculate (see [Bowman, 1958]).

This example shows how the power series solution can be calculated for $\nu = 0$. Similarly, the power series solution for (A.1) can also be found. Also, the Confluent Hypergeometric Functions of the first and second kind are defined as power series

$$\Phi(a; b; \varrho) = \sum_{n=0}^{\infty} \frac{(a)_n \varrho^n}{(b)_n n!} \tag{A.12}$$

and

$$\Psi(a; b; \varrho) = \frac{\Gamma(1-b)}{\Gamma(1+a-b)} \Phi(a; b; \varrho) + \frac{\Gamma(b-1)}{\Gamma(a)} \varrho^{1-b} \Phi(1+a-b; 2-b; \varrho), \tag{A.13}$$

with $(a)_n = a(a+1)(a+2) \cdots (a+n-1)$ known as the Pochhammer symbol or the rising factorial. The power series describing Confluent Hypergeometric Functions are more complicated, but still can be evaluated for most values except for $b \in \mathbb{Z}$. For these values transformations exist [Slater, 1960]. For some special values of a and b these series can again be simplified, for instance into the Bessel function. The Confluent Hypergeometric Function of the first kind $\Phi(a; b; \varrho)$ is also often written as ${}_1F_1(a; b; \varrho)$ because it is a special case of the Hypergeometric Series which is a solution of the Hypergeometric Differential Equation [Seaborn, 1991]. This Hypergeometric ODE can be used to calculate the solution to more complicated ODEs [Seaborn, 1991]. However, only a few power series solutions exist for the Hypergeometric Differential Equation, hence it is numerically problematic to calculate the solutions for certain parameter regions of the arguments in terms of accuracy and calculation time. Therefore, we restrict ourselves to the Confluent Hypergeometric Functions and the Bessel

functions. Many algorithms exist to calculate the solutions for specific value ranges of the arguments allowing an efficient and accurate numerical calculation of the solutions.

A.3 Numerical evaluation

The numerical evaluation of the Bessel functions and Confluent Hypergeometric Functions is a complex process. Many different algorithms need to be combined to calculate the solution for a large range of ν , a , b and ρ . Generally, there are three types of algorithms to calculate the solution: 1) the power series solutions which can be evaluated up to a desired precision (truncation); 2) iterative algorithms based on recursive relations; 3) asymptotic expansions, in value ranges where the Bessel function reduces to more simple functions often for large values of the arguments.

In this thesis, Matlab[®] is used to calculate the solutions of the Bessel function at specific values of the argument and order. This implementation is based on the algorithm described in [Amos, 1986] originally implemented in FORTRAN[®] 66. It calculates the modified Bessel functions $I(\nu, z)$ and $K(\nu, z)$ using different algorithms based on truncated power series, asymptotic expansions, recursions, etc. The other Bessel functions and related special functions are expressed in terms of these functions, e.g., $J(\nu, z) = i^\nu I(\nu, -iz)$. The complexity of the calculation becomes clear in Figure A.1 [Amos, 1985], showing the algorithm used for the calculation of the modified Bessel function of the first kind $I(\nu, z)$ and the different approximations used. The, complex and negative real planes are calculated using analytic continuation formulas [Amos, 1985]. In certain regions, called overflow and underflow, it is difficult to calculate accurate results.

The Confluent Hypergeometric Function of the first and second kind are less commonly used in practice. Consequently, there are not many efficient algorithms to calculate specific solutions for these functions. Although both Confluent Hypergeometric Functions are implemented in Matlab (2012b). That the computational time was longer than expected, probably because only the standard power series described in (A.12) and (A.13) are implemented. Moreover, in the case of the Confluent Hypergeometric Function of the second kind, the solutions were often inaccurate without warning. Therefore, Matlab was linked to Mathematica[®] such that it is possible to calculate the solutions using Mathematica's implementation. In Mathematica, the exact implementation is not described. However, the library for $\Phi(a; b; \rho)$ contains twelve different power series representations and six asymptotic series expansions [Wolfram Research, 2014]. Testing the numerical solutions gave accurate results within acceptable computational time. Bessel and Confluent Hypergeometric Functions can be calculated using different approximations, however, the implementation is complex. Consequently, we will rely on the algorithms used in Matlab (Bessel function) and Mathematica (Confluent Hypergeometric Functions).

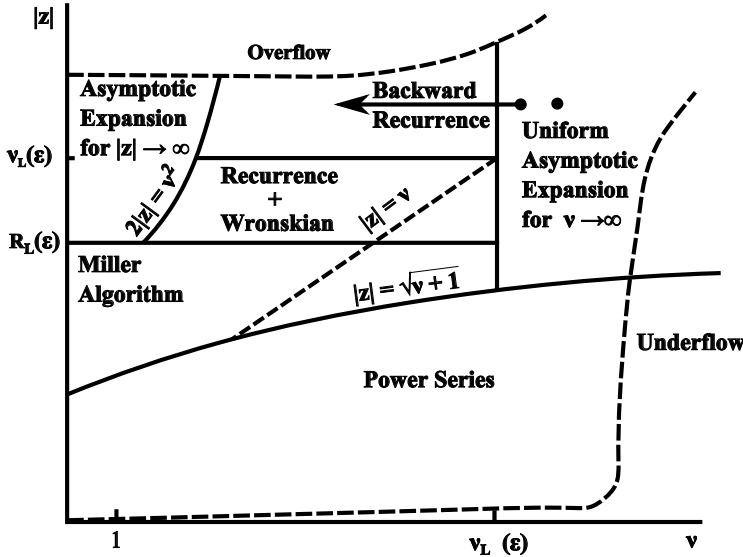


Figure A.1. Computation Diagram for $I(\nu, z)$, $Re(z) \geq 0$ based on Figure 1 in [Amos, 1985].

The optimization techniques considered in this thesis require also the derivatives of the special functions. The derivatives with respect to the argument z can be expressed in terms of the original functions [Bateman, 1953] and consequently do not pose any problem. However, derivatives with respect to the order ν or the parameters a and b are more problematic. These derivatives can again be described in terms of power series. The power series of the Bessel functions with respect to the order, including (half-)integer orders, can be found in [Magnus, 1966]. The derivatives of the Confluent Hypergeometric functions result in power series involving the digamma function ψ , which is logical considering that the derivative of the rising factorial is

$$\frac{d(a)_n}{da} = (a)_n [\psi(a+n) - \psi(a)] \text{ with } \psi(x) = \frac{d}{dx} (\ln(\Gamma(x))). \quad (\text{A.14})$$

Note that calculating the derivatives with respect to a and b in (A.4) is still an active research area and therefore needs to be performed with caution [Ancarani, 2008]. The derivatives with respect to the order ν and parameters a and b are not implemented in Matlab. Therefore, Mathematica is used to numerically evaluate these derivatives [Wolfram Research, 2014]. Except for the derivatives of the Bessel functions with respect to order ν , which are numerically approximated in Matlab using finite difference except for values of ν near (half-)integer values. This implementation is computationally more efficient compared to Mathematica with acceptable accuracy.

In the last two sections it is discussed how to derive and calculate the eigen functions used in this thesis. The next section shows how to transform the general form of the PDEs used in this thesis into either the Bessel Differential Equation (A.2) or Confluent Hypergeometric Differential Equation (A.1).

A.4 Solutions in terms of Bessel and confluent hypergeometric functions

This section describes how to solve the following second order complex valued ODE in terms of Bessel and Confluent Hypergeometric functions

$$(a_2x + b_2) Z''(s, x) + (a_1x + b_1) Z'(s, x) + (a_0x + b_0) Z(s, x) = 0, \quad (\text{A.15})$$

with $(a_2, a_1, a_0, b_2, b_1, \text{ and } b_0) \in \mathbb{C}$. This ODE is a generalized form of (2.12) and (2.14), but can also be the resulting ODE of the Laplace transform of a slab geometry description with linear parameter dependencies. The complex valued ODE in (A.15) can be solved in terms of its complex eigenfunctions, resulting in following general solution

$$Z(s, x) = E_1 \xi(s, x) + E_2 \zeta(s, x), \quad (\text{A.16})$$

with ξ and ζ the complex valued eigenfunctions and E_1 and E_2 the boundary constants, may depend on s and thus can be complex valued. These eigenfunctions will be either exponential functions, Bessel functions, or Confluent Hypergeometric Functions. The exponential functions are the resulting eigenfunctions in case no spatial dependencies are assumed, i.e., $a_2 = a_1 = a_0 = 0$.

The ODE with linear dependencies (A.15) can be transformed into the Bessel or Confluent Hypergeometric Differential Equation to find the arguments and order of the Bessel and Confluent Hypergeometric Functions. In [Murphy, 1960; von Kamke, 1959] the different steps are explained to transform (A.15) into either (A.1) or (A.2).

These are summarized in Table A.2, which is based on [Polyanin, 2003]. The different cases need to be distinguished to avoid zero divisions. However, it is important to remember that the solutions are still multiplied by the boundary constants, which can result in slightly different results compared to the derivations in Table A.2. The special cases where (A.15) reduces to a first order ODE are excluded from the table. An important case is the cylindrical geometry with constant coefficients for which the argument ϱ and coefficients a and b are derived in (A.4).

A.4.1 Cylindrical geometry with constant coefficients

The analytic solutions to the ODE in cylindrical geometry with constant transport coefficients is extensively used in this thesis. Therefore, in this subsection

Constraints	ξ	ζ	k	λ	μ	Parameters
$a_2 \neq 0, a_1^2 \neq 4a_0a_2$	$e^{kx}\Psi(a, b; u)$	$e^{kx}\Phi(a, b; u)$	$\frac{\sqrt{D}-a_1}{2a_2}$	$\frac{-a_2}{2a_2k+a_1}$	$-\frac{b_2}{a_2}$	$a = B(k) / (2a_2k + a_1)$
if $b \neq 0, -1, -2, \dots$						$b = (a_2b_1 - a_1b_2) a_2^{-2}$
$a_2 \neq 0, a_1^2 \neq 4a_0a_2$	$e^{kx}x^{1-b}$	$e^{kx}x^{1-b}$	$\frac{\sqrt{D}-a_1}{2a_2}$	$\frac{-a_2}{2a_2k+a_1}$	$-\frac{b_2}{a_2}$	$a^* = a - b + 1$
if $b = 0, -1, -2, \dots$	$\Psi(a^*, 2 - b; u)$	$\Phi(a^*, 2 - b; u)$				
$a_2 = 0, a_1 \neq 0$	$e^{kx}\Psi(a, \frac{1}{2}; \beta u^2)$	$e^{kx}\Phi(a, \frac{1}{2}; \beta u^2)$	$-\frac{a_0}{a_1}$	1	$\frac{2b_2k+b_1}{-a_1}$	$a = B(k) / (2a_1)$ $\beta = -a_1 / (2b_2)$
$a_2 \neq 0, a_1^2 = 4a_0a_2$	$e^{kx}u^{\nu/2}Y(\nu, \beta\sqrt{u})$	$e^{kx}u^{\nu/2}J(\nu, \beta\sqrt{u})$	$-\frac{a_1}{a_2}$	a_2	$-\frac{b_2}{a_2}$	$\nu = 1 - (2b_2k + b_1) a_2^{-1}$ $\beta = 2\sqrt{B(k)}$
$a_2 = a_1 = 0, a_0 \neq 0$	$e^{kx}\sqrt{u}Y(1, \beta u^{3/2})$	$e^{kx}\sqrt{u}J(1, \beta u^{3/2})$	$-\frac{b_1}{2b_2}$	1	$\frac{b_1^2 - 4b_0b_2}{4a_0b_2}$	$\beta = \frac{2}{3} \left(\frac{a_0}{b_2} \right)^{1/2}$
$a_2 = a_1 = a_0 = 0$	$\exp(\lambda_1 x)$	$\exp(\lambda_2 x)$			$\lambda_{1,2} = \frac{-b_1 \mp \sqrt{b_1^2 - 4b_2b_0}}{2b_2}$	
	$u = (x - \mu) / \lambda,$	$D = a_1^2 - 4a_0a_2,$				$B(k) = b_2k^2 + b_1k + b_0$

Table A.2. Solutions of (A.15) for different values of $a_2, a_1, a_0 \in \mathbb{C}, b_2, b_1,$ and $b_0 \in \mathbb{C}.$

the argument ϱ and corresponding a and b of (A.4) are derived. Therefore, consider again the complex valued ODE in (2.14)

$$\frac{3}{2}(s + \tau_{inv}) \Theta(\rho, s) = \frac{1}{\rho} \frac{d}{d\rho} \left(\rho \chi \frac{\partial \Theta(\rho, s)}{\partial \rho} + \rho V \Theta(\rho, s) \right),$$

which can be expanded resulting in

$$0 = \chi \frac{\partial^2 \Theta(\rho, s)}{\partial \rho^2} + \frac{1}{\rho} \chi \frac{\partial \Theta(\rho, s)}{\partial \rho} + \frac{1}{\rho} V \Theta(\rho, s) + V \frac{\partial \Theta(\rho, s)}{\partial \rho} - \frac{3}{2}(s + \tau_{inv}) \Theta(\rho, s). \quad (\text{A.17})$$

Rearranging yields

$$0 = \chi \frac{\partial^2 \Theta(\rho, s)}{\partial \rho^2} + \left(\frac{1}{\rho} \chi + V \right) \frac{\partial \Theta(\rho, s)}{\partial \rho} + \left(\frac{1}{\rho} V - \frac{3}{2}(s + \tau_{inv}) \right) \Theta(\rho, s). \quad (\text{A.18})$$

This can be multiplied by $-\rho$ resulting in

$$0 = -\chi \rho \frac{\partial^2 \Theta(\rho, s)}{\partial \rho^2} + (-\chi - V \rho) \frac{\partial \Theta(\rho, s)}{\partial \rho} + \left(-V + \frac{3}{2}(s + \tau_{inv}) \rho \right) \Theta(\rho, s). \quad (\text{A.19})$$

This gives $a_2 = -\chi$, $b_2 = 0$, $a_1 = -V$, $b_1 = -\chi$, $a_0 = \frac{3}{2}(\tau_{inv} + s)$, $b_0 = -V$ in (A.15). Table A.2 can be used to calculate the resulting coefficients, which give the resulting argument ϱ and corresponding a and b in (2.15).

Appendix B

Derivation of approximations using continued fractions

This appendix summarizes a number of derivations of approximations based on continued fractions and asymptotic expansions. They lead to approximations for χ and τ_{inv} in terms of z , in approximations for χ , V , and τ_{inv} , and approximations for χ in case V and τ_{inv} are negligible.

B.1 Continued J -fraction of the ratio of Bessel functions of the second kind

The continued J -fraction of the ratio between $K_1(z)/K_0(z)$ is given in (4.1) and is based on p. 364 in [Cuyt, 2008]. It is used to calculate three approximations of which two are given in (2.47) and (4.7). The approximation considering two terms is given by

$$\frac{\Theta'}{\Theta} = -z - \frac{1}{2\rho} + \frac{1}{\rho} \left(\frac{1/4}{2z\rho + 2} \right), \quad (\text{B.1})$$

where $z = \sqrt{\frac{3}{2} \frac{i\omega + \tau_{inv}}{\chi}}$ and Θ'/Θ is defined according to (2.25). It can be written in polynomial form, i.e.

$$0 = 8\rho^2 z^2 + \left(8\rho^2 \frac{\Theta'}{\Theta} + 4\rho \right) z + 8 \frac{\Theta'}{\Theta} \rho - 3. \quad (\text{B.2})$$

This polynomial is solved in terms of z to calculate χ (see Table 4.1).

B.2 Continued C -fraction of the ratio of Bessel functions of the second kind

The following continued C -fraction of the ratio $K_1(z)/K_0(z)$ is based on p. 363 in [Cuyt, 2008]

$$\frac{K_1(z\rho)}{K_0(z\rho)} = \frac{1}{1 - \frac{\frac{1}{2z\rho}}{1 + \frac{\frac{\frac{3}{2} \frac{1}{2z\rho}}{\text{I}}}{1 + \frac{\frac{1}{2} \frac{1}{2z\rho}}{1 + \frac{\frac{\frac{5}{2} \frac{1}{2z\rho}}{\text{II}}}{1 + \dots}}}}}}. \quad (\text{B.3})$$

It is used to approximate (2.23). Here, it is chosen to truncate only at locations I and II to reduce the number of approximations. If (B.3) is truncated at location I, this results in the following polynomial in terms of z

$$0 = 4\rho z^2 + \left(3 + 4\frac{\Theta'}{\Theta}\rho\right)z + \frac{\Theta'}{\Theta}, \quad (\text{B.4})$$

which needs to be solved to find χ and τ_{inv} . In case (B.3) is truncated at location II, it gives the following polynomial, which can also be used to find χ and τ_{inv}

$$0 = 16\rho^2 z^3 + \left(36\rho + 16\rho^2\frac{\Theta'}{\Theta}\right)z^2 + \left(15 + 28\rho\frac{\Theta'}{\Theta}\right)z + 3\frac{\Theta'}{\Theta}. \quad (\text{B.5})$$

B.3 Continued T -fraction of the ratio of Bessel functions of the first kind

The following continued T -fraction of $I_1(z\rho)/I_0(z\rho)$ is based on [Cuyt, 2008](p. 363) and is useful for approximating (2.51). The continued T -fraction is given by

$$\frac{I_1(z\rho)}{I_0(z\rho)} = \frac{z\rho}{2 + z\rho|_{\text{III}} + \frac{-3z\rho}{3 + 2z\rho|_{\text{IV}} + \frac{-5z\rho}{4 + 2z\rho + \dots}}}, \quad (\text{B.6})$$

which needs to be substituted into (2.51) to find explicit solutions. This continued fraction is truncated at locations III and IV.

a) Truncating (B.6) at location III results in the polynomial,

$$0 = \rho z^2 - \frac{\Theta'}{\Theta} \rho z - 2 \frac{\Theta'}{\Theta}. \quad (\text{B.7})$$

b) Truncating (B.6) at location IV results in the following third order polynomial

$$0 = 2\rho^2 z^3 + \left(3\rho - 2\rho^2 \frac{\Theta'}{\Theta}\right) z^2 - 4\rho \frac{\Theta'}{\Theta} z - 6 \frac{\Theta'}{\Theta}. \quad (\text{B.8})$$

Again, continued fractions with more terms result in fourth order or higher order polynomials.

B.4 Continued C -fraction of the ratio of confluent hypergeometric functions of the first kind

The continued C -fraction for $\Phi(a + 1, b + 1, z) / \Phi(a, b, z)$ given in (5.7) is used to derive several approximations.

a) Truncating (5.7) at location I and substituting it into (2.50) results in the following logarithmic temperature derivative

$$\frac{\Theta'}{\Theta} = \lambda_1 + \lambda_2 \frac{1}{1 - \frac{\lambda_2 - \lambda_1 - \lambda_2}{2} \frac{\rho}{1 + \frac{\lambda_2 + (\lambda_2 - \lambda_1)}{6} \rho}}. \quad (\text{B.9})$$

This can be further simplified by partly substituting λ_1 and λ_2

$$\frac{\Theta'}{\Theta} = \frac{2\lambda_1^2 \rho + \lambda_1 \lambda_2 \rho + 2\lambda_2^2 \rho - 6 \frac{V}{\chi}}{6 - 2 \frac{V}{\chi} \rho}, \quad (\text{B.10})$$

where $2\lambda_1^2 + \lambda_1 \lambda_2 + 2\lambda_2^2 = 2 \left(\frac{V}{\chi}\right)^2 + \frac{9}{2} \frac{\tau_{inv} + \omega i}{\chi}$ such that

$$\left(6 - 2 \frac{V}{\chi} \rho\right) \frac{A'}{A} + \left(6 - 2 \frac{V}{\chi} \rho\right) i \phi' = \left(2 \left(\frac{V}{\chi}\right)^2 + \frac{9}{2} \frac{\tau_{inv} + \omega i}{\chi}\right) \rho - 6 \frac{V}{\chi}. \quad (\text{B.11})$$

By splitting (B.11) in its real and imaginary part, i.e.,

$$\left(6 - 2 \frac{V}{\chi} \rho\right) \phi' = \frac{9}{2} \frac{\omega}{\chi} \rho \quad (\text{B.12})$$

and

$$\left(6 - 2\frac{V}{\chi}\rho\right) \frac{A'}{A} = 2\left(\frac{V}{\chi}\right)^2 \rho + \frac{9}{2}\frac{\tau_{inv}}{\chi}\rho - 6\frac{V}{\chi}, \quad (\text{B.13})$$

χ can be calculated. The imaginary part for $V = 0$ yields an approximation for χ , i.e.,

$$\chi_{Is\phi} = \frac{3}{4}\frac{\omega}{\phi'}\rho \quad \text{and} \quad \tau_{Is\phi} = \frac{\omega}{\phi'}\frac{A'}{A}, \quad (\text{5.3})$$

which is also found using asymptotic expansions and in (5.3) using a continued fraction based on Bessel functions. If τ_{inv} is assumed to be zero, then solving (B.12) and (B.13) together gives

$$\chi_{\Phi 2V} = \frac{9\rho\omega}{4\phi'\left(\frac{A'}{A}\rho + 3\right)}, \quad (\text{B.14})$$

and

$$V_{\Phi 2V} = -\frac{9\frac{A'}{A}\rho\omega}{4\phi'\left(\frac{A'}{A}\rho + 3\right)}. \quad (\text{B.15})$$

The mixed case of χ , V , and τ_{inv} cannot be solved, due to the system of equations even if one harmonic is added.

b) Truncating (5.7) at location II and substituting it into (2.50) results in following logarithmic temperature derivative by substituting λ_1 and λ_2

$$\frac{\Theta'}{\Theta} = \frac{4\rho(4V^2 + 5\chi(\tau_{inv} + i\omega))}{(\rho^2(2V^2 + 5\chi(\tau_{inv} + i\omega)) - 16\rho V\chi + 40\chi^2)} - \frac{\rho^2 V(6V^2 + 19\chi(\tau_{inv} + i\omega)) + 120V\chi^2}{3\chi(\rho^2(2V^2 + 5\chi(\tau_{inv} + i\omega)) - 16\rho V\chi + 40\chi^2)}. \quad (\text{B.16})$$

The complexity of (B.16) makes it difficult to calculate approximations by hand. Therefore, Mathematica[©] has been used to calculate the approximations for χ , V , and τ_{inv} .

b1) If $\tau_{inv} = 0$, (B.16) results in

$$\chi_{\Phi 4V} = \frac{3}{2} \frac{6859\rho^3\omega\phi'}{l_2 - l_3 \left(-2\frac{A'}{A}\rho \pm l_1 + 30\right)}, \quad (\text{B.17})$$

with

$$l_1 = \sqrt{4\left(\frac{A'}{A}\rho + 15\right)^2 - 285\rho^2(\phi')^2}, \quad (\text{B.18})$$

$$l_2 = 114\rho^2(\phi')^2 \left(32\frac{A'}{A}\rho \pm l_1 + 62\right), \quad (\text{B.19})$$

and

$$l_3 = 6 \frac{A'}{A} \rho \left(15 \frac{A'}{A} \rho + 32 \right) + 680. \quad (\text{B.20})$$

There are two solutions possible, the second option ($-$ in \pm) gives a solution in a region with poor approximations and is disregarded. Hence, $+$ solution is used. The connectivity V is given by

$$V_{\Phi 4V} = \chi_{\Phi 4V} \frac{-l_1 - 17 \frac{A'}{A} \rho + 30}{19\rho}. \quad (\text{B.21})$$

b2) If A'_1/A_1 , ϕ'_1 , and ϕ'_2 are used, only one solution is found

$$\chi_{\Phi 4b} = \frac{3}{2} \frac{6859d\omega\rho^3\omega_1\phi'_1}{8(19d\omega + o_2)},$$

$$\frac{\omega_2^2 \left((dA)^2 + (\phi'_1)^2 \right) + \omega_1\phi'_2(d\omega - \omega_2\phi'_1)}{(1444d\omega^2 + 456d\omega o_2 + 45o_2^2)}, \quad (\text{B.22})$$

with

$$d\omega = \omega_1\phi'_2 - \omega_2\phi'_1 \quad (\text{B.23})$$

and

$$o_2 = \frac{A'_1}{A_1} \rho \omega_1 \phi'_2 - \frac{A'_2}{A_2} \rho \omega_2 \phi'_1 - 4d\omega. \quad (\text{B.24})$$

The corresponding V and τ_{inv} are given by

$$V_{\Phi 4b} = -\chi_{\Phi 4b} \frac{30o_2}{38\rho d\omega}, \quad (\text{B.25})$$

and (subscripts $\Psi 4b$ have been omitted)

$$\tau_{\Phi 4b} = \frac{3}{2} \chi \frac{-15 \frac{A'_1}{A_1} \rho^2 \omega \frac{1}{\chi} - 24 \left(\frac{V}{2\chi} \right)^2 \rho^2 \phi' - 120\phi'}{15\rho^2\phi'}$$

$$+ \frac{3}{2} \chi \frac{-38 \left(\frac{V}{2\chi^2} \right) \rho^2 \omega + 96 \left(\frac{V}{2\chi} \right) \rho \phi' + 60\rho\omega \frac{1}{\chi}}{15\rho^2\phi'}. \quad (\text{B.26})$$

This equation is exactly the same as (5.10).

b3) The approximation using the same truncation as (B.22) and A'_1/A_1 , A'_2/A_2 and ϕ'_1 , is given in (5.8) in the main text. Also, a T -fraction is given in [Cuyt, 2008; Jones, 1980], but it showed less accurate results than the continued C -fraction.

B.5 Continued J -fraction in case $V = \tau_{inv} = 0$

From (4.3), i.e.

$$z = - \left(\frac{A'}{A} + i\phi' + \frac{1}{2\rho} \right),$$

two other approximations can be derived in case only diffusivity is considered ($V = \tau_{inv} = 0$). Substituting z and expanding results in

$$\frac{3}{2} \frac{i\omega}{\chi} = \left(\frac{A'}{A} + \frac{1}{2\rho} \right)^2 + 2i\phi' \left(\frac{A'}{A} + \frac{1}{2\rho} \right) - (\phi')^2. \quad (\text{B.27})$$

If the imaginary part is rewritten in terms of χ , it results in

$$\chi_{s1} = \frac{3}{4} \frac{\omega}{(\phi')^2}. \quad (\text{B.28})$$

This variation was also derived in [Fredrickson, 1986] based on Bessel functions and can be derived in slab-geometry. The real part gives

$$\chi_{Kj1A} = \frac{3\omega}{4 \left(\frac{A'}{A} + \frac{1}{2\rho} \right)^2}. \quad (\text{B.29})$$

The continued fractions with more terms lead to a mix between amplitude and phase, which are complicated to solve. Hence, they are not calculated here.

B.6 Approximation for the continued S -fraction for $V = \tau_{inv} = 0$

If $\tau_{inv} = 0$ and $V = 0$, the truncation of (5.1) with the last term a_2 is given by

$$0 = \left(\left(\frac{A'}{A} + i\phi' \right) \rho^2 - 4\rho \right) \frac{3}{2} \frac{\omega i}{\chi} + 8 \left(\frac{A'}{A} + i\phi' \right). \quad (\text{B.30})$$

The real part is given by

$$0 = -\phi' \rho^2 \frac{3}{2} \frac{\omega}{\chi} + 8 \frac{A'}{A} \quad (\text{B.31})$$

and the imaginary part is given by

$$0 = \frac{A'}{A} \rho^2 \frac{3}{2} \frac{\omega i}{\chi} - 4\rho \frac{3}{2} \frac{\omega i}{\chi} + 8i\phi'. \quad (\text{B.32})$$

Solving for A'/A and ϕ' and rewriting in terms of χ yields

$$\chi_{Is2A} = \omega \frac{3\rho^3 \sqrt{4 - A'/A\rho}}{16\rho^2 \sqrt{A'/A}} \quad (\text{B.33})$$

and

$$\chi_{Is2\phi} = 3\omega\rho \frac{2 + \sqrt{4 - \rho^2 (\phi')^2}}{16\phi'}. \quad (\text{B.34})$$

B.7 Asymptotic expansion based on the Bessel function of the second kind

From [Abramowitz, 1976] the asymptotic expansion for $z\rho \approx 0$ and fixed integer order $\nu \neq 0$ is given by

$$K_\nu \sim \frac{1}{2}\Gamma(\nu) \left(\frac{1}{2}z\rho\right)^{-\nu}, \quad (\text{B.35})$$

and for order $\nu = 0$ is given by

$$K_0 \sim -\ln(z\rho). \quad (\text{B.36})$$

These can be substituted into (2.23) to describe Θ'/Θ around $z\rho \approx 0$

$$\frac{\Theta'}{\Theta} = -z \frac{\left(\frac{1}{2}\Gamma(1) \left(\frac{1}{2}z\rho\right)^{-1}\right)}{(-\ln(z\rho))}. \quad (\text{B.37})$$

Simplifying yields

$$\frac{\Theta'}{\Theta} = \frac{1}{\rho \ln(z\rho)}. \quad (\text{B.38})$$

This can again be expressed in terms of z

$$z = \rho^{-1} \exp\left(\left(\rho \frac{\Theta'}{\Theta}\right)^{-1}\right), \quad (\text{B.39})$$

which can be solved using the techniques given in Table 4.1.

Appendix C

Distribution functions of A and ϕ and numerical calculation of confidence bounds

In this appendix the PDFs and CDFs of amplitude and phase are given, which are necessary to calculate the confidence bounds on amplitude and phase. This section is partly based on [Simon, 2005; Whalen, 1971]. In addition, a short discussion is added on how to calculate the confidence bounds from PDFs or CDFs, which cannot be calculated analytically.

C.1 Distributions of amplitude and phase

The PDF of the amplitude can be found by integrating (6.3) over the phase

$$f_A(A) = \int_0^{2\pi} f_{A\phi}(A, \phi) d\phi, \quad (\text{C.1})$$

which results in

$$f_A(A) = \frac{A}{2\pi\sigma_F^2} \exp\left(-\frac{A^2 + M^2}{2\sigma_F^2}\right) \int_0^{2\pi} \exp\left(\frac{AM \cos(\theta - \phi)}{\sigma_F^2}\right) d\phi. \quad (\text{C.2})$$

The resulting amplitude distribution is given by

$$f_A(A) = \frac{A}{\sigma_F^2} \exp\left(-\frac{A^2 + M^2}{2\sigma_F^2}\right) I_0\left(\frac{AM}{\sigma_F^2}\right), \quad (\text{C.3})$$

where I_0 denotes the modified Bessel function of the first kind of zero order. The confidence bounds are calculated using the CDF. The CDF of the amplitude $F_A(R)$ can be found by integrating the PDF $f_A(A)$ from 0 to R ,

$$F_A(R) = \int_0^R f_A(A) dA = 1 - Q_1\left(\frac{M}{\sigma_F}, \frac{R}{\sigma_F}\right), \quad (\text{C.4})$$

where Q_1 denotes the Marcum Q-function [Whalen, 1971]. The Rician distribution is non-symmetric, which means that two confidence bounds need to be determined separately in terms of a confidence \mathbf{p} , e.g. $\mathbf{p} = 0.95$. A central confidence interval is constructed such that the lower bound is defined as $F_A(A_{min}) = (1 - \mathbf{p})/2$ and the upper bound as $F_A(A_{max}) = (1 + \mathbf{p})/2$. These bounds are calculated by inverting (C.4) numerically (see C.2).

The PDF of the phase ϕ is derived by integrating the CCND in polar coordinates (6.3) over A

$$f_\phi(\phi) = \int_0^\infty f_{A\phi}(A, \phi) dA. \quad (\text{C.5})$$

This integral can be solved using the substitution $\kappa = A - M \cos(\theta - \phi)$ [Simon, 2005] resulting in

$$f_\phi(\phi) = \exp\left(-\frac{M^2}{2\sigma^2}\right) \left[\frac{1}{2\pi} + \frac{M \cos(\theta - \phi)}{2\sigma_F \sqrt{2\pi}} \right. \\ \left. \exp\left(\frac{M^2 \cos^2(\theta - \phi)}{2\sigma_F^2}\right) \operatorname{erfc}\left(\frac{M \cos(\theta - \phi)}{\sigma_F \sqrt{2}}\right) \right]. \quad (\text{C.6})$$

This distribution is sometimes referred to as the Rician phase distribution [Simon, 2005]. Again, we are interested in the confidence bounds, which can be calculated via the CDF

$$F_\phi(\Phi) = \int_{-\pi}^\Phi f_\phi(\phi) d\phi \quad (\text{C.7})$$

where $-\pi < \Phi \leq \pi$. This integral does not have a closed-form expression, but can be approximated numerically, which is explained next.

C.2 Numerical calculation confidence bounds

The CDF of (6.18) necessary to calculate the confidence bounds on χ when using the product $A'/A\phi'$ and the CDF of the phase (C.7) necessary to calculate the confidence bounds on the phase do not have a closed-form expression. Therefore, here is explained how the confidence bounds can be calculated numerically exploiting properties of the integrals. The CDF of $h(\chi(\mu_p))$ defined in (6.18) is

given by the integral

$$H(X) = \int_{-\infty}^X \frac{3}{4} \frac{\omega}{\chi^2} \frac{1}{\sqrt{2\pi\sigma_p^2}} \exp\left(-\frac{\left(\frac{3\omega}{4\chi} - \mu_p\right)^2}{2\sigma_p^2}\right) d\chi. \quad (\text{C.8})$$

This integral needs to be evaluated numerically and then needs to be inverted. However, integrating from minus infinity is impractical. Therefore, this integral is split into two parts

$$H(X) = \int_{-\infty}^0 h(\chi(\mu_p)) d\chi + \int_0^X h(\chi(\mu_p)) d\chi, \quad (\text{C.9})$$

where the first term can be evaluated analytically giving

$$H_0 = \int_{-\infty}^0 h(\chi(\mu_p)) d\chi = \frac{1}{2} \left(1 - \operatorname{erf}\left(\frac{\mu_p}{\sqrt{2}\sigma_p}\right)\right). \quad (\text{C.10})$$

If the diffusion coefficient is assumed to be always positive, this term should be always smaller than the lower confidence bound $H_0 < (1 - \mathbf{p})/2$ and certainly smaller than the upper confidence bound $H_0 < (1 + \mathbf{p})/2$. This is of course not guaranteed numerically as the product $A'/A\phi'$ can become negative and hence also its confidence bounds. However, both special cases can be easily evaluated and if the lower bound is negative we have decided to simply set it to zero ($\chi > 0$). If both bounds are negative the solution is not physical. Hence, to calculate proper confidence bounds it suffices to numerically integrate

$$H(X) = H_0 + \int_{\varepsilon}^X \frac{3}{4} \frac{\omega}{\chi^2} \frac{1}{\sqrt{2\pi\sigma_p^2}} \exp\left(-\frac{\left(\frac{3\omega}{4\chi} - \mu_p\right)^2}{2\sigma_p^2}\right) d\chi, \quad (\text{C.11})$$

where 0 has been replaced by a very small number ε and verifying that $H_0 < (1 - \mathbf{p})/2$ and $H_0 < (1 + \mathbf{p})/2$.

Calculating the CDF of the phase $F_\phi(\Phi)$ is straightforward as the distribution $f_\phi(\phi)$ is symmetric around the mean θ and its integration interval is already bounded, i.e., $-\pi < \Phi \leq \pi$.

Now, the question is how to invert these relationships to find the confidence bounds X_{bnd} for $H(X_{bnd}) = (1 \pm \mathbf{p})/2$. The CDF is a (non-decreasing) monotonic function and is bounded in the domain 0 to 1. Therefore, $H(X) - (1 - \mathbf{p})/2$ has only one zero crossing at $X_{bnd} = X$, which can be found numerically using various techniques [Forsythe, 1977]. This technique is also applied to find the confidence bounds for (C.4) and (6.11). In case of (C.4) and (6.11) we found it useful to use the property $H(|X|) = |H(X)|$, which allows also the use of negative X such that an unconstrained algorithm can be used.

Bibliography

- Abramowitz, M. and Stegun, I. [1976]. *Handbook of mathematical functions: with formulas, graphs, and mathematical tables*, Dover, Mineola (NY).
- Amos, D. [1985]. A Subroutine Package for Bessel Functions of a Complex Argument and Nonnegative Order, *Technical Report SAND85- 1018 Unlimited Release UC-32*, Sandia National Laboratories.
- Amos, D. [1986]. Algorithm 644: A portable package for bessel functions of a complex argument and nonnegative order, *Acm. T. Math. Software* **12**(3): 265–273.
- Ancarani, L. U. and Gasaneo, G. [2008]. Derivatives of any order of the confluent hypergeometric function ${}_1F_1(a, b, z)$ with respect to the parameter a or b, *J. Math. Phys.* **49**: 063508.
- Anderson, M. P. [2005]. Heat as a ground water tracer, *Ground Water* **43**(6): 951–968.
- Angioni, C., Fable, E., Greenwald, M., Maslov, M., Peeters, A. G., Takenaga, H. and Weisen, H. [2009]. Particle transport in tokamak plasmas, theory and experiment, *Plasma Phys. Control. Fusion* **51**(12): 124017.
- Aroian, L. A., Taneja, V. S. and Cornwell, L. W. [1978]. Mathematical forms of the distribution of the product of two normal variables, *Commun. Stat. Theory* **7**(2): 165–172.
- Åström, K. J. [1980]. Maximum likelihood and prediction error methods, *Automatica* **16**(5): 551 – 574.
- Balescu, R. [2005]. *Aspects of anomalous transport in plasmas*, Institute of Physics, Bristol.
- Banks, H. T., Crowley, J. and Kunisch, K. [1983]. Cubic spline approximation techniques for parameter estimation in distributed systems, *IEEE Trans. Autom. Control* **28**(7): 773–786.
- Banks, H. T. and Lamm, P. K. [1985]. Estimation of variable coefficients in parabolic distributed systems, *IEEE Trans. Autom. Control* **30**(4): 386–398.

- Banks, H. T. and Kunisch, K. [1989]. *Estimation Techniques for Distributed Parameter Systems*, Birkhauser, Boston (MA).
- Bateman, H. and Erdélyi, A. [1953]. *Higher transcendental functions*, McGraw-Hill, New York (NY).
- Bhikkaji, B. and Söderström, T. [2001]. Reduced order models for diffusion systems, *Int. J. Contr.* **74**(15): 1543–1557.
- Billingsley, P. [2012]. *Probability and measure*, John Wiley and Sons, Hoboken (NJ).
- Bishop, C. M. and Connor, J. W. [1990]. Heat-pulse propagation in tokamaks and the role of density perturbations, *Plasma Phys. Control. Fusion* **32**(3): 203.
- Bornatici, M., Cano, R., Barbieri, O. D. and Engelmann, F. [1983]. Electron cyclotron emission and absorption in fusion plasmas, *Nucl. Fusion* **23**(9): 1153.
- Bowman, F. [1958]. *Introduction to Bessel functions*, Courier Dover Publications, New York (NY).
- Brillinger, D. R. [2001]. *Time series: data analysis and theory*, SIAM, Philadelphia (PA).
- Callen, J. D. and Jahns, G. L. [1977]. Experimental measurement of electron heat diffusivity in a tokamak, *Phys. Rev. Lett.* **38**: 491–494.
- Canuto, C., Hussaini, M. Y., Quarteroni, A. and Zang, T. A. [1988]. *Spectral methods in fluid dynamics*, Springer-Verlag, Berlin-Heidelberg.
- Carslaw, H. S. and Jaeger, J. C. [1959]. *Conduction of heat in solids*, Vol. 1, Clarendon Press, Oxford.
- Cernuschi, F., Russo, A., Lorenzoni, L. and Figari, A. [2001]. In-plane thermal diffusivity evaluation by infrared thermography, *Rev. Sci. Instrum.* **72**(10): 3988–3995.
- Citrin, J., Artaud, J. F., Garcia, J., Hogewij, G. M. D. and Imbeaux, F. [2010]. Impact of heating and current drive mix on the ITER hybrid scenario, *Nucl. Fusion* **50**(11): 16.
- Cox, M. G., Eiø, C., Mana, G. and Pennechi, F. [2006]. The generalized weighted mean of correlated quantities, *Metrologia* **43**(4): S268.
- Craig, C. C. [1936]. On the frequency function of xy , *Ann. Math. Stat.* **7**(1): 1–15.
- Curtain, R. F. and Zwart, H. J. [1995]. *An Introduction to Infinite-Dimensional Linear Systems Theory*, Vol. 21, Springer-Verlag, Berlin-Heidelberg.
- Curtain, R. F. and Morris, K. [2009]. Transfer functions of distributed parameter systems: A tutorial, *Automatica* **45**(5): 1101–1116.
- Cuyt, A., Petersen, V. B., Verdonk, B., Waadeland, H. and Jones, W. B. [2008]. *Handbook of continued fractions for special functions*, Springer-Verlag, Berlin-Heidelberg.

- De Haas, J. C. M., O'Rourke, J., Sips, A. C. C. and Lopes Cardozo, N. J. [1991]. Interpretation of heat and density pulse measurements in JET in terms of coupled transport, *Nucl. Fusion* **31**: 1261.
- DeBoo, J., Cirant, S., Luce, T., Manini, A., Petty, C., Ryter, F., Austin, M., Baker, D., Gentle, K., Greenfield, C., Kinsey, J. and Staebler, G. [2005]. Search for a critical electron temperature gradient in DIII-D L-mode discharges, *Nucl. Fusion* **45**(6): 494.
- DeBoo, J., Petty, C., White, A., Burrell, K., Doyle, E., Hillesheim, J., Holland, C., McKee, G., Rhodes, T., Schmitz, L. et al. [2012]. Electron profile stiffness and critical gradient studies, *Phys. Plasmas* **19**: 082518.
- deGrassie, J. S. [2009]. Tokamak rotation sources, transport and sinks, *Plasma Phys. Control. Fusion* **51**(12): 124047.
- Diamond, P. H., Itoh, S.-I., Itoh, K. and Hahm, T. S. [2005]. Zonal flows in plasma – a review, *Plasma Phys. Control. Fusion* **47**(5): R35.
- Diversi, R., Guidorzi, R. and Soverini, U. [2007]. Maximum likelihood identification of noisy input-output models, *Automatica* **43**(3): 464 – 472.
- Dudok de Wit, T., Duval, B. P., Joye, B. and Lister, J. B. [1991]. Measurement of hydrogen transport in deuterium discharges using the dynamic response of the effective mass, *Nucl. Fusion* **31**: 359.
- Emerson, R. C. [1953]. First probability densities for receivers with square law detectors, *J. Appl. Phys.* **24**(9): 1168–1176.
- Erdélyi, A. [1956]. *Asymptotic expansions*, Courier Dover Publications, New York (NY).
- Escande, D. F. and Sattin, F. [2012]. Calculation of transport coefficient profiles in modulation experiments as an inverse problem, *Phys. Rev. Lett.* **108**(12): 125007.
- Eurofusion [2015].
URL: <https://www.euro-fusion.org/>
- Forsythe, G. E., Moler, C. B. and Malcolm, M. A. [1977]. *Computer methods for mathematical computations*, Prentice Hall, Upper Saddle River (NJ).
- Fredrickson, E. D., Callen, J. D., McGuire, K., Bell, J. D., Colchin, R. J., Efthimion, P. C., Hill, K. W., Izzo, R., Mikkelsen, D. R., Monticello, D. A., V., P., Taylor, G. and Zarnstorff, M. [1986]. Heat pulse propagation studies in TFTR, *Nucl. Fusion* **26**(7): 849.
- Fredrickson, E. D., Austin, M. E., Groebner, R., Manickam, J., Rice, B., Schmidt, G. and Snider, R. [2000]. Heat pulse propagation studies on DIII-D and the Tokamak Fusion Test Reactor, *Phys. Plasmas* **7**: 5051.
- Freidberg, J. P. [2007]. *Plasma Physics and Fusion Energy*, Cambridge University Press, Cambridge.

- Gabano, J.-D. and Poinot, T. [2011]. Fractional modelling and identification of thermal systems, *Signal Process.* **91**(3): 531 – 541.
- Gambier, D. J., Evrard, M. P., Adam, J., Becoulet, A., Corti, S., Hennequin, P., Jacquinet, J., Start, D. F. H., Thomsen, K., Tubbing, B. J. D. et al. [1990]. ICRF power deposition profile and determination of the electron thermal diffusivity by modulation experiments in JET, *Nucl. Fusion* **30**(1): 23.
- Garbet, X., Mantica, P., Ryter, F., Cordey, G., Imbeaux, F., Sozzi, C., Manini, A., Asp, E., Parail, V., Wolf, R. and the JET EFDA Contributors [2004]. Profile stiffness and global confinement, *Plasma Phys. Control. Fusion* **46**(9): 1351.
- Gentle, K. W. [1988]. Dependence of heat pulse propagation on transport mechanisms: Consequences of nonconstant transport coefficients, *Phys. Fluids B-Plasma* **31**: 1105.
- Giannone, L., Erckmann, V., Gasparino, U., Hartfuss, H. J., Kuhner, G., Maassberg, H., Stroth, U. and Tutter, M. [1992]. Electron thermal conductivity from heat wave propagation in Wendelstein 7-AS, *Nucl. Fusion* **32**(11): 1985.
- Giannone, L., Baldzuhn, J., Burhenn, R., Grigull, P., Stroth, U., Wagner, F., Brakel, R., Fuchs, C., Hartfuss, H., McCormick, K. et al. [2000]. Physics of the density limit in the W7-AS stellarator, *Plasma Phys. Control. Fusion* **42**(6): 603.
- Goedheer, W. [1986]. Inference of electron heat conductivity from the propagation of a temperature perturbation in the outer confinement region of a tokamak, *Nucl. Fusion* **26**(8): 1043.
- Goodman, N. R. [1963]. Statistical analysis based on a certain multivariate complex Gaussian distribution (an introduction), *Ann. Math. Stat.* **34**(1): 152–177.
- Goodwin, G. C. and Payne, R. L. [1977]. *Dynamic system identification: experiment design and data analysis*, Academic press, New York (NY).
- Greenwald, M. [2002]. Density limits in toroidal plasmas, *Plasma Phys. Control. Fusion* **44**(8): R27.
- Haberman, R. [1983]. *Elementary applied partial differential equations*, Prentice Hall, Englewood Cliff (NJ).
- Hall, B. [2010]. *Nonparametric Estimation of Derivatives with Applications*, Doctoral dissertations, Paper 114, University of Kentucky.
URL: http://uknowledge.uky.edu/gradschool_diss/114
- Hangyu, Z., Zhengying, C., Shigeru, M., Bingzhong, F., Motoshi, G., Ping, S., Beibin, F., Xuewu, C., Ping, L., Qingwei, Y. and Xuru, D. [2014]. Spectral analysis in EUV range for study of core impurity behavior in HL-2A, *Plasma Sci. Technol.* **16**(2): 89.
- Hartfuss, H. J., Geist, T. and Hirsch, M. [1997]. Heterodyne methods in millimetre wave plasma diagnostics with applications to ECE, interferometry and reflectometry, *Plasma Phys. Control. Fusion* **39**: 1693–1769.

- Heath, M. [1997]. *Scientific computing*, McGraw-Hill, New York (NY).
- Heijmans, S. [2013]. Heat transport modeling in tokamaks : for acquiring a simulation model by using different spatial discretization methods., *Internal report, cst, no. 2013.043*, Eindhoven University of Technology.
- Hogeweyj, G. M. D., O'Rourke, J. and Sips, A. C. C. [1991]. Evidence of coupling of thermal and particle transport from heat and density pulse measurements in JET, *Plasma Phys. Control. Fusion* **33**(3): 189.
- Hogeweyj, G. M. D., Lopes Cardozo, N. J., Luca, F. D., Gorini, G., Jacchia, A. and Mantica, P. [1992]. The analysis of coupled heat and particle transport in tokamaks by means of fourier transform, *Plasma Phys. Control. Fusion* **34**: 641.
- Hözl, M., Günter, S., Classen, I., Yu, Q., the TEXTOR Team and Delabie, E. [2009]. Determination of the heat diffusion anisotropy by comparing measured and simulated electron temperature profiles across magnetic islands, *Nucl. Fusion* **49**(11): 115009.
- Howard, N. T., Greenwald, M., Mikkelsen, D. R., Reinke, M. L., White, A. E., Ernst, D., Podpaly, Y. and Candy, J. [2012]. Quantitative comparison of experimental impurity transport with nonlinear gyrokinetic simulation in an Alcator C-Mod L-mode plasma, *Nucl. Fusion* **52**(6): 063002.
- Hutchinson, I. [2002]. *Principles of Plasma Diagnostics*, second edn, Cambridge University Press, Cambridge.
- Ida, K., Inagaki, S., Sakamoto, R., Tanaka, K., Funaba, H., Takeiri, Y., Ikeda, K., Michael, C., Tokuzawa, T., Yamada, H., Nagayama, Y. et al. [2006]. Slow transition of energy transport in high-temperature plasmas, *Phys. Rev. Lett.* **96**: 125006.
- Inagaki, S., Takenaga, H., Ida, K., Isayama, A., Tamura, N., Takizuka, T., Shimozuma, T., Kamada, Y., Kubo, S., Miura, Y. et al. [2006]. Comparison of transient electron heat transport in LHD helical and JT-60U tokamak plasmas, *Nucl. Fusion* **46**(1): 133.
- Inagaki, S., Tokuzawa, T., Itoh, K., Ida, K., Itoh, S.-I., Tamura, N., Sakakibara, S., Kasuya, N., Fujisawa, A., Kubo, S. et al. [2011]. Observation of long-distance radial correlation in toroidal plasma turbulence, *Phys. Rev. Lett.* **107**: 115001.
- Inagaki, S., Tokuzawa, T., Tamura, N., Itoh, S.-I., Kobayashi, T., Ida, K., Shimozuma, T., Kubo, S., Tanaka, K., Ido, T. et al. [2013]. How is turbulence intensity determined by macroscopic variables in a toroidal plasma?, *Nucl. Fusion* **53**(11): 113006.
- Ito, K. and Kunisch, K. [2008]. *Lagrange multiplier approach to variational problems and applications*, Vol. 15, SIAM, Philadelphia (PA).
- Jacchia, A., Mantica, P., De Luca, F. and Gorini, G. [1991]. Determination of diffusive and nondiffusive transport in modulation experiments in plasmas, *Phys. Fluids B-Plasma* **3**(11): 3033–3040.

- Jahns, G. L., Soler, M., Waddell, B. V., Callen, J. D. and Hicks, H. R. [1978]. Internal disruptions in tokamaks, *Nucl. Fusion* **18**(5): 609.
- Jalloul, A., Jelassi, K., Melchior, P. and Trigeassou, J.-C. [2011]. Comparison of identification techniques for fractional models, *IEEE Multi-Conference on Systems, Signals and Devices*, pp. 1–6.
- Jenko, F., Dorland, W., Kotschenreuther, M. and Rogers, B. N. [2000]. Electron temperature gradient driven turbulence, *Phys. Plasmas* **7**(5): 1904–1910.
- Jones, W. B. and Fractions, W. J. T. [1980]. *Continued Fractions: Analytic Theory and Applications*, Vol. 11, Addison-Wesley Publishing Company, London.
- Kaufman, S. and Libby, W. F. [1954]. The natural distribution of tritium, *Phys. Rev.* **93**: 1337–1344.
- Kravaris, C. and Seinfeld, J. H. [1985]. Identification of parameters in distributed parameter systems by regularization, *SIAM J. Control Optim.* **23**(2): 217–241.
- Kroese, D. P., Taimre, T. and Botev, Z. I. [2011]. *Handbook of Monte Carlo Methods*, Vol. 706, John Wiley and Sons, Hoboken (NJ).
- Kunisch, K. and Peichl, G. [1991]. Estimation of a temporally and spatially varying diffusion coefficient in a parabolic system by an augmented Lagrangian technique, *Numer. Math.* **59**(1): 473–509.
- Lao, L., Ferron, J., Groebner, R., Howl, W., John, H. S., Strait, E. and Taylor, T. [1990]. Equilibrium analysis of current profiles in tokamaks, *Nucl. Fusion* **30**(6): 1035.
- Lin, Z., Hahm, T. S., Lee, W., Tang, W. M. and White, R. B. [1998]. Turbulent transport reduction by zonal flows: Massively parallel simulations, *Science* **281**(5384): 1835–1837.
- Ljung, L. [1993]. Some results on identifying linear systems using frequency domain data, *IEEE Conference on Decision and Control*, pp. 3534–3538.
- Ljung, L. [1999]. *System identification: theory for the user*, 2nd edn, Prentice Hall, Upper Saddle River (NJ).
- Lopes Cardozo, N. J., Tubbing, B. D., Tibone, F. and Taroni, A. [1988]. Heat pulse propagation: Diffusive models checked against full transport calculations, *Nucl. Fusion* **28**(7): 1173.
- Lopes Cardozo, N. J. and de Haas, J. C. M. [1990]. Heat pulse analysis in JET limiter and X-point plasmas, *Nucl. Fusion* **30**(3): 521.
- Lopes Cardozo, N. J. [1995]. Perturbative transport studies in fusion plasmas, *Plasma Phys. Control. Fusion* **37**: 799.
- Luce, T. C., Petty, C. C. and de Haas, J. C. M. [1992]. Inward energy transport in tokamak plasmas, *Phys. Rev. Lett.* **68**: 52–55.

- Luke, Y. L. [1969]. *The special functions and their approximations*, Vol. 1, Academic Press, New York (NY).
- Magnus, W., Oberhettinger, F. and Soni, R. [1966]. *Formulas and theorems for the special functions of mathematical physics*, Vol. 257, Springer-Verlag, Berlin-Heidelberg.
- Mantica, P., Peters, M., De Luca, F., De Lauri, A., Gorini, G., Hogeweij, G. M. D., Jacchia, A. and Lopes Cardozo, N. J. [1996]. Radial profile and q dependence of electron heat diffusion measured with ECH modulation in RTP, *Nucl. Fusion* **36**(10): 1317.
- Mantica, P., Gorini, G., Hogeweij, G. M. D., Lopes Cardozo, N. J. and Schilham, A. M. R. [2000]. Heat convection and transport barriers in low-magnetic-shear rijnhuizen tokamak project plasmas, *Phys. Rev. Lett.* **85**: 4534–4537.
- Mantica, P. and Ryter, F. [2006a]. Perturbative studies of turbulent transport in fusion plasmas, *C. R. Phys.* **7**(6): 634–649.
- Mantica, P., Ryter, F., Capuano, C., Fahrbach, H. U., Leuterer, F., Suttrop, W., Weiland, J. and ASDEX Upgrade Team [2006b]. Investigation of electron heat pinch in ASDEX Upgrade, *Plasma Phys. Control. Fusion* **48**(3): 385.
- Mantica, P., Srintzi, D., Tala, T., Giroud, C., Johnson, T., Leggate, H., Lerche, E., Loarer, T., Peeters, A., Salmi, A. et al. [2009]. Experimental study of the ion critical-gradient length and stiffness level and the impact of rotation in the JET tokamak, *Phys. Rev. Lett.* **102**(17): 175002.
- Mantica, P., Tala, T., Ferreira, J., Peeters, A., Salmi, A., Srintzi, D., Weiland, J., Brix, M., Giroud, C., Corrigan, G. et al. [2010]. Perturbative studies of toroidal momentum transport using neutral beam injection modulation in the Joint European Torus: Experimental results, analysis methodology, and first principles modeling, *Phys. Plasmas* **17**(9): 092505.
- Martin, B. [2012]. *Statistics for Physical Sciences: An Introduction*, Academic Press, Waltham (MA).
- McCracken, G. and Stott, P. [2005]. *Fusion, The Energy of the Universe*, Elsevier Academic Press, Burlington (MA).
- Mechhoud, S., Witrant, E., Dugard, L. and Moreau, D. [2015]. Estimation of heat source term and thermal diffusion in tokamak plasmas using a Kalman filtering method in the early lumping approach, *IEEE T. Contr. Syst. T.* **23**(2): 449–463.
- Mochi, M., Pacelli, G., Recchioni, M. C. and Zirilli, F. [1999]. Inverse problem for a class of two-dimensional diffusion equations with piecewise constant coefficients, *J. Optimiz. Theory App.* **100**(1): 29–57.
- Monteyne, G. [2013]. *Identification in nuclear and thermal energy: Moderator temperature coefficient estimation via noise analysis and black-box Modeling of Heat Transfer*, PhD thesis, Vrije Universiteit Brussel.

- Moret, J. M., Wit, T., Joye, B. and Lister, J. B. [1993]. Investigation of plasma transport processes using the dynamical response of soft X-ray emission, *Nucl. Fusion* **33**: 1185–1200.
- Moret, J. M., Duval, B. P., Le, H. B., Coda, S., Felici, F. and Reimerdes, H. [2015]. Tokamak equilibrium reconstruction code LIUQE and its real time implementation, *Fusion Eng. Des.* **91**(0): 1 – 15.
- Murphy, G. M. [1960]. *Ordinary differential equations and their solutions*, Van Nostrand, New York (NY).
- Nielsen, N. [1906]. *Handbuch der theorie der Gammafunktion*, Von B.G. Teubner, Leipzig.
- Oliveira, A., Teresa, A. and Seijas-Macias, A. [2013]. The influence of ratios and combined ratios on the distribution of the product of two independent gaussian random variables, *59th World Statistics Congress of the International Statistical Institute*.
- Pandya, S. N., Peterson, B. J., Sano, R., Mukai, K., Drapiko, E. A., Alekseyev, A. G., Akiyama, T., Itomi, M. and Watanabe, T. [2014]. Calibration of a thin metal foil for infrared imaging video bolometer to estimate the spatial variation of thermal diffusivity using a photo-thermal technique, *Rev. Sci. Instrum.* **85**(5): 054902.
- Peters, M. [1996]. *Electron Heat Transport in Current Carrying and Currentless Thermonuclear Plasmas: Tokamaks and Stellarators compared*, PhD thesis, Eindhoven University of Technology.
- Peterson, B. J. [2000]. Infrared imaging video bolometer, *Rev. Sci. Instrum.* **71**(10): 3696–3701.
- Pintelon, R., Schoukens, J. and Rolain, Y. [2003]. Uncertainty of transfer function modelling using prior estimated noise models, *Automatica* **39**(10): 1721–1733.
- Pintelon, R., Schoukens, J., Pauwels, L. and Van Gheem, E. [2005]. Diffusion systems: Stability, modeling, and identification, *IEEE Trans. Instrum. Meas.* **54**(5): 2061–2067.
- Pintelon, R., Schoukens, J., Vandersteen, G. and Barbé, K. [2010]. Estimation of non-parametric noise and FRF models for multivariable systems-Part I: Theory, *Mech. Syst. Signal Pr.* **24**(3): 573–595.
- Pintelon, R. and Schoukens, J. [2012]. *System Identification: A Frequency Domain Approach*, John Wiley and Sons, Hoboken (NJ).
- Polyanin, A. D. and Zaitsev, V. F. [2003]. *Handbook of Exact Solutions for Ordinary Differential Equations*, Vol. 2, Chapman & Hall/CRC, London.
- Prater, R. [2004]. Heating and current drive by electron cyclotron waves, *Phys. Plasmas* **11**(5): 2349–2376.

- Rafajlowicz, E. [1983]. Optimal experiment design for identification of linear distributed-parameter systems: Frequency domain approach, *IEEE Trans. Autom. Control* **28**(7): 806–808.
- Rojas, C. R., Welsh, J. S., Goodwin, G. C. and Feuer, A. [2007]. Robust optimal experiment design for system identification, *Automatica* **43**(6): 993–1008.
- Rosenberry, D. O. and LaBaugh, J. W. [2008]. Field techniques for estimating water fluxes between surface water and ground water, *Technical report*, Rep. 4-D2, 128 pp, U.S. Geological Survey.
- Roux, N., Tanaka, S., Johnson, C. and Verrall, R. [1998]. Ceramic breeder material development, *Fusion Eng. Des.* **41**(1–4): 31–38.
- Ryter, F., Tardini, G., Luca, F. D., Fahrbach, H.-U., Imbeaux, F., Jacchia, A., Kirov, K., Leuterer, F., Mantica, P., Peeters, A., Pereverzev, G., Suttrop, W. and the ASDEX Upgrade Team [2003]. Electron heat transport in ASDEX Upgrade: experiment and modelling, *Nucl. Fusion* **43**(11): 1396.
- Ryter, F., Angioni, C., Peeters, A. G., Leuterer, F., Fahrbach, H.-U. and Suttrop, W. [2005]. Experimental study of trapped-electron-mode properties in tokamaks: Threshold and stabilization by collisions, *Phys. Rev. Lett.* **95**: 085001.
- Ryter, F., Dux, R., Mantica, P. and Tala, T. [2010]. Perturbative studies of transport phenomena in fusion devices, *Plasma Phys. Control. Fusion* **52**: 124043.
- Sattin, F., Escande, D. F., Auriemma, F., Urso, G. and Terranova, D. [2014]. Difficulties and solutions for estimating transport by perturbative experiments, *Plasma Phys. Control. Fusion* **56**(11): 114008.
- Sattler, S. and Hartfuss, H. J. [1993]. Intensity interferometry for measurement of electron temperature fluctuations in fusion plasmas, *Plasma Phys. Control. Fusion* **35**(9): 1285.
- Schoukens, J. and Pintelon, R. [1991]. *Identification of linear systems: a practical guideline to accurate modeling*, Pergamon press, New York (NY).
- Schoukens, J., Pintelon, R., Vandersteen, G. and Guillaume, P. [1997]. Frequency-domain system identification using non-parametric noise models estimated from a small number of data sets, *Automatica* **33**(6): 1073–1086.
- Seaborn, J. B. [1991]. *Hypergeometric functions and their applications*, Springer-Verlag, Berlin-Heidelberg.
- Seijas-Macias, A. and Oliveira, A. [2012]. An approach to distribution of the product of two normal variables, *Discussiones Mathematicae Probability and Statistics* **32**: 87–99.
- Simon, M. K. and Alouini, M.-S. [2005]. *Digital communication over fading channels*, Vol. 95, John Wiley and Sons, Hoboken (NJ).

- Slater, L. [1960]. *Confluent hypergeometric functions*, Cambridge University Press, Cambridge.
- Smith, G. D. [1985]. *Numerical solution of partial differential equations: finite difference methods*, Oxford University Press, Oxford.
- Söderström, T. and Halvarsson, S. [1999]. Parameter estimation for diffusion models, *Technical report*, Dept. of Information Technology, Uppsala University, Sweden.
URL: <http://www.it.uu.se/research/reports/1999-003/1999-003.pdf>
- Söderström, T. [2007]. Errors-in-variables methods in system identification, *Automatica* **43**(6): 939 – 958.
- Söderström, T., Hong, M., Schoukens, J. and Pintelon, R. [2010]. Accuracy analysis of time domain maximum likelihood method and sample maximum likelihood method for errors-in-variables and output error identification, *Automatica* **46**(4): 721–727.
- Soler, M. and Callen, J. [1979]. On measuring the electron heat diffusion coefficient in a tokamak from sawtooth oscillation observations, *Nucl. Fusion* **19**(6): 703.
- Spakman, G. W., Hogeweyj, G. M. D., Jaspers, R., Schüller, F. C., Westerhof, E., Boom, J. E., Classen, I. G. J., Delabie, E., Domier, C., Donné, A. J. H. et al. [2008]. Heat pulse propagation studies around magnetic islands induced by the Dynamic Ergodic Divertor in TEXTOR, *Nucl. Fusion* **48**: 115005.
- Tala, T., Zastrow, K.-D., Ferreira, J., Mantica, P., Naulin, V., Peeters, A. G., Tardini, G., Brix, M., Corrigan, G., Giroud, C. and Srintzi, D. [2009]. Evidence of inward toroidal momentum convection in the JET Tokamak, *Phys. Rev. Lett.* **102**: 075001.
- Tardini, G., Ferreira, J., Mantica, P., Peeters, A., Tala, T., Zastrow, K. D., Brix, M., Giroud, C., Pereverzev, G. V. and contributors, J. [2009]. Angular momentum studies with NBI modulation in JET, *Nucl. Fusion* **49**(8): 085010.
- Terry, P. W. [2000]. Suppression of turbulence and transport by sheared flow, *Rev. Mod. Phys.* **72**: 109–165.
- Ucinski, D. [2004]. *Optimal measurement methods for distributed parameter system identification*, CRC Press, Boca Raton (FL).
- Valério, D. and da Costa, J. S. [2007]. Identification of fractional models from frequency data, *Advances in Fractional Calculus*, Springer-Verlag, Berlin-Heidelberg, pp. 229–242.
- van Berkel, M., Vandersteen, G., Zwart, H. J., Hogeweyj, G. and de Baar, M. R. [2013]. Maximum likelihood estimation of diffusion and convection in tokamaks using infinite domains, *IEEE Multi-conference on Systems and Control*, pp. 1230–1234.
- van Berkel, M., Zwart, H. J., Tamura, N., Hogeweyj, G. M. D., Inagaki, S., de Baar, M. R. and Ida, K. [2014a]. Explicit approximations to estimate the perturbative diffusivity in the presence of convectivity and damping I Semi-infinite slab approximations, *Phys. Plasmas* **21**: 112507.

- van Berkel, M., Hogeweij, G. M. D., Tamura, N., Zwart, H. J., Inagaki, S., de Baar, M. R. and Ida, K. [2014b]. Explicit approximations to estimate the perturbative diffusivity in the presence of convectivity and damping II Semi-infinite cylindrical approximations, *Phys. Plasmas* **21**: 112508.
- van Berkel, M., Tamura, N., Hogeweij, G. M. D., Zwart, H. J., Inagaki, S., de Baar, M. R. and Ida, K. [2014c]. Explicit approximations to estimate the perturbative diffusivity in the presence of convectivity and damping III Cylindrical approximations for heat waves traveling inwards, *Phys. Plasmas* **21**: 112509.
- van Berkel, M., Zwart, H. J., Hogeweij, G. M. D., Vandersteen, G., van den Brand, H., de Baar, M. R. and the ASDEX Upgrade Team [2014d]. Estimation of the thermal diffusion coefficient in fusion plasmas taking frequency measurement uncertainties into account, *Plasma Phys. Control. Fusion* **56**: 105004.
- van Berkel, M., Vandersteen, G., Geerardyn, E., Pintelon, R., Zwart, H. J. and de Baar, M. R. [2014e]. Frequency domain sample maximum likelihood estimation for spatially dependent parameter estimation in PDEs, *Automatica* **50**(8): 2113 – 2119.
- Vogel, C. R. [2002]. *Computational methods for inverse problems*, SIAM, Philadelphia (PA).
- von Kamke, E. [1959]. *Differentialgleichungen: Lösungsmethoden und Lösungen*, Geest & Portig, Leipzig.
- Wagner, F. and Stroth, U. [1993]. Transport in toroidal devices-the experimentalist's view, *Plasma Phys. Control. Fusion* **35**(10): 1321.
- Ware, R. and Lad, F. [2003]. Approximating the distribution for sums of products of normal variables, *Technical report UCDMS 15*, University of Canterbury, England.
URL: <http://www.math.canterbury.ac.nz/research/ucdms2003n15.pdf>
- Wesson, J. [2011]. *Tokamaks*, Vol. 149, Oxford University Press, Oxford.
- Whalen, A. D. [1971]. *Detection of signals in noise*, Vol. 6, Academic Press, New York (NY).
- Witvoet, G., de Baar, M. R., Westerhof, E., Steinbuch, M. and Doelman, N. J. [2011]. Systematic design of a sawtooth period feedback controller using a Kadomtsev-Porcelli sawtooth model, *Nucl. Fusion* **51**(7): 073024.
- Wolfram Research [2014]. Mathematica implementation of ${}_1F_1$, i.e., $\Phi(a, b; \varrho)$.
URL: <http://functions.wolfram.com/HypergeometricFunctions/Hypergeometric1F1>
- Zurro, B., Hollmann, E., Baciero, A., Ochando, M., Medina, F., McCarthy, K., Blanco, E., de la Cal, E., Carralero, D., Pedrosa, M. et al. [2011]. Transport studies using laser blow-off injection of low-Z trace impurities injected into the TJ-II stellarator, *Nucl. Fusion* **51**(6): 063015.

Summary

Estimation of heat transport coefficients in fusion plasmas

In the future, sustainable, clean, and safe power plants are needed. A promising future energy source that could possibly fulfill these requirements is nuclear fusion. In tokamaks and stellarators, two different types of nuclear fusion reactors, a hot plasma is magnetically confined. The magnetized plasma consists of nested flux surfaces, in which the magnetic field lines are embedded. As the transport of heat and particles parallel to the magnetic field lines is significantly higher than the perpendicular transport, the flux surfaces can be considered to have constant temperature. Consequently, the transport perpendicular to the flux surfaces determines the quality of the confinement and hence the reactor performance (efficiency). As such transport is generally modeled by a one-dimensional heat equation with as effective transport coefficients, the diffusivity, convectivity, and damping.

The transport of heat and particles due to Coulomb collisions between ions and electrons in tokamaks and stellarators can be calculated in detail using the neo-classical theory. The experimentally determined diffusivity exceeds the theoretical predictions by a few orders of magnitude. This difference is attributed to turbulent transport mechanism. Intriguingly, in some cases the turbulence can be damped.

Various physics oriented studies have been performed to study the transport and its intriguing behavior. A standard method is to follow the propagation of heat waves through the plasma as a probe for the transport. These heat waves are often induced using a localized heat source, e.g., electron cyclotron resonance heating. Various approximations have been put forward in the literature to explicitly derive the transport coefficients from the experimentally measured amplitude and phase of the perturbation. However, these methods generally determine only the diffusivity and the analysis is limited to a single harmonic. In addition, a systematic analysis of the validity of the resulting diffusivity was not done.

Therefore, in this thesis, the methods to estimate the transport coefficients in various geometries, i.e., the diffusivity, convectivity, and damping, are systematically re-assessed. New explicit approximations are introduced to estimate the transport coefficients, and the concept of Maximum Likelihood Estimation to improve the determination of the transport coefficients under noisy conditions is developed. In addition, the confidence and the validity of the transport coefficients are determined.

An important aspect of this thesis is that it introduces a number of new approximations to directly estimate the perturbative diffusivity, convectivity, and damping in slab and cylindrical geometry from measurement data. These approximations are in-line with the standard methods used in the fusion literature, because they also use the logarithmic spatial derivative of the amplitude and the spatial derivative of the phase of the heat waves induced by a localized heat source. Different approximations are necessary in cylindrical geometry for heat waves that travel towards the wall and towards the center, which is a distinction not made within the literature. Therefore, next to the classically used semi-infinite domain also a Neumann boundary condition is used to derive approximations. The approximations are derived based on one or two harmonics using continued fractions and asymptotic expansions of Bessel functions and Confluent Hypergeometric functions, and are based on standard assumptions used in the literature, e.g., constant transport coefficients.

The quality of the different approximations depends on the combination of the frequency of the modulation, transport coefficients, and radius. However, by combining various approximations the transport coefficients can be estimated well over a wide parameter space and for various regimes. This is under the assumption that the spatial derivatives of amplitude and phase are correct, that the parameters are not estimated near the real boundary, and that local parameter changes are small. As this is often not the case, the effect of these errors on the estimation of the transport coefficients is studied.

Another important aspect is that measurements used to estimate the diffusivity suffer from stochastic noise. Therefore, accurate estimation of the diffusivity should take this into account, which is not the case for the derived approximations in the literature and the newly introduced approximations. As such diffusivity estimates using these approximations have often an unnecessarily large uncertainty and suffer from a bias, i.e., a difference between the estimated value and the actual value that remains even if more measurements are added. If specifically the slab geometry approximations are analyzed, the probability density function of the resulting diffusivity is given by an inverse non-central chi-square distribution if the measurement noise in the frequency domain is given by a Complex Circular Normal Distribution. Consequently, the diffusivity that is found by sampling this inverse distribution will always be biased, and averaging of multiple estimated diffusivities will not necessarily improve the estimation. Based on this distribution also confidence bounds are constructed to

illustrate the uncertainty in the diffusivity using different approximations, which are equivalent in the noiseless case. To reduce the uncertainty when combining different diffusivity estimates a different method based on weighted averaging with the variances is suggested, which reduces the uncertainty significantly. Results are presented for both slab and cylindrical geometry approximations based on the noise properties of ASDEX Upgrade measurements. The results clearly show that it is impossible to get an unbiased estimate with minimum variance of the diffusivity. On the other hand, the method is explicit such that it is easily implementable.

It is possible to get an unbiased estimate of the transport coefficients with minimum variance. Therefore, a new method is developed based on sample Maximum Likelihood Estimation (MLE) in the frequency domain. This method directly analyzes the resulting Fourier coefficients from perturbative transport experiments using an optimization algorithm. Hence, it also avoids the use of spatial derivatives of amplitude and phase, which are difficult to estimate from noisy measurements. Instead, local transfer functions based on semi-infinite domains are used, which describe the transport coefficients between two measurement points. This model (transfer function) is chosen, because it is the most local approximation and follows the standard assumptions and approximation steps used in the literature. As such its results are much better comparable to the methods used in the literature. The MLE estimates the transport coefficients with minimum variance given some assumptions, which is quantified through confidence bounds. In addition, different validation tests can be applied to verify if the estimated transport coefficients belonging to the transport model really describe the experimental data.

Finally, the MLE is extended to take three measurement points into account, giving the most local estimate of the transport coefficients without making additional assumptions on the boundary conditions. Hence, it does not suffer from the errors generally occurring when using semi-infinite domains. The three point MLE still allows to use a cost function validation test and allows for the estimation of the confidence bounds. The MLE methods are successfully applied to simulations of a heat equation (parabolic PDE) with varying transport coefficients.

Societal summary

Estimation of heat transport coefficients in fusion plasmas

Our daily price of living is significantly determined by energy prices. In addition, the most important current energy sources result in undesired emissions and waste, which negatively influences our living environment. An example is the burning of fossil fuels resulting in the emission of greenhouse gases. Therefore, there is an increasing need for cheaper and cleaner energy sources.

A possible new energy source, which is clean and virtually inexhaustible is the nuclear fusion of lightweight atoms, a process very similar to how our sun produces its energy. However, to achieve nuclear fusion in a reactor we need to minimize the heat losses to sustain the fusion reaction. Therefore, it is necessary to investigate and reduce the heat losses to achieve fusion energy production.

In the PhD-thesis of Matthijs van Berkel advanced methods are developed to get a better understanding of what drives these heat losses. These losses can be described in terms of transport coefficients, diffusivity and convectivity. They are determined by analyzing temperature fluctuations at different spatial locations in the reactor. This allows us to obtain a better understanding of the heat losses. This better understanding enables us to further reduce the heat losses and brings us closer to controlled fusion energy production in a reactor. In addition, many other applications in physics exist in which diffusion and convection of heat, and hence, the physical parameters such as the transport coefficient, play an important role. The developed methods can also be used in those applications.

Acknowledgements

In the past four years I have been part of four institutions and have been living outside the Netherlands for almost one and a half year. In this time I met a number of extraordinary people, who helped me with my research and made me feel at home wherever I was.

First, I want to thank my co-promotor Hans Zwart. Hans, without your support, down to earth mathematical explanations, critical look, our weekly meetings and telephone sessions, corrections both mathematical and content wise, this thesis would not have existed. Especially, I am thankful for your quick processing of the heaps of paperwork with which I regularly spammed your mailbox.

I am also very grateful to my promoters Marco de Baar and Gerd Vandersteen. Marco, your enthusiasm, goal driven approach, and taking the time to aid me when it was really necessary was a great help bringing this project to a good end. I also want to specifically thank you for taking the time almost every week on skype when I was in Japan. I also really enjoyed your optimism, but as you know there were a few days when I wished you left your rose-tinted glasses at home. Gerd, a long time ago you asked me to come to the VUB and work together. This has had a huge impact on me and this thesis. Without this opportunity, I would probably still be playing in the fusion sandbox. I really enjoyed working together and the evenings that followed after a working day, which never made the trip to Brussels feel as a burden.

I also want to specifically thank Dick Hogewei. You were my tower of strength when it came to fusion and transport. Your answers were always to the point and I could always ask you for help. Also I am thankful you were open to the system theory ideas, which made working together much easier for me.

I also want to express my gratitude to my other committee members; Siep Weiland, Niek Lopes Cardozo, and Katsumi Ida for taking the time to read my thesis and for the discussions we had. Especially, I want to thank Niek Lopes Cardozo again as he was also part of my graduation committee and Ida-sensei

for receiving me in NIFS and for the inspiring conversations we had.

I also want to thank my BEP students; Marc, Bas, Joep, and Stefan for their effort and contributions. In addition, I want to thank Maarten Steinbuch for providing the facilities and support for performing this research and the fun times during the conferences, especially those in Brussels and Hyderabad.

Living as a nomad between different institutions also means I shared offices with many persons, which is not always easy, in particular, if you want to work quietly. In my first period at the TU/e, I had the pleasure to share my office with Stijn, Maarten, and Gillis. Then, I came into the warm bath in Brussels and I had the pleasure of sharing my office with Griet and Diana. In the meantime, I had a ghost office in Eindhoven, which I regularly haunted till the end of my PhD (and maybe beyond). Thanks for your hospitality, Bart, Nick, Chris, Menno, Emanuel, Behnam, Victor, and Xi, and for taking care of my books during my absence. Back at the TU/e, I had the pleasure of sharing the office with my study friend Pieter, whom not only provided his bed in the past, but also good advice and introduced me to the stressful live of a PhD student. Unfortunately, I rarely saw him after he was moved up north.

Most importantly, I want to thank Hugo. He has been my officemate for the most extensive time. Hugo, not only did you help me to understand physics and physicists better, we had a great time making jokes about almost everything. Your critical view and help improved this work significantly, thank you so much. I also apologize for the dusty office after the knocking incident.

Also I had some very nice officemates in Japan; Ohno-san, Pandya-san, and Sano-san. Specifically, I want to thank Ohno-san with helping me move, translating my rental contract, and driving me around when necessary, but more importantly for sharing my fascination for cheap Japanese sushi.

At this point, I also want to specifically thank a number of my great colleagues and supervisors at the National Institute for Fusion Science. In the first place, I want to thank Naoki Tamura for taking care of me during my stay at NIFS. Hiroe Igami who helped me with setting up my crazy excitations and who was imperative in making the LHD experiments a success. The same holds for Tatsuya Kobayashi who helped me with almost everything related to LHD and with whom I had a lot of fun during the nomikai. Also I want to express my gratitude to everyone in NIFS who made me feel at home, especially, Akiyama-san, Aoki-san, Hayashi-san, Kameyama-san, Mukai-san, Moon-san, Wang-san, Timo, Byron, and Ken (for our evening bus history sessions).

I should certainly not forget to thank the proffice, Rik, Johan, and Yves, for allowing me to come as a Hollander to the VUB and the great input they gave me after eavesdropping my conversations with Gerd. This also holds for my colleagues who made me feel at home in Brussels, especially, Adam, Alexander, Anna, Hannes, John, Koen, Maarten, Matthias, and Roland. I specifically want to thank Egon for always helping out, and the mini courses when I was learning the frequency way. I also want to thank Uwe for the fruitful collaboration.

I noticed that the HNS-group contains most of the sociable people, which still astonishes me when you think what they are doing behind their desks. Thanks, Bas, Behnam, Tom, Duarte, Niek, Eelco, and Victor. Of course I want to thank all the members of -1 (and Nick's lab) with whom I regularly shared coffee and beer during various occasions, especially, Alessandro, Benjamin, Bram, Cesar, David, Dennis, Elise, Emilia, Frank, Janno, Joost, Joris, Kees, Koos, Michiel, Ran, Rob van G., Rolf, Robbert (old and new one), Rick and Annemiek van der Maas, Sinan, Sava, Tom, Vital, Thijs, Thijs and Tijs (from whom I inherited the friends of WFW). Ohh yes, there were these two other guys who joined Uncle Sam. Nick and Menno, I miss you guys and the many fun activities we had!

I also want to thank a number of the staff members, specifically, Petra, Geertje, Rob, and Tom, for the nice conversations I had with them during my PhD, which also made live at 0 pleasurable.

This acknowledgements would be far from complete without thanking my fusion colleagues for everything we did together Hugo, Bart, Gert, Gillis, Bert, Thomas, Federico, Menno, and Pieter Nuij. I want to specifically thank Gert and Pieter for laying the foundation of this thesis during my graduation project. It is also important to mention the members at the other side of the road (physics) and those at FOM DIFFER who made the FOM120-meetings and conferences enjoyable, especially, Tony Donné, Merlijn Jakobs, Hans Oosterbeek, Willem Haverkort, Wolf Weymiens, Stefan Paquay, and Jonathan Citrin.

On a more personal note, I want to thank my two high school friends, Jack and Jeroen, for the great times, holidays, parties, and experiences we had together in the last 4 years (and the 14 years before that) and my friends Erik and Pieter whom all were a great support in the last four years. In Japan there are also a number of important people who always supported me, thanks, Yuta, Renat, Yukimi, Noboru, and Christine. Thanks to Kiyo I also met a new group of people, Chika, Moises, Kazue, Pon-chan, Hiroyo, Yuko, Yuka and James, thank you for so openly receiving me and for all the fun times we had within and outside Japan in the last two and half years.

Finally, I want to thank my family for their unwavering support and for always providing a home, Mathieu, Jutta, Jasper, Anju, and not to forget Toine and Tinie. Also, I want to thank Okaa-san for her hospitality and raising such a wonderful daughter. However, first and foremost, I want to thank my saint for always being there and supporting me in everything, but most of all for being so much fun.

List of publications

Peer-reviewed journal articles

- van Berkel, M., Zwart, H. J., Tamura, N., Hogeweij, G. M. D., Inagaki, S., de Baar, M. R. and Ida, K. [2014]. Explicit approximations to estimate the perturbative diffusivity in the presence of convectivity and damping I Semi-infinite slab approximations, *Phys. Plasmas* **21**: 112507.
- van Berkel, M., Hogeweij, G. M. D., Tamura, N., Zwart, H. J., Inagaki, S., de Baar, M. R. and Ida, K. [2014]. Explicit approximations to estimate the perturbative diffusivity in the presence of convectivity and damping II Semi-infinite cylindrical approximations, *Phys. Plasmas* **21**: 112508.
- van Berkel, M., Tamura, N., Hogeweij, G. M. D., Zwart, H. J., Inagaki, S., de Baar, M. R. and Ida, K. [2014]. Explicit approximations to estimate the perturbative diffusivity in the presence of convectivity and damping III Cylindrical approximations for heat waves traveling inwards, *Phys. Plasmas* **21**: 112509.
- van Berkel, M., Zwart, H. J., Hogeweij, G. M. D., Vandersteen, G., van den Brand, H., de Baar, M. R. and the ASDEX Upgrade Team [2014]. Estimation of the thermal diffusion coefficient in fusion plasmas taking frequency measurement uncertainties into account, *Plasma Phys. Control. Fusion* **56**: 105004.
- van Berkel, M., Vandersteen, G., Geerardyn, E., Pintelon, R., Zwart, H. J. and de Baar, M. R. [2014]. Frequency domain sample maximum likelihood estimation for spatially dependent parameter estimation in PDEs, *Automatica* **50**(8): 2113 – 2119.
- van Berkel, M., Witvoet, G., de Baar, M. R., Nuij, P. W. J. M., ter Morsche, H. G. and Steinbuch, M. [2011]. Real-time wavelet detection of crashes in limit cycles of non-stationary fusion plasmas, *Fusion Eng. Des.* **86**(12): 2908–2919.

Submitted journal articles

- Schneidewind, U., van Berkel, M., Anibas, C., Vandersteen, G., Schmidt, C., Joris, I., Seuntjens, P., Batelaan, O. and Zwart, H.J. [2015]. LPMLE3 - A novel method to quantify vertical variations of exchange flux across streambeds using heat as a tracer, *Submitted to Water Resour. Res.*

Peer-reviewed articles in conference proceedings

- van Berkel, M., Vandersteen, G., Zwart, H. J., Hogeweij, G. M. D. and de Baar, M. R. [2013]. Maximum likelihood estimation of diffusion and convection in tokamaks using infinite domains, *IEEE Multi-conference on Systems and Control*, pp. 1230–1234, Hyderabad, India.
- van Berkel, M., Witvoet, G., de Baar, M. R., Nuij, P. W. J. M., ter Morsche, H. G. and Steinbuch, M. [2012]. Real-time period determination for relaxation oscillators using wavelets, *Proceedings of the American Control Conference*, pp. 5055–5060, Montreal, Canada.
- de Baar, M. R., Bongers, W. A., Berkel, M. van, Doelman, N. J., Hennen, B. A., Nuij, P. W. J. M., Oosterbeek, J. W., Steinbuch, M. and Witvoet, G. [2011]. Control of sawteeth and neo-classical tearing modes in tokamaks using electron cyclotron waves, *Proceedings of the 2011 IEEE International Conference on Control Applications*, pp. 294–300, Denver, (CO).

Presentations published as abstracts

- van den Brand, H., de Baar, M. R., van Berkel, M., Bongers, W. A., Doelman, N., Giannone, L., Kasperek, W., Stober, J. K., Westerhof, E. and the ASDEX Upgrade team [2014]. Detection of MHD instabilities with ECE, *18th Joint Workshop on Electron Cyclotron Emission and Electron Cyclotron Resonance Heating (EC-18)*, Nara, Japan
- van Berkel, M., de Baar, M. R., Hogeweij, G. M. D., van den Brand, H., Zwart, H. J., Vandersteen, G. and the ASDEX Upgrade team [2014]. How to do more with ECE noise?, *18th Joint Workshop on Electron Cyclotron Emission and Electron Cyclotron Resonance Heating (EC-18)*, Nara, Japan.
- van Berkel, M., Vandersteen, G. and de Baar, M. R. [2013]. Identification of heat transport in fusion plasmas, *32nd Benelux Meeting on Systems and Control*, Houffalize, Belgium.
- van Berkel, M., Hogeweij, G. M. D., Vandersteen, G. and de Baar, M. R. [2012]. Identification of the local heat-diffusion in fusion plasmas, *17th Joint Workshop on Electron Cyclotron Emission and Electron Cyclotron Resonance Heating (EC-17)*, Deurne, The Netherlands.

- van Berkel, M. and de Baar, M. R. [2011]. Wavelet analysis for real-time determination of the sawtooth behavior in fusion plasmas, *30th Benelux Meeting on Systems and Control*, Lommel, Belgium.

Poster presentations

- Schneidewind, U., van Berkel, M., Anibas, C., Vandersteen, G., Joris, I., Seuntjens, P. and Batelaan, O. [2015]. LPMLE3: A new analytical approach to determine vertical groundwater-surface water exchange flux under uncertainty and heterogeneity, *Geophysical Research Abstracts 17, EGU2015-5107*, Vienna, Austria.
- van Berkel, M., Zwart, H. J., Hogeweij, G. M. D., Vandersteen, G., van den Brand, H., de Baar, M. R. and ASDEX Upgrade team [2014]. Estimation of the thermal diffusion coefficient in fusion plasmas taking frequency measurement uncertainties into account, *4th Asia Pacific Transport Working Group (APTWG)*, Kasuga, Japan.
- van den Brand, H., de Baar, M. R., van Berkel, M., Bongers, W. A., Gianone, L. and Kasperek, W. [2014]. Microwave detection of instabilities in fusion plasmas, *26th Symposium Plasma Physics and Radiation Technology*, Lunteren, The Netherlands.
- van Berkel, M., Hogeweij, G. M. D., Vandersteen, G. and de Baar, M. R. [2013]. Determination of localized heat transport in fusion plasmas, *Physics@FOM*, Veldhoven, Netherlands.
- van Berkel, M., Hogeweij, G. M. D., and de Baar, M. R. [2012]. Determination of localized heat transport in fusion plasmas, *24th Symposium Plasma Physics and Radiation Technology*, Lunteren, The Netherlands.
- van Berkel, M., Hogeweij, G. M. D., de Baar, M. R., Nuij, P. W. J. M. and de Baar, M. R. [2012]. Real-time estimation of the thermal transport for real-time control purposes and experimental applications, *Physics@FOM*, Veldhoven, Netherlands.

Curriculum vitae

Matthijs van Berkel was born in 's-Hertogenbosch, the Netherlands, on June 11, 1983. He received his secondary education at the Technisch Instituut Sint-Jansberg in Maaseik, Belgium. At this institute he received his TSO degree in Industriële wetenschappen in 2003. In the same year he began his studies in Mechanical Engineering at the Eindhoven University of Technology, Eindhoven, the Netherlands. In 2010, he received the M.Sc. degree (*with great appreciation*) in Mechanical Engineering: Control Systems Technology. The subject of his Master's Thesis was wavelet analysis for real-time determination of the sawtooth behavior in non-stationary fusion plasmas. In the winter of 2008, he performed his master internship in Japan at Nagoya University's Department of Aerospace Engineering, where he worked on Control Moment Gyroscopes. After a three-month period as a full-time researcher in the Control Systems Technology group and a short break he started his Ph.D. research in 2011.

The subject of his Ph.D. research is the estimation of heat transport coefficients in fusion plasmas with a focus on electron heat transport. His Ph.D. research is performed within a formal collaboration between the Tokamak Physics group at the Dutch Institute For Fundamental Energy Research (FOM DIF-FER) and the Control Systems Technology Group at the Eindhoven University of Technology. In addition, there has been an intense collaboration with the Department of Fundamental Electricity and Instrumentation at the Vrije Universiteit Brussel, at which he also spent four months. In 2013, he received a short-term postdoctoral fellowship from the Japan Society for the Promotion of Science (JSPS) to conduct research at the National Institute for Fusion Science, Toki, Japan, where he stayed one year.